Institut für Physik und Astronomie
Universität Potsdam

Modeling Changes in Climate during Past Mass Extinctions

Kumulative Dissertation

zur Erlangung des akademischen Grades
„doctor rerum naturalium“(Dr. rer. nat.)
in der Wissenschaftsdisziplin „Klimaphysik“

eingereicht an der
Mathematisch-Naturwissenschaftlichen Fakultät
der Universität Potsdam

angefertigt am
Potsdam-Institut für Klimafolgenforschung

von

Julia Brugger

Ort und Tag der Disputation: Potsdam, 5. November 2021

Hauptbetreuer: Prof. Dr. Stefan Rahmstorf
Zweitbetreuer und 1. Gutachter: Dr. habil. Georg Feulner
2. Gutachter: Prof. Dr. Wolfgang Lucht
3. Gutachter: Prof. Dr. Kai Wünnemann

Published online on the
Publication Server of the University of Potsdam:
https://doi.org/10.25932/publishup-53246
https://nbn-resolving.org/urn:nbn:de:kobv:517-opus4-532468

Abstract

The evolution of life on Earth has been driven by disturbances of different types and magnitudes over the 4.6 million years of Earth's history (Raup, 1994, Alroy, 2008). One example for such disturbances are mass extinctions which are characterized by an exceptional increase in the extinction rate affecting a great number of taxa in a short interval of geologic time (Sepkoski, 1986). During the 541 million years of the Phanerozoic, life on Earth suffered five exceptionally severe mass extinctions named the "Big Five Extinctions". Many mass extinctions are linked to changes in climate (Feulner, 2009). Hence, the study of past mass extinctions is not only intriguing, but can also provide insights into the complex nature of the Earth system. This thesis aims at deepening our understanding of the triggers of mass extinctions and how they affected life. To accomplish this, I investigate changes in climate during two of the Big Five extinctions using a coupled climate model.

During the Devonian (419.2–358.9 million years ago) the first vascular plants and vertebrates evolved on land while extinction events occurred in the ocean (Algeo *et al.*, 1995). The causes of these formative changes, their interactions and their links to changes in climate are still poorly understood. Therefore, we explore the sensitivity of the Devonian climate to various boundary conditions using an intermediate-complexity climate model (Brugger *et al.*, 2019). In contrast to Le Hir *et al.* (2011), we find only a minor biogeophysical effect of changes in vegetation cover due to unrealistically high soil albedo values used in the earlier study. In addition, our results cannot support the strong influence of orbital parameters on the Devonian climate, as simulated with a climate model with a strongly simplified ocean model (De Vleeschouwer *et al.*, 2013, 2014, 2017). We can only reproduce the changes in Devonian climate suggested by proxy data by decreasing atmospheric CO_2. Still, finding agreement between the evolution of sea surface temperatures reconstructed from proxy data (Joachimski *et al.*, 2009) and our simulations remains challenging and suggests a lower δ^{18}O ratio of Devonian seawater. Furthermore, our study of the sensitivity of the Devonian climate reveals a prevailing mode of climate variability on a timescale of decades to centuries. The quasi-periodic ocean temperature fluctuations are linked to a physical mechanism of changing sea-ice cover, ocean convection and overturning in high northern latitudes.

In the second study of this thesis (Dahl *et al.*, submitted) a new reconstruction of atmospheric CO_2 for the Devonian, which is based on CO_2-sensitive carbon isotope fractionation in the earliest vascular plant fossils, suggests a much earlier drop of atmospheric CO_2 concentration than previously reconstructed, followed by nearly constant CO_2 concentrations during the Middle and Late Devonian. Our simulations for the Early Devonian with identical boundary conditions as in our Devonian sensitivity study (Brugger *et al.*, 2019), but with a low atmospheric CO_2 concentration of 500 ppm, show no direct conflict with available proxy and paleobotanical data and confirm that under the simulated climatic conditions carbon isotope fractionation represents a robust proxy for atmospheric CO_2. To explain the earlier CO_2 drop we suggest that early forms of vascular land plants have already strongly influenced weathering. This new perspective on the Devonian questions previous ideas about the climatic conditions and earlier explanations for the Devonian mass extinctions.

The second mass extinction investigated in this thesis is the end-Cretaceous mass extinction (66 million years ago) which differs from the Devonian mass extinctions in terms of the processes involved and the timescale on which the extinctions occurred. In the two studies presented here (Brugger *et al.*, 2017, 2021), we model the climatic effects of the Chicxulub impact, one of the proposed causes of the end-Cretaceous extinction, for the first millennium after the impact. The light-dimming effect of stratospheric sulfate aerosols causes severe cooling, with a decrease of global annual mean surface air temperature of at least 26°C and a recovery to pre-impact temperatures after more than 30 years. The sudden surface cooling of the ocean induces deep convection which brings nutrients from the deep ocean via upwelling to the surface ocean. Using an ocean biogeochemistry model we explore the combined effect of ocean mixing and iron-rich dust originating from the impactor on the marine biosphere. As soon as light levels have recovered, we find a short, but prominent peak in marine net primary productivity. This newly discovered mechanism could result in toxic effects for marine near-surface ecosystems. Comparison of our model results to proxy data (Vellekoop *et al.*, 2014, 2016, Hull *et al.*, 2020) suggests that carbon release from the terrestrial biosphere is required in addition to the carbon dioxide which can be attributed to the target material. Surface ocean acidification caused by the addition of carbon dioxide and sulfur is only moderate. Taken together, the results indicate a significant contribution of the Chicxulub impact to the end-Cretaceous mass extinction by triggering multiple stressors for the Earth system.

Although the sixth extinction we face today is characterized by human intervention in nature, this thesis shows that we can gain many insights into future extinctions from studying past mass extinctions, such as the importance of the rate of change (Rothman, 2017), the interplay of multiple stressors (Gunderson *et al.*, 2016), and changes in the carbon cycle (Rothman, 2017, Tierney *et al.*, 2020).

Zusammenfassung

In den 4,6 Milliarden Jahren Erdgeschichte wurde die Entwicklung des Lebens durch Störungen unterschiedlichster Art geprägt (Raup, 1994, Alroy, 2008). Ein Beispiel für solche Störungen sind Massenaussterben. Diese sind durch einen außergewöhnlichen Anstieg der Aussterberate einer großen Anzahl von Taxa in einem kurzen geologischen Zeitintervall gekennzeichnet (Sepkoski, 1986). Während der 541 Millionen Jahre des Phanerozoikums traten fünf außergewöhnlich schwere Massenaussterben auf. Viele Massenaussterben stehen mit Klimaveränderungen im Zusammenhang (Feulner, 2009). Die Untersuchung vergangener Massenaussterben ist daher nicht nur faszinierend, sondern gibt auch Einblicke in die komplexen Prozesse des Erdsystems. Diese Dissertation möchte unser Verständnis für die Auslöser von Massenaussterben sowie deren Auswirkungen auf das Leben erweitern. Dazu untersuche ich die Klimaveränderungen während zwei der fünf großen Aussterbeereignisse mit Hilfe eines gekoppelten Klimamodells.

Während des Devons (vor 419,2-358,9 Millionen Jahren) entwickelten sich die ersten Gefäßpflanzen und Wirbeltiere an Land, während im Ozean Massenaussterben stattfanden (Algeo *et al.*, 1995). Die Ursachen dieser tiefgreifenden Veränderungen, ihre Wechselwirkungen und ihre Zusammenhänge mit Klimaveränderungen sind noch wenig verstanden. Daher untersuchen wir die Sensitivität des Klimas des Devons bezüglich verschiedener Randbedingungen mit einem Klimamodell mittlerer Komplexität (Brugger *et al.*, 2019). Im Gegensatz zu Le Hir *et al.* (2011), die unrealistisch hohe Albedo Werte für den Boden verwenden, finden wir nur einen geringen biogeophysikalischen Einfluss von Änderungen der Vegetationsbedeckung. Außerdem können unsere Simulationen den starken Einfluss von Orbitalparametern, der mit einem Klimamodell mit stark vereinfachtem Ozeanmodell (De Vleeschouwer *et al.*, 2013, 2014, 2017) simuliert wurde, nicht reproduzieren. Die in Proxydaten gefundenen klimatischen Veränderungen im Devon können wir nur durch eine Verringerung des atmosphärischen CO_2 simulieren. Dennoch bleibt es eine Herausforderung, eine Übereinstimmung zwischen der aus Proxydaten (Joachimski *et al.*, 2009) rekonstruierten Entwicklung der Meeresoberflächentemperaturen und unseren Simulationen zu finden. Dies deutet auf ein niedrigeres δ^{18}O-Verhältnis des Meerwassers im Devon hin. Außerdem finden wir im Rahmen unserer Sensitivitätsstudien eine Klimavariabilität auf einer Zeitskala von Jahrzehnten bis Jahrhunderten.

Die quasi-periodischen Schwankungen der Ozeantemperatur werden durch einen physikalischen Mechanismus aus sich verändernder Meereisbedeckung, Konvektion und Umwälzbewegung in den hohen nördlichen Breiten des Ozeans angetrieben.

In der zweiten Studie dieser Dissertation (Dahl *et al.*, submitted) präsentieren wir eine neue Rekonstruktion des atmosphärischen CO_2 für das Devon, die auf CO_2-sensitiver Kohlenstoffisotopenfraktionierung in den frühesten Gefäßpflanzenfossilien basiert. Diese zeigt einen viel früheren Abfall der atmosphärischen CO_2-Konzentration als bisherige Rekonstruktionen, gefolgt von nahezu konstanten CO_2-Konzentrationen während des Mittel- und Spätdevon. Unsere Simulationen für das frühe Devon mit identischen Randbedingungen wie in unserer Sensitivitätsstudie (Brugger *et al.*, 2019), jedoch mit einer niedrigen atmosphärischen CO_2-Konzentration von 500 ppm, zeigen keinen direkten Konflikt mit verfügbaren Proxy- und paläobotanischen Daten. Zusätzlich bestätigen die Simulationen, dass unter den simulierten klimatischen Bedingungen die Kohlenstoff-Isotopenfraktionierung einen robusten Proxy für atmosphärisches CO_2 darstellt. Um den früheren CO_2-Abfall zu erklären, schlagen wir vor, dass frühe Formen von vaskulären Landpflanzen die Verwitterung bereits stark beeinflusst haben. Diese neue Sichtweise auf das Devon stellt bisherige Vorstellungen über die klimatischen Bedingungen und frühere Erklärungen für die devonischen Massenaussterben in Frage.

Das zweite in dieser Arbeit untersuchte Massenaussterben ist das Massenaussterben der späten Kreidezeit (vor 66 Millionen Jahren), das sich von denen im Devon in Bezug auf die beteiligten Prozesse und die Zeitskala der Aussterben unterscheidet. Eine der diskutierten Ursachen dieses Massenaussterbens ist der Chicxulub-Meteoriten-Einschlag. In den beiden hier vorgestellten Studien (Brugger *et al.*, 2017, 2021) modellieren wir die klimatischen Auswirkungen des Chicxulub Einschlags für das erste Jahrtausend nach dem Einschlag. Die durch die stratosphärischen Sulfataerosole verringerte Sonneneinstrahlung verursacht eine starke Abkühlung: die global und jährlich gemittelte Oberflächenlufttemperatur nimmt um mindestens 26°C ab und erholt sich erst nach mehr als 30 Jahren. Die plötzliche Abkühlung der Ozeanoberfläche löst bis in große Tiefen reichende Konvektion aus, die zum Nährstofftransport aus dem tiefen Ozean an die Ozeanoberfläche führt. Mit Hilfe eines biogeochemischen Modells des Ozeans untersuchen wir die kombinierte Wirkung dieser Durchmischung des Ozeans und eisenreichen Staubs aus dem Meteoriten auf die marine Biosphäre. Sobald wieder genügend Sonneneinstrahlung auf die Erdoberfläche trifft, erreicht die marine Nettoprimärproduktion ein kurzes, aber markantes Maximum. Dieser neu entdeckte Mechanismus könnte toxische Folgen für oberflächennahe Ökosysteme des Ozeans haben. Der Vergleich unserer Modellergebnisse mit Proxydaten (Vellekoop *et al.*, 2014, 2016, Hull *et al.*, 2020) deutet darauf hin, dass zusätzlich zum CO_2 aus dem Gestein des Einschlagortes Kohlenstoff aus der terrestrischen Biosphäre freigesetzt wird. Die Versauerung des Oberflächenozeans durch die

Zugabe von CO_2 und Schwefel ist nur moderat. Insgesamt deuten die Ergebnisse darauf hin, dass der Chicxulub Einschlag einen wesentlichen Beitrag zum Massenaussterben der späten Kreidezeit leistete, indem er das Erdsystem multiplen Stressoren aussetzte.

Auch wenn das heutige sechste Aussterben durch menschliche Eingriffe in die Natur geprägt ist, zeigt diese Dissertation, dass wir aus dem Studium vergangener Massenaussterben viele Erkenntnisse über zukünftige Massenaussterben gewinnen können, wie z. B. die Bedeutung der Änderungsrate (Rothman, 2017), ein besseres Verständnis des Zusammenspiels multipler Stressoren (Gunderson *et al.*, 2016) und die Rolle von Veränderungen im Kohlenstoffkreislauf (Rothman, 2017, Tierney *et al.*, 2020).

Contents

Publications

This thesis is based on the following manuscripts and publications:

A1: Brugger *et al.*, 2019: Brugger, J., Hofmann, M., Petri, S., & Feulner, G. 2019. On the Sensitivity of the Devonian Climate to Continental Configuration, Vegetation Cover, Orbital Configuration, CO_2 Concentration, and Insolation. *Paleoceanography and Paleoclimatology*, 34(8), 1375–1398.

A2: Dahl *et al.*, submitted: Dahl, T. W., Harding, M. A. R., Brugger, J., Feulner, G., Norrman, K. & Junium, C. Low atmospheric CO_2 levels before the emergence of forested ecosystems. *Submitted, Nat. Commun.*

A3: Brugger *et al.*, 2017: Brugger, J., Feulner, G., & Petri, S. 2017. Baby, it's cold outside: Climate model simulations of the effects of the asteroid impact at the end of the Cretaceous. *Geophys. Res. Lett.*, 44(1), 419–427.
Due to copyright reasons the accepted version of the manuscript is included here.

A4: Brugger *et al.*, 2021: Brugger, J., Feulner, G., Hoffmann, M., & Petri, S. 2021. A pronounced spike in ocean productivity triggered by the Chicxulub impact. *Geophys. Res. Lett.*, 48, e2020GL092260.

1 Introduction

During the 4.6 billion years of Earth's history, the Earth system has experienced many disturbances of different magnitudes and durations. From the beginning to today these formative changes have been crucial for the evolution of life (Sepkoski, 1986, Raup, 1994, Alroy, 2008, Lenton & Watson, 2011, p. 44-59). After more than 3 billion years which were dominated by simple forms of life, the Cambrian explosion (541.0 Ma, 1 Ma = 1 million years ago)[1] marked the starting point for the development of all groups of animals, initiated by the sudden appearance of hard-shelled and skeletal marine organisms (Hallam & Wignall, 1997, p. 29-30). This heralds the Phanerozoic which spans the time from 541 Ma to present. The evolution of life during the Phanerozoic was marked by several periods of mass extinctions which restructured the biosphere and were crucial for the subsequent development of the Earth system (Raup & Sepkoski, 1982, Hull, 2015). Five particularly severe mass extinctions are named the "Big Five Extinctions". Despite the long-lasting interest in the investigation of Phanerozoic extinctions (Cuvier & Jameson, 1818, Chamberlin, 1909, Newell, 1967 for early examples), our understanding about initial triggers of mass extinctions and how these triggers impact life is still vague. In many cases extinctions are linked to changes in climate (Feulner, 2009), yet these changes can be very different in nature, magnitude and speed.

This thesis investigates changes in climate utilizing simulations with a coupled climate model during two periods of mass extinction: the Devonian and the end Cretaceous. These two periods are chosen as they exhibit very different mechanisms of extinction. The Middle and Late Devonian as a whole is an interesting period for the investigation of extinctions as it is marked by multiple episodic decreases in biodiversity. However, these might not be caused by extinction in the first place, but rather by reduced origi-

1 The time data given here for the beginning and ending of eons, eras, periods, epochs and ages are based on the International Chronostratigraphic Chart, published by the International Commission on Stratigraphy (`https://stratigraphy.org/`). The times given for the mass extinctions are based on the mid points of the substages considered in Bambach (2006) unless otherwise noted.

nation (Bambach *et al.*, 2004, Alroy, 2008). Instead of standing out as a catastrophic event, it is debated whether the Frasnian-Famennian extinction (376.3 Ma) in the Late Devonian deserves a place among the five major Phanerozoic events (Bambach *et al.*, 2004). Therefore, our first study about the Devonian investigates the sensitivity of the Devonian Earth system to several forcings instead of focusing on the Frasnian-Famennian extinction (Brugger *et al.*, 2019). Proposed causes for the biodiversity decreases during the Devonian are diverse and uncertain (Algeo *et al.*, 1995), but one frequently cited hypothesis links the apparent extinction to the colonisation of land by plants (Algeo *et al.*, 1995, Algeo & Scheckler, 1998, Le Hir *et al.*, 2011). Hence, one of the investigated forcings in our study is the biogeophysical impact of increased vegetation cover. The second study of this thesis presents a new reconstruction of Devonian atmospheric CO_2 concentrations and casts doubt on the previously recognized idea of the influence of the evolution of land plants on atmospheric CO_2 concentrations (Dahl *et al.*, submitted).
The other period of mass extinction that is considered in this thesis is the end-Cretaceous mass extinction ($\approx$ 66 Ma). It is well-known for the proposed catastrophic cause by an asteroid impact (Alvarez *et al.*, 1980) and the long-running debate whether the impact or large volcanic eruptions caused the mass extinction (e.g. Keller, 1988, 2003). The two studies about the end-Cretaceous mass extinction explore changes in the Earth system in the immediate aftermath of the asteroid impact, demonstrating major disruptions of climate and the biosphere and thus supporting the impact hypothesis (Brugger *et al.*, 2017, 2021).
The role of catastrophes in the evolution of life on Earth has been a long debate (Cuvier, 1825, Darwin, 1859). Mass extinctions are seen as catastrophes today (Hallam & Wignall, 1997, p. 1, Raup, 1994), but how catastrophic a mass extinction is differs greatly. The gradual processes during the Devonian extinctions in contrast to the catastrophic asteroid impact scenario for the end-Cretaceous extinction illustrate two different manifestations of severe biodiversity crises. The fact that these two events unfolded in such different fashion makes them interesting candidates for the study of mass extinctions.

Besides the pure fascination to study the Earth's past, this work also aims to improve our understanding of the profound changes observed in the present Earth system which is already in the middle of a sixth extinction (Barnosky *et al.*, 2011). Human-induced biodiversity loss and climate change might represent the two most threatening problems for human civilization already today and will have much more far-reaching consequences in the future. Although the present mass extinction is not primarily caused by climate change, but can largely be attributed to overexploitation and land-use changes (Maxwell *et al.*, 2016, Leclère *et al.*, 2020), climate change is expected to exacerbate the mass extinction in the future (Urban, 2015). Thus, it is currently of great importance to better understand how mass extinction events and changes in climate are connected.

The following sections are intended to provide an introduction to the four manuscripts which form the main part of this thesis. Section 1.1 defines a mass extinction, Section 1.2 gives an overview over past mass extinctions while focusing on the Late Devonian and end-Cretaceous mass extinction and Section 1.3 outlines the motivation to model climatic changes during mass extinctions.

1.1. Characterization of mass extinctions

Sepkoski (1986) defines a mass extinction as "any substantial increase in the amount of extinction (i.e., lineage termination) suffered by more than one geographically widespread higher taxon[1] during a relatively short interval of geologic time, resulting in an at least temporary decline in their standing diversity." Within the scope of this definition mass extinctions are not a homogeneous group of events, but can differ in their specific characteristics (Bambach, 2006). Sepkoski (1986) notes that his definition is intentionally vague in order to contain a large number of uncertainties including the magnitude of decrease of a taxon, the number of affected taxa, the area over which a taxon is distributed, and the duration of an extinction event. These uncertainties arise due to the limited temporal, spatial and taxonomic resolution of biostratigraphic[2] studies (Sepkoski, 1986).

The given definition of a mass extinction and the mentioned uncertainties show how challenging it is to measure extinction. A common way is to determine the percent extinction or the extinction rate. To calculate the percent extinction the number of extinctions in an interval of geologic time (total extinction) is divided by the total taxa present (usually on family or genus level). To derive the extinction rate the percent extinction is divided by the estimated duration of the time interval (Hallam & Wignall, 1997, p. 16, Raup & Sepkoski, 1984). Although the extinction rate allows a better comparison of extinction events than the percent extinction, it contains a large uncertainty as the exact stage duration is poorly known and the choice of interval length critically determines the appearance of extreme values (Foote, 1994). In general, extinction data must be interpreted with caution considering several aspects: (i) Different data are based on different compilations of the fossil record. (ii) Some data are on family level, other are on genus level. (iii) The usage of different tabulation methods and levels of stratigraphic resolution for the evaluation of extinction data makes it difficult to compare extinction metrics (Bambach, 2006). (iv) The quality of a single database

1 In biology, a taxon describes a group of organisms with similar characteristics which differentiate them from other groups. Taxa are assigned a taxonomic rank in the hierarchical order of taxonomy. The highest taxonomic rank is the domain, followed by the kingdom, phylum (fauna) or division (flora), class, order, family, genus and species (Knoop & Müller, 2009, p.51-56).

2 Stratigraphy studies rock layers and layering. Biostratigraphy is a subdiscipline which correlates rocks and determines the age of rocks through the fossil content of the layers (Eide, 2005).

varies for different times due to uneven preservation and sampling (Alroy *et al.*, 2008).

Note that compilations of the fossil record suitable to derive extinction metrics are often limited to marine invertebrates as their fossil record provides closely spaced and abundant samples, less uncertainty in stratigraphic information and broad geographic coverage. In contrast, the record of continental life, in particular for vertebrate tetrapods, is scarce and incomplete (Hallam & Wignall, 1997, p. 4).

A well-known and widely-used database for analyzing past mass extinctions is the Sepkoski database (Sepkoski, 2002): It documents stratigraphic ranges for 36,000 marine genera on the substage level. Bambach (2006) analyses and compares the results of three different tabulation methods and different levels of stratigraphic resolution for evaluating the Sepkoski genus database. By focusing on the common features Bambach (2006), is able to highlight signals of particular importance in the extinction record. He identifies 18 peaks in the extinction rate (see Figure 1.1) which can be classified as a mass extinction following the definition of Sepkoski (1986). These are, however, largely diverse in terms of possible causes, magnitude and subsequent consequences for the marine fauna. In agreement with many other studies (Raup & Sepkoski, 1982, Raup, 1994), 5 of the 18 mass extinctions can be designated as particularly severe, known as the "Big Five Mass Extinctions" (Raup & Sepkoski, 1982). The end-Ordovician, the end-Permian and the end-Cretaceous extinctions show remarkably high extinction rates which are purely caused by extinction as opposed to decreased origination (Bambach, 2006, Alroy, 2008). In particular, the end-Permian and the end-Cretaceous extinction stand out as they mark a shift in the observed ecological equilibrium on a functional/morphological and anatomical/physiological level (Bambach *et al.*, 2002). The late-Frasnian and end-Triassic mass extinctions are not primarily characterized by high extinction rates, but by a combination of increased extinction with decreased origination leading to a loss in global diversity (Bambach *et al.*, 2004, Alroy, 2008). Information on the percentage of extinction given in this thesis is based on the Sepkoski database as this is a renowned and widely-used data source.

The peaks in extinction are superimposed on a continuous background extinction. In contrast to mass extinctions, background extinctions are mostly local extinctions which are limited to a few species or genera (Raup & Sepkoski, 1982). Background extinction, but also origination, have decreased since the Cambrian (Raup, 1994, Alroy, 2008). One cause for this is seen in the accumulation of species of higher taxa through time which decreases the chance of extinction (Alroy, 2008).
It is noticeable that there are several peaks in extinction during the Cambrian which are of the same magnitude as the peaks of the Big Five mass extinctions (see Figure 1.1). These are not counted among the severe extinctions as the absolute number of extinct

genera is small compared to the Big Five extinctions due to the much lower amount of existing taxa (Erwin, 2008). In addition, the loss in diversity could also be an artefact in the fossil record caused by the high abundance of well-preserved fossils for the Early Cambrian in contrast to the later Cambrian (Butterfield, 2003).

There has been a long discussion about a possible periodic cycle of ≈ 26 Myr of mass extinctions (Fischer & Arthur, 1977, Raup & Sepkoski, 1984, 1986, Sepkoski & Raup, 1986, Sepkoski, 1989, Benton, 1995, Kirchner & Weil, 2000, Rohde & Muller, 2005). Among the reasons given for the periodicity were asteroid impacts linked to extinction as well as the time needed to form new species which can be threatened by extinction (Alroy, 2008). However, more recent studies (Alroy, 2008, Bailer-Jones, 2009) do not find sufficient evidence to support this "most debated hypothesis by paleontologists over the last quarter century" (Alroy, 2008) .

Each of the Big Five mass extinctions is shortly characterized in Section 1.2, with a focus on the Late-Devonian and end-Cretaceous extinctions as these will be investigated in the main part of this thesis. The extinction is measured as percent extinction on the marine genus level based on the Sepkoski database and tabulated using Sepkoski's sorting routine, as given in Bambach (2006).

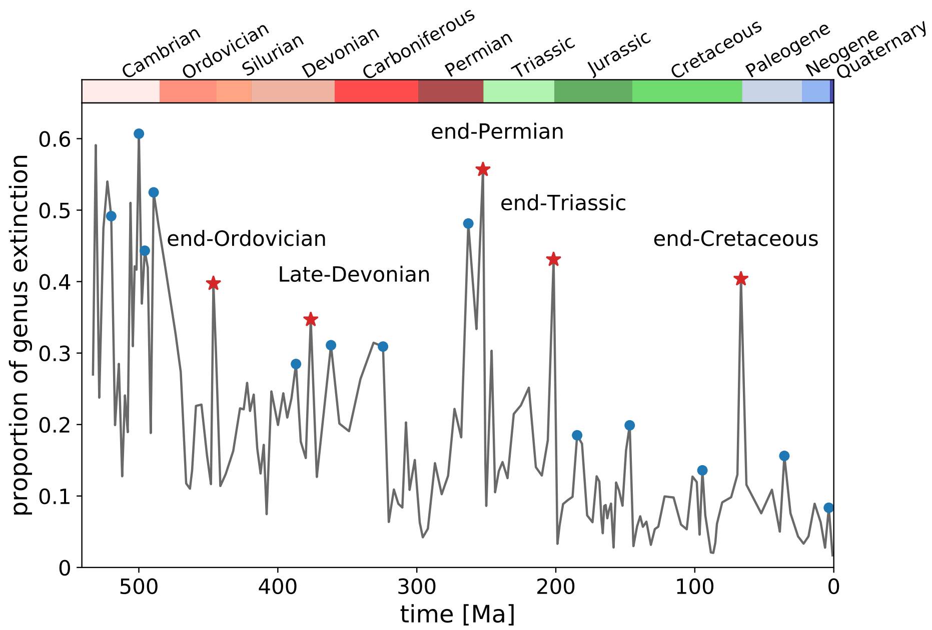

Figure 1.1 *Proportion of genus extinction for substages, based on the Sepkoski data in the Supplementary Information of Bambach (2006). The 18 mass extinctions which Bambach (2006) found to be peak extinctions for three different tabulation methods and different levels of stratigraphic resolution are marked with blue dots. The Big Five extinctions are marked with red stars and names. There are some additional substages for which the proportion of extinction shows peaks, but which extend over longer intervals and therefore have lower rates of extinction.*

1.2. The Big Five extinctions of the past

1.2.1. End-Ordovician Extinction (445 Ma)

During the Ordovician (485.4 – 443.8 Ma) life was flourishing and diversifying, in particular in the ocean (Great Ordovician Biodiversity Event, Servais & Harper, 2018). Marine diversity was however struck by a major mass extinction in the Late Ordovician. The end-Ordovician extinction is composed of two pulses with a genus-level percent extinction of 40% for the first pulse and 31% for the second (substage level) (Bambach, 2006). It is suspected that the extinction was linked to the southward movement of the continent Gondwana into polar regions resulting in the formation of a large ice sheet on Gondwana. The resulting decrease in sea level caused drained shelf regions limiting the habitat of marine organisms. In addition, tropical ocean temperatures critically decreased during the Late Ordovician (Finnegan *et al.*, 2012). To explain the observed glaciations, the high atmospheric CO_2 concentrations reconstructed for the Late Ordovician (14-22 times preindustrial levels, Lenton *et al.*, 2012) must have dropped below eight times preindustrial levels (Herrmann *et al.*, 2003). Hence, it was suggested that, among geologic processes, the earliest forms of non-vascular land plants increased weathering and therefore lowered atmospheric CO_2 levels. The associated change in nutrient input to the ocean which resulted in a productivity increase and regional ocean anoxia could have linked this process to the observed oceanic mass extinction (Lenton *et al.*, 2012, Porada *et al.*, 2016).

1.2.2. Late-Devonian Extinctions (387 and 376 Ma)

The Devonian period The Devonian (419.2 – 358.9 Ma) was a period of fundamental changes in the atmosphere, the ocean and the biosphere. Recent records of the atmospheric CO_2 concentration suggest a drop from high Early Devonian CO_2 concentrations of ≈ 2000 ppm to less than 1000 ppm in the Late Devonian, with strong fluctuations in between (Foster *et al.*, 2017). Sea surface temperature reconstructions from $\delta^{18}O$ show a time evolution similar to atmospheric CO_2 concentrations, with decreasing temperatures in the Early Devonian, increasing temperatures in the Middle Devonian and a decrease towards the end of the Devonian (Joachimski *et al.*, 2009). However, uncertainties in the proxy data is high: Sea surface temperature reconstructions for the Devonian are based on regional $\delta^{18}O$ proxy evaluation for different locations which likely do not represent global values for the Devonian (Joachimski *et al.*, 2009). Furthermore, the conversion from $\delta^{18}O$ to temperature is uncertain, as discussed in Brugger *et al.* (2019) and Henkes *et al.* (2018). In addition to the changes in CO_2, atmospheric oxygen concentrations increased from 75% to 125% of present levels during the Devonian (Dahl & Arens, 2020, Wade *et al.*, 2019).

The described changes in atmospheric conditions and climate were accompanied by important progress in the evolution of land plants: The Early Devonian saw the rise of root-building vascular plants on land which followed the spread of non-vascular plants already during the Ordovician and the colonization of non-rooted vascular plants during the preceding Silurian (Dahl & Arens, 2020). However, as the Early Devonian plants still lacked water-conducting cells and roots were shallow, they were restricted to wet lowlands (Algeo & Scheckler, 1998, Boyce & Lee, 2017). The evolution of deep-rooting arborescent trees in the Middle Devonian was followed by the first evolution of seeds in the Late Devonian. Deep roots and a reproduction which was not dependent on water transport of sperm made the spread of plants to drier upland areas possible (Dahl & Arens, 2020). In addition to the floral evolution, the first tetrapods settled on land (Clack, 2007).

The Devonian ocean was characterized by a large diversity in fish (Dahl *et al.*, 2010) and peak extent of stromatoporoid reefs in the Middle Devonian (Copper & Scotese, 2003). However, the Middle and Late Devonian ocean was also plagued by a series of mass extinctions: The Givetian extinction (387 Ma) in the Middle Devonian with a genus-level percent extinction of 25% was followed by the Frasnian-Famennian extinction (376 Ma, 35% genus-level percent extinction) which is one of the Big Five extinctions and consists of two peaks called the Lower and Upper Kellwasser events (Bambach, 2006). The most striking feature in the extinction record shows the collapse of reef ecosystems. The Kellwasser events are characterized by a sea-surface temperature drop of 3 and 6 °C, respectively, found in low latitude oxygen isotopes, and marine black shale deposition (Dahl & Arens, 2020). During the Upper Kellwasser event $\delta^{13}C$ values increase and there is evidence for ocean anoxia (Bambach, 2006, Dahl & Arens, 2020). This interplay points to an increased transport of the bio-limiting nutrient phosphorous (P) to the ocean which might have increased ocean productivity and therefore depleted oxygen concentration. By the end of the Devonian a third mass extinction (Hangenberg event, 362 Ma) with a genus-level percent extinction of 31% was observed in the ocean (Bambach, 2006). The Hangenberg event is characterized by a global increase of $\delta^{13}C$, sea-surface temperature and sea-level decrease and anoxic water masses (Dahl & Arens, 2020).

The Devonian features in general a high background genus-level percent extinction of 19% (without taking into account the peaks in extinction) and turnover processes with the described extinction events superimposed (Bambach, 2006). As the percent extinction is significantly lower than for the other four severe mass extinction, the Devonian period is often seen as a period of prolonged diversity decline combined with reduced origination rates rather than a period consisting of several mass extinctions (Bambach, 2006, Fan *et al.*, 2020). The lack of a coherent theory which can explain the extinctions supports this approach. In addition, the uncertain knowledge not only about the extinctions, but also about the characteristics of the Devonian Earth system in general motivates the investigation of the sensitivity of the Devonian climate depending on various parameters which have been linked to the Devonian extinctions (Brugger *et al.*, 2019). The two most widely discussed theories for the Devonian extinctions are shortly introduced below as they are key to understanding the sensitivity analysis in (Brugger *et al.*, 2019) and the novel finding of low atmospheric CO_2 concentrations already in the Early Devonian (Dahl *et al.*, submitted).

Influence of land plant evolution on oceanic mass extinction Land plants can influence weathering via the "weatherability" which describes how susceptible a surface is for weathering, and the weathering feedback which depends on temperature and CO_2. Processes via which plants affect weathering include the secretion of acids by roots and fungi, reworking of regoliths caused by the growth of roots and their effect on the hydrological cycle (Dahl & Arens, 2020). Hence, during the different steps of land plant evolution, continental weathering flux increased on a timescale of less than one million years (Dahl & Arens, 2020). This resulted in a decrease of atmospheric CO_2 and an increased P flux to the ocean via rivers. As P is a limiting nutrient in the ocean, this led to an increase in ocean productivity which increased oxygen consumption resulting in ocean anoxia and mass extinctions (Algeo *et al.*, 1995, Algeo & Scheckler, 1998, Dahl & Arens, 2020). On a longer timescale the system must have approached a new equilibrium as the increase in weathering flux is limited by the availability of weatherable rocks and weathering fluids (Dahl & Arens, 2020). However, each step in the evolution of land plants during the Devonian (deepening of roots, emergence of trees, first seed plants) might have caused an increase in the weathering flux. Temporal coincidence, information from proxy data and simple model simulations indicate that the Frasnian-Famennian extinction is connected to the emergence of trees and the Hangenberg event to the emergence of the first seed plants (Zhang *et al.*, 2020, Dahl & Arens, 2020).

Orbital cycles perturb Devonian carbon cycle The amount as well as the spatial and temporal distribution of solar radiation reaching Earth are determined by the shape of Earth's orbit and the tilt and orientation of its rotational axis which all change cyclically. Therefore, the values of the orbital parameters influence climate in a cyclical way, described by the Milankovitch theory (Milankovitch, 1941). The stratigraphic record of the Late Devonian shows evidence that both the Lower and Upper Kellwasser events are linked to a combination of a 405-kyr eccentricity minimum with a minimum of the million-years long eccentricity cycle. The resulting decreased seasonality led to carbon accumulation on land, visible in an increase in marine $\delta^{13}C$. The following transition into the 405-kyr eccentricity maximum is accompanied by a rise in temperature and an intensification of the hydrological cycle resulting in increased weathering with the consequences described above. The many evolutionary changes during the Late Devonian resulted already in a climate state characterized by vigorous carbon cycle disturbance. The described additional perturbation of the carbon cycle caused by the Earth's orbital parameters was likely the final trigger for the Frasnian-Famennian mass extinction (De Vleeschouwer *et al.*, 2017).

1.2.3. End-Permian Extinction (252 Ma)

The end-Permian extinction was the most severe of the Big Five extinctions, with 56% marine genus extinction (substage level) (Bambach, 2006), $\approx$ 90% loss on the marine species level (Sahney & Benton, 2008) and a selectivity towards strongly calcifying organisms (Payne *et al.*, 2004). On land, many tetrapod families (Irmis & Whiteside, 2012) and several orders of insects (Labandeira, 2005) went extinct. In contrast to earlier studies (Cascales-Miñana & Cleal, 2014), it was recently suggested that the extinction did not affect land plants (Nowak *et al.*, 2019). There is increasing evidence that this mass extinction is strongly correlated with volcanic eruptions forming the Siberian Traps large igneous province (LIP, Ernst & Youbi, 2017) and triggered in particular by the emplacement of sill intrusions which led to an increase of atmospheric CO_2 concentrations for several ten thousand years (Burgess *et al.*, 2017). A combination of proxy data and model results shows a series of severe consequences for marine life: The increased CO_2 concentrations together with a strong warming led to an acidified surface ocean and increased weathering. As a consequence of the enhanced weathering, the higher nutrient input increased marine export productivity which finally resulted in euxinic conditions in the ocean. This sequence of difficult life conditions culminated in the mass extinction at the very end of the Permian and in the Early Triassic (Jurikova *et al.*, 2020).

1.2.4. End-Triassic Extinction (202 Ma)

The Late Triassic is characterized by a prolonged interval of stepwise decreased diversity (Rigo *et al.*, 2020, Lucas & Tanner, 2018) which might have been caused not primarily by extinction, but in combination with reduced origination (Bambach *et al.*, 2004). Combining the two latest stages of the Triassic, the marine genus-level percent extinction was 47% (Bambach, 2006) with strong regional decimation of reefs (Lucas & Tanner, 2018) and complete extinction of conodonts (Ginot & Goudemand, 2020). The extinction record for terrestrial tetrapods and plants is very ambiguous, but it likely suggests a turnover rather than an extinction, with regional, but not global extent (Lucas & Tanner, 2015, Tanner *et al.*, 2004). As for the end-Permian extinction, the cause of this extinction is usually thought to be eruptions that form LIPs. Several perturbations found in the $\delta^{13}C$ record for the Late Triassic can be linked to the pulsed activity of the Central Atlantic Magmatic Province (CAMP, Lindström *et al.*, 2017). Climate and carbon-cycle modeling of pulsed volcanic carbon and sulfur emissions suggest that the individual volcanic pulses had only a minor effect, but the recurrence of the disturbances which resulted in changes of temperature, ocean pH, sea level, and ocean circulation represented the largest stress factor for marine life (Landwehrs *et al.*, 2020).

1.2.5. End-Cretaceous Extinction (66 Ma)

The Late Cretaceous and the end-Cretaceous mass extinction The Cretaceous (145.0 – 66.0 Ma) is the final period of the Mesozoic Era. It is characterized by a greenhouse climate with a reduced equator-to-pole temperature gradient with maximum temperatures in the earlier Late Cretaceous ($\approx$ 100 – 98 Ma) which decreased towards the Late Cretaceous (O'Brien *et al.*, 2017, Huber *et al.*, 2018). This temperature decrease is attributed to a decline in atmospheric CO_2 concentrations from $\approx$ 1.000 ppm in the early Late Cretaceous to $\approx$ 500 ppm in the Latest Cretaceous (Foster *et al.*, 2017), possibly caused by less volcanic activity linked to reduced sea-floor spreading rates (Larson, 1991), and continental rifting (Brune *et al.*, 2017) as well as by changes in ocean circulation (Friedrich *et al.*, 2012).

Life in the Late Cretaceous was diverse: The marine realm was, among others, populated by fish and reptiles in various sizes, ammonites and rudists as well as single-celled organisms like planktonic and benthic forminifera and coccolithophorid algae (Ebersole *et al.*, 2013, Hallam & Wignall, 1997, p. 190-201). The continents were inhabited by dinosaurs, other reptiles, birds (Vajda & Bercovici, 2014), the first mammals (Wilson *et al.*, 2016) and a high diversity of insects (Gao *et al.*, 2019). The first angiosperm plants evolved in the Early Cretaceous, followed by their rapid distribution in the Late Cretaceous (Hess, 2005), and forests expanded to high latitudes (Sewall *et al.*, 2007).

The end-Cretaceous mass extinction ($\approx$ 66 Ma, Renne *et al.*, 2013) had a genus-level percent extinction of 40% (Bambach, 2006) and was thus not the most severe mass extinction, but it became certainly the most famous one due to the disappearance of the dinosaurs. Not only disappeared the nonavian dinosaurs (Fastovsky & Sheehan, 2005), but also pterosaurs, many marine reptiles, the ammonites, marine protists and certain groups of planktic foraminifera and coccolithophorids (Vajda & Bercovici, 2014, D'Hondt, 2005). Among land plants various angiosperm species went extinct, whereas some bryophytes and ferns recovered quickly, indicated by spore spikes which are dated to the centuries after the impact (Vajda & Bercovici, 2014). Many other organisms (for example benthic foraminifera, crocodilians, mammals) did not suffer from dramatic extinction, but were reduced in abundance and diversity or experienced a widespread turnover (Vajda & Bercovici, 2014). The timing of the extinction of many of the organisms relative to the Cretaceous-Paleogene (K-Pg) boundary is still uncertain (for example D'Hondt, 2005, O'Leary *et al.*, 2013).

From the stratigraphic perspective, the K-Pg boundary is generally characterised by a clay layer, whose thickness varies with distance from the impact site (Artemieva & Morgan, 2009). It contains microkrystites, shocked mineral grains (Smit & Brinkhuis, 1996) and soot (Robertson *et al.*, 2013). A closer inspection of the fine-grained material revealed a significantly increased concentration in iridium (Alvarez *et al.*, 1980). As the Earth's crust is typically depleted in iridium, the observation of high iridium concentrations led to the famous and still debated hypothesis of Alvarez *et al.* (1980) that the end-Cretaceous mass extinction was caused by an asteroid impact.

The Chicxulub impact Alvarez *et al.* (1980) proposed that the impact of a large asteroid (diameter of 10±4 km) led to the formation of huge amounts of dust which blocked sunlight, therefore reduced photosynthesis and disrupted food webs. It was further suggested that the darkness caused an "impact winter", i.e. a cold period caused by the impact (Covey *et al.*, 1994).
The discovery of the Chicxulub crater on the Yucatán Peninsula, Mexico, was an important piece of the puzzle to strengthen the recognition of the impact theory (Hildebrand *et al.*, 1991): The formation of the crater could be dated to the K-Pg boundary (although this was later debated by e.g., Keller *et al.*, 2007) and was of the right size to fit the hypothesis of Alvarez *et al.* (1980).
However, it was shown that only submicrometer-size dust particles can reach the stratosphere to cause global and longer-lasting cooling whereas larger particles are washed out from the troposphere on a timescale of days to months (Pope *et al.*, 1997, Pope, 2002, Pierazzo *et al.*, 2003). As the fraction of fine dust was small, the dust had only a small and short-term effect on radiation (Pope *et al.*, 1997, Pope, 2002). Instead of the impact dust, the specific characteristics of the impact target on the Yucatán Peninsula, rich in sulfur-bearing evaporites and carbonates, were critical to the environmental effects of the impact (Pierazzo *et al.*, 1998). When sulfate aerosols formed and entered the stratosphere, they were distributed globally and absorbed longwave radiation, but scattered shortwave radiation for several years. This led to a stratospheric warming and a cooling of the Earth's surface (Toon *et al.*, 1997, Pierazzo *et al.*, 1998, 2003). The reduced solar irradiation decreased photosynthesis, but in particular caused a severe temperature drop lasting for two to three decades (Brugger *et al.*, 2017). In contrast, the formation of CO_2 from vaporized carbonates caused a long-term global warming (Toon *et al.*, 1997) which can be effective for thousands of years (Smit & Brinkhuis, 1996).
A further aspect to consider is the generation of wildfires which are indicated by soot and charcoal found in the K-Pg boundary layer (Kring, 2007) and the Chicxulub crater (Gulick *et al.*, 2019). Local fires could have been triggered by the impactor while approaching the Earth or by the rising fireball close to the impact site, whereas ejecta reentering the atmosphere could have ignited fires globally (Toon *et al.*, 1997). When reaching the stratosphere, the soot from fires had a light-blocking effect for several

years which is suggested to act stronger on limiting photosynthesis compared to sulfate aerosols (Bardeen *et al.*, 2017). Additionally, the atmospheric CO_2 levels were increased by the combustion of terrestrial carbon (Tyrrell *et al.*, 2015).
Although the impact dust did not have the light-dimming effect predicted by Alvarez *et al.* (1980), it was likely important for delivering huge amounts of nurtrients to the ocean causing an algal bloom with devastating consequences for the marine ecosystem (Brugger *et al.*, 2021).
The detailed picture we have today of the Chicxulub impact is based on a combination of the investigation of the global ejecta layer (Kring, 2007, Schulte *et al.*, 2010) with results from several drilling programs at the impact site (Urrutia-Fucugauchi *et al.*, 1996, 2004, Gulick *et al.*, 2019) and numerical modeling of the impact (Pierazzo *et al.*, 1998, 2003, Artemieva & Morgan, 2009, Artemieva *et al.*, 2017). For the exploration of the link between the climatic effects of the impact and the end-Cretaceous mass extinction, the data from impact modeling (Pierazzo *et al.*, 2003, Artemieva *et al.*, 2017) have been of high importance (Brugger *et al.*, 2017, 2021).

Two competing theories: Impact or volcanism? Since its publication, the impact hypothesis of Alvarez *et al.* (1980) has been debated and criticised to not being consistent with the observed, much more gradual changes across the K-Pg boundary (Keller, 1988, 1994, 2003, Schoene *et al.*, 2015, Keller *et al.*, 2020). Among the many other suggested causes of the end-Cretaceous mass extinction (e.g., reversal of the magnetic field, Reid *et al.*, 1976; warming, McLean, 1985; variations in solar radiation, Sonnenfeld, 1978), the eruptions of the Deccan Traps, a large igneous province on the Deccan Plateau in India, has become a competing hypothesis (McLean, 1985, Keller, 2003, Schoene *et al.*, 2015, Keller *et al.*, 2020). Large igneous provinces are proposed causes for various other mass extinctions as well (see Section 1.3.1).
The most recent studies agree that Deccan volcanism was not the dominant cause for the mass extinction, but the proposed scenarios differ: finding maximum eruption rates before and after the Chicxulub impact, Schoene *et al.* (2019) favor an interplay of Deccan Trap volcanism and the Chixculub impact in causing the extinction. In contrast, Sprain *et al.* (2019) find the largest eruptions after the K-Pg boundary and deduce that Deccan Trap volcanism cannot be responsible for the changes observed at the K-Pg boundary, but the Chicxulub impact could have triggered the intense eruptions following the K-Pg boundary. Also, Hull *et al.* (2020) support Deccan Trap eruptions before and after the Chicxlub impact, but the mass extinction and carbon cycle changes coincide only with the impact. In summary, after four decades of debate it is no longer questioned that the Chicxulub impact played a major role in the cause of the end-Cretaceous mass extinction, but the contribution of Deccan Trap volcanism and the interplay of both needs to be further investigated.

1.3. Modeling climate during mass extinctions

The given definition of mass extinctions (see Section 1.1) and the brief summary of the Big Five mass extinctions (see Section 1.2) suggest that mass extinctions are induced by strong and relatively fast perturbations of the Earth system which critically disturb the living conditions to which the ecosystems' structure and functions are accustomed (Hull & Darroch, 2013, Hull, 2015). Climate plays a significant role for determining the living conditions and hence, mass extinctions are strongly linked to changes in climate (Crowley & North, 1988, Twitchett, 2006, Feulner, 2009, Fan *et al.*, 2020). The description of the five mass extinctions and their possible causes (Section 1.2) has shown this connection already. In this section, the mechanisms underlying this relationship will be summarized, followed by a discussion of suitable climate models for modeling climatic changes during mass extinctions. Following this, a statement about the need to model climatic changes during mass extinctions motivates the four studies which form the main part of this thesis.

1.3.1. Climatic changes as causes of mass extinctions

Climatic changes during mass extinctions include changes in annual or seasonal temperature or the hydrological cylce, sea-level rise or regression, formation or melting of sea ice, ice sheets and glaciers, and changes in atmospheric and oceanic circulation. The affected climate variables interact with each other and influence the marine and terrestrial biogeochemical cycles, in particular the carbon cycle. These complex interactions include feedback mechanisms which can amplify or dampen the initial change in climate (Crowley & North, 1988, Twitchett, 2006, Ruddiman, 2013, p.15-16, Alley *et al.*, 2002). The diverse proposed drivers for these changes in climate will be described together with the response of the climate system and possible consequences for the biosphere.

Impacts of comets or asteroids Extraterrestrial events have been proposed as a possible cause for mass extinctions, with impacts of comets or asteroids being the most widely discussed. The characteristics and magnitude of the climatic consequences of impacts described here strongly depend on the respective impact's energy.
The high kinetic energy of an impactor induces local and short-term effects on the biosphere. When striking the Earth's surface, part of the object's kinetic energy is converted into blast waves, seismic waves and, if the impact is marine, tsunami waves (Toon *et al.*, 1997). Compared to a terrestrial impact of the same size, marine impacts and the resulting tsunami waves affect a larger area (Wünnemann & Weiss, 2015). The blast damages, earthquakes and tsunamis can have devastating consequences for the biosphere on a local scale, but cannot trigger global mass extinction events (Toon *et al.*, 1997). In addition, the strong shock waves arising during the impact process produce nitrogen oxide when moving through air. Its strongest and most harmful effect is the

depletion of the ozone layer which can be reinforced by other chemical processes in the perturbed atmosphere (Toon *et al.*, 1997) and would allow ultraviolet radiation to reach the Earth's surface with its dangerous effects for life.
The largest fraction of the impact energy is, however, transformed into kinetic energy of the impact debris and thermal energy which lead to the ejection of pulverized and vaporized projectile and target material. As already discussed for the Chicxulub impact (see Section 1.2.5), products with atmospheric effects formed during an impact depend on the characteristics of the target and projectile material. Typically, they consist of dust with a short-term dimming and cooling effect of days to months, soot which can cause a stronger darkness with associated cold on timescales of several years, and warming greenhouse gases (in particular CO_2 and water vapor) which cause a warming for thousands of years (Toon *et al.*, 1997). In addition to the effects of an impact on the atmosphere, the cooling as well as the addition of dust, CO_2 and S to the ocean perturbs the marine nutrient and carbon cycle (Tyrrell *et al.*, 2015, Brugger *et al.*, 2017, 2021).

Although impacts of the size of the Chicxulub impact are statistically to be expected every 100 – 200 million years on the Earth (Chapman & Morrison, 1994, Neukum *et al.*, 2001) and the impact hypothesis has been proposed for extinctions other than the end-Cretaceous mass extinction, there is no evidence for a significant global contribution of an impact for any of the other mass extinctions (Grieve, 1998, McGhee *et al.*, 1984, Schmieder & Kring, 2020). Possibly, the specific nature of the target rocks on the Yucatán Peninsula containing sulfates played a key role for having such severe consequences for the biosphere after the Chicxulub impact (Grieve, 1998).

Supernova explosions or gamma-ray bursts An additional extraterrestrial cause for mass extinctions could be nearby supernovae explosions (Ellis & Schramm, 1995) or gamma-ray bursts (Melott *et al.*, 2004) which would destroy the ozone layer. This has been proposed for the end-Ordovician mass extinction (Melott *et al.*, 2004) and recently for the Hangenberg event which is the last of the Devonian extinctions (Fields *et al.*, 2020). Although the suggested mechanisms seem reasonable (Ellis & Schramm, 1995), there is a lack of evidence to support these hypotheses with geologic and paleontologic data.

Large volcanic eruptions In contrast to the discussed extraterrestrial drivers, large volcanic eruptions, often forming LIPs, are part of the Earth system itself and could trigger changes in climate and mass extinctions. LIPs are formed over 1-3 million years during several pulses (hundred thousands to a million years long), consisting of many decadal-length eruptions (Self *et al.*, 2014, Bond & Wignall, 2014), and release both sulfur dioxide (SO_2) and CO_2 into the atmosphere. When reaching the stratosphere, SO_2 can induce short-term cooling (timescale of years) (Bond & Wignall, 2014) and environmental acidification (Schmidt *et al.*, 2016) by the formation of sulfate aerosols. The

interaction of individual successive eruptions can prolong the cooling phase. However, the detailed course of environmental perturbations caused by SO_2 injection is strongly dependent on how explosive the eruptions are and the cooling shows a non-linear relation with the amount of injected SO_2 (Schmidt *et al.*, 2016). Degassing of volcanic CO_2 leads to a long-term warming on a timescale of thousands of years (Zeebe, 2012) and can cause ocean acidification and anoxia (Jurikova *et al.*, 2020). Although the effect of CO_2 degassing by single volcanic eruptions is likely small, the total release of CO_2 during LIP formation can be several times the CO_2 mass in today's atmosphere (Bond & Wignall, 2014). Hence, due to the long-lasting warming effect of CO_2, the warming adds up to be significant (Bond & Wignall, 2014).
For mass extinctions, the longer-lasting temperature increase and the perturbations of the marine carbon cycle (e.g., changes in ocean productivity, ocean acidification, formation of ocean anoxia Bond & Wignall, 2014, Self *et al.*, 2014, Jurikova *et al.*, 2020) are of particular relevance. The strong variations in climate during LIP formation, induced by their pulsed eruptions, could represent an additional significant stress for marine life (Landwehrs *et al.*, 2020). Other gases emitted during volcanic eruptions have a negligible effect on temporal and spatial scales relevant for mass extinction (Bond & Wignall, 2014).

Furthermore, there are several climate forcings which could be relevant for mass extinctions if they reach unusual or extreme states, are changed over shorter timescales than usual, and/or are combined with other factors:

Plate tectonics Changes in the continental configuration, driven by moving tectonic plates, influence the reflection and absorption of incoming solar radiation as well as oceanic and atmospheric circulation and hence, heat transport (Hay, 1996). These changes strongly determine the living conditions on land. However, as they usually only change gradually, they are only linked to mass extinctions if extreme continental configurations are reached or if they change in combination with other factors. An example is the importance of the poleward movement of Gondwana during the Late Ordovician mass extinction (see Section 1.2.1).
Furthermore, plate tectonics strongly determines the carbon cycle: On the one hand, CO_2 is released to the atmosphere or ocean by volcanism at the margins of converging and diverging plates, or by metamorphism of carbonate rocks at converging plates (Brune *et al.*, 2017). On the other hand, weathering, acting as CO_2 sink, increases during the process of tectonic uplifting which brings fresh and unweathered rock to the surface. The weathering feedback mechanism, determined by temperature and precipitation, is also influenced when continents move in different climate zones (Ruddiman, 2013, p. 110-117).

Orbital configuration Changes in solar radiation received by the Earth's surface which are relevant for mass extinctions are largely caused by changes in the orbital configuration.

The three orbital parameters influence the absolute amount of insolation as well as the strength of the seasonalities and change cyclically (Ruddiman, 2013, p. 160-172). A combination of specific orbital parameters can induce strong and relatively fast changes in insolation with the potential to alter climate and living conditions significantly (De Vleeschouwer *et al.*, 2014, De Vleeschouwer *et al.*, 2017), as discussed for the Late Devonian in Section 1.2.2 and in Brugger *et al.* (2019).

Marine and terrestrial biogeochemical perturbations Climatic effects of changes in the chemical composition of the atmosphere and the ocean have already been described in the paragraphs about the extraterrestrial drivers and large-scale volcanism. Changes in the composition of atmosphere and ocean can also be the result of perturbations in the terrestrial and oceanic biogeochemical cycles (in particular carbon cycle, nitrogen cycle, phosphorus cycle, oxygen cycle). The described effect of plate tectonics and the influence of plants on the biogeochemical cycles, as described for the Late Ordovician (Section 1.2.1) and for the Devonian (Section 1.2.2), play a major role here. The anthropogenic perturbation of the biogeochemical cycles, and in particular the carbon cycle, is the most recent example (Ciais *et al.*, 2013, p. 465-570, Rothman, 2017). There is evidence that perturbations of the carbon cycle which exceed a critical rate (at longer timescales) or a critical size (at shorter timescales) result in mass extinctions. The anthropogenic perturbation of the marine carbon cycle is approaching this critical size already by 2100 (Rothman, 2017).

The drivers for changes in climate linked to mass extinctions work on very different timescales, implying that the resulting climatic changes also have different timescales. These timescales critically determine the various progressions of mass extinction events and how catastrophic they are.

Due to the chaotic and non-linear nature of the climate system, the climate can change abruptly by crossing a threshold driving the climate system in a different climate state at a rate which is faster than the forcing and determined by positive feedbacks and interactions in the climate system (Alley *et al.*, 2002, p.14). There is evidence for abrupt climate transitions in the past in the paleontologic record which sometimes coincide with observed changes in the biosphere or even extinction (Crowley & North, 1988, Westerhold *et al.*, 2020). The low resolution of the paleontologic and paleoclimatic record, before the Cenozoic in particular (Westerhold *et al.*, 2020), together with the challenge of understanding and modeling abrupt transitions, limit the existing information on the link between past abrupt climatic changes and changes in the biosphere. However, as we approach several tipping points[1] of the Earth system (Steffen *et al.*, 2018), further investigation of past abrupt climate transitions and their link to changes in the biosphere seems to be of high importance to broaden the understanding.

1.3.2. Suitable climate models for modeling past climates

The investigation of past climate is based on two methods: On the one hand, proxy data stored in climate archives like marine and terrestrial sediment cores, corals, ice cores and tree rings can be evaluated. As a direct measurement of climate variables of the deep past is impossible, "proxies" are a substitute for a climate variable. Biotic proxies are used to reconstruct climate based on the occurrence of plants or animals. Geological-geochemical proxies give information about past climate by tracing the movement of physical or chemical material through the climate system (Ruddiman, 2013, p. 56-69). On the other hand, numerical climate models of different complexity can be used to address a variety of questions considering past climate states. The combination of both methods leads to a very comprehensive approach for understanding past climates. Examples for such combinations are the evaluation of model results with proxy data or the inclusion of chemical tracers comparable with proxy data in models (Tierney *et al.*, 2020). Additionally, as proxy signals are restricted to a specific time and location, further investigations with models can complete and broaden the picture and can help to understand the underlying processes.

Climate models aim to replicate the behavior of the climate system or of several components of the climate system. The climate system is composed of the atmosphere, the hydrosphere (consisting of the ocean, lakes, rivers and the global water cycle), the cryosphere (consisting of all forms of ice), the pedosphere (the Earth's continental surface), the litosphere (the Earth's crust and the upper mantle) and the biosphere (consisting of all ecosystems, i.e. including all living beings) (Claussen *et al.*, 2002). There is broad consensus that today the anthroposphere (consisting of the human interventions in the system) forms an additional relevant component which likely will have increasing importance (Schellnhuber, 1999, Donges *et al.*, 2017). The term "Earth system" is suggested to consist of both the "natural" climate system and the anthroposphere (Schellnhuber, 1999, Claussen *et al.*, 2002). Each component has a characteristic temporal and spatial scale which is crucial for understanding the climate system and which needs to be taken into account when developing climate models (Stocker, 2018,

1 The term "tipping point" is defined similar, but broader than "abrupt climate change" in terms of the rate of change and by not focusing on climatic variables. Although the term "tipping point" can be applied for all periods of Earth's history, the definition can be easily applied in particular to those tipping points which are connected to anthropogenic climate change (Lenton *et al.*, 2008).

p. 5, 6). The components of the climate system are non-linear systems which interact non-linearly with each other and hence form a highly complex system. Climate models describe the processes of each component and their interaction using mathematical and physical equations (McFarlane, 2011). The equations are based on knowledge from different scientific disciplines, including physics, biology, chemistry, geology, but also social sciences to integrate the human influence (Weart, 2013, Donges *et al.*, 2017, Stocker, 2018, p. 14). Due to the complexity of the climate system, the model equations cannot be solved analytically. To solve, them they are discretized in time and space, i.e. the continuous time is substituted by discrete time steps and the surface or volume is divided into grid cells (McGuffie & Henderson-Sellers, 2014, p. 282). In addition, processes which are either not resolved on the model grid or are poorly understood are replaced by a parametrization, i.e. a simplified or statistical description of the process (McFarlane, 2011).

The complexity of a climate model is determined by its spatial dimension and resolution, the included components of the climate system and the number of represented processes (Stocker, 2018, p. 23-26). It is important to keep in mind that a more complex model is not necessarily a better model, but the research questions determine the suitability of a model (Schellnhuber, 1999, Feulner, 2009, Tierney *et al.*, 2020, Stocker, 2018, p.23). Therefore, the well-considered choice of a suitable model is of high importance.
The simplest climate model is an energy-balance model with zero dimension. It is based on an energy conservation equation stating that the heat content of the atmosphere is determined by the solar radiation absorbed by the Earth's surface and the long wave radiation emitted by the Earth surface. The processes described in this model are a strong simplification of the complex radiative and atmospheric processes and in particular do not include the greenhouse effect. (Stocker, 2018, p. 30-34).
The most complex models are three dimensional general circulation models (GCMs) which couple models of the atmosphere, the ocean (often including biogeochemical processes), terrestrial vegetation and sea ice. GCMs explicitly calculate the exchange of energy, mass and relevant tracers within and among model components (Stocker, 2018, p. 26). As GCMs aim to represent the Earth system as accurately as possible, the basic differential equations describing the behavior of the climate system are discretised and solved (McGuffie & Henderson-Sellers, 2014, p. 282). The model variables of the state-of-the-art GCMs are calculated on a lateral grid of $2^\circ \times 2^\circ$ or less (e.g., Beljaars *et al.*, 2018, Danabasoglu *et al.*, 2020, Dunne *et al.*, 2020). The large amount of processes represented in three dimensions on a fine grid makes the operation of these GCMs computationally very expensive and limits their use to simulations of several hundred years (Eyring *et al.*, 2016). However, many paleoclimate studies require simulations of several thousand years or large ensembles of sensitivity simulations. With these sensitivity simulations the range of possible climate states induced by the uncertainty

in boundary conditions like solar constant, continental configuration, atmospheric CO_2 concentration, orbital configuration, vegetation cover can be explored (Feulner, 2009). Therefore, Earth system models of intermediate complexity (EMICs) are a useful tool for paleoclimate studies (Feulner, 2009, Schellnhuber, 1999). EMICs employ coarser grid structures, increase process parametrisation and reduce either the atmosphere or the ocean dimension to achieve faster integration times (Claussen *et al.*, 2002, McGuffie & Henderson-Sellers, 2014, p. 240-272).

This motivates the choice of an intermediate complexity model for the studies in this thesis. The EMIC CLIMBER-3α (Montoya *et al.*, 2005) consists of the three-dimensional ocean general circulation model Modular Ocean Model v3 (MOM3) which has a horizontal resolution of 3.75°× 3.75 ° and 24 vertical layers of 25 m thickness at the surface to ≈500 m thickness for the deep ocean (Pacanowski & Griffies, 1999). MOM3, as implemented in CLIMBER-3α, is supplemented with some additional parametrizations and numerical schemes (Montoya *et al.*, 2005, Hofmann & Morales Maqueda, 2006). The atmospheric component is the fast atmospheric model POTSDAM2 with a coarse resolution of 22.5 ° in longitude and 7.5 ° in latitude. POTSDAM2 is a statistical-dynamical model, based on the assumption that the long-term evolution of the atmosphere can be described by large-scale fields of the main atmospheric variables and synoptic-scale processes are expressed in a statistical way (Petoukhov *et al.*, 2000). Another simplification of the atmosphere model is the reduction to 2.5 dimensions, i.e. temperature and specific humidity are only modeled explicitly on the surface level. For higher atmospheric levels, temperature is scaled linearly and specific humidity exponentially with height (Petoukhov *et al.*, 2000). In addition, CLIMBER-3α includes the dynamic/thermodynamic sea-ice model ISIS which has the same horizontal resolution as the ocean model. It models one layer of ice and one layer of snow (Montoya *et al.*, 2005, Fichefet & Morales Maqueda, 1997). The interactions between atmosphere and surface are described by a land-surface model which includes biogeophysical effects of terrestrial vegetation. The surface types need to be prescribed (open ocean, sea ice, forest, grass, bare soil or glaciers) and are characterized by values for albedo, roughness and evapotranspiration. CLIMBER-3α can be extended to CLIMBER-3α+C (Hofmann *et al.*, 2019) by including a dynamical biogeochemical ocean module which takes into account marine biogeochemistry and the marine carbon cycle (Six & Maier-Reimer, 1996). With the inclusion of the marine biogeochemistry and carbon cycle it is possible to model the influence of changes in climate on marine life which makes CLIMBER-3α+C particularly suitable for the investigation of marine mass extinction (Brugger *et al.*, 2021). We use a CLIMBER-3α version with improved lapse rate parametrization and more realistic ice and snow albedo values which was used successfully in other deep-time paleoclimate studies (e.g., Feulner & Kienert, 2014, Feulner, 2017, Landwehrs *et al.*, 2020).

1.3.3. The need of climate simulations of mass extinctions

In order to make further progress in the exploration of mass extinctions, the processes involved need to be understood on an ecological timescale, i.e. the short timescale on which the process of life and death takes place (Bambach, 2006). In addition, the geographic distribution of extinctions need to be investigated (Bambach, 2006). Paleontological data can give information about past mass extinctions, both about the extinct genera and species by evaluation of the fossil record, but also about mechanisms which could have caused the mass extinction. However, although techniques have significantly improved and make it possible to evaluate deep-time paleontological data on timescales of less than 1000 years at well-preserved locations with high sedimentation rates (for example Vellekoop *et al.*, 2014, 2016), the temporal and spatial resolution of geological data is inherently limited (Tierney *et al.*, 2020). Another issue of proxy records is their limitation to give information about correlations, but not about causality. Instead, climate models are an important tool in the study of the causal story of a mass extinction.

1.4. Scope and content of this thesis

This thesis is written with a climate physicist's eye on mass extinctions and therefore focuses in particular on analyzing the interaction of changes in the climate system's different components during mass extinctions by using climate models. The approach aims to better understand the causal relationship between changes in climate and mass extinctions. Still, comparison with proxy data is always integrated as the combination of paleoclimate modeling with proxy evaluation is key for understanding past changes in the Earth system, but also for being able to transfer knowledge of the past to predictions of the future (Tierney *et al.*, 2020).

The following questions guide this thesis:

(I) How sensitive was the Devonian Earth system to changes in continental configuration, vegetation cover, orbital configuration, CO_2 concentration and insolation?

(II) What effect did land plant evolution have during the Devonian on the atmospheric CO_2 concentration?

(III) Which climatic effects did the formation of sulfate aerosols have after the Chicxulub impact?

(IV) What role did the impact dust play in the end-Cretaceous mass extinction?

These questions are addressed in four scientific articles, of which three are published and one is under review.

In the following, I give an overview of the individual articles that are presented in Chapter 2. Supplementary material to articles 1, 2 and 4 can be found in the Appendix.

Article 1

On the Sensitivity of the Devonian Climate to Continental Configuration, Vegetation Cover, Orbital Configuration, CO_2 Concentration, and Insolation

J. Brugger, M. Hofmann, S. Petri, G. Feulner

In this article the characteristics of the Devonian climate are explored in a number of sensitivity experiments using the coupled climate model CLIMBER-3α. The sensitivity to continental configuration, vegetation cover, orbital configuration, CO_2 concentration and insolation is first tested separately. Subsequently, three best-guess simulations are constructed which aim to represent best the three climate states of the Early, Middle and Late Devonian. Their results are compared with proxy data. In addition, a discovered mode of climate variability on centennial timescales is described and investigated. Julia Brugger and Georg Feulner designed the study. Julia Brugger carried out the model simulations and analyzed them together with all coauthors. Julia Brugger and Matthias Hofmann explored and explained the centennial-scale climate variability. Julia Brugger and Stefan Petri performed and evaluated various test experiments which showed strong evidence that this climate variability is not a numerical artefact. Julia Brugger and Georg Feulner wrote the article, with input from all coauthors. Julia Brugger created Figures 1 to 4, 6 to 10 and 12. Georg Feulner created Figures 5 and 11.
Published in Paleoceanography and Paleoclimatology (2019).

Article 2

Low atmospheric CO_2 levels before the emergence of forested ecosystems

T. W. Dahl, M. A. R. Harding, J. Brugger, G. Feulner, K. Norrman, C. Junium

Based on CO_2-sensitive carbon isotope fractionation in Early Devonian vascular plant fossils the previous atmospheric CO_2 records are revised and a lower atmospheric CO_2 concentration of $\approx 500\,$ppm is reconstructed for the Early Devonian. This suggests a strong drawdown of atmospheric CO_2 concentrations already during the rise of the earliest vascular plants, but before the emergence of forests. Simulations with the coupled climate model CLIMBER-3α for the Early Devonian support the use of these plant fossils for the reconstruction of atmospheric CO_2 concentrations. Tais Dahl designed and led the study. He wrote the manuscript together with input from all coauthors. Julia

Brugger performed the modeling with CLIMBER-3α, created the figures to support the model output, and analyzed the model output together with Georg Feulner. Julia Brugger, Georg Feulner and Tais Dahl discussed how to reconcile model output and proxy data.
This manuscript is submitted to Nature Communications.

Article 3
Baby, it's cold outside: Climate model simulations of the effects of the asteroid impact at the end of the Cretaceous
J. Brugger, G. Feulner, S. Petri

In this study, the coupled climate model CLIMBER-3α is used to simulate climate in the immediate aftermath of the Chicxulub impact. Based on information from geophysical impact modeling, different scenarios for the short-term darkening due to sulfate aerosols and the long-term warming from atmospheric CO_2 are elaborated and tested in model experiments. Julia Brugger and Georg Feulner designed the study. Stefan Petri implemented model adjustments and improvements. Julia Brugger carried out the model simulations and analyzed them together with Georg Feulner. Julia Brugger and Georg Feulner wrote the article with input from all coauthors. Julia Brugger created all figures supporting the article.
Published in Geophysical Research Letters (2017).
Due to copyright reasons the accepted version of the manuscript is included here.

Article 4
A pronounced spike in ocean productivity triggered by the Chicxulub impact
J. Brugger, G. Feulner, M. Hoffmann, S. Petri

Building on our first article on the end-Cretaceous mass extinction (Brugger *et al.*, 2017), this study focuses on changes in the marine realm in the immediate aftermath of the Chicxulub impact using CLIMBER-3α+C which comprises the coupled climate model CLIMBER-3α extended by a biogeochemical ocean module. In addition to the investigation of the atmospheric effects of sulfur and CO_2, their effect in the ocean is analyzed. Furthermore, impact dust from the projectile is modeled and the effect of the nutrients contained in the dust on ocean productivity is explored. Julia Brugger and Georg Feulner designed the study. Matthias Hofmann implemented a dust module, with

the help from Julia Brugger and Stefan Petri. Julia Brugger and Matthias Hofmann implemented model adjustments and improvements, with the help from Stefan Petri. Julia Brugger carried out the model simulations and analyzed them together with Georg Feulner and Matthias Hofmann. Julia Brugger and Georg Feulner wrote the paper with input from all coauthors. Julia Brugger created all figures supporting the article.
Published in Geophysical Research Letters (2021).

2

Original manuscripts

On the Sensitivity of the Devonian Climate to Continental Configuration, Vegetation Cover, Orbital Configuration, CO_2 Concentration, and Insolation
J. Brugger, M. Hofmann, S. Petri, G. Feulner
Published in Paleoceanography and Paleoclimatology (2019), doi:10.1029/2019PA003562
https://agupubs.onlinelibrary.wiley.com/doi/full/10.1029/2019PA003562

Low atmospheric CO_2 levels before the emergence of forested ecosystems
T. W. Dahl, M. A. R. Harding, J. Brugger, G. Feulner, K. Norrman, C. Junium
This manuscript is submitted to Nature Communications.

Baby, it's cold outside: Climate model simulations of the effects of the asteroid impact at the end of the Cretaceous
J. Brugger, G. Feulner, S. Petri
Published in Geophysical Research Letters (2017), doi:10.1002/2016GL072241
https://agupubs.onlinelibrary.wiley.com/doi/full/10.1002/2016GL072241
Due to copyright reasons the accepted version of the manuscript is included here.

A pronounced spike in ocean productivity triggered by the Chicxulub impact
J. Brugger, G. Feulner, M. Hoffmann, S. Petri
Published in Geophysical Research Letters (2021), doi:10.1029/2020GL092260
https://agupubs.onlinelibrary.wiley.com/doi/10.1029/2020GL092260

2.1. On the Sensitivity of the Devonian Climate to Continental Configuration, Vegetation Cover, Orbital Configuration, CO_2 Concentration, and Insolation

Paleoceanography and Paleoclimatology

RESEARCH ARTICLE
10.1029/2019PA003562

Key Points:
- We investigate the sensitivity of the Devonian climate using a coupled ocean-atmosphere model
- The observed cooling is mainly caused by decreasing atmospheric carbon dioxide levels
- Higher temperatures inferred from proxies suggest different oxygen isotope ratios in the Devonian

Supporting Information:
- Supporting Information S1

Correspondence to:
J. Brugger and G. Feulner,
brugger@pik-potsdam.de;
feulner@pik-potsdam.de

Citation:
Brugger, J., Hofmann, M., Petri, S., & Feulner, G. (2019). On the sensitivity of the Devonian climate to continental configuration, vegetation cover, orbital configuration, CO_2 concentration, and insolation. *Paleoceanography and Paleoclimatology*, *34*, 1375–1398. https://doi.org/10.1029/2019PA003562

Received 12 FEB 2019
Accepted 12 JUL 2019
Accepted article online 21 JUL 2019
Published online 23 AUG 2019

On the Sensitivity of the Devonian Climate to Continental Configuration, Vegetation Cover, Orbital Configuration, CO_2 Concentration, and Insolation

Julia Brugger[1,2,3], Matthias Hofmann[1], Stefan Petri[1], and Georg Feulner[1]

[1]Potsdam-Institut für Klimafolgenforschung (PIK), Mitglied der Leibniz-Gemeinschaft, Postfach 60 12 03, Potsdam, Germany, [2]Institut für Physik und Astronomie, Karl-Liebknecht-Straß, Universität Potsdam, Potsdam, Germany, [3]Berlin-Brandenburgisches Institut für Biodiversitätsforschung, Altensteinstraß, Berlin, Germany

Abstract During the Devonian (419 to 359 million years ago), life on Earth witnessed decisive evolutionary breakthroughs, most prominently the colonization of land by vascular plants and vertebrates. However, it was also a period of major marine extinctions coinciding with marked changes in climate. The cause of these changes remains unknown, and it is therefore instructive to explore systematically how the Devonian climate responds to changes in boundary conditions. Here we use coupled climate model simulations to investigate separately the influence of changes in continental configuration, vegetation cover, carbon dioxide (CO_2) concentrations, the solar constant, and orbital parameters on the Devonian climate. The biogeophysical effect of changes in vegetation cover is small, and the cooling due to continental drift is offset by the increasing solar constant. Variations of orbital parameters affect the Devonian climate, with the warmest climate states at high obliquity and high eccentricity. The prevailing mode of decadal to centennial climate variability relates to temperature fluctuations in high northern latitudes which are mediated by coupled oscillations involving sea ice cover, ocean convection, and a regional overturning circulation. The temperature evolution during the Devonian is dominated by the strong decrease in atmospheric CO_2. Albedo changes due to increasing vegetation cover cannot explain the temperature rise found in Late Devonian proxy data. Finally, simulated temperatures are significantly lower than estimates based on oxygen isotope ratios, suggesting a lower δ^{18}O ratio of Devonian seawater.

1. Introduction

The Devonian (419 to 359 Ma, 1 Ma = 1 million years ago) is a key period in Earth's history characterized by fundamental changes in the atmosphere, the ocean, and the biosphere. With respect to the evolution of life, the Devonian is best known for the diversification of fish as well as the colonization of the continents by vascular plants and vertebrates. Although microbial mats and nonvascular plants could be found on land even before the Devonian (Boyce & Lee, 2017), the appearance of vascular land plants beginning in the Early and Middle Devonian was certainly an important first step toward modern land ecosystems. By the Late Devonian, vascular plants had vastly diversified, going hand in hand with the evolution of more advanced leaves and root systems (Algeo & Scheckler, 1998; Algeo et al., 1995). In the ocean, coral stromatoporoid reefs reached their largest extent during the Phanerozoic in the Middle Devonian (Copper & Scotese, 2003) and fish evolved into rich diversity (Dahl et al., 2010). Finally, in the Late Devonian, the first tetrapods moved from ocean to land (Brezinski et al., 2009; Clack, 2007).

While the Devonian is best known for these evolutionary breakthroughs, it is also a period of species mass extinctions. The extinction rate during the Devonian is marked by three distinct peaks (Bambach, 2006), with the highest pulse (the Frasnian-Famennian mass extinction, 378–375 Ma) ranking among the "Big Five," that is, the five most severe mass extinctions in Earth's history (Bambach, 2006). The cause of these extinctions, which mostly took place in the ocean (Bambach, 2006), is still under debate, as it is challenging to explain the episodic nature and duration of the extinctions (Algeo et al., 1995). Discussed causes for the Frasnian-Famennian extinction are a bolide impact (McGhee, 1996; McGhee et al., 1984), volcanic activity (Ma et al., 2016), changes in sea level (Bond & Wignall, 2008; Ma et al., 2016), rapid temperature variations (McGhee, 1996; Ma et al., 2016), and the development of ocean anoxic waters (Bond & Wignall, 2008; Ma et al., 2016).

Paleoceanography 10.1029/2019PA003562

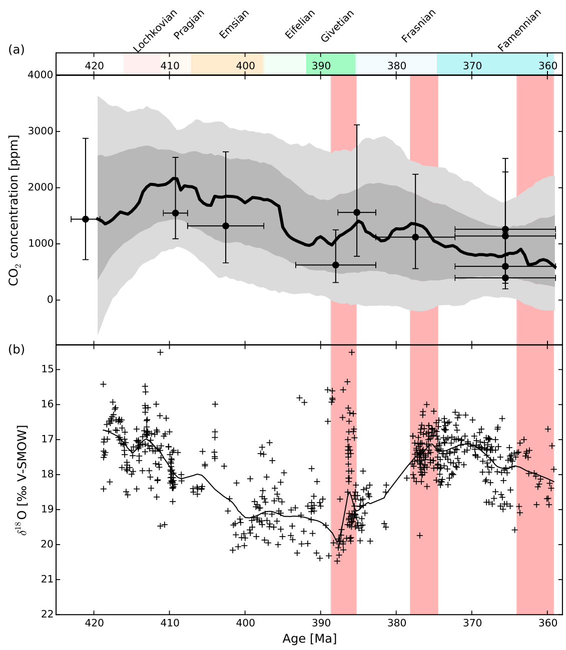

Figure 1. (a) Atmospheric CO_2 concentration in the Devonian following Foster et al. (2017). The black circles represent the data from different proxies. The thick black line is the most likely LOESS fit taking into account the uncertainties in both age and CO_2. The dark and light gray bands show the 68% and 95% confidence intervals. (b) $\delta^{18}O$ values from conodont apatite from Joachimski et al. (2009) but using a different NBS120c standard for calibration (Lécuyer et al., 2003). Note the inverted scale on the *y* axis since an increase in $\delta^{18}O$ translates into a temperature decrease. The light pink shading indicates the time intervals of the three Devonian periods of mass extinction: the late Givetian extinction from 389 to 385 Ma, the Frasnian-Famennian extinction (or Kellwasser event) from 378 to 375 Ma, and the Late Famennian extinction (Hangenberg event) from 364 to 359 Ma (Bambach, 2006).

The multitude of remarkable biospheric changes during the Devonian occurred against a backdrop of considerable changes in atmospheric composition. Although the uncertainties of CO_2 estimates for the Devonian from proxy compilations are large, they suggest a decrease from about 2,000 ppm in the Early Devonian to below 1,000 ppm in the Late Devonian (Foster et al., 2017); see Figure 1a. Note that this recent CO_2 compilation agrees with older compilations in the general decreasing trend during this time but reports lower CO_2 concentrations for the Devonian than older proxy studies (Royer, 2006) due to screening and revision of some records (see Methods in Foster et al., 2017); the values in the new compilation are also much lower than the CO_2 concentrations based on the GEOCARB model (Berner, 1994, 2006; Berner & Kothavala, 2001) frequently used in earlier modeling studies. In contrast to the decrease in carbon dioxide, oxygen levels witnessed an exceptionally strong rise about 400 Ma (Dahl et al., 2010; Wade et al., 2018). Recent modeling studies have investigated the forcing due to changes in the atmospheric O_2 concentration, suggesting a climate state-dependent climate response which is, however, small compared to the influence of CO_2 during the Phanerozoic (Poulsen et al., 2015; Wade et al., 2018).

These changes in atmospheric composition, and in particular the drop in atmospheric CO_2 concentrations, also resulted in climatic changes, which in turn affected the biosphere. Indeed, $\delta^{18}O$ oxygen isotope data from marine microfossils (a proxy for seawater temperature shown in Figure 1b) indicate a greenhouse climate in the Early Devonian and much cooler temperatures in the Middle Devonian (Joachimski et al., 2009). For the Late Devonian, proxy studies (Joachimski et al., 2009; van Geldern et al., 2006) indicate rising temperatures again which are still challenging to reconcile with the decreasing CO_2 concentrations. During the late Famennian, Earth's climate cooled again (Brezinski et al., 2009; Joachimski et al., 2009), with some studies even indicating glaciations (Brezinski et al., 2008, 2009; Caputo, 1985; Caputo et al., 2008). Furthermore, the Late Devonian was a period of fast sea level variations (Brezinski et al., 2009; Haq & Schutter, 2008; Johnson et al., 1985; Ma et al., 2016; Sandberg et al., 2002), with periods of sea level transgression being linked to the development of ocean anoxic conditions (Bond & Wignall, 2008; Johnson et al., 1985).

As any other period in Earth's history, the 60 million years spanning the Devonian is characterized not only by long-term changes in temperature but also by large fluctuations in temperature around these longer-term trends (see Figure 1b). Furthermore, there are several studies stressing the importance of astronomical forcing for the climate during the Devonian. The geologic record of the Devonian shows cyclic structures (De Vleeschouwer et al., 2013, 2017) which can be interpreted as the result of astronomical cycles according to Milankovitch theory (Milankovitch, 1941). The configuration of Earth's orbit and rotational axis determines the total amount as well as the spatial and temporal distribution of solar radiation and therefore impacts climate. In addition, identifying astronomical cycles in the geologic record can help assign a timescale to cyclic features observed in the geologic record and thus a timescale for palaeoclimatic changes (De Vleeschouwer et al., 2013, 2014, 2017).

In an effort to link the changes in the various components of the Devonian Earth system, there are several studies investigating potential connections between land plant evolution, climate change, and the oceanic mass extinction (Algeo & Scheckler, 1998; Algeo et al., 1995; Berner, 1994; Goddéris & Joachimski, 2004; Le Hir et al., 2011; Simon et al., 2007). It is suggested, for example, that the increase of weathering due to the spreading of plants on land could have been a cause of the decrease in atmospheric carbon dioxide (Algeo & Scheckler, 1998; Algeo et al., 1995; Berner, 2006). Additionally, the increased weathering rates could have lead to a higher transport of phosphorus to the ocean, promoting eutrophication with its negative consequences for life in the ocean (Algeo & Scheckler, 1998; Algeo et al., 1995).

Given the multitude of changes in the Earth system during the Devonian and the intricate coupling of atmosphere, ocean, and biosphere, it is challenging to disentangle causes and effects and to determine which forcings are most important for Devonian climate change. In this study, we test the sensitivity of the Devonian climate to different forcings in order to quantify their relevance. We therefore set up simulations with a coupled ocean-atmosphere model considering three different continental configurations representing the Early, Middle, and Late Devonian. In addition, changes in the solar constant, in atmospheric carbon dioxide concentrations, in orbital parameters, and in the spatial distribution of vegetation are systematically tested. Concerning the influence of land plants, this study focuses on their impact on the climate via biogeophysical effects, in particular changes in albedo and evapotranspiration.

This paper is organized as follows. Section 2 describes the coupled climate model used in this study, the various sensitivity experiments which serve to investigate the influence of changes in different parameters throughout the Devonian as well as the boundary conditions for three simulations which are representative for climate states of the Early, Middle, and Late Devonian. Results from the sensitivity simulations are presented and discussed in section 3. Section 4 highlights an ocean-sea ice mechanism resulting in climate oscillations at high northern latitudes. Section 5 discusses the climate evolution through the Devonian based on simulations for three time slices and compares the results to other modeling as well as proxy studies. Finally, Section 6 summarizes our key findings and discusses the broader implications of our results.

2. Modeling Setup

2.1. Model Description

To be able to assess the sensitivity of the Devonian climate to a wide range of parameters, we use CLIMBER-3α, a relatively fast coupled Earth system model of intermediate complexity (Montoya et al., 2005). Its main component consists of a modified version of the ocean general circulation model MOM3 (Hofmann & Morales Maqueda, 2006; Pacanowski & Griffies, 1999) used at a horizontal resolution of 3.75° × 3.75° with 24 vertical levels. The coupled model further includes a dynamic/thermodynamic sea ice model (Fichefet & Morales Maqueda, 1997) operated at the resolution of the ocean model and a fast statistical-dynamical atmosphere model (Petoukhov et al., 2000) with a coarse spatial resolution of 22.5° in longitude and 7.5° in latitude. Atmosphere-surface interactions (including the biogeophysical effect of terrestrial vegetation) are modeled by a land surface model distinguishing six prescribed surface types (open ocean, sea ice, forest, grass, bare soil, and glaciers) characterized by albedo, roughness, and evapotranspiration. CLIMBER-3α compares well with other models in model intercomparison projects (e.g., Eby et al., 2013; Zickfeld et al., 2013). For the simulations of the Devonian climate presented in this paper, we employ a model version with improved lapse rate parametrization and more realistic ice and snow albedo values

Paleoceanography 10.1029/2019PA003562

Table 1
Overview of Simulations Investigating the Sensitivity of the Devonian Climate System to Various Parameters

Sensitivity experiments	Continents	S (W/m^2)	CO_2 (ppm)	Land cover	ε (°)	e	ω (°)
	415 Ma						
Continental configuration	380 Ma	1,319.1	1,500	Bare	23.5	0	0
	360 Ma						
		1,315.3					
Solar constant	380 Ma	1,319.1	1,500	Bare	23.5	0	0
		1,321.3					
			1,000				
CO_2 concentration	380 Ma	1,319.1	1,500	Bare	23.5	0	0
			2,000				
Vegetation distribution	380 Ma	1,319.1	1,500	Bare	23.5	0	0
				Early Devonian vegetation			
				Middle Devonian vegetation			
				Late Devonian vegetation			
				All shrub			
				All trees			
					22.0	0	0
					22.0	0.030	0, 45, 90, 135, 180, 225, 270, 315
					22.0	0.069	0, 45, 90, 135, 180, 225, 270, 315
					23.5	0	0
Orbital parameters	380 Ma	1,319.1	1,500	Bare	23.5	0.030	0, 45, 90, 135, 180, 225, 270, 315
					23.5	0.069	0, 45, 90, 135, 180, 225, 270, 315
					24.5	0	0
					24.5	0.030	0, 45, 90, 135, 180, 225, 270, 315
					24.5	0.069	0, 45, 90, 135, 180, 225, 270, 315
	415 Ma	1,315.3	2,000	Early Devonian Vegetation			
Best-guess simulations	380 Ma	1,319.1	1,500	Middle Devonian Vegetation	23.5	0	0
	360 Ma	1,321.3	1,000	Late Devonian Vegetation			

Note. Settings for the continental configuration, the solar constant S, the atmospheric CO_2 concentration, the vegetation distribution, the obliquity ε of Earth's axis, the eccentricity e of its orbit, and the precession angle ω are listed for all simulations.

(Feulner & Kienert, 2014) already used in studies of a wide variety of deep-time palaeoclimate problems (e.g., Brugger et al., 2017; Feulner, 2017; Feulner et al., 2015). The surface model of CLIMBER-3α is also used in the coarser-resolution model CLIMBER-2 and compares well with more sophisticated models when simulating the biogeophysical effects of vegetation on climate (Ganopolski et al., 2001).

2.2. Boundary Conditions and Design of the Numerical Experiments

The main aim of this study is to simulate the climate evolution through the Devonian by designing three "best guess simulations" representative of the Early, Middle, and Late Devonian. These simulations use the most likely boundary conditions in terms of the distribution of continents, vegetation, the solar constant, and the atmospheric carbon dioxide level. In addition, we systematically investigate the sensitivity of the Devonian climate to changes in continental configuration, vegetation distribution, solar constant, atmospheric carbon dioxide levels, and orbital parameters by varying each of these boundary conditions separately while keeping all others fixed. The insights gained from these sensitivity experiments help to interpret the results from the best guess simulations and thus to identify the dominant drivers to climate changes during the Devonian.

Table 1 summarizes the experiments and their parameter values. In order to facilitate comparisons for the sensitivity experiments, we keep as many boundary conditions as possible fixed at values representative of the Middle Devonian around 380 Ma. The sensitivity experiments considering the influence of continental

Paleoceanography 10.1029/2019PA003562

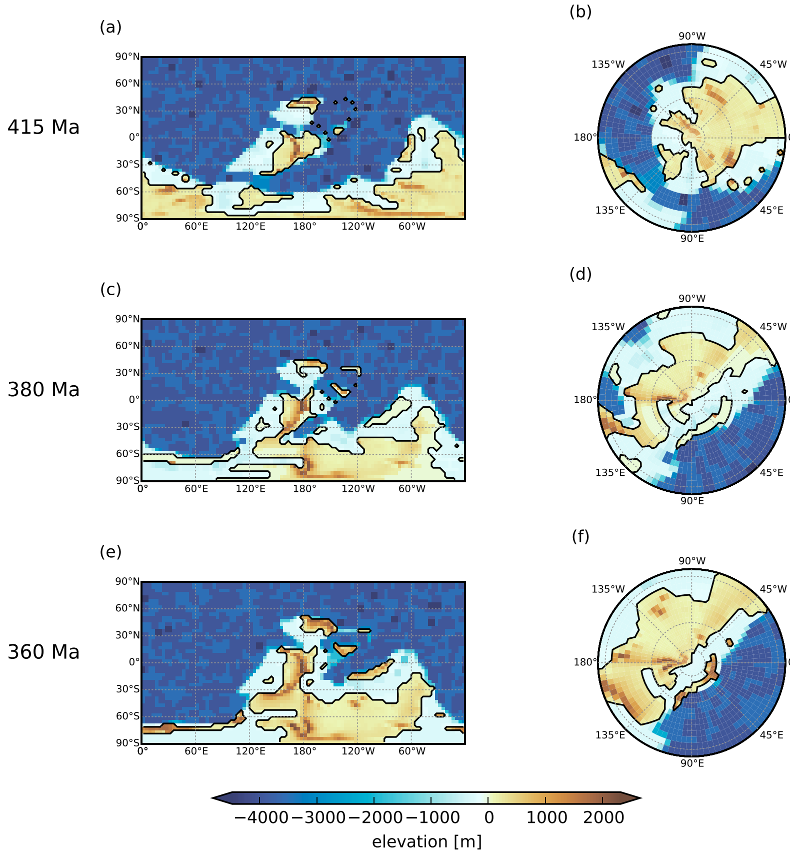

Figure 2. Continental configuration, ocean depth, and elevation for the three Devonian time slices at the spatial resolution of our ocean model. (left column) Global maps. (right column) South Polar view, from 26°S to 90°S. (a, b) 415 Ma. (c, d) 380 Ma. (e, f) 360 Ma.

configuration, vegetation, and orbital configuration are therefore run at a solar constant of $S = 1,319.1$ W/m^2 (section 2.2.2) and a fixed carbon dioxide concentration of 1,500 ppm (section 2.2.3). Vegetation is set to bare land in all simulations, except for the sensitivity experiments considering vegetation (section 2.2.4). Apart from the sensitivity experiments investigating the influence of changes in orbital parameters (section 2.2.5), we use orbital parameters of an idealized (or median) orbit with obliquity $\varepsilon = 23.5°$ and eccentricity $e = 0$. This obliquity is similar to the present-day value; using a circular orbit makes this configuration independent of precession; that is, it minimizes seasonality for a given obliquity. All model simulations are initialized from an ice-free state with constant present-day ocean salinity and a smoothed sea surface temperature (SST) profile which is symmetrical about the equator and approximates modern observations. The simulations are integrated for 4,000 model years until climate equilibrium is approached. The design of the sensitivity experiments (sections 2.2.1 to 2.2.4) as well as of the best guess simulations (section 2.2.6) will be described in more detail in the following.

2.2.1. Continental Configurations

To test the influence of the continental configuration on the Devonian climate, we set up three model runs using continental configurations representing three time slices during the Early Devonian (415 Ma), Middle Devonian (380 Ma), and Late Devonian (360 Ma), respectively, based on reconstructions (Scotese, 2014). The three different Devonian continental configurations, shown in Figure 2, are characterized by an arrangement of the continents' largest fraction in the Southern Hemisphere and no land northward of 60°N. Throughout the Devonian, the most significant changes affect the distribution of land and ocean areas around the South Pole. For our sensitivity experiments with respect to these three Devonian continental configurations, it is assumed that there are no land plants; that is, the land surface type is set to bare land throughout, and all other boundary conditions remain fixed; see Table 1.

2.2.2. Solar Constant

The effect of changes in the solar constant is investigated by adjusting the solar constant for each Devonian timeslice based on the best estimate (Kopp & Lean, 2011) for the present-day solar constant of 1,361 W/m^2 and a scaling according to a standard solar evolution model (Bahcall et al., 2001), yielding values of 1,315.3, 1,319.1, and 1,321.3 W/m^2 for the Early, Middle, and Late Devonian, respectively. All other parameters are fixed: We use continental configuration and a CO_2 concentration (1,500 ppm) representative for the Middle Devonian (380 Ma) orbital parameters for the median orbit and set vegetation to bare land.

2.2.3. CO_2 Concentration

We test the influence of changes in the atmospheric carbon dioxide level on the Devonian climate using CO_2 concentrations of 2,000, 1,500, and 1,000 ppm. These particular values have been chosen because they are representative for the values reconstructed for the Early (415 Ma), Middle (380 Ma), and Late Devonian (360 Ma) periods, each lying within one standard deviation of the pCO_2 probability maximum given in Foster et al. (2017); see Figure 1a. Note that we chose to use approximate values rather than reading off the fitted values for the three time slices because of the sparse temporal sampling and large error bars of the CO_2 reconstruction. All other parameters are fixed: We use the continental configuration and solar constant ($S = 1,319.1\mathrm{W/m^2}$) representative for the Middle Devonian (380 Ma), idealized orbital parameters, and set vegetation to bare land.

2.2.4. Vegetation Distributions

The biogeophysical influence of the spread of vascular land plants on the Devonian climate is investigated by different idealized vegetation distributions. These are roughly representative of the situation during the Early, Middle, and Late Devonian and will thus be also used in the simulations representing the three Devonian time slices described in section 2.2.6. The sensitivity experiments with respect to the effect of vegetation cover alone, however, are based on the continental configuration for 380 Ma to isolate the biogeophysical effect of vegetation cover from the changes due to continental drift.

The design of the vegetation distributions is based on palaeontological evidence for the evolution of vascular plants during the Devonian (Boyce & Lee, 2017). In particular, the evolving ability of land plants to spread upcountry is taken into account, which we quantify by imposing limits in terms of distance from the coast and elevation at the original resolution of the continental reconstruction. Furthermore, the evolution of plant communities from bryophyte-dominated coastal vegetation toward the first forests is considered by varying the mix of plant types and their biogeophysical properties albedo, roughness length, and evapotranspiration; see Table 2. Finally, vegetation distribution is constrained by climate. The derivation of the vegetation distributions for the different Devonian time slices is explained in detail in the following and shown in Figure 3.

Nonvascular land plants arose as early as in the Mid-Ordovician (Rubinstein et al., 2010) and may have spread widely already during the Ordovician (Porada et al., 2016). The first vascular plants evolved during the Late Ordovician (Steemans et al., 2009). During the Late Silurian and Early Devonian, the first vascular land plants were distributed across all latitudes (Boyce & Lee, 2017), but due to shallow roots and no water conducting cells, they were restricted to wet lowland areas (Algeo & Scheckler, 1998; Algeo et al., 1995; Boyce & Lee, 2017). For the very Early Devonian, we therefore assume that land plants are restricted to areas closer than 500 km to the coast and up to 500 m in altitude. Areas closer than 300 km to the coast and/or with an altitude lower than 300 m are covered by 60% vegetation. Areas with a coastal distance between 300 and 500 km and/or an altitude between 300 and 500 m are covered by 10% vegetation. To represent the dominance of nonvascular vegetation, we assume the plant cover to consist of two-thirds bryophytic vegetation mixed with one-third grass-like vegetation for the Early Devonian (see Table 2). Note that grass has evolved much later in Earth's history and that the grass-like surface type in our model approximates the basic biogeophysical properties of any shrub-like vegetation. For the remaining surface area the land surface type in the model is set to bare land.

By the Middle Devonian, vascular land plants gained in importance and the first arborescent vegetation evolved (Algeo & Scheckler, 1998). Thus, for our shrub-like vegetation, we mix four fifths of the vegetation of shrub-like characteristics with one-fifth vegetation of bryophyte characteristics. We add a second vegetation type representing an early type of trees (see Table 2). We assume 70% Middle Devonian shrub-like vegetation

Paleoceanography 10.1029/2019PA003562

Table 2
Albedo, Roughness Length, and Evapotranspiration (as Determined by the LAI) for the Different Surface Types Used in the Model Simulations

Vegetation type	Albedo (vis/near IR)	Roughness (m)	Evapotranspiration (LAI)
Bare soil	0.14/0.22	0.050	0
Shrubs	0.080/0.30	0.10	3.0
Trees	0.050/0.20	1.0	6.0
Early Devonian			
shrub mix	0.073/0.37	0.047	2.3
(two-thirds bryophytes, one-third shrubs)			
Bryophytes	0.070/0.40	0.020	2.0
Middle Devonian			
Shrub mix	0.078/0.32	0.084	2.8
(one-fifth bryophytes, four-fifths shrubs)			
Bryophytes	0.070/0.40	0.020	2.0
Middle Devonian trees	0.070/0.24	0.60	4.5
Late Devonian			
Shrub mix	0.078/0.32	0.084	2.8
(one-fifth bryophytes, four-fifths shrubs)			
Bryophytes	0.070/0.40	0.020	2.0
Late Devonian trees	0.050/0.20	1.0	6.0

Note. Parameters of bare soil, shrubs, and trees are the standard values in our model. Albedo and roughness values for the early trees are based on the woodland parameters in Dickinson et al. (1993); the evapotranspiration value is an estimate based on the values used for shrubs and trees. The bryophytes' albedo is an average value of the moss types in Stoy et al. (2012); roughness length and LAI are taken from Dickinson et al. (1993) for short grass. Evapotranspiration is proportional to LAI; see equation (45) in Dickinson et al. (1986). LAI = Leaf Area Index.

cover and 10% early tree vegetation cover in areas lower than 500 m in altitude and closer than 500 km to the coast and set the remaining surface area to bare land.

In the Late Devonian, trees grew larger and diversified (Algeo & Scheckler, 1998) and vegetation was more widespread but did not extend in upland areas (Boyce & Lee, 2017). Therefore, for this model setup, we use the same shrub-like vegetation mix as in the Middle Devonian but a tree type with characteristics of an evergreen forest after Dickinson et al. (1993). Coastal areas lower than 500 m in altitude and closer than 500 km to the coast are covered by 40% of shrub-like vegetation and 40% of trees. On areas from 500 to 1,000 m in altitude and/or between 500 and 1,000 km from the coast we assume 30% shrub-like vegetation and 30% trees.

As vegetation and climate do not interact dynamically in our model, we implement temperature and precipitation limits to avoid vegetation on land areas with unsuitable climate. Trees do not cover cells for which the average temperature of the coldest month is below −25 °C, whereas the growth of shrub-like vegetation is not restricted by temperature (Schaphoff et al., 2018; supporting information Table S4). The value for the temperature limit for trees is an estimate based on an average of different types of trees. Additionally, we restrict all vegetation to areas with annual precipitation above 700 mm. This value is based on Lieth (1973, Figure 3) taking into account that Devonian plants can store less water compared to present-day plants. The areas unsuitable for vegetation according to these limits are determined using a simulation with all land cover set to bare land and are indicated in Figure 3. There is a marked increase in the fraction of land covered by vegetation from 15.1% during the Early Devonian to 28.5% during the Middle Devonian and 37.3% during the Late Devonian.

The resulting vegetation distributions at 1° spatial resolution are then used to calculate vegetation fractions on the coarser atmospheric grid of the model. The bias due to the coarse model resolution should be lim-

Paleoceanography 10.1029/2019PA003562

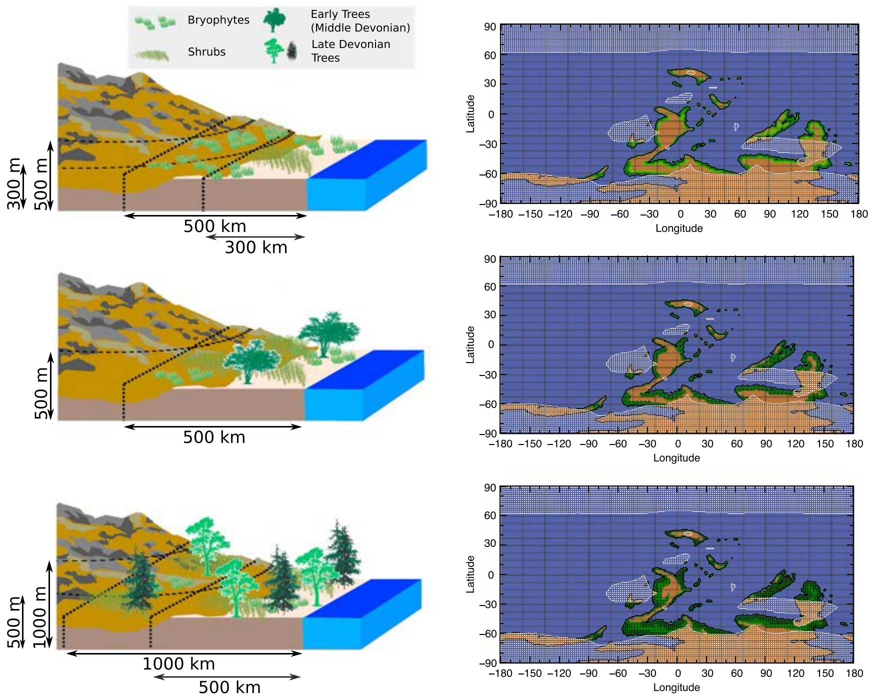

Figure 3. Vegetation distributions for the Early (top row), Middle (middle row) and Late Devonian (bottom row). (left column) The change in vegetation cover with time is based on the evolution of plants and their properties as well as their increasing spread from the coast as measured by coastal distance and elevation (see text for details). (right column) Resulting vegetation distributions for the three timeslices, shown on the Middle Devonian (380 Ma) continental configuration and at the resolution of the original continental reconstruction (Scotese, 2014). Green shading indicates the land fraction covered by vegetation; the black dots show the density of trees. The areas shaded in white cannot be covered by vegetation due to specified limitations of temperature and precipitation (see text for details). Fractions covered by vegetation are 15.1% for the Early Devonian, 28.5% for the Middle Devonian, and 37.3% for the Late Devonian.

ited, however, because the atmosphere model takes subgrid fractions into account when calculating surface fluxes.

In order to assess the influence of the different vegetation types separately, we add three simulations representing extreme scenarios in which all land is covered by bare soil, shrub-like vegetation, and trees, respectively, irrespective of coastal distance, elevation, temperature, and precipitation.

All sensitivity simulations for the different vegetation distributions are run for a fixed carbon dioxide concentration of 1,500 ppm, a solar constant of $S = 1,319.1$ W/m^2 and orbital parameters of a median orbit; see also Table 1.

2.2.5. Orbital Parameters

To assess the influence of orbital configurations on Devonian climates, a large set of 51 simulations is performed for obliquity values ϵ of 22.0°, 23.5°, and 24.5°; eccentricity values e of 0, 0.03, and 0.069; and perihelion angles ω (defined relative to autumnal equinox) ranging from 0° to 315° in intervals of 45° for nonzero eccentricity. All other boundary conditions are held fixed at a continental configuration representing 380 Ma, a solar constant of $S = 1,319.1$ W/m^2, a carbon dioxide concentration of 1,500 ppm, and bare land; see Table 1. Note that our simulations are equilibrium simulations; that is, we do not simulate transient changes through the Milankovitch cycles.

2.2.6. Best Guess Simulations for the Early, Middle, and Late Devonian

In addition to the sensitivity simulations described above, we perform a set of three model experiments representing the most likely state of the boundary conditions for the Early, Middle, and Late Devonian. As the main aim of these "best guess simulations" is a better understanding of the drivers of longer-term climate change during the Devonian rather than shorter-term fluctuations, orbital parameters are kept fixed and set to the values of a median orbit (obliquity $\varepsilon = 23.5°$, eccentricity $e = 0$). Note that the uncertainty arising from the unknown orbital configuration can be estimated based on the results of the sensitivity test to orbital configuration (section 2.2.5). Continental configurations are based on reconstructions for 415, 380, and 360 Ma for the Early, Middle, and Late Devonian, respectively (see section 2.2.1). The solar constant is increasing with time, with values of 1,315.3, 1,319.1, and 1,321.3 W/m^2 for the three time periods in question (see section 2.2.2). Values for the atmospheric CO_2 concentrations of 2,000, 1,500, and 1,000 ppm are chosen for the three timeslices to capture the long-term decrease of CO_2 through the Devonian (see section 2.2.3). Finally, the progressing evolution of land plants is taken into account by choosing the vegetation mix and distribution as described in section 2.2.4. For the Early Devonian, vegetation consists of coastal shrub dominated by bryophytes. For the Middle Devonian simulation, vegetation cover is more extended, and first trees are added to the mix. For the Late Devonian, vegetation is spread even more widely and the tree fraction is increased to represent the first forests.

3. Sensitivity of the Devonian Climate to Changes in Boundary Conditions

3.1. Influence of the Continental Configuration

First, we investigate the sensitivity of the Devonian climate to changes in continental configuration while keeping all other boundary conditions fixed (CO_2 concentration 1,500 ppm, solar constant 1,319.1 W/m^2, bare land, and median orbital parameters; see Table 1 and section 2.2.1). We compare three simulations using the continental configurations shown in Figure 2 and find that the change in the distribution of continents throughout the Devonian leads to a decrease of global annual mean surface air temperature over time. However, the global mean temperature differences between the climate states for the three continental configurations are small: for the Early Devonian, global annual mean surface air temperature is 21.3 °C, decreasing to 21.2 °C for the continental configuration of 380 Ma and 20.8 °C or 360 Ma. Land surface air temperatures are 17.2 °C for the Early Devonian, 16.2 °C for the Middle Devonian, and 17.0 °C for the Late Devonian.

Although the decreasing trend in surface air temperature for the three Devonian continental configurations is small, regional effects caused by changes in continental drift are significant: The largest temperature differences are found at high southern latitudes and can mostly be attributed to the differences in the distribution of land and ocean areas (see Figure S1). Furthermore, differences in orography between the three continental configurations result in regional temperature differences. Finally, part of the differences in temperature can be attributed to changes in ocean circulation between the different continental configuration as indicated by the ocean surface velocities and temperatures shown in Figure S2. Note that changes in continental configuration could in principle effect the climate-carbon feedback which is not represented in our model, possibly inducing stronger climatic changes than modeled here.

3.2. Influence of the Solar Constant

Annual global mean surface air temperatures increase from 20.9 °C to 21.2 °C and 21.4 °C with increasing solar constant (1,315.3 W/m^2 in the Early, 1,319.1 W/m^2 in the Middle, and 1,321.3 W/m^2 in the Late Devonian) while keeping all other boundary conditions fixed (see Table 1 and section 2.2.2). These temperature changes are consistent with what one would expect from the change in solar forcing. The effect of an increasing solar constant is largest in the high northern latitudes (see Figure S3), in particular during the winter months. This is closely linked to differences in Arctic sea ice triggered by the differences in global mean temperature. Note that, on a global scale, the warming due to the brightening Sun is very similar in magnitude to the cooling due to continental drift over the Devonian described in section 3.1 above. Both effects will therefore roughly cancel each other. Regionally, however, the cooling due to continental drift is stronger at high southern latitudes, whereas the warming due to the increasing solar constant is more pronounced at high northern latitudes.

3.3. Influence of CO_2 Concentrations

Next, we evaluate the impact of the decrease in atmospheric CO_2 concentrations throughout the Devonian (2,000 ppm in the Early, 1,500 ppm in the Middle, 1,000 ppm in the Late Devonian; see section 2.2.3) on the Devonian climate while keeping all other boundary conditions fixed (see Table 1). Global annual mean surface air temperature decreases from 22.4 °C for 2,000 ppm to 21.2 °C for 1,500 ppm and 19.4 °C for 1,000 ppm. The temperature difference of 2.9 °C between the climate states with 2,000 and 1,000 ppm of atmospheric

AGU 100 ADVANCING EARTH AND SPACE SCIENCE
Paleoceanography 10.1029/2019PA003562

carbon dioxide is, of course, equivalent to the model's equilibrium climate sensitivity to CO_2 doubling for Devonian boundary conditions. This value is in good agreement with the range for the present-day climate sensitivity given in IPCC (2013, p.1110). For the relatively warm Devonian climate state, climate sensitivity is smaller than for cooler configurations analyzed with the same model (Feulner & Rahmstorf, 2010; Feulner & Kienert, 2014), predominantly due to the smaller ice-albedo feedback.

With respect to regional climate change, differences in surface air temperature between different CO_2 concentrations are significantly larger for higher latitudes, especially in the Northern Hemisphere (see Figure S4). This is similar to the phenomenon of Arctic amplification under present-day global warming (Serreze & Barry, 2011) which is mainly caused by the ice-albedo feedback effect. We will encounter the same pattern when analyzing the best guess simulations in section 5.

Looking at the results of the sensitivity studies so far, it is important to note that the magnitude of the global temperature change due to CO_2 is considerably larger than the effects of continental drift and changes in the solar constant.

3.4. Influence of the Vegetation Distribution

To assess the potential climate impact of the colonization of land by vascular plants during the Devonian, we investigate the sensitivity of the climate to the biogeophysical effects of different vegetation distributions: We use the three vegetation distributions constructed to represent the three Devonian periods on the 380-Ma continental configuration (see section 2.2.4) but first compare the three extreme scenarios of bare land, shrubs, and trees covering the entire continents of the 380-Ma configuration.

Global mean surface air temperatures are 21.2 °C for the bare land case, 20.7 °C for the shrub-covered continents, and 21.6 °C for the tree-covered continents. The continental temperature differences are much more significant with 16.2 °C for the bare land case, 13.4 °C for the shrub-covered continents, and 15.0 °C for the tree-covered case.

Maps of differences in surface air temperature, evaporation, surface albedo, and atmospheric water vapor content for the shrub-covered case minus the bare land case and the tree-covered case minus the bare land case (see Figure 4, first two rows) help to understand the origin of temperature differences. Comparing patterns of evaporation and surface air temperature differences over continents, it is obvious that changes in evaporation determine continental surface air temperature differences for the shrub-covered case. For the tree-covered case, this is only true for latitudes up to 60°. Stronger evaporation results in lower temperatures due to evaporational cooling and dominates over the warming effect of a decreasing surface albedo. This trend is in agreement with the climatic effect of modern tropical forests (Betts, 2000; Bonan, 2008). For modern boreal forests, in contrast, the negative climate forcing of evaporation is counteracted by the low albedo (Betts, 2000; Bonan, 2008). (The effects of modern temperate forests are very uncertain.) Furthermore, simulated total cloud cover is higher over continents in case of vegetation cover, with only small differences between the shrub-covered and the tree-covered case, leading to additional cooling (Figure S5).

Interestingly, surface air temperatures over the ocean are higher for the tree-covered case than for the bare land case. Trees increase the atmospheric water vapor content which leads to an increased greenhouse effect, resulting in higher surface air temperatures. Although this is a global trend, it dominates surface air temperature differences only for oceanic regions (see Figure 4e). For continental regions, this effect is counteracted by the evaporative cooling described above. The warmer temperatures over the ocean for the tree-covered case lead to less snow in the high southern latitudes, decreasing the albedo and hence increasing continental temperatures. In contrast, for the high southern latitudes of the shrub-covered case there are a small increase in albedo as the continental snow cover increases due to lower temperatures. In the Arctic temperature and albedo changes are closely linked to changes in sea ice cover for both the shrub-covered and the tree-covered case.

The understanding of the basic mechanisms gained by the extreme scenarios can now be used to understand the differences in climate for the three Devonian vegetation distributions. Overall, the changes in vegetation cover during the Devonian have little influence on global mean surface air temperature in our simulations (21.1 °C for the Early Devonian vegetation, 21.1 °C for the Middle Devonian vegetation, and 21.2 °C for the Late Devonian vegetation). The mean continental temperature is 15.6 °C for the Early Devonian vegetation, 15.3 °C for the Middle Devonian vegetation, and 15.3 °C for the Late Devonian vegetation. Still, the regional temperature differences on land are more pronounced (Figure 4, third to fifth row) and

Paleoceanography 10.1029/2019PA003562

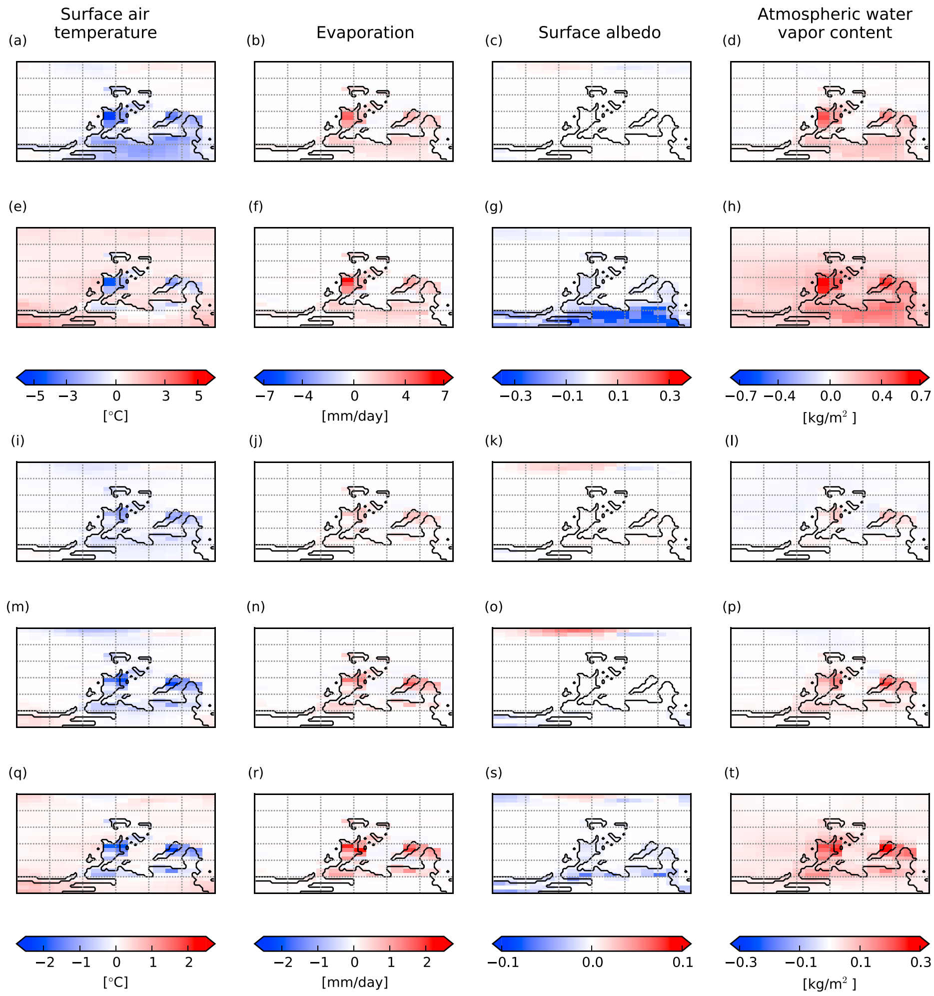

Figure 4. Surface air temperature,evaporation, surface albedo, and atmospheric water vapor content. Shown are differences of the vegetation scenarios minus the bare land vegetation simulation: First row (a–d) shrub-covered continents minus bare-land continents, second row (e–h) tree-covered continents minus bare-land continents, third row (i–l) Early Devonian vegetation minus bare-land continents, fourth row (m–p) Middle Devonian vegetation minus bare-land continents, fifth row (q–t) Late Devonian vegetation minus bare-land continents.

can largely be understood with the explanations derived from the more extreme idealized simulations discussed above. Plant evolution during the Devonian is accompanied by an increase in evaporation, leading to cooling over the continents. This cooling effect dominates changes in continental temperature except for the high southern latitudes where the climatic limits (see Figure 2) preclude vegetation. Here, temperature differences are negligible for the Early and Middle Devonian vegetation distribution compared to the bare land case. For the Late Devonian the higher atmospheric water vapor content caused by the higher fraction of trees increases the atmospheric water vapor content globally which dominates surface air temperature patterns over the ocean and over the continents at high southern latitudes. Changes in albedo are very small over continental areas, and therefore, their effect is insignificant in our simulations. Note that land surface albedo may not have changed too much during the Devonian due to the early presence of microbial mats (Boyce & Lee, 2017). As observed for the extreme scenarios, albedo changes in the Arctic region are linked to changes in temperature and sea ice cover for all three Devonian vegetation distributions.

Paleoceanography 10.1029/2019PA003562

In the following we compare our results of the influence of the Devonian vegetation changes with an earlier modeling study. Le Hir et al. (2011) investigate the Late Devonian climate using a coupled climate-carbon-vegetation model focusing on the impact of changing surface properties on climate. Similar to our approach, they use three representative settings for the Early, Middle, and Late Devonian. As forcing, they use the solid Earth degassing rate, continental configurations, and an increasing solar constant. Although they simulate a strong decrease in CO_2 (5,144 ppm for the Early Devonian, 4,843 ppm for the Middle Devonian, and 2,125 ppm for the Late Devonian), they find an almost unchanged temperature of 23.4 and 23.5 °C for the Early and Middle Devonian, and considering the strong CO_2 decrease, the temperature decrease to 22.2 °C for the Late Devonian is comparatively small. Note that in Le Hir et al. (2011) CO_2 decreases by more than a factor of 2 from the Early to the Late Devonian; the expected cooling for a halving of the CO_2 concentration is about 3 °C (Section 3.3). Le Hir et al. (2011) conclude that the decrease in albedo accompanying the evolution of land plants is counteracting the carbon dioxide decrease. In contrast to our simulations, however, they use relatively high values for the bare soil albedo (0.24 vs. 0.14 in the visible and 0.40 vs. 0.22 in the infrared), whereas their albedo values for vegetation differ only marginally from ours (for trees 0.06 vs. 0.05 in the visible and 0.18 vs. 0.2 in the infrared).

To investigate the impact of the choice of albedo for the different surface types, we repeat our bare-land simulation and our tree-covered simulation with the albedo values used in Le Hir et al. (2011). The comparison with our original vegetation simulation results illustrates how strongly the modeled climate impact of differences in vegetation is determined by the choice of albedo values: Due to the albedo increase for bare land global mean surface air temperature decreases by 1.7 to 19.5 °C and mean continental temperature by 4.2 to 12.3 °C. The strong warming over the continents is shown in Figure S6a. For the tree-covered case, the small differences in albedo have only negligible effects on global mean temperatures, but small regional differences can be seen in Figure S6b.

We note, however, that the soil albedo value used in Le Hir et al. (2011) is very high; given the early presence of microbial mats (Boyce & Lee, 2017) which have a much lower albedo (Sanromá et al., 2013) than the one used in Le Hir et al. (2011), our low value for the soil albedo is better suited to represent rocks covered with microbial mats and therefore appears to be more plausible.

It is important to bear in mind that, in addition to this biogeophysical effects, changes in the weathering process due to the evolution of deeper roots strongly influence the carbon cycle and therefore climate. Hence, these results only give a rough idea of the influence of the land plant evolution on climate. The combined effect of vegetation distribution and decreased CO_2 concentration is discussed in the context of the best guess simulations in section 5.

3.5. Influence of the Orbital Configuration

As a further sensitivity test, we investigate the influence of orbital configuration on the Devonian climate using simulations for a range of different orbital parameters while keeping all other boundary conditions fixed (continental configuration for 380 Ma, carbon dioxide concentration 1,500 ppm, solar constant 1,319.1 W/m^2, and bare land). In these simulations, we systematically test different values for the obliquity (ε = 22.0°, 23.5°, and 24.5°), the eccentricity (e = 0, 0.03 and 0.069), and precession (ω from 0° to 315°); see section 2.2.5.

Figure 5 shows global annual mean surface air temperatures for the three fixed obliquity values when varying eccentricity and precession values. Global annual means of surface air temperature increase with increasing obliquity. For fixed values of $e = 0$ and $\omega = 0$, global temperature values are 21.0 °C for $\varepsilon = 22.0°$, 21.2 °C for $\varepsilon = 23.5°$, and 21.4 °C for $\varepsilon = 24.5°$. Increased obliquity increases seasonal radiation differences on both hemispheres. Although this does not influence annual and global mean values of solar radiation, the strong southward shift of the continents amplifies the stronger seasonal insolation at the South Pole for higher obliquity values, resulting in higher global annual mean surface air temperatures.

Concerning the influence of the shape of Earth's elliptical orbit on the Devonian climate, global annual mean surface air temperatures increase with eccentricity due to the higher annual mean insolation for more eccentric orbits. Surface air temperature differences for different precession angles are negligible in our sensitivity experiments.

Lowest global annual mean surface air temperatures are reached for the configurations with $\varepsilon = 22.0°$ and $e = 0$ (21.0 °C), whereas the maximum is reached for the configurations with $\varepsilon = 24.5°$ and $e = 0.069$

Paleoceanography 10.1029/2019PA003562

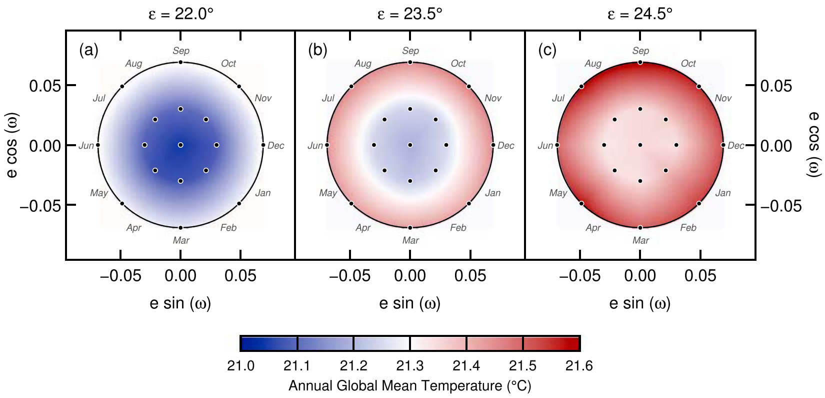

Figure 5. Annual global mean surface air temperature for three different obliquities ((a) $\varepsilon = 22.0°$, (b) $\varepsilon = 23.5°$, (c) $\varepsilon = 24.5°$) and varying eccentricity and precession. Note that for each obliquity 17 individual simulations for three different eccentricity values and eight precession angles in intervals of 45° were performed (marked by the black dots); temperatures for all other eccentricity and precession values were derived using bilinear interpolation.

(21.6 °C). Hence, for our median orbit simulations the uncertainty arising due to the unknown exact orbital configuration is $^{+0.4}_{-0.2}$ °C.

We note that the differences in climate between orbital configurations in the Devonian might be larger in reality than in our idealized simulations at fixed carbon dioxide levels due to feedbacks involving the carbon cycle.

We can compare our results with an earlier modeling study on the impact of orbital parameters on the Devonian climate (De Vleeschouwer et al., 2014). This study finds a strong dependence of the Devonian climate on orbital parameters and supports a link between ocean anoxic events during the Devonian and orbital forcing. Using cyclostratigraphic techniques, De Vleeschouwer et al. (2017) see the root cause of the Frasnian-Famennian extinction event in strong perturbations of the carbon cycle (e.g., as an effect of the land plant evolution) but suggest that it is triggered by a particular succession of orbital parameters. This proposed link makes a comparison to the model results of De Vleeschouwer et al. (2014) particularly interesting. De Vleeschouwer et al. (2014) use an atmospheric general circulation model coupled to a slab ocean model with a fixed prescribed oceanic heat transport, a Late Devonian continental configuration, a solar constant of 1,324 W/m^2, and a CO_2 concentration of 2,180 ppm.

Except for a small eccentricity offset of the coldest state and a slight dependence on precession, De Vleeschouwer et al. (2014) also find that global mean temperature increases with obliquity and eccentricity. However, they report significantly larger temperature variations with orbital parameters. Indeed, their coldest state for low obliquity and eccentricity has a global mean temperature of 19.5 °C (1.5 °C lower than our value for corresponding orbital parameters), while their warmest state for high obliquity and eccentricity has a temperature of 27 °C values (more than 5 °C higher than the warmest state in our simulations).

Using selected model output kindly provided by David De Vleeschouwer, we are able to investigate the discrepancies between De Vleeschouwer et al. (2014) and our model results in more depth. We find generally good agreement for the median orbit simulations of the two models and for patterns over continents. Differences primarily arise for other orbital configurations and for ocean areas, in particular over the Arctic ocean where we find significant differences in the sea ice distribution between the two studies. For example, De Vleeschouwer et al. (2014) report no sea ice at all in their $\varepsilon = 24.5°$, $e = 0$ simulation, whereas our model simulates sea ice, leading to temperature differences at high latitudes. Although we are not able to fully explain these discrepancies based on the available data and although we cannot rule out a contribution from our simplified atmosphere model, the observed differences in the sea ice distribution make it reasonable to assume that the differences arise from differences in ocean circulation, ocean heat flux, and ocean heat transport and their interplay with sea ice formation and dynamics. Note that, in contrast to our study, the slab ocean model used in De Vleeschouwer et al. (2014) does not explicitly model ocean dynamics and uses the same prescribed ocean heat transport for all orbital configurations. Furthermore, they use different

Paleoceanography 10.1029/2019PA003562

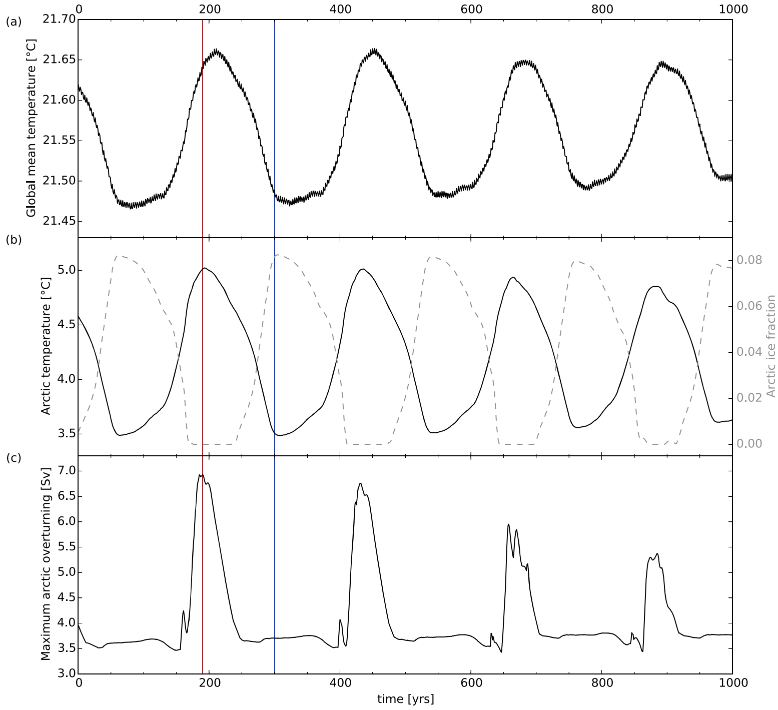

Figure 6. Typical mode of climate variability in the Devonian as diagnosed in a representative 1,000-year period of the model simulation for 380 Ma, 1,500 ppm of CO_2, $S = 1,319.1$ W/m^2, $\varepsilon = 24.5°$, $e = 0.069$, and $\omega = 315°$. (a) Global annual mean surface air temperature. (b) Arctic annual surface air temperature, averaged from 60°N to 90°N (black solid line), and Arctic annual sea ice fraction (gray dashed line). (c) Maximum of the Arctic overturning circulation in the ocean between 60°N and 90°N in latitude and between 500- and 3,000-m depths. The red and blue lines mark the points which are chosen for diagnostic snapshots of the warm and cold mode in the following.

boundary conditions with a higher CO_2 concentration (2,180 vs. 1,500 ppm) and solar constant (1,324 vs. 1,319.1 W/m^2) as well as a Late Devonian continental configuration and vegetation cover, resulting in a warmer climate state, leading to differences in sea ice cover, for instance. Test simulations with our model using similar boundary conditions show, however, that the amplitude of temperatures changes between different orbital configurations remains small and that sea ice is present at high latitudes in all cases.

4. Devonian Climate Variability: Flips Between Two Climate States in the Arctic

While studying the sensitivity of the Devonian climate, we have discovered that the dominant mode of variability on centennial timescales in our model simulations of the Devonian climate relates to quasi-periodic variations in the global mean surface temperature on the order of 0.2 °C with an average periodicity of about 300 years. As an example, Figure 6a shows these variations for a representative time period in one of our sensitivity simulations. These fluctuations in global mean temperature originate from the Arctic region where they are driven by the pace of North Polar SST changes. Indeed, the values of annual mean surface air temperatures averaged over the Arctic between 60 and 90°N oscillate between about 3.5 and 5.0 °C (Figure 6b).

The large regional temperature fluctuations in the Arctic and the waxing and waning of winter sea ice cover with a periodicity of several centuries have the potential to impact Arctic marine ecosystems considerably. For example, Harada (2016) reports significant changes in the biogeochemical cycling due to the anthropogenic climate change in the western Arctic Ocean at all trophic levels. As marine life in the Devonian underwent considerable changes (Copper & Scotese, 2003; Dahl et al., 2010; McGhee, 1996), it is important to further investigate the described mechanism, although verification from proxy data might prove difficult

Paleoceanography 10.1029/2019PA003562

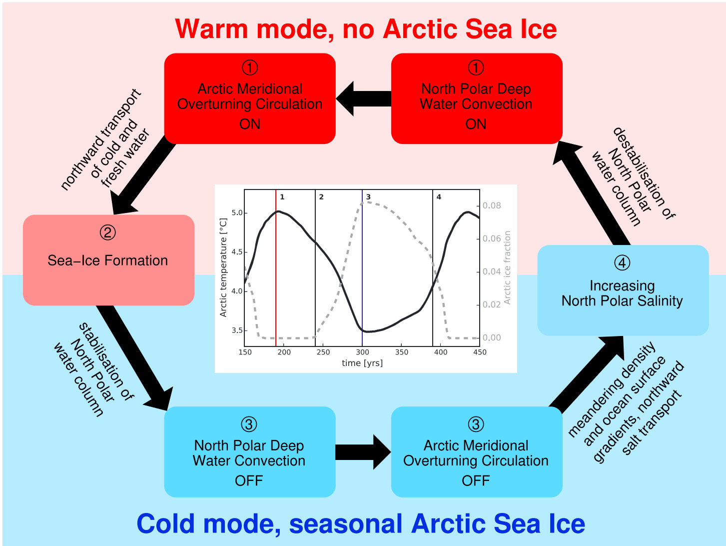

Figure 7. Mechanism describing the flip between the two climate states in the Arctic: In the warm mode, the North Polar water column is destabilized by the northbound transport of warmer and saltier waters to the ocean surface. This inhibits the growth of sea ice and is connected to the establishment of a North Polar deep water convection. The accompanying Arctic meridional overturning circulation transports cold and fresh water northward, leading to the flip into the cold mode. The formation of sea ice stops the deep water convection and the Arctic meridional overturning circulation. The resulting meandering density and ocean surface gradients lead to a northbound salt transport, increasing surface salinity at the North Pole and thereby triggering the flip back into the warm mode.

due to the short timescale and the regional focus of the effect. Furthermore, it is crucial for a meaningful interpretation of the data of this study to take into account these temperature variations. Therefore, in the analysis of our sensitivity studies (section 3) and the best guess simulations (section 5) we evaluate long-term mean values (averaged over 1,000 years) in order to represent an average climate state rather than one of the extreme cases.

The flips between cold and warm climate states in the Arctic can be attributed to coupled changes in sea ice cover (shown in Figure 6b), ocean convection, and ocean overturning (Figure 6c) in the region around the North Pole. A schematic overview of the mechanism is shown in Figure 7 and described in more detail in the following. During the discussion we will often refer to Figure 8 where salinity, northern sea ice cover, ocean surface velocities, and the mixed layer depth are shown for the warm mode, the cold mode, and the two transition states.

During the warm mode (Figures 8a–8c) the situation is characterized by the presence of high-salinity surface water at the North Pole, causing a destabilization of the water column and thus open ocean convection. As a consequence, warmer and saltier water masses are injected into the surface ocean layer while inhibiting the growth of sea ice during the warm mode. Deep ocean convection at the North Pole is, however, intimately connected with the establishment of an Arctic meridional overturning circulation (ArcMOC); see Figures 6c and 9a. The water masses from the surface of the North Pol sink toward the bottom while spreading southward and resurface between 60°N and 70°N.

While flowing back at sea surface toward the North Pole, the water masses transported by the ArcMOC deliver relatively fresh waters from the latitudinal band between 70°N and 80°N, which promotes the recurrence of sea ice formation and thus the transition from the warm into the cold mode (Figures 8d–8f). As seasonal sea ice grows, deep convection at the North Pole weakens and ultimately ceases because the layer of sea ice inhibits heat losses from sea surface. As a consequence, the ArcMOC collapses (Figures 6c and 9b) and the system lapses into the cold mode.

Within the time interval of the cold mode (Figures 8g–8i), the formation of seasonal sea ice in the Arctic leads to a lowering of the sea surface salinity around the North Pole caused by the impacts of brine rejection

Paleoceanography 10.1029/2019PA003562

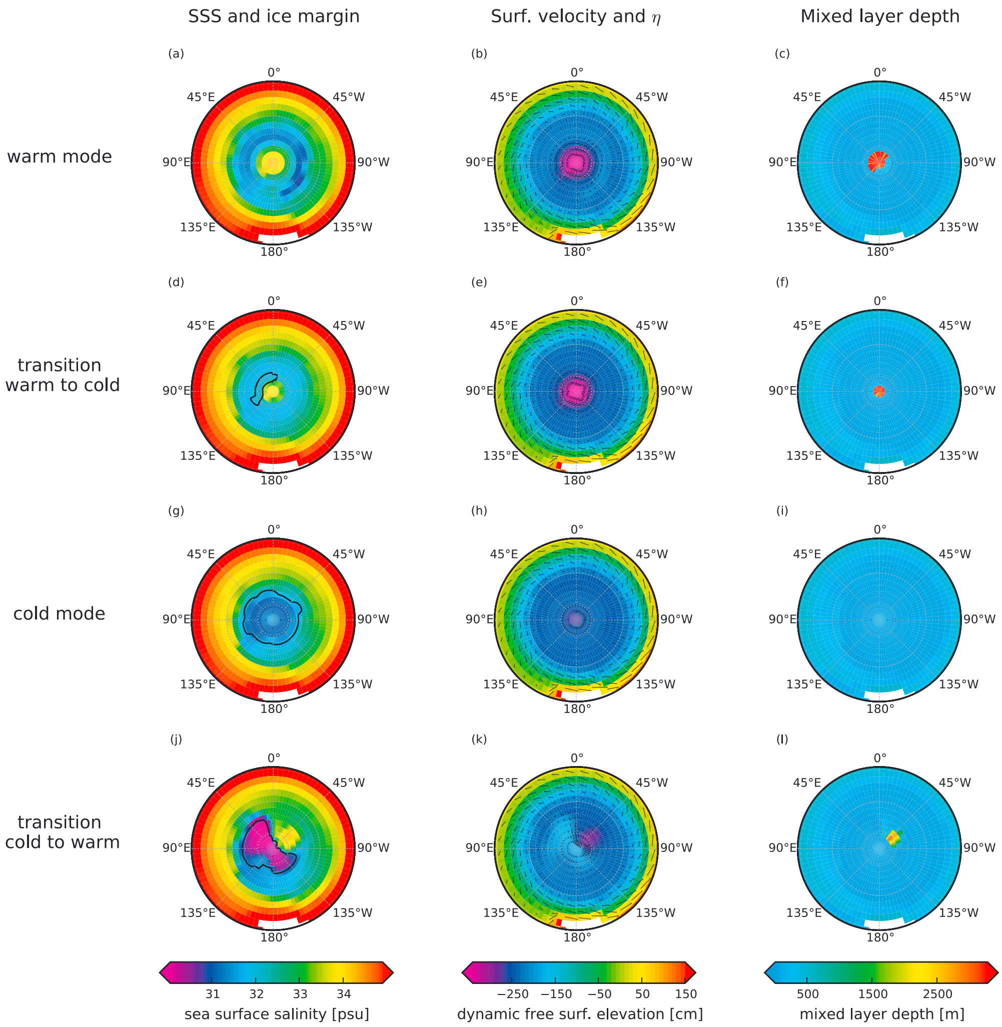

Figure 8. Physical properties of the Northern Hemisphere ocean between 40°N and the North Pole for the warm mode (first row, a–c), the transition between warm and cold modes (second row, d–f), the cold mode (third row, g–i), and the transition between cold and warm modes (fourth row, j–l). Quantities shown are sea surface salinities (SSS) in practical salinity unit and the area covered with at least 10% of sea ice during winter as black line (left column: a, d, g, j), dynamic free surface elevation η in centimeters overlaid by sea surface velocity vectors in centimeter per second (middle column: b, e, h, k), and mixed layer depth in meters (right column: c, f, i, l).

during sea ice formation and a freshening of sea surface waters during its melting period (Bouttes et al., 2010). Consequently, the cold mode is characterized by a shallow mixed layer and strong stratification of Polar water masses where cold and relatively fresh water lies above warmer and salty water masses. The surface velocities follow almost a cyclonic flow pattern south of 60°N and a weaker anticyclonic pattern north of 70°N, combined with a circularly symmetric shaped dynamical free surface η.

However, due to deviations from perfect circular symmetry of water mass properties around the North Pole, the cold mode is unstable, and the system begins the transition back into the warm mode (Figures 8j–8l). As sea ice forms and melts over the years, the relatively fresh surface water layer accumulating around the North Pole spreads slightly asymmetrically toward the south. Therefore, the concomitant formation of a meandering density front within the latitudinal band between 60°N and 80°N reshapes the dynamic free surface η according to the geostrophical balance (Marshall & Plumb, 2008). The resulting deflection of the

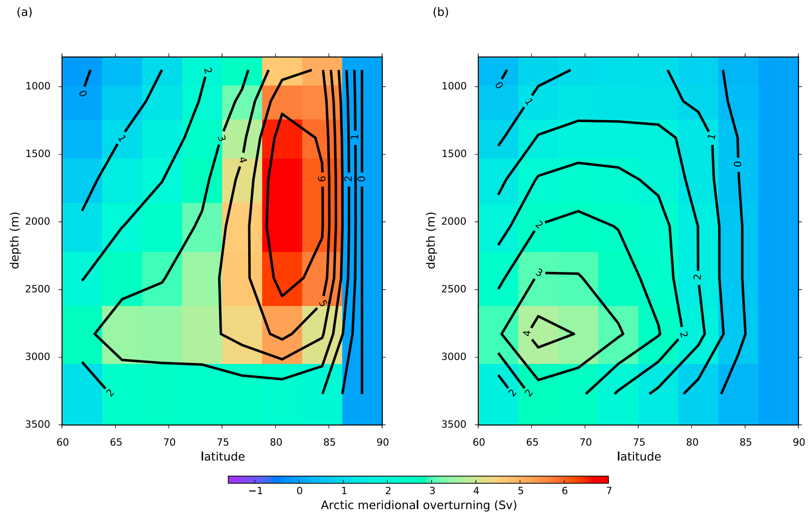

Figure 9. Northern part (60°N to 90°N) of the global overturning stream function between depths of 780 and 3,500 m. The maximum and minimum of this Arctic meridional overturning circulation can be observed in the warm mode (a) and the cold mode (b), respectively. For the cold mode, the maximum overturning is both smaller and shifted toward lower latitudes.

circular flow from lower latitudes of around 60°N toward the North Pole drives patches of highly saline surface water masses toward the Pole.

This advancing salinification of surface waters at the North Pole ultimately causes a destabilization of the water column, open ocean convection at the pole, and the restart of the ArcMOC, thus switching the system back into the warm mode.

Oscillations like the one described here could in principle also result from numerical instabilities caused by a long simulation time step (12 hr by default), the splitting of tracer, and dynamic time steps employed in our ocean model (Montoya et al., 2005) or by rounding errors due to optimization during code compilation. We have performed a large set of test experiments including simulations with short time steps (as short as 1 hr) and without splitting of ocean time steps, experiments on different platforms and with different compiler versions, and optimization settings to verify that the oscillations described above are a real phenomenon rather than a numerical artefact.

Our results suggest that similar modes of climate variability could be a more general feature of climate states with open water at one pole. Indeed, Poulsen and Zhou (2013) describe a climate state-dependent Arctic variability pattern in simulations of the mid-Cretaceous climate. Investigating the influence of different atmospheric CO_2 concentrations, they find a link between temperature variability and changes in sea ice cover for low (preindustrial) CO_2 but additionally observe temperature variability for warmer, ice-free climate states (10× preindustrial CO_2 concentration). For both cases, they describe an intensification of the Northern Hemisphere meridional overturning circulation during the warm mode, similar to the maximum ArcMOC in our simulations, connected to northward transport of lower-salinity and lower-density water and coupled to a strong feedback involving low-level clouds.

5. Climate States of the Early, Middle, and Late Devonian

After having investigated the sensitivity of the Devonian climate system to a range of parameters, we performed three simulations with the aim to represent the most likely state for the Early, Middle, and Late Devonian by choosing the most appropriate combination of parameter values (Table 1), as explained in section 2.2.6.

The simulated global temperature decreases significantly throughout the Devonian: During the Early Devonian, global annual mean surface air temperature is 22.0 °C, decreasing to 21.1 °C for the Middle Devonian

Paleoceanography 10.1029/2019PA003562

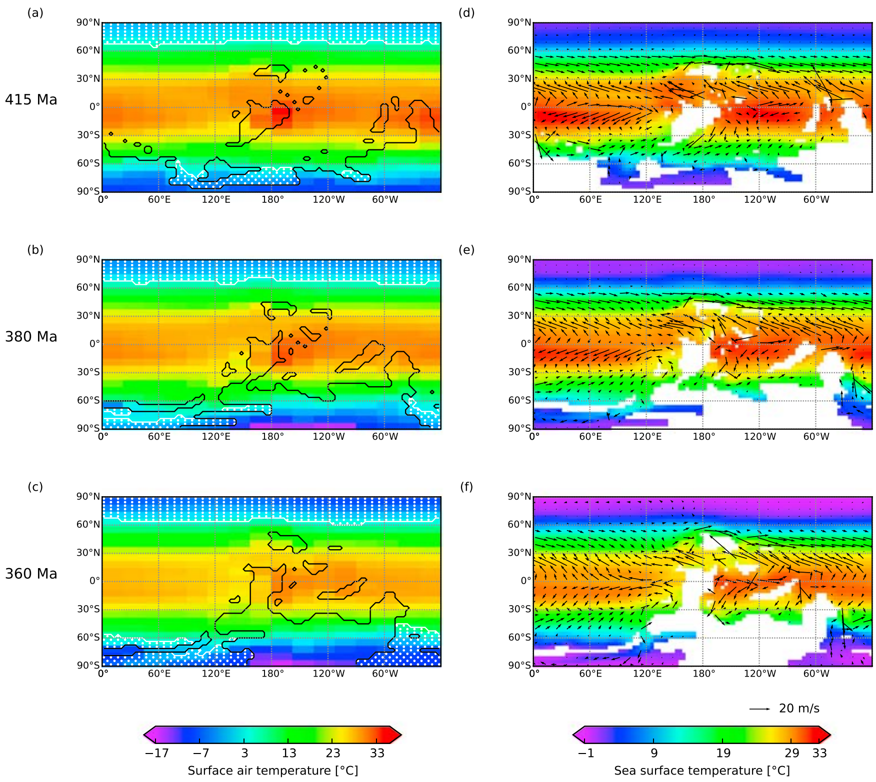

Figure 10. Temperature maps for the three Devonian best guess simulations. (first column) Annual mean surface air temperatures during the Early (a), Middle (b), and Late Devonian (c). The white dots indicate ocean cells where the annual mean sea ice fraction is above zero. The black line indicates the coastline at the resolution of the ocean model, whereas surface air temperatures are shown at the coarser resolution of the atmosphere model. (second column) Annual mean sea surface temperatures (shading) and ocean surface velocities (arrows) during the Early (d), Middle (e), and Late Devonian (f).

and 19.3 °C for the Late Devonian. Annual mean continental temperatures are 17.8 °C for the Early Devonian, 15.3 °C for the Middle Devonian, and 14.1 °C for the Late Devonian (Figure 10).

The contributions of the different forcings to the global cooling over the Devonian seen in the set of best guess simulations can be quantified and compared with the help of the sensitivity experiments described in section 3; see the summary shown in Figure 11. The cooling is dominantly driven by the strong decrease in CO_2 concentration (section 3.3) from 2,000 ppm for the Early Devonian to 1,000 ppm for the Late Devonian. The temperature decrease due to changes in the continental configuration (section 3.1) and the temperature rise caused by the increasing solar constant (section 3.2) approximately cancel each other. Finally, the influence of differences in vegetation cover on global mean surface air temperature, as described in section 3.4, can be neglected compared to the temperature changes induced by the other forcings.

While the impact of continental drift on the global climate during the Devonian is relatively small, the effect on continental and regional temperature distributions and ocean surface circulation is significant (Figure 10). A comparison of temperature patterns and land-ocean masks for the three continental configurations shows that the temperature distribution in the southern high latitudes is largely due to the differences in continental configuration. It is difficult to disentangle the influence of the different parameters on land temperature, but the sensitivity study of the vegetation's influence showed that vegetation has a cooling effect on the continental temperature north of 60°S which therefore likely contributes to the continental temperature decrease and the continental temperature patterns of the best guess simulations. Finally, the stronger cooling effect of the CO_2 decrease at high northern latitudes observed for the CO_2 sensitivity

Paleoceanography 10.1029/2019PA003562

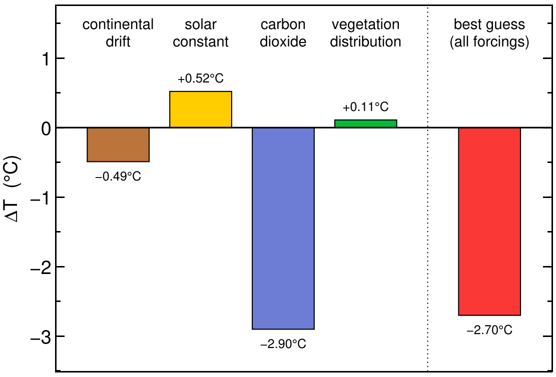

Figure 11. Simulated temperature change between the Early and the Late Devonian caused by changes in individual boundary conditions described in section 3 and by the combined forcing used in the best guess simulations.

simulations (section 2.2.3) is visible in the temperature maps of the best guess simulations as well and dominates over the warming expected in this region due to the increasing solar constant (section 2.2.2).

Note that we have fixed orbital parameters for the best guess simulations to a median orbit as the main aim of these simulations is the investigation of longer-term trends. This results in an uncertainty of ±0.3 °C which can be derived from the sensitivity experiments with respect to changes in orbital configuration (see section 3.5).

In the following, we want to compare our results with other proxy and modeling studies considering the climate throughout the Devonian. In their modeling study investigating the impact of orbital forcing on the Devonian climate (see the discussion in section 3.5) De Vleeschouwer et al. (2014) provide maps of December, January, and February and June, July, and August surface temperatures for a Late Devonian median orbit ($\varepsilon = 23.5°$ and $e = 0$) climate simulation. Keeping in mind that they use higher values for the CO_2 concentration and the solar constant, the seasonal temperature patterns agree well with our Late Devonian simulation. Furthermore, the patterns for the difference of evaporation and precipitation in our simulations (see Figure S7) match the model results and lithic indicators of palaeoclimate presented in De Vleeschouwer et al. (2014) reasonably well. We can therefore conclude that our model exhibits a good latitudinal representation of the major climate zones during the Devonian.

Simon et al. (2007) investigate the evolution of the atmospheric CO_2 concentration during the Devonian using a global biogeochemical model coupled to an energy balance climate model, taking into account the changes in continental configuration, sea level changes, and the increase of vegetation covered by land plants. The modeled CO_2 concentration of 3,000 ppm for the Early Devonian is very high (see Figure 1) and shows a general decreasing trend throughout the Devonian going along with the evolution of land plants, reaching low concentrations of 1,000 ppm already around 390 Ma and then fluctuating around this value during the following 30 million years. For the three Devonian periods covered by our best guess simulations, the low-latitude temperatures of Simon et al. (2007) compare well with their equivalent in our simulations although both studies are based on very different modeling approaches.

Considering proxy data, several studies determine tropical SSTs using $\delta^{18}O$. Van Geldern et al. 2006 use $\delta^{18}O$ from brachiopod shells to derive SSTs ranging from 24 to 27 °C in tropical to subtropical latitudes for the Early and Middle Devonian. For the Late Devonian, they discuss that their temperature estimates of 31 to 41 °C are significantly too warm for providing good living conditions for the diverse marine life found in their investigated successions, possibly suggesting an increase in $\delta^{18}O$ of seawater (Jaffrés et al., 2007) from the Devonian to present-day.

Joachimski et al. (2009) point out difficulties in the interpretation of $\delta^{18}O$ brachiopod shell signals and provide a $\delta^{18}O$ record derived from conodonts (see Figure 1b) which they argue to be a more reliable palaeotemperature record. In Figure 12 we compare their tropical SST estimates for different calibration standards and temperature equations with the SSTs from our best guess simulations. We averaged our SSTs between 10°S to 30°S since all the sections used for the temperature reconstruction in Joachimski et al. (2009) are located at palaeolatitudes in this range. Our tropical SSTs decrease from 28.9 °C for the Early Devonian to 28.3 °C for the Middle Devonian to 27.1 °C for the Late Devonian. For the Early Devonian, the new SST curve (M. Joachimski, private communication, January, 30th, 2018) calculated using the new calibration standard and temperature curve (Lécuyer et al., 2003, 2013) shows warm SSTs of 35 to 37 °C, with a cooling trend, continuing in the Middle Devonian, to temperatures of 23 to 27 °C. This is followed by an increase to 36 °C in the early Late Devonian and a slight decrease to 30 °C toward the end of the Devonian.

We note that the large spread of the data as well as the model uncertainty make the comparison of the model results with the temperatures from $\delta^{18}O$ difficult. Nevertheless, except for the Middle Devonian, we can state that the modeled temperatures from our best guess simulations shown in Figure 12 generally compare better with the lower SSTs values given in Joachimski et al. (2009) rather than the SSTs calculated using the new calibration standard and temperature curve. Together with the fact that these very high SSTs are

Paleoceanography 10.1029/2019PA003562

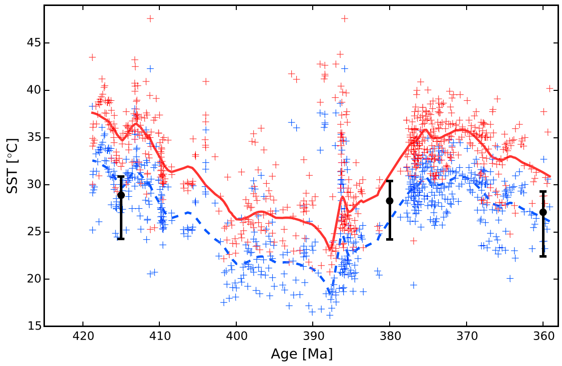

Figure 12. Comparison of reconstructed and modeled tropical sea surface temperatures for the Devonian. The blue crosses represent temperature estimates based on $\delta^{18}O$ data as shown in Joachimski et al. (2009); the red crosses (M. Joachimski, private communication) are based on the same data but use an updated NBS120c calibration standard of 21.7 (Lécuyer et al., 2003) rather than 22.6 (Vennemann et al., 2002) and assume a different temperature equation (Lécuyer et al., 2013). The solid red and dashed blue lines show local regression fits to the data points. The filled black circles are modeled SSTs from our best guess simulations averaged from 10°S to 30°S since all the sections used for the temperature reconstruction in Joachimski et al. (2009) are located at palaeolatitudes in this range. The error bar indicates the temperature range from 10°S to 30°S for each time slice. Note that the additional error due to uncertainties in the boundary conditions is much smaller than this temperature range; in the sensitivity experiments, SSTs at 10°S and 30°S vary by ± 1 °C at most for the range of CO_2 concentrations, orbital parameters, and vegetation distributions tested. Additional seasonal temperature variations (not shown) would mostly affect the lower end of the indicated temperature ranges; typical seasonal variations are roughly ± 2 °C at 30°S and ± 0.5 °C at 10°S. SST = sea surface temperature.

beyond the mortality limit for diverse ecosystems of higher marine life (van Geldern et al., 2006), this could indicate lower $\delta^{18}O$ levels of Devonian ocean water as compared to the present-day ocean (van Geldern et al., 2006; Jaffrés et al., 2007).

Considering the temperature trend, our model results, like other modeling studies (Simon et al., 2007), cannot reproduce the higher temperatures of the late Frasnian and early Famennian compared to the Middle Devonian, suggested by SST proxy data (Joachimski et al., 2009; van Geldern et al., 2006) and palaeontological studies (Streel et al., 2000). This could suggest missing forcings in the models, for example, the forcing induced by a change in O_2 concentration or an increase in the CO_2 concentration not resolved in the CO_2 proxy compilation.

Despite important differences, the general agreement of our results with the modeling studies of De Vleeschouwer et al. (2014) and Simon et al. (2007) is encouraging: We find similar temperature patterns for the median orbit simulations of De Vleeschouwer et al. (2014) and the low-latitude temperatures of Simon et al. (2007) compare well with ours. It is important, however, to keep the limitations of our model in mind. First, our it does not model vegetation dynamically. For this reason, climatic limits for the Devonian vegetation distributions had to be imposed from a simulation without vegetation cover (see section 2.2.4). We would argue, however, that our modeling approach is a reasonable approximation and complementary to studies with dynamic vegetation models since the limited knowledge of Devonian plant and soil properties could make the accurate representation of Devonian vegetation dynamics in these models difficult. Second, the increase in weathering due to the spread of land plants and the development of deeper roots are not modeled explicitly but only by imposing a reduction of CO_2 during the Devonian. Hence, the climate weathering feedback is not taken into account. The main effect, however, is captured by the decreasing atmospheric CO_2 concentration throughout the Devonian; hence, this seems to be a reasonable approach. Third, we employ a coupled climate model with a simplified, coarse-resolution atmosphere model. However, there is good agreement between our model and models with a more sophisticated atmosphere in a number of studies for a wide range of different time periods, for example, for the Neoproterozoic (Liu et al., 2013; Feulner & Kienert, 2014), for the last millennium (Feulner, 2011; Schurer et al., 2014), or for the 21st century (Feulner & Rahmstorf, 2010; Meehl et al., 2013). Furthermore, Ganopolski et al. (2001) investigate the effect of vegetation surface cover modeled by the coarser-resolution model CLIMBER-2, but with the same surface scheme as CLIMBER-3α, and find good agreement with results from more sophisticated models. Therefore, we do not consider the atmosphere model to be a serious limitation of this study.

6. Conclusions

In an attempt to disentangle the various factors influencing Earth's climate during the Devonian, we have systematically performed and analyzed a large set of sensitivity simulations with a coupled climate model, focussing in particular on the impact of changes in continental configuration, the biogeophysical effects of increasing vegetation cover, and variations related to Earth's orbital parameters. The key findings of our paper can be summarized as follows:

1. The impact of changes in orbital parameters (at a fixed CO_2 concentration) on the Devonian climate is in line with earlier findings in the sense that annual global mean temperature increases with obliquity and eccentricity. However, the differences in global mean temperature are much smaller in our simulations using an ocean general circulation model (rather than a simple slab ocean model with fixed heat transport) because of changes in ocean heat transport counteracting the insolation changes.

Paleoceanography 10.1029/2019PA003562

2. The most important mode of Devonian climate variability on centennial timescales relates to coupled changes in Arctic meridional ocean overturning, northern sea ice cover and deep ocean convection around the North Pole. Our results and a similar variability pattern described for the mid-Cretaceous (Poulsen & Zhou, 2013) suggest that this mode of climate variability is a more general feature of climate states with open water at one pole.
3. Best guess simulations for three time slices approximately representing the Early, Middle, and Late Devonian based on estimates of continental configuration, vegetation cover, solar constant, and atmospheric carbon dioxide concentration show a general climatic cooling trend in accordance with proxy estimates. This cooling is predominantly driven by decreasing levels of atmospheric CO_2 as derived from reconstructions. Furthermore, the biogeophysical impact of an increasing vegetation cover on the Devonian climate is small. In particular, the associated albedo changes cannot completely compensate for the falling CO_2 concentrations even under the assumption of a relatively high bare-soil albedo. The increase in temperatures around 390 Ma observed in reconstructions therefore remains difficult to reconcile with reconstructions indicating falling CO_2 levels.
4. Finally, simulated tropical SSTs for our Devonian time slices are generally significantly lower than the estimates based on δ^{18}O and the latest temperature calibration. This discrepancy and the fact that reconstructed temperatures are at times beyond the lethal limit for higher life (van Geldern et al., 2006) could indicate a general difference in the oxygen isotope ratio between the Devonian and modern oceans.

Our results on the Devonian climate highlight that much remains to be done to improve our understanding of this crucial period in Earth's history. Open issues include a better quantification of the biogeochemical impact of the spread of vascular land plants, the puzzling warming at the beginning of the Late Devonian despite falling atmospheric carbon dioxide levels, the climate response of an increase in the atmospheric oxygen concentration during the Devonian, and the interplay between terrestrial changes and the marine extinction events.

Data Availability Statement

All model input and output files as well as the preprocessing and postprocessing scripts used to generate model input and the figures in the paper are available online (http://www.pik-potsdam.de/data/doi/10.5880/PIK.2019.002/). The source code for the model used in this study is archived at the Potsdam Institute for Climate Impact Research and is made available upon request.

Author Contributions

J. B. and G. F. designed the study; all authors carried out and analyzed model simulations; J. B. and G. F. wrote the paper with input from M. H. and S. P.

Conflicts of Interest

The authors declare that they have no conflict of interest.

Acknowledgments
We thank Christopher Scotese for providing palaeocontinental reconstruction in electronic form, Michael Joachimski for sending their δ^{18}O and temperature data, David De Vleeschouwer for providing model output, and Jan Wohland for helpful comments. We are grateful to the Editors and anonymous reviewers for their helpful comments. The European Regional Development Fund (ERDF), the German Federal Ministry of Education and Research, and the Land Brandenburg are gratefully acknowledged for supporting this project by providing resources on the high performance computer system at the Potsdam Institute for Climate Impact Research. J. B. acknowledges funding by the German Federal Ministry of Education and Research BMBF within the Collaborative Project "Bridging in Biodiversity Science—BIBS" (funding 01LC1501A-H).

References

Algeo, T. J., Berner, R. A., Barry, M. J., & Scheckler, S. E. (1995). Late Devonian oceanic anoxic events and biotic crises: "Rooted" in the evolution of vascular land plants? *GSA Today*, *5*(3), 45, 64–66.
Algeo, T. J., & Scheckler, S. E. (1998). Terrestrial-marine teleconnections in the Devonian: Links between the evolution of land plants, weathering processes, and marine anoxic events. *Transactions of the Royal Society B: Biological Sciences*, *353*, 113–130. https://doi.org/10.1098/rstb.1998.0195
Bahcall, J. N., Pinsonneault, M. H., & Basu, S. (2001). Solar models: Current epoch and time dependences, neutrinos, and helioseismological properties. *The Astrophysical Journal*, *555*(2), 990–1012. https://doi.org/10.1086/321493
Bambach, R. K. (2006). Phanerozoic biodiversity mass extinctions. *Annual Review of Earth and Planetary Sciences*, *34*, 127–155. https://doi.org/10.1146/annurev.earth.33.092203.122654
Berner, R. A. (1994). GEOCARBII: A revised model of atmospheric CO_2 over Phanerozoic time. *American Journal of Science*, *294*, 56–91. https://doi.org/10.2475/ajs.301.2.182
Berner, R. A. (2006). GEOCARBSULF: A combined model for Phanerozoic atmospheric O_2 and CO_2. *Geochimica et Cosmochimica Acta*, *70*(23), 5653–5664. A Special Issue Dedicated to Robert A. Berner) https://doi.org/10.1016/j.gca.2005.11.032
Berner, R. A., & Kothavala, Z. (2001). Geocarb III: A revised model of atmospheric CO_2 over Phanerozoic time. *American Journal of Science*, *301*(2), 182–204. https://doi.org/10.2475/ajs.301.2.182

Paleoceanography 10.1029/2019PA003562

Betts, R. A. (2000). Offset of the potential carbon sink from boreal forestation by decreases in surface albedo. *Nature*, *408*, 187–190. https://doi.org/10.1038/35041545
Bonan, G. B. (2008). Forests and climate change: Forcings, feedbacks, and the climate benefits of forests. *Science*, *320*(5882), 1444–1449. https://doi.org/10.1126/science.1155121
Bond, D. P. G., & Wignall, P. B. (2008). The role of sea-level change and marine anoxia in the Frasnian-Famennian (Late Devonian) mass extinction. *Palaeogeography, Palaeoclimatology, Palaeoecology*, *263*(3-4), 107–118. https://doi.org/10.1016/j.palaeo.2008.02.015
Bouttes, N., Paillard, D., & Roche, D. M. (2010). Impact of brine-induced stratification on the glacial carbon cycle. *Climate of the Past*, *6*, 575–589. https://doi.org/10.5194/cp-6-575-2010
Boyce, C. K., & Lee, J.-E. (2017). Plant evolution and climate over geological timescales. *Annual Review of Earth and Planetary Sciences*, *45*, 61–87. https://doi.org/10.1146/annurev-earth-063016-015629
Brezinski, D. K., Cecil, C. B., Skema, V. W., & Kertis, C. A. (2009). Evidence for long-term climate change in Upper Devonian strata of the central Appalachians. *Palaeogeography, Palaeoclimatology, Palaeoecology*, *284*(3), 315–325. https://doi.org/10.1016/j.palaeo.2009.10.010
Brezinski, D. K., Cecil, C. B., Skema, V. W., & Stamm, R. (2008). Late Devonian glacial deposits from the eastern United States signal an end of the mid-Paleozoic warm period. *Palaeogeography, Palaeoclimatology, Palaeoecology*, *268*(3), 143–151. https://doi.org/10.1016/j.palaeo.2008.03.042
Brugger, J., Feulner, G., & Petri, S. (2017). Baby, it's cold outside: Climate model simulations of the effects of the asteroid impact at the end of the Cretaceous. *Geophysical Research Letters*, *44*, 419–427. https://doi.org/10.1002/2016GL072241
Caputo, M. V. (1985). Late Devonian glaciation in South America. *Palaeogeography, Palaeoclimatology, Palaeoecology*, *51*, 291–317. https://doi.org/10.1016/0031-0182(85)90090-2
Caputo, M. V., de Melo, J. H. G., Streel, M., & Isbell, J. L. (2008). Late Devonian and Early Carboniferous glacial records of South America. In C. R. Fielding, T. D. Frank, & J. L. Isbell (Eds.), *Resolving the Late Paleozoic ice age in time and space* (Vol. 441, pp. 161–173). Boulder, Colorado: Geol S Am S. https://doi.org/10.1130/2008.2441(11)
Clack, J. A. (2007). Devonian climate change, breathing, and the origin of the tetrapod stem group. *Integrative and Comparative Biology*, *47*(4), 510–523. https://doi.org/10.1093/icb/icm055
Copper, P., & Scotese, C. (2003). Megareefs in Middle Devonian supergreenhouse climates. In M. A. Chan, & A. W. Archer (Eds.), *Extreme depositional environments: Mega end members in geologic time*. Boulder, Colorado: Geol S Am S, 370, pp. 209–230.
Dahl, T. W., Hammarlund, E. U., Anbar, A. D., Bond, DavidP. G., Gill, B. C., Gordon, G. W., et al. (2010). Devonian rise in atmospheric oxygen correlated to the radiations of terrestrial plants and large predatory fish. *Proceedings of the National Academy of Sciences of the United States of America*, *107*(42), 17,911–17,915. https://doi.org/10.1073/pnas.1011287107
De Vleeschouwer, D., Crucifix, M., Bounceur, N., & Claeys, P. (2014). The impact of astronomical forcing on the Late Devonian greenhouse climate. *Global Planet Change*, *120*, 65–80. https://doi.org/10.1016/j.gloplacha.2014.06.002
De Vleeschouwer, D., Da Silva, A.-C., Sinnesael, M., Chen, D., Day, J. E., Whalen, M. T., et al. (2017). Timing and pacing of the Late Devonian mass extinction event regulated by eccentricity and obliquity. *Nature Communications*, *8*, 2268. https://doi.org/10.1038/s41467-017-02407-1
De Vleeschouwer, D., Rakocinski, M., Racki, G., Bond, D., Sobie, K., Bounceur, N., et al. (2013). The astronomical rhythm of Late-Devonian climate change (Kowala section, Holy Cross Mountains, Poland). *Earth and Planetary Science Letters*, *365*, 25–37. https://doi.org/10.1016/j.epsl.2013.01.016
Dickinson, R. E., Henderson-Sellers, A., & Kennedy, P. J. (1993). Biosphere-Atmosphere Transfer Scheme (BATS) version 1e as coupled to the NCAR Community Climate Model (*NCAR Technical Note NCAR/TN-387+STR*). Boulder, Colorado: National Center Atmospheric Research. https://doi.org/10.5065/D67W6959
Dickinson, R. E., Henderson-Sellers, A., Kennedy, P. J., & Wilson, M. F. (1986). Biosphere-Atmosphere Transfer Scheme (BATS) for the NCAR Community Climate Model (*NCAR Technical Note NCAR/TN-275+STR*). Boulder, Colorado: National Center Atmospheric Research. https://doi.org/10.5065/D6668B58
Eby, M., Weaver, A. J., Alexander, K., Zickfeld, K., Abe-Ouchi, A., Cimatoribus, A. A., et al. (2013). Historical and idealized climate model experiments: An intercomparison of Earth system models of intermediate complexity. *Climate of the Past*, *9*, 1111–1140. https://doi.org/10.5194/cp-9-1111-2013
Feulner, G. (2011). Are the most recent estimates for Maunder Minimum solar irradiance in agreement with temperature reconstructions? *Geophysical Research Letters*, *38*, L16706. https://doi.org/10.1029/2011GL048529
Feulner, G. (2017). Formation of most of our coal brought Earth close to global glaciation. *Proceedings of the National Academy of Sciences of the United States of America*, *114*, 11,333–11,337. https://doi.org/10.1073/pnas.1712062114
Feulner, G., Hallmann, C., & Kienert, H. (2015). Snowball cooling after algal rise. *Nature Geosci.*, *8*, 659–662. https://doi.org/10.1038/ngeo2523
Feulner, G., & Kienert, H. (2014). Climate simulations of Neoproterozoic snowball Earth events: Similar critical carbon dioxide levels for the Sturtian and Marinoan glaciations. *Earth and Planetary Science Letters*, *404*, 200–205. https://doi.org/10.1016/j.epsl.2014.08.001
Feulner, G., & Rahmstorf, S. (2010). On the effect of a new grand minimum of solar activity on the future climate on Earth. *Geophysical Research Letters*, *37*, L05707. https://doi.org/10.1029/2010GL042710
Fichefet, T., & Morales Maqueda, M. A. (1997). Sensitivity of a global sea ice model to the treatment of ice thermodynamics and dynamics. *Journal of Geophysical Research*, *102*(C6), 12,609–12,646. https://doi.org/10.1029/97JC00480
Foster, G. L., Royer, D. L., & Lunt, D. J. (2017). Future climate forcing potentially without precedent in the last 420 million years. *Nature Communications*, *8*, 14845. https://doi.org/10.1038/ncomms14845
Ganopolski, A., Petoukhov, V., Rahmstorf, S., Brovkin, V, Claussen, M., Eliseev, A., & Kubatzki, C. (2001). CLIMBER-2: a climate system model of intermediate complexity. Part II: Model sensitivity. *Climate Dynamics*, *17*, 735–751. https://doi.org/10.1007/s003820000144
Goddéris, Y., & Joachimski, M. (2004). Global change in the Late Devonian: Modelling the Frasnian-Famennian short-term carbon isotope excursions. *Palaeogeography, Palaeoclimatology, Palaeoecology*, *202*, 309–329. https://doi.org/10.1016/S0031-0182(03)00641-2
Haq, B. U., & Schutter, S. R. (2008). A chronology of Paleozoic sea-level changes. *Science*, *322*(5898), 64–68. https://doi.org/10.1126/science.1161648
Harada, N. (2016). Review: Potential catastrophic reduction of sea ice in the western Arctic Ocean: Its impact on biogeochemical cycles and marine ecosystems. *Global and Planetary Change*, *136*, 1–17. https://doi.org/10.1016/j.gloplacha.2015.11.005
Hofmann, M., & Morales Maqueda, M. A. (2006). Performance of a second-order moments advection scheme in an Ocean General Circulation Model. *Journal of Geophysical Research*, *111*, C05006. https://doi.org/10.1029/2005JC003279
IPCC (2013). *Climate change 2013: The physical science basis. Contribution of working group I to the fifth assessment report of the intergovernmental panel on climate change*. (T. Stocker et al., Eds.) Cambridge, United Kingdom and New York, NY, USA: Cambridge University Press. https://doi.org/10.1017/CBO9781107415324

Jaffrés, J. B. D., Shields, G. A., & Wallmann, K. (2007). The oxygen isotope evolution of seawater: A critical review of a long-standing controversy and an improved geological water cycle model for the past 3.4 billion years. *Earth-Science Reviews*, *83*(1), 83–122. https://doi.org/10.1016/j.earscirev.2007.04.002
Joachimski, M., Breisig, S, Buggisch, W., Talent, J., Mawson, R., Gereke, M, et al. (2009). Devonian climate and reef evolution: Insights from oxygen isotopes in apatite. *Earth and Planetary Science Letters*, *284*, 599–609. https://doi.org/10.1016/j.epsl.2009.05.028
Johnson, J. G., Klapper, G., & Sandberg, C. A. (1985). Devonian eustatic fluctuations in Euramerica. *GSA Bulletin*, *96*(5), 567. https://doi.org/10.1130/0016-7606(1985)96h567:DEFIEi2.0.CO;2
Kopp, G., & Lean, J. L. (2011). A new, lower value of total solar irradiance: Evidence and climate significance. *Geophysical Research Letters*, *38*, L01706. https://doi.org/10.1029/2010GL045777
Lécuyer, C., Amiot, R., Touzeau, A., & Trotter, J. (2013). Calibration of the phosphate δ^{18}O thermometer with carbonate water oxygen isotope fractionation equations. *Chemical Geology*, *347*, 217–226. https://doi.org/10.1016/j.chemgeo.2013.03.008
Lécuyer, C., Picard, S., Garcia, J.-P., Sheppard, S. M. F., Grandjean, P., & Dromart, G. (2003). Thermal evolution of Tethyan surface waters during the Middle-Late Jurassic: Evidence from δ^{18}O values of marine fish teeth. *Paleoceanography*, *18*(3), 1076. https://doi.org/10.1029/2002PA000863
Le Hir, G., Donnadieu, Y., Goddéris, Y., Meyer-Berthaud, B., Ramstein, G., & Blakey, R. C. (2011). The climate change caused by the land-plant invasion in the Devonian. *Earth and Planetary Science Letters*, *310*, 203–212. https://doi.org/10.1016/j.epsl.2011.08.042
Lieth, H. (1973). Primary production: Terrestrial ecosystems. *Human Ecology*, 1(4), 303–332. https://doi.org/10.1007/BF01536729
Liu, Y., Peltier, W. R., Yang, J., & Vettoretti, G. (2013). The initiation of Neoproterozoic "snowball" climates in CCSM3: The influence of paleocontinental configuration. *Climate of the Past*, *9*, 2555–2577. https://doi.org/10.5194/cp-9-2555-2013
Ma, X., Gong, Y., Chen, D., Racki, G., Chen, X., & Liao, W. (2016). The Late Devonian Frasnian Famennian Event in South China Patterns and causes of extinctions, sea level changes, and isotope variations. *Palaeogeography, Palaeoclimatology, Palaeoecology*, *448*, 224–244. https://doi.org/10.1016/j.palaeo.2015.10.047
Marshall, J., & Plumb, R. A. (2008). *Atmosphere, ocean, and climate dynamics: An introductory text*, vol. 93. Amsterdam: Elsevier Academic Press: International Geophysics Series.
McGhee, G. R. (1996). *The Late Devonian mass extinction—The Frasnian/Famennian crisis*. New York: Columbia University Press.
McGhee, G. R., Gilmore, J. S., Orth, C. J., & Olsen, E. (1984). No geochemical evidence for an asteroidal impact at late Devonian mass extinction horizon. *Nature*, *308*(5960), 629–631. https://doi.org/10.1038/308629a0
Meehl, G. A., Arblaster, J. M., & Marsh, D. R. (2013). Could a future "Grand Solar Minimum" like the Maunder Minimum stop global warming? *Geophysical Research Letters*, *40*, 1789–1793. https://doi.org/10.1002/grl.50361
Milankovitch, M. (1941). *Kanon der Erdbestrahlung und seine Anwendung auf das Eiszeitenproblem*. Belgrad: Königlich Serbische Akademie.
Montoya, M., Griesel, A., Levermann, A., Mignot, J., Hofmann, M., Ganopolski, A., & Rahmstorf, S. (2005). The earth system model of intermediate complexity CLIMBER-3α. Part I: Description and performance for present-day conditions. *Climate Dynamics*, *25*(2-3), 237–263. https://doi.org/10.1007/s00382-005-0044-1
Pacanowski, R. C., & Griffies, S. M. (1999). The MOM-3 Manual (*Tech. Rep. No. 4*). Princeton, NJ: GFDL Ocean Group, NOAA/Geophysical Fluid Dynamics Laboratory.
Petoukhov, V., Ganopolski, A., Brovkin, V., Claussen, M., Eliseev, A., Kubatzki, C., & Rahmstorf, S. (2000). CLIMBER-2: A climate system model of intermediate complexity. Part I: Model description and performance for present climate. *Climate Dynamics*, *16*(1), 1–17. https://doi.org/10.1007/PL00007919
Porada, P., Lenton, T. M., Pohl, A., Weber, B., Mander, L., Donnadieu, Y., et al. (2016). High potential for weathering and climate effects of non-vascular vegetation in the Late Ordovician. *Nature Communications*, *7*, 12113. https://doi.org/10.1038/ncomms12113
Poulsen, C. J., Tabor, C., & White, J. D. (2015). Long-term climate forcing by atmospheric oxygen concentrations. *Science*, *348*(6240), 1238–1241. https://doi.org/10.1126/science.1260670
Poulsen, C. J., & Zhou, J. (2013). Sensitivity of Arctic climate variability to mean state: Insights from the Cretaceous. *Journal of Climate*, *26*(18), 7003–7022. https://doi.org/10.1175/JCLI-D-12-00825.1
Royer, D. L. (2006). CO_2-forced climate thresholds during the Phanerozoic. *Geochimica et Cosmochimica Acta*, *70*(23), 5665–5675. https://doi.org/10.1016/j.gca.2005.11.031
Rubinstein, C. V., Gerrienne, P., de la Puente, G. S., Astini, R. A., & Steemans, P. (2010). Early Middle Ordovician evidence for land plants in Argentina (eastern Gondwana). *New Phytologist*, *188*(2), 365–369. https://doi.org/10.1111/j.1469-8137.2010.03433.x
Sandberg, C. A., Morrow, J. R., & Ziegler, W. (2002). Late Devonian sea-level changes, catastrophic events, and mass extinctions. In C. Koeberl, & K. G. MacLeod (Eds.), *Catastrophic events and mass extinctions: Impacts and beyond* (vol. 356, pp. 473–487). Boulder, Colorado: Geol S Am S. https://doi.org/10.1130/0-8137-2356-6.473
Sanromá, E., Pallé, E., & García Munõz, A. (2013). On the effects of the evolution of microbial mats and land plants on the Earth as a planet. Photometric and spectroscopic light curves of Paleo-Earths. *The Astrophysical Journal*, *766*, 133. https://doi.org/10.1088/0004-637X/766/2/133
Schaphoff, S., von Bloh, W., Rammig, A., Thonicke, K., Biemans, H., Forkel, M., et al. (2018). LPJmL4—A dynamic global vegetation model with managed land—Part 1: Model description. *Geoscientific Model Development*, *11*(4), 1343–1375. https://doi.org/10.5194/gmd-11-1343-2018
Schurer, A. P., Tett, S. F. B., & Hegerl, G. C. (2014). Small influence of solar variability on climate over the past millennium. *Nature Geoscience*, *7*, 104–108. https://doi.org/10.1038/ngeo2040
Scotese, C. R. (2014). *Atlas of Devonian Paleogeographic Maps, PALEOMAP Atlas for ArcGIS, Volume 4, The Late Paleozoic, Maps 65-72 (Mollweide Projection)*. Evanston, IL: PALEOMAP Project. https://doi.org/10.13140/2.1.1542.5280
Serreze, M. C., & Barry, R. G. (2011). Processes and impacts of Arctic amplification: A research synthesis. *Global and Planetary Change*, *77*(12), 85–96. https://doi.org/10.1016/j.gloplacha.2011.03.004
Simon, L., Goddéris, Y., Buggisch, W., Strauss, H., & Joachimski, M. M. (2007). Modeling the carbon and sulfur isotope compositions of marine sediments: Climate evolution during the Devonian. *Chemical Geology*, *246*(1), 19–38. https://doi.org/10.1016/j.chemgeo.2007.08.014
Steemans, P., Hérissé, A. L., Melvin, J., Miller, M. A., Paris, F., Verniers, J., & Wellman, C. H. (2009). Origin and radiation of the earliest vascular land plants. *Science*, *324*, 353–353. https://doi.org/10.1126/science.1169659
Stoy, P. C., Street, L. E., Johnson, A. V., Prieto-Blanco, A., & Ewing, S. A. (2012). Temperature, heat flux, and reflectance of common subarctic mosses and lichens under field conditions: Might changes to community composition impact climate-relevant surface fluxes? *Arctic, Antarctic, and Alpine Research*, *44*(4), 500–508. https://doi.org/10.1657/1938-4246-44.4.500

Paleoceanography 10.1029/2019PA003562

Streel, M., Caputo, M. V., Loboziak, S., & Melo, J. H. G. (2000). Late Frasnian-Famennian climates based on palynomorph analyses and the question of the Late Devonian glaciations. *Earth-Science Reviews*, *52*, 121–173. https://doi.org/10.1016/S0012-8252(00)00026-X

van Geldern, R., Joachimski, M. M., Day, J., Jansen, U., Alvarez, F., Yolkin, E. A., & Ma, X.-P. (2006). Carbon, oxygen and strontium isotope records of Devonian brachiopod shell calcite. *Palaeogeography, Palaeoclimatology, Palaeoecology*, *240*(1), 47–67. https://doi.org/10.1016/j.palaeo.2006.03.045

Vennemann, T., Fricke, H., Blake, R., O'Neil, J., & Colman, A. (2002). Oxygen isotope analysis of phosphates: A comparison of techniques for analysis of Ag_3PO_4. *Chemical Geology*, *185*, 321–336. https://doi.org/10.1016/S0009-2541(01)00413-2

Wade, D. C., Abraham, N. L., Farnsworth, A., Valdes, P. J., Bragg, F., & Archibald, A. T. (2018). Simulating the climate response to atmospheric oxygen variability in the Phanerozoic. *Climate of the Past Discussions*, *2018*, 1–35. Retrieved from https://www.clim-past-discuss.net/cp-2018-149/, https://doi.org/10.5194/cp-2018-149

Zickfeld, K., Eby, M., Weaver, A. J., Alexander, K., Crespin, E., Edwards, N. R., et al. (2013). Long-term climate change commitment and reversibility: An EMIC intercomparison. *Journal of Climate*, *26*, 5782–5809. https://doi.org/10.1175/JCLI-D-12-00584.1

2.2. Low atmospheric CO_2 levels before the emergence of forested ecosystems

Low atmospheric CO_2 levels before the emergence of forested ecosystems

Dahl TW[1], Harding MAR[1], Brugger J[2,3,4], Feulner G[2], Norrman K[5], and Junium CK[6]

[1]GLOBE institute, University of Copenhagen, Øster Voldgade 5-7, DK-1350 Copenhagen K, Denmark
[2]Earth System Analysis, Potsdam Institute for Climate Impact Research, Member of the Leibniz Association, Potsdam, Germany
[3]Senckenberg Biodiversity and Climate Research Centre (SBiK-F), Frankfurt am Main, Germany
[4]Institute for Physics and Astronomy, University of Potsdam, Potsdam, Germany
[5]Center for Integrative Petroleum Research, King Fahd University of Petroleum and Minerals, Saudi Arabia
[6]Department of Earth and Environmental Sciences, Syracuse University, Syracuse New York, 13244, USA

The largest atmospheric pCO_2 decline in recorded Earth history has been linked to the Devonian radiation of land plants that fundamentally altered weathering processes and afforested the continents. However, the near absence of pCO_2 constraints before the emergence of forests limits our ability to quantify the climatic impact of expanding forested ecosystems. Here, we report CO_2-sensitive carbon isotope fractionation in the earliest vascular plant fossils and revise Devonian paleo-CO_2 records to find low atmospheric CO_2 levels before continents were afforested and modest pCO_2 decline, and in fact, a small increase coinciding with the emergence of trees with deeper root systems. Specifically, atmospheric CO_2 levels were 500^{+130}_{-28} ppm CO_2 (CI = 95‰) ~410 million years ago (Ma) and subsequently declined in two stages as inferred from young Devonian plants. This means that the main phase of CO_2 removal was over when plants evolved tree stature. Earth System modeling suggests the evolution of shallow vascular ecosystems could have forever changed continental weathering processes and caused both climatic cooling and atmospheric oxygenation long before the rise of forests.

Keywords:
Land plants; Climate; atmospheric CO_2; Carbon isotopes; Paleozoic; Earth System Models

Main text

Atmospheric CO_2 is a greenhouse gas that has affected Earth's climate throughout geological history[1,2]. In the absence of anthropogenic fossil fuel combustion, the dominant atmospheric CO_2 source is volcanic outgassing, and this source is balanced by the removal that occurs when CO_2–bearing fluids chemically react and weather continental rocks followed by marine carbonate precipitation[3]. The dissolution of silicate rocks in the weathering zone occurs via interactions between the terrestrial ecosystem and geological processes that make fresh rock surface available for reaction, but the governing feedbacks on CO_2 removal and how it affects the global level is still debated[4–7]. Enhanced continental weathering by the evolving land flora is predicted to have caused a ~10-fold decline in atmospheric pCO_2 to near modern levels, coupled to a slow transition from greenhouse to icehouse conditions from the Ordovician-Silurian into the Devonian-Carboniferous[2]. The temporal correlation between atmospheric pCO_2 and glaciation has been disputed[6], and models suggest glaciations could persist even at 12-14 times pre-industrial atmospheric levels (PIAL)[8]. Therefore, a precise reconstruction of atmospheric pCO_2 in relation to plant evolution is key to assess the impact of the terrestrial biota on Earth's climate.

However, existing records of Paleozoic atmospheric pCO_2 are scant and mostly rely on proxies with large uncertainties[9,12]. High pCO_2 levels of 12–24 PIAL prior to the radiation of vascular plants are indicated from CO_2 hosted in pedogenic goethite in a Late Ordovician paleosol from Potter's Mill in New York, USA[9]. The uncertainty of this estimate represents only analytical error, and the error could be much larger since this proxy has never been verified in modern soils or applied at any other time in Earth history (see supplementary info). Lower and declining atmospheric CO_2 levels from 5 to 0.7 PIAL through the Devonian has been inferred from the carbon isotope compositions of pedogenic carbonate [10,11,1], but this approach depends critically on parameters that cannot be constrained from the rock record, including the proportion and isotope signature of soil-respired CO_2 in the soil carbonate. Another line of evidence for high atmospheric pCO_2 around ~16 PIAL in the early Devonian is reported from extinct fossil land plants with low stomatal density and low ratios of stomata to epidermal cells, characteristic of plant growth at high ambient pCO_2[12]. However, some extant Devonian plants (e.g., *Baragwanathia* sp.) of same age have higher stomatal densities suggestive of lower atmospheric pCO_2 closer to ~1 PIAL

(Table S3). Initially, we calibrated the stomatal proxy for three species of clubmosses (lycophytes) at today's pCO_2 level (~410 ppm) to find that the full range of stomatal densities observed in early Devonian plant fossils is also represented in their nearest living representatives today (supplementary material). Therefore, well-calibrated proxies are needed to reconstruct atmospheric pCO_2 during early plant evolution.

Δ_{leaf} – a robust paleo-CO_2 barometer

Here, we measured pCO_2-sensitive carbon isotope fractionation in fossilized plant fragments of the ~410 Ma *Baragwanathia* flora in Australia and compared to a compilation of younger Devonian C3 plants[13]. *Baragwanathia* marks the first appearance of clubmosses (lycophytes) and the genus is found worldwide in Late Silurian-Early Devonian strata. We studied well-preserved specimens from the younger of two plant assemblages found in Victoria (see Methods and supplementary information for details on the materials and geological settings).

During photosynthesis land plants favor the lighter of the two stable isotopes, ^{12}C and ^{13}C, primarily during carboxylation by the Rubisco enzyme and secondarily during CO_2 diffusion into the cell. The isotopic offset between CO_2 in ambient air and plant organic matter, Δ_{leaf}, reflects the balance between photosynthesis and stomatal conductance, and the magnitude of the isotope fractionation varies with climate and plant characteristics[14,15]. Modern culture experiments show that atmospheric pCO_2 exerts prime control on Δ_{leaf} with ~9‰ (5–15%) larger fractionation in C3 plants grown at 4000 ppm compared to equivalent plants grown at 400 ppm (Figure 1) with greater accuracy at lower pCO_2. This fractionation has been observed in cultivated spore-bearing plants across a wide range of ambient CO_2 levels for a series of land plants that are physiologically similar to Devonian land plants, including the lycophyte (*Selaginella kraussiana*), monilophytes (*Equisetum telmateia*), but also in non-stomatal plants (i.e. thalloid liverworts: *Marchantia polymorpha*, *Lunularia cruciata*)[16,17]. The Δ_{leaf} response to pCO_2 has been successfully verified for average Holocene C3 plants, where ice core data independently constrain a rise in atmospheric pCO_2[18], although a lesser sensitivity to CO_2 has been suggested by comparison to proxy records of the 100 Myr[19]. Even if the Δ_{leaf} method was less sensitive than first assumed, it can provide a better constraint of the Paleozoic atmospheric pCO_2 than previously used methods.

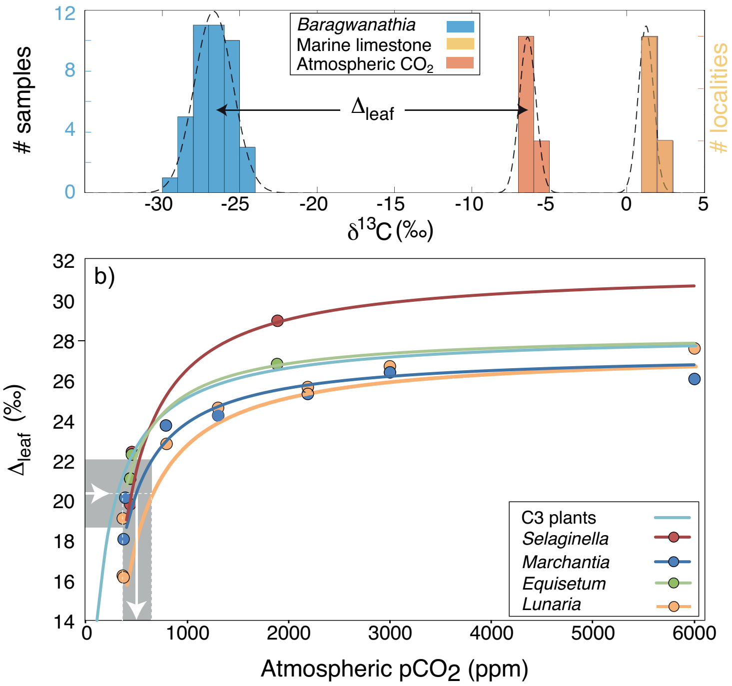

Figure 1. Atmospheric pCO_2 levels as derived from the carbon isotope fractionation in ancient plants. a) Carbon isotope composition of the *Baragwanathia* flora (blue), marine carbonates (yellow) and calculated atmospheric CO_2 (orange), see Table S2. b) Carbon isotope fractionation in plants increases with ambient CO_2 levels in controlled experiments with spore-bearing tracheophytes, including lycophyte (*Selaginella kraussiana*), thalloid liverworts (*Marchantia polymorpha*, *Lunularia cruciata*) and monilophytes (*Equisetum telmateia*)[16,17] and average Pleistocene-Holocene C3 plants (see legend)[18]. The data fits hyperbolic relationships with two parameters *a* and Δ_{max}, i.e. $(\Delta_{leaf} - \Delta_{max})^{-1} = a \cdot pCO_2$.

The oldest fossilized plant fragments from the *Baragwanathia* flora have carbon isotope compositions ($\delta^{13}C = -26.8 \pm 0.5‰$, 1SD, n = 26) similar to equivalent modern tropical plants (Figure 1; Table S1). The isotopic variance in the studied plant fossil assemblage matches the expected physiological variation of Devonian lycophytes[13]. Hence, we take the average value as representative of tropical C3 plants ~410 Ma. The isotope fractionation exerted by the paleoflora is calculated from the composition of the contemporaneous atmosphere (–6.4±1.0‰, 2 SE), constrained by the carbon isotopic record of marine carbonates from multiple paleocontinents[20] (see details in SI). This means that the spore-bearing *Baragwanathia* flora on average exerted a carbon isotope fractionation of $\Delta_{leaf} = 20.4 \pm 1.1‰$, characteristic of growth in an atmosphere with 500^{+130}_{-29} ppm CO_2 (2 SE, Figure 1). The uncertainty represents the full range of physiological responses observed in four comparable modern spore-bearing plants species (*S. kraussiana*, *M. polymorpha, L. cruciata*, and *E. telmateia*)[16,17], which is greater than the propagated uncertainty from the isotope data alone. A similar, but even lower, pCO_2 estimate (309^{+125}_{-82} ppm) is obtained if the conversion was based on the paleorecord from Pleistocene-Holocene[18] fossils, but this calibration includes angiosperms and other more recent C3 plant lineages with a distinct physiological response than that of the spore-bearing Devonian flora[17]. Consequently, the Δ_{leaf} proxy data imply low atmospheric pCO_2 levels before the emergence of forests.

Two confounding factors on the magnitude of photosynthetic carbon isotope fractionation are humidity and atmospheric O_2 levels. First, plants down-regulate stomatal conductance and increase their water utilization efficiency (WUE)[21] in drier habitats. This effect is clearly expressed in modern plants where it reduces the magnitude of isotope fractionation in habitats where the mean annual precipitation is below ~1000 mm/yr (Figure S1). To explore this effect on the *Baragwanathia* flora, we used a coupled atmosphere-ocean paleoclimate model of intermediate complexity (CLIMBER-3α) to evaluate the Devonian climate at 500 ppm pCO_2 and specifically conditions in the tropics where the *Baragwanathia* flora lived (see Methods). The model predicts a temperate planet with the flora growing at 25-27°C in the monsoonal belt with high precipitation rates (>2000 mm/yr). Thus, the studied plants grew at sufficiently high humidity that they should not have downregulated their stomatal conductance (see SI). Secondly, atmospheric O_2 also affect the carbon isotope fractionation in plants, photosynthetic CO_2 fixation will compete with photosynthetic O_2 fixation on the Rubisco enzyme[16]. This effect is more pronounced at low ambient CO_2, but still only affects Δ_{leaf} by less than 0.7‰ in *Marchantia polymorpha* corresponding to an offset in atmospheric pCO_2 by up to 50 ppm, since atmospheric pO_2 was at least 15 atm% at this time[22]. Therefore, the isotope fractionations exerted by the *Baragwanathia* flora 410 Ma, is best ascribed to modest atmospheric pCO_2 levels in the 300–700 ppm range.

Other variables that affect Δ_{leaf} such as temperature and light is not expected to significantly influence the results[16]. Nonetheless, we acknowledge that the present may not necessarily provide the key to unlock the past if early land plants were physiologically distinct from their modern descendants. Specifically, we speculate that smaller fractionations might arise among early land plants if they were coated in thicker cuticular waxes, e.g. for desiccation resistance. With limited diffusive CO_2 escape out of the cell, the Rubisco enzyme should be less isotopically selective. However, there is no information on the presence or distribution of waxes in early land plants[23]. To test this, we compared our results from the *Baragwanathia* flora to other Devonian land plants[13] to find that all plants from lycophytes (e.g., *Drepanophycus*) to progymnosperm trees (*Archaeopteris*) show remarkably low Δ_{leaf} values evocative of growth at low ambient pCO_2.

Atmospheric CO_2 and early afforestation

We computed Δ_{leaf} from carbon isotope records of Devonian land plants and marine carbonates 410–360 Ma to establish an atmospheric pCO_2 curve for the subsequent evolution of vascular ecosystems when trees with deeper root systems emerged (Figure 2). The isotope records of both terrestrial plants and marine carbonates span data from the tropics and subtropics across several paleocontinents and may therefore carry a small bias towards underestimating pCO_2 due to the WUE effect[13] (see SI). Further, the record may also include erroneous pCO_2 variability over time periods shorter than ~1 My due to imprecise temporal correlation between the interpolated terrestrial and marine records. Nevertheless, atmospheric pCO_2 was persistently low with two stages of slowly declining CO_2 levels from ~500 to ~300 ppm interrupted by a sudden pCO_2 increase near the Mid-Late Devonian boundary, ~385 Ma.

The Mid-Paleozoic climate

The Devonian climate has previously been described mostly as a warm greenhouse that transited into a colder state with polar glaciations in the Late Devonian-Carboniferous[24,2]. We ran Early Devonian paleoclimate models with 500 ppm CO_2 (CLIMBER-3α) to find that predict a clement climate mean annual temperatures of 14.8–15.7°C and a strong latitudinal temperature gradient not too dissimilar from today. Average tropical temperatures of ~25-27°C are consistent with paleotemperature records[25], and deviates from previous models as it predicts polar sea ice and snowfall on Gondwana during winters. The model is not coupled to a dynamic ice sheet model, so the extent and persistence of ice sheets is not determined. Yet, we find that the Earth system was climatically stable, and ice-albedo feedbacks that could cascade into a snowball-style glaciations were highly unlikely, a condition that is also supported by model simulations bracketing the Early Devonian[26,27,28]. In line with other paleoclimate models[8,29,30], our results suggest that Earth's climate was in an icehouse state with partial glaciation above 60-80°S paleolatitude of the south polar continent Gondwana (Fig. S12).

Direct evidence for glaciation occurs in Late Devonian – Carboniferous deposits[31], but is rare in Early- and Mid Devonian strata. Indirect evidence of eustatic sea level change occurs in Early Devonian strata in North Africa that could potentially have a glaciogenic origin[32]. Further, paleo-temperature records from the shallow tropical and subtropical oceans broadly fit with the predicted paleoclimate, but also contains considerable local temperature variations[33,25]. Further, Devonian plant fossil assemblages are mostly found at lower-mid paleolatitudes (~45°S), where the continent is predicted permanently ice-free. One exception is the rich *Cooksonia* flora from the Paraná basin in Brazil positioned at higher paleolatitudes (~70°S)[34], although it also occurs in older strata of early Lockhovian (~419 Ma) age. Even at 500 ppm O_2, we find that the snow cover on Gondwana was not always perennial (Fig S15). Therefore, the Pananá flora might well have grown either during warmer Southern summers or when Earth was warmer due to higher levels of pCO_2 or other greenhouse gases (e.g., CH_4, N_2O). Therefore, evidence from the geological record is consistent with low atmospheric CO_2 levels both before forested ecosystems appeared in the Mid-Devonian (~385 Ma)[35].

Our results add to the growing body of evidence that polar glaciation is not strictly a function of atmospheric pCO_2 only. The Late Ordovician[36] glaciation occurred at the time when 'weak' pCO_2 proxy data indicate high atmospheric pCO_2 of 12–24 PIAL[9]. And, paleoclimate modeling shows that Gondwanan glaciations could be stable at up to 10-12 PIAL and that the glacial extent also depends on topography and the basal drag coefficient assumed in the model[8].

Early vascular plants and CO_2 removal

Berner proposed that the emergence of land plants caused a 10-fold decline in atmospheric pCO_2. Indeed, if the Late Ordovician pCO_2 constraint is robust, then implies that a dramatic drop (17^{+7}_{-5} to $1.8^{+0.6}_{-0.3}$ PIAL) occurred faster than previously thought, between ~440 Ma and ~410 Ma, coinciding with the Silurian appearance of vascular ecosystems. Intriguingly, this coincides with a dramatic shift in the physical weathering regime driven by the evolving the terrestrial ecosystems that forever increased the retainment of fine-grained sediment in continental deposits[37]. We propose that the exposure of more mineral surface area to weathering fluids on the continents led to an increase in silicate weathering, and that the earliest vegetation weathered more due to a greater nutrient loss from the primitive root systems. Consequently, atmospheric CO_2 levels declined. To simulate how the evolving vascular ecosystems might have affected continental weathering processes, we used a dynamic Earth System Model (COPSE) for the coupled biogeochemical cycles to predict trajectories of atmospheric pO_2 and pCO_2 (see Methods).

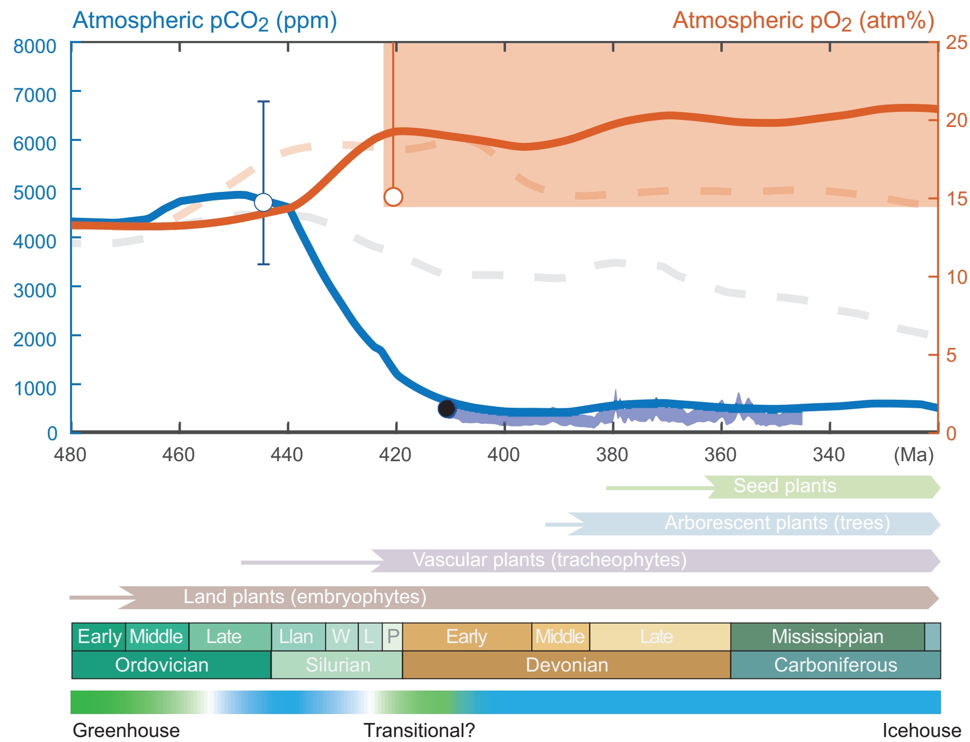

Figure 2. Summary of plant evolution and evolving atmospheric composition. Atmospheric pCO_2 constraints from carbon isotope fractionation of the 410 Ma *Baragwanathia* flora (black circle), Devonian C3 plants (transparent blue curve) and pedogenic goethite (blue circle). Atmospheric pO_2 is constrained constraints by charcoal evidence of wildfire to >15 atm% after 420 Ma (red circle, transparent red field). Modelled evolution of atmospheric pCO_2 (blue curve) and atmospheric pO_2 (red curve) derived from the COPSE Earth System Model using a more dramatic increase in continental weathering efficiency by early vascular ecosystems. The previous COPSE reloaded model result is shown for comparison (transparent dashed curves)[22]. See supplementary information for derivations. The emergence of land plants, vascular plants, arborescent plants with deep root systems and seed plants are shown with thin lines representing their origin by molecular clock estimates and thicker arrows representing fossil occurrences.

We find a massive atmospheric CO_2 decline from 3800 ppm to 500 ppm could have happened in ~30 Myr in response to enhanced silicate weathering by vascular plants (Fig. 2). To exemplify such a scenario, we adopted recent COPSE models[22,38] and adjusted the weathering forcing in proportion to the plant-induced effect on mudrock retention in continental deposits[40]. This is justified because mineral surface area is a key factor facilitating mineral dissolution during chemical weathering. Also, we scaled up plant evolution faster than in previous COPSE models in an attempt to both capture extensive plant coverage and to mimic the greater weathering demand of primitive vascular vegetation, which presumably recycled nutrients less efficiently and, thus, more nutrients were lost from soils compared to subsequent plants with complex root systems[42]. Lastly, volcanic outgassing rates in the Early-Mid Devonian was adjusted from 1.5 to 0.9 times modern levels to meet the low atmospheric pCO_2 constraints.

The impact of the evolving vascular ecosystems not only affected pCO_2, but simultaneously caused a rise in atmospheric pO_2. Previous models have evoked selective P weathering to simultaneously maintain high pCO_2 and high pO_2 in the Silurian, but our new data and model offers a simpler solution that fits evidence for wildfire and > 15 atm% pO_2 since ~420 Ma (red area in Figure 2) and various lines of geochemical evidence for Earth's oxygenation[22]. Hence, the evolution of early vascular ecosystems could have caused both massive atmospheric pO_2 rise and pCO_2 decline.

Ultimately, the Earth's atmospheric composition is governed by biological processes and how land plants and their root symbionts affect the physical and chemical weathering processes on land[40,41]. We suggest the early vascular flora enhanced continental weathering processes by dissolving more continental rock than the subsequent forest ecosystems with deeper and more complex root systems. In this view, the small atmospheric pCO_2 rise observed in our record during the emergence of progymnosperm forests (~385Ma) could represent a lost global CO_2 sink (less weathering) associated with deeper root systems acting to stabilize and recycle nutrients more effectively, therefore reducing the weathering need to sustain growth. Conclusively, the low atmospheric CO_2 levels before the emergence of forested ecosystems demonstrate that Earth's climate is less affected by afforestation and *growth up* than the *growth down* by which the terrestrial biosphere extracts and maintains nutrients from its planetary substrate.

References

1. Foster, G. L., Royer, D. L. & Lunt, D. J. Future climate forcing potentially without precedent in the last 420 million years. *Nat. Commun.* **8**, 14845 (2017).
2. Berner, R. A. Paleozoic Atmospheric CO_2: Importance of Solar Radiation and Plant Evolution. *Science* **261**, 68–70 (1993).
3. Walker, J. C. G., Hays, P. B. & Kasting, J. F. A negative feedback mechanism for the long-term stabilization of Earth's surface temperature. *J. Geophys. Res.* **86**, 9776 (1981).
4. Caves, J. K., Jost, A. B., Lau, K. V. & Maher, K. Cenozoic carbon cycle imbalances and a variable weathering feedback. *Earth Planet. Sci. Lett.* **450**, 152–163 (2016).
5. Maher, K. & Chamberlain, C. P. Hydrologic Regulation of Chemical Weathering and the Geologic Carbon Cycle. *Science* **343**, 1502–1504 (2014).
6. Goddéris, Y. *et al.* Onset and ending of the late Palaeozoic ice age triggered by tectonically paced rock weathering. *Nat. Geosci.* **10**, 382–386 (2017).
7. Ibarra, D. E. *et al.* Modeling the consequences of land plant evolution on silicate weathering. *Am. J. Sci.* **319**, 1–43 (2019).
8. Pohl, A. *et al.* Glacial onset predated Late Ordovician climate cooling. *Paleoceanography* **31**, 800–821 (2016).
9. Yapp, C. J. & Poths, H. Ancient atmospheric CO_2 pressures inferred from natural goethites. *Nature* **355**, 342–344 (1992).
10. Mora, C. I., Driese, S. G. & Colarusso, L.A. Middle to Late Paleozoic Atmospheric CO_2 Levels from Soil Carbonate and Organic Matter. *Science* **271**, 1105-1107 (1996)
11. Ekart, D.D., Cerling, T.E., Montanez, I.P. & Tabor, N.J. A 400 million year carbon isotope record of pedogenic carbonate: implications for paleoatmospheric carbon dioxide. *Am. J. Sci.*, **299**: 805-827 (1999).
12. McElwain, J. & Chaloner, W. Stomatal Density and Index of Fossil Plants Track Atmospheric Carbon Dioxide in the Palaeozoic. *Ann. Bot.* **76**, 389–395 (1995).

13. Wan, Z. *et al.* Environmental influences on the stable carbon isotopic composition of Devonian and Early Carboniferous land plants. *Palaeogeogr. Palaeoclimatol. Palaeoecol.* **531**, 109100 (2019).

14. Farquhar, G., O'Leary, M. & Berry, J. On the Relationship Between Carbon Isotope Discrimination and the Intercellular Carbon Dioxide Concentration in Leaves. *Funct. Plant Biol.* **9**, 121 (1982).

15. Diefendorf, A. F., Mueller, K. E., Wing, S. L., Koch, P. L. & Freeman, K. H. Global patterns in leaf 13C discrimination and implications for studies of past and future climate. *Proc. Natl. Acad. Sci.* **107**, 5738–5743 (2010).

16. Fletcher, B. J., Brentnall, S. J., Quick, W. P. & Beerling, D. J. BRYOCARB: A process-based model of thallose liverwort carbon isotope fractionation in response to CO_2, O_2, light and temperature. *Geochim. Cosmochim. Acta* **70**, 5676–5691 (2006).

17. Porter, A. S., Yiotis, C., Montañez, I. P. & McElwain, J. C. Evolutionary differences in Δ13C detected between spore and seed bearing plants following exposure to a range of atmospheric O_2:CO_2 ratios; implications for paleoatmosphere reconstruction. *Geochim. Cosmochim. Acta* **213**, 517–533 (2017).

18. Schubert, B. A. & Jahren, A. H. Global increase in plant carbon isotope fractionation following the Last Glacial Maximum caused by increase in atmospheric pCO_2. *Geology* **43**, 435–438 (2015).

19. Schlanser, K., Diefendorf, A. F., Greenwood, D. R., Mueller, K. E., West, C. K., Lowe, A. J., Basinger, J. F., Currano, E. D., Flynn, A. G., Fricke, H. C., Geng, J., Meyer, H. W. & Peppe, D. J. On geologic timescales, plant carbon isotope fractionation responds to precipitation similarly to modern plants and has a small negative correlation with pCO_2, Geochim. Cosmochim. Acta, **270**, 264-281 (2020)

20. Saltzman, M. R. & Thomas, E. Carbon Isotope Stratigraphy. in *The Geologic Time Scale* 207–232 (Elsevier, 2012). doi:10.1016/B978-0-444-59425-9.00011-1.

21. Kohn, M. J. Carbon isotope compositions of terrestrial C3 plants as indicators of

(paleo)ecology and (paleo)climate. *Proc. Natl. Acad. Sci.* **107**, 19691–19695 (2010).

22. Lenton, T. M. *et al.* Earliest land plants created modern levels of atmospheric oxygen. *Proc Natl Acad Sci U A* **113**, 9704–9 (2016).

23. Edwards, D., Abbott, G. & Raven, J. Cuticles of early land plants: a palaeoecophysiological evaluation. (1996).

24. Berner, R. A. Atmospheric Carbon Dioxide Levels Over Phanerozoic Time. *Science* **249**, 1382–1386 (1990).

25. Joachimski, M. M. *et al.* Devonian climate and reef evolution: Insights from oxygen isotopes in apatite. *Earth Planet. Sci. Lett.* **284**, 599–609 (2009).

26. Liu, Y., Peltier, W. R., Yang, J. & Vettoretti, G. The initiation of Neoproterozoic “snowball” climates in CCSM3: the influence of paleocontinental configuration. *Clim Past* 23 (2013).

27. Feulner, G. Climate simulations of Neoproterozoic snowball Earth events: Similar critical carbon dioxide levels for the Sturtian and Marinoan glaciations. *Earth Planet. Sci. Lett.* 6 (2014).

28. Feulner, G. Formation of most of our coal brought Earth close to global glaciation. *Proc. Natl. Acad. Sci.* **114**, 11333–11337 (2017).

29. De Vleeschouwer, D., Crucifix, M., Bounceur, N. & Claeys, P. The impact of astronomical forcing on the Late Devonian greenhouse climate. *Glob. Planet. Change* **120**, 65–80 (2014).

30. Brugger, J., Hofmann, M., Petri, S. & Feulner, G. On the Sensitivity of the Devonian Climate to Continental Configuration, Vegetation Cover, Orbital Configuration, CO_2 Concentration, and Insolation. *Paleoceanogr. Paleoclimatology* **34**, 1375–1398 (2019).

31. Isbell, J. L. *et al.* Glacial paradoxes during the late Paleozoic ice age: Evaluating the equilibrium line altitude as a control on glaciation. *Gondwana Res.* **22**, 1–19 (2012).

32. Gindre, L., Le Heron, D. & Bjørnseth, H. M. High resolution facies analysis and

sequence stratigraphy of the Siluro-Devonian succession of Al Kufrah basin (SE Libya). *J. Afr. Earth Sci.* **76**, 8–26 (2012).

33. Grossman, E. L. Oxygen Isotope Stratigraphy. in *The Geologic Time Scale* 181–206 (2012). doi:10.1016/b978-0-444-59425-9.00010-x.

34. Gerrienne, P., Bergamaschi, S., Pereira, E., Rodrigues, M.-A. C. & Steemans, P. An Early Devonian flora, including Cooksonia, from the Paraná Basin (Brazil). *Rev. Palaeobot. Palynol.* **116**, 19–38 (2001).

35. Stein, W. E. *et al.* Mid-Devonian Archaeopteris Roots Signal Revolutionary Change in Earliest Fossil Forests. *Curr. Biol.* **30**, 421-431.e2 (2020).

36. Ghienne, J.-F., Le Heron, D. P., Moreau, J., Denis, M. & Deynoux, M. The Late Ordovician Glacial Sedimentary System of the North Gondwana Platform. in *Glacial Sedimentary Processes and Products* (eds. Hambrey, M. J., Christoffersen, P., Glasser, N. F. & Hubbard, B.) 295–319 (Blackwell Publishing Ltd., 2009). doi:10.1002/9781444304435.ch17.

37. McMahon, W. J. & Davies, N. S. Evolution of alluvial mudrock forced by early land plants. *Science* **359**, 1022–1024 (2018).

38. Lenton, T. M., Daines, S. J. & Mills, B. J. W. COPSE reloaded: An improved model of biogeochemical cycling over Phanerozoic time. *Earth-Sci. Rev.* **178**, 1–28 (2018).

39. Porada, P. *et al.* High potential for weathering and climate effects of non-vascular vegetation in the Late Ordovician. *Nat Commun* **7**, 12113 (2016).

40. Algeo, T. J., Scheckler, S. E. & Scott, A. C. Terrestrial-Marine Teleconnections in the Devonian: Links between the Evolution of Land Plants, Weathering Processes, and Marine Anoxic Events [and Discussion]. *Philos. Trans. Biol. Sci.* **353**, 113–130 (1998).

41. Dahl, T. W. & Arens, S. K. M. The impacts of land plant evolution on Earth's climate and oxygenation state – An interdisciplinary review. *Chem. Geol.* **547**, 119665 (2020).

Methods

Samples

Plant macrofossils from the fossil collection of Museums Victoria were originally by Isabel Cookson from Mt Pleasant Rd, Victoria, Australia[1]. The fossils are preserved as incrustations in fine-grained sandstone sandwiched in a 130 m thick stratigraphic section of mostly siltstone and shale (Figure S1), interpreted as occasional bursts of high-energy turbidites carrying allochthonous fossils from shallower waters into very-low-energy marine depositional environment[2]. Index fossils (*Uncinatograptus* sp. cf. *U. thomasi* and *Nowakia* sp. ex gr. *N. acuaria*) confines the flora to the Pragian or earliest Emsian, corresponding to ~409.1 ±1.5 Ma according to GTS2020[3].

Small fossil fragments found in four specimens (#15154, #15173, #15174, #15183) which also contain larger fragments of e.g. *Baragwanathia longifolia,* were selected for analyses based on the preservation of black organic matter contained within a brown mineralized fossils (Fig. S2-S4). From each fragment (37 in total), 0.05–7.34 mg of material was extracted using a scalpel or a 0.8 mm Dremel drill. Only material visibly containing black organic matter was extracted.

Carbon isotope analyses

Carbon isotopic analyses for were performed in the Syracuse University GAPP Lab using an automated 'nano-EA' system adapted from that described in Polissar et al. (2009)[4]. The Syracuse University nano-EA comprises an Elementar Isotope Cube elemental analyzer coupled to an Isoprime 100 continuous-flow stable isotope mass spectrometer via an Isoprime Trace Gas analyzer. Though the presence of carbonate was not suspected, nor observed via testing of sample powders with 6N HCl under a binocular scope, we decided to decarbonate the sample materials prior to analysis to ensure that sample materials were carbonate free. Sample powders were fumigated in ashed glass vials in the presence of neat hydrochloric acid within an evacuated glass bell jar for 24 hours and then were dried in an oven at 40°C. For isotopic analysis, sample materials were transferred to quartz cups (6 x 6 mm; EA Consumables) and nested in a small amount of quartz wool to ensure retention of sample materials within the cup. The cups and quartz wool were ashed at 480°C for 8 hours. Sample materials were loaded into cups within a Class 100 laminar flow isolation cabinet with HEPA filtered air to minimize the potential of particulate contamination.

During isotopic analysis, sample cups were evacuated and purged with helium prior to introduction into the EA. Reaction conditions were as follows: oxidation and reduction reactor temperatures were 1100 °C and 650 °C, respectively; helium carrier gas flow was 158 ml/min and the O_2 pulse was set for 45 seconds. Carbon dioxide generated during sample combustion was trapped within the EA in a molecular sieve trap. Following passage of the N_2 peak, the primary EA trap was heated and carbon dioxide was released to a secondary, silica gel-filled cryotrap which was immersed in liquid nitrogen. Trapping duration was calibrated using the EA thermal conductivity detector data to ensure complete collection of the CO_2 peak. Following collection of CO_2, the cryotrap gas flow was switched to a lower-flow He carrier gas (~1 ml/min) via an automated Vici Valco 6-port valve. The trap was warmed and sample gas was released to the IRMS through an Agilent CarboBond capillary chromatography column (25m x 0.53mm x 5μm). The resulting raw carbon isotope data are blank-corrected using direct blank subtraction and normalized to the VPDB scale using the two-point correction scheme[5] with the international reference materials NIST 1547-Peach Leaves ($\delta^{13}C$ = 26.0 ± 0.2‰) and IAEA C6-sucrose ($\delta^{13}C$ = -10.45 ± 0.03‰). Reproducibility of the $\delta^{13}C$ values of reference materials with carbon contents greater than 50 nanomoles is ±0.3‰ (1σ) and is equivalent to that previously reported[4].

TOF-SIMS analyses

Time-Of-Flight Secondary Ion Mass Spectrometry (TOF-SIMS) was used to produce semi-quantitative maps of the elemental composition in sample #15153.
This technique bombards the surface with Bi ions that causes a collision cascade in the uppermost atom layers of the specimen (~10 nm). This releases secondary ions that are accelerated in an electric field and their time of flight to the detector in vacuum is a function of their mass and sample depth[6–8]. Figure S5 shows elements bound to organic matter (incl. C, N, P) in the sample that produce polyatomic charged species, such as CN- and CNO- when emitted from the same sample depth. The correlations of organic-bound elements enable us to distinguish the presence of organic carbon from inorganic phases (e.g., carbonate minerals) in the sample.

Paleoclimate modelling

The relatively fast coupled Earth-system model of intermediate complexity CLIMBER-3α[9] was used to simulate the Devonian climate with an atmospheric CO_2 level of 500 ppm. CLIMBER-3α encompasses a modified version of the ocean circulation model (MOM3[10,11]) with a horizontal resolution of 3.75° x 3.75° and 24 vertical levels, a dynamic/thermodynamic sea-ice model[12] with the same resolution and a fast atmospheric model[13] of 22.5° longitudinal and 7.5° latitudinal resolution. The model does not explicitly model ice sheet growth on the continents, but snow cover on the continents is considered. The model was run for Early Devonian boundary conditions in terms of continental configuration, solar luminosity and vegetation cover[14]. Based on the results in Brugger et al. (2019)[14], three different orbital configurations were explored: the standard configuration (obliquity 23.5°, eccentricity e=0) as well as cold (obliquity 22.0°, eccentricity e=0) and warm (obliquity 24.5°, eccentricity e=0.069, precession angle 0°) orbital configurations. A sensitivity analysis considering seasonal surface air temperatures and sea-ice distribution for these different patterns of solar insolation is shown in Figure S12.

Long-term global biogeochemical modeling with the COPSE model framework

We used the Carbon-Oxygen-Phosphorous-Sulfur Evolution (COPSE) Earth system model to predict the histories atmospheric pCO_2 and pO_2 and ocean composition over the Phanerozoic (550 Ma–today). The forward modeling approach enables hypothesis testing of mechanistic cause-effect relationships in the Earth system. A set of coupled differential equations describing the dynamic evolution of the C, O, P and S cycles were solved using an inbuilt variable timestep solver for 'stiff' Ordinary Differential Equation systems in Matlab®. Two distinct versions of the model (COPSE2016 and COPSE reloaded, Figure S14-S15) were adapted in a previous version of the code[15] to explore the effect on different parameterizations of climate sensitivity, ocean anoxia, and marine P cycle[16,17]. As input, we adjusted the forcings on plant weathering (W), plant evolution (E), selective P weathering (F), volcanic outgassing (D), and C/P ratio of buried terrestrial biomass in a manner to simultaneously fit the effect of shallow vascular ecosystems on weathering processes and produce outputs consistent with the paleorecords. Figure 2 shows the atmospheric pO_2 and pCO_2 trajectories predicted by the revised version of COPSEreloaded with forcings shown in Figure S15.

Methods references

1. Cookson, I. IV—On plant-remains from the Silurian of Victoria, Australia, that extend and connect floras hitherto described. *Philos. Trans. R. Soc. Lond. B. Biol. Sci.* **225**, 127–148 (1935).
2. Earp, C. *Costulatotheca schleigeri* (Hyolitha: Orthothecida) from the Walhalla Group (Early Devonian) at Mount Pleasant, central Victoria, Australia. *Alcheringa Australas. J. Palaeontol.* **43**, 220–227 (2019).
3. Cohen, K. M., Finney, S. C., Gibbard, P. L. & Fan, J.-X. The ICS International Chronostratigraphic Chart. *Episodes* **36**, 199–204 (2013).
4. Polissar, P. J., Fulton, J. M., Junium, C. K., Turich, C. C. & Freeman, K. H. Measurement of ^{13}C and ^{15}N Isotopic Composition on Nanomolar Quantities of C and N. *Anal. Chem.* **81**, 755–763 (2009).
5. Coplen, T. B. *et al.* New Guidelines for δ13C Measurements. *Anal. Chem.* **78**, 2439–2441 (2006).
6. Bertrand, P. & Lu-Tao, W. Time-of-Flight Secondary Ion Mass Spectrometry (ToF-SIMS). in *Microbeam and Nanobeam Analysis* (eds. Benoit, D., Bresse, J.-F., Van't dack, L., Werner, H. & Wernisch, J.) 167–182 (Springer Vienna, 1996). doi:10.1007/978-3-7091-6555-3_8.
7. Belu, A. M., Graham, D. J. & Castner, D. G. Time-of-flight secondary ion mass spectrometry: techniques and applications for the characterization of biomaterial surfaces. *Biomaterials* **24**, 3635–3653 (2003).
8. Sodhi, R. N. S. Time-of-flight secondary ion mass spectrometry (TOF-SIMS):—versatility in chemical and imaging surface analysis. *The Analyst* **129**, 483–487 (2004).
9. Montoya, M., Griesel, A., Levermann, A., Mignot, J., Hofmann, M., Ganopolski, A. & Rahmstorf, S. The Earth system model of intermediate complexity CLIMBER-3. Part I: Description and performance for present-day conditions, *Clim. Dyn.*, **25**(2–3), 237– 263 (2005)
10. Pacanowski, R. & Griffies, S. The MOM 3 manual, alpha version. NOAA. *Geophys. Fluid Dyn. Lab.* (1999).

11. Hofmann, M. & Morales Maqueda, M. A. Performance of a second-order moments advection scheme in an Ocean General Circulation Model. *J. Geophys. Res.* **111**, C05006 (2006).

12. Fichefet, T. & Maqueda, M. A. M. Sensitivity of a global sea ice model to the treatment of ice thermodynamics and dynamics. *J. Geophys. Res. Oceans* **102**, 12609–12646 (1997).

13. Petoukhov, V. *et al.* CLIMBER-2: a climate system model of intermediate complexity. Part I: model description and performance for present climate. *Clim. Dyn.* **16**, 1–17 (2000).

14. Brugger, J., Hofmann, M., Petri, S. & Feulner, G. On the Sensitivity of the Devonian Climate to Continental Configuration, Vegetation Cover, Orbital Configuration, CO_2 Concentration, and Insolation. *Paleoceanogr. Paleoclimatology* **34**, 1375–1398 (2019).

15. Mills, B., Watson, A. J., Goldblatt, C., Boyle, R. & Lenton, T. M. Timing of Neoproterozoic glaciations linked to transport-limited global weathering. *Nat. Geosci.* **4**, 861–864 (2011).

16. Lenton, T. M. *et al.* Earliest land plants created modern levels of atmospheric oxygen. *Proc Natl Acad Sci U A* **113**, 9704–9 (2016).

17. Lenton, T. M., Daines, S. J. & Mills, B. J. W. COPSE reloaded: An improved model of biogeochemical cycling over Phanerozoic time. *Earth-Sci. Rev.* **178**, 1–28 (2018).

Acknowledgements

We thank T. Ziegler and F. McSweeney for providing specimens from the paleobotanical collection of Museum Victoria. T.W.D. was funded by the Carlsberg Foundation through its Distinguished Associate Professsor program (grant no. CF16–0876) and the Danish Council for Independent Research (grant nos. 7014-00295B, 8102-00005B). C. J. was funded by the National Science Foundation (NSF EAR-1455258). The authors gratefully acknowledge the European Regional Development Fund (ERDF), the German Federal Ministry of Education and Research and the Land Brandenburg for supporting this project by providing resources on the high-performance computer system at the Potsdam Institute for Climate Impact Research. J. B. and G. F. acknowledge funding by the German Federal Ministry of Education and Research BMBF within the Collaborative Project “Bridging in Biodiversity Science – BIBS” (funding number 01LC1501A-H).

Author contributions

T.W.D. led the study, conceived the idea for the study, and wrote the manuscript with input from all authors. T.W.D selected the samples from the collection of Museum of Victoria and undertook the sedimentological, palynological characterization with M. A. R. H, who extracted the fossil material for analyses. C. J. performed the isotope analyses. K.N. performed the TOF-SIMS analysis together with M.A.R.H. T.W.D. compiled existing paleoproxy records. J.B. and G.F. undertook the paleoclimate modelling with CLIMBER-3α. T.W.D performed the COPSE Earth system modeling. T.W.D., C. J., and G.F. acquired funding for the modeling and experimental tasks. All co-authors commented on the manuscript and provided input to its final version.

Competing interest declaration

The authors declare no competing interests.

Supplementary Information is available for this paper.

Correspondence and requests for materials should be addressed to Tais W. Dahl, email: tais.dahl@sund.ku.dk

2.3. Baby, it's cold outside: Climate model simulations of the effects of the asteroid impact at the end of the Cretaceous

Due to copyright reasons the accepted version of the manuscript is included here.

GEOPHYSICAL RESEARCH LETTERS, VOL. ???, XXXX, DOI:10.1002/,

Baby, it's cold outside: Climate model simulations of the effects of the asteroid impact at the end of the Cretaceous

Julia Brugger,[1,2,3] Georg Feulner,[1,3] and Stefan Petri[1]

Key Points.

- We use a coupled climate model to investigate the effects of sulfate aerosols and carbon dioxide from the Chicxulub impact.
- We find severe cooling suggesting a major role of the impact in the mass extinction event.
- Surface cooling of the ocean results in vigorous mixing which could have caused a plankton bloom.

66 million years ago, the end-Cretaceous mass extinction ended the reign of the dinosaurs. Flood-basalt eruptions and an asteroid impact are widely discussed causes, yet their contributions remain debated. Modelling the environmental changes after the Chicxulub impact can shed light on this question. Existing studies, however, focused on the effect of dust or used one-dimensional, non-coupled atmosphere models. Here, we explore the longer-lasting cooling due to sulfate aerosols using a coupled climate model. Depending on aerosol stratospheric residence time, global annual mean surface air temperature decreased by at least 26°C, with 3 to 16 years subfreezing temperatures and a recovery time larger than 30 years. The surface cooling triggered vigorous ocean mixing which could have resulted in a plankton bloom due to upwelling of nutrients. These dramatic environmental changes suggest a pivotal role of the impact in the end-Cretaceous extinction.

1. Introduction

During the mass extinction at the Cretaceous-Paleogene boundary, a substantial number of biological groups experienced major extinctions, including non-avian dinosaurs, other vertebrates, marine reptiles and invertebrates, planktonic foraminifera and ammonites [*Bambach*, 2006]. The severity of this event, recently dated at 66.043 ± 0.043 Ma [*Renne et al.*, 2013], and the fact that it marks the demise of the dinosaurs account for the continued interest in understanding its origin. Yet the ultimate cause of the end-Cretaceous extinction remains debated. Most investigations today focus on two theories based on events roughly coinciding with the extinction: On the one hand, large-scale volcanic eruptions occurred around that time, with the main phase of the eruptions lasting from 66.3 to 65.5 Ma [*Schoene et al.*, 2015] as documented in the flood basalts from the Deccan plateau (India). These eruptions released sulfur dioxide and carbon dioxide leading to climatic changes which could have induced the mass extinction. On the other hand, the impact of an asteroid resulting in the Chicxulub crater (Mexico), dated to coincide with the extinction event within the errors [*Renne et al.*, 2013], resulted in dramatic local and short-term consequences, but would also have produced large amounts of dust, sulfate aerosols and greenhouse gases which affected the climate globally and on longer timescales [*Kring*, 2007; *Schulte et al.*, 2010]. In addition to improvements in sampling and dating the geological and palaeontological record, modelling studies of the environmental changes associated with these events can help to assess competing theories [*Feulner*, 2009]. In this paper, we use coupled climate model simulations to explore the effects of the Chicxulub impact on Earth's climate.

The initial impact hypothesis proposed that dust particles produced during the impact were responsible for shutting down photosynthesis after the impact [*Alvarez et al.*, 1980]. Early modeling studies investigating the climate changes associated with the Chicxulub impact therefore mostly focused on these effects [e.g. *Covey et al.*, 1994]. More recent studies of the debris in the impact layer suggest, however, that the fraction of sub-micron-sized dust particles in the stratosphere was too small to cause the observed environmental changes [*Pope*, 2002]. Instead, the production of sulfur-bearing gases from the impact target's evaporites is considered the key source of climatic effects, as they form stratospheric sulfate aerosols which block sunlight and thus cool down the Earth's atmosphere and hamper photosynthesis [*Pierazzo et al.*, 1998]. The few existing studies focusing on the aerosols' effect used non-coupled climate models [*Pope et al.*, 1994, 1997; *Pierazzo et al.*, 2003] and are limited to short time periods after the impact without investigating the longer-term changes.

Here, we use a coupled climate model [*Montoya et al.*, 2005] – consisting of an ocean general circulation model, a fast atmosphere and a dynamic/thermodynamic sea-ice model – to explore the climatic effects of sulfate aerosols and CO_2 following the impact. We explicitly focus on global and longer term changes and do not consider local and short-term phenomena like the extreme heat, strong winds, wildfires and tsunamis close to the impact site [*Kring*, 2007].

2. Modelling Set-Up

2.1. Pre-Impact Climate Model Simulations

The simulations of the end-Cretaceous climate and the effects of the impact are carried out with a coupled climate model [*Montoya et al.*, 2005] consisting of a modified version of the ocean general circulation model MOM3 [*Pacanowski and Griffies*, 1999; *Hofmann and Morales Maqueda*, 2006] run at a horizontal resolution of $3.75° \times 3.75°$ with 24 vertical levels, a dynamic/thermodynamic sea-ice model [*Fichefet and Maqueda*, 1997] and a fast statistical-dynamical atmosphere model [*Petoukhov et al.*, 2000] with a coarse resolution of 22.5° in longitude and 7.5° in latitude.

Our impact simulations are based on a climate simulation of the end-Cretaceous climate state using a Maastrichtian (70 Ma) continental configuration [*Sewall et al.*, 2007]. The solar constant is scaled to 1354 W/m^2, based on the present-day solar constant of 1361 W/m^2 [*Kopp and Lean*, 2011] and

[1]Earth System Analysis, Potsdam Institute for Climate Impact Research, Potsdam, Germany.
[2]Universität Potsdam, Potsdam, Germany.
[3]Berlin-Brandenburg Institute of Advanced Biodiversity Research, Berlin, Germany.

a standard solar model [*Bahcall et al.*, 2001]. Orbital parameters are idealised with a circular orbit and an obliquity of 23.5°. Proxy estimates for the atmospheric CO_2 concentration range from 500 ppm to 1500 ppm for the late Cretaceous [*Royer*, 2006], during the period directly preceding the impact it was likely below 800 ppm [*Hong and Lee*, 2012; *Royer et al.*, 2012]. We have therefore performed a baseline simulation with 500 ppm of atmospheric CO_2 and a sensitivity experiment at a higher CO_2 concentration of 1000 ppm. Both pre-impact simulations are integrated for about 2200 model years until climate equilibrium is approached.

The simulated global annual mean surface air temperature during the latest Cretaceous is 18.9°C or about 4°C above pre-industrial temperatures for the 500 ppm simulation, and 21.6°C or roughly 7°C warmer than the pre-industrial climate for the 1000 ppm model experiment.

2.2. Modelling the Effects of the Impact

To model the climatic effects of the impact, we use literature information from geophysical impact modeling indicating that for a 2.9 km thick target region consisting of 30% evaporites and 70% water-saturated carbonates and a dunite projectile with 50% porosity, a velocity of 20 km/s and a diameter between 15 and 20 km, a sulfur mass of 100 Gt is produced [*Pierazzo et al.*, 1998]. For comparison, this corresponds to about 10,000 times the amount of sulfur released during the 1991 Pinatubo eruption [*McCormick et al.*, 1995]. Note that the amount of sulfur released during the impact depends on the composition of the targeted bedrock, vaporization criteria, the condensation of vaporised ejecta, possible back reactions and the impactors velocity and size [*Pierazzo et al.*, 1998; *Gupta et al.*, 2001]. However, the results do not strongly depend on the precise amount of sulfur released during the impact, since the radiative forcing does not increase for sulfur masses larger than 30 Gt [*Pierazzo et al.*, 2003].

The effects of the stratospheric sulfate aerosols on radiation are based on a simple sulfate aerosol model coupled to a column radiation model [*Pierazzo et al.*, 2003]. Sulfur is assumed to be ligated in the forms of SO_2 (80%) and SO_3 (20%). The ratio of SO_3 to SO_2 determines the amount of stratospheric sulfate aerosols formed and their concentration with time. *Ohno et al.* [2014] suggest a SO_3/SO_2 ratio of 100/1 , which implies a higher initial sulfate aerosol concentration but faster decay. Compared to the ratio used in our study this would lead to a slightly faster decay of stratospheric aerosols [*Pierazzo et al.*, 2003]. Only the aerosols in the stratosphere are considered because aerosols are quickly washed out as soon as they enter the troposphere. The stratospheric residence time of tracers in a present-day steady-state atmosphere is about 2 years [*Holton et al.*, 1995]. We follow *Pierazzo et al.* [2003] and include the effect of a possible longer residence time in a perturbed atmosphere after the impact by simulating the effects of the impact for 2.1, 4.3 and 10.6 years stratospheric residence time, respectively.

To model the time after the impact, we use time sequences of visible transmission taken from *Pierazzo et al.* [2003] for the different stratospheric residence times discussed above. With this model set-up, solar flux at the surface is drastically reduced immediately after the impact from a pre-impact value of 169.5 W/m^2 to the minimum value of 2.28 W/m^2 for 2.1 years stratospheric residence time, reached in the first year after the impact, and 2.03 W/m^2 for 4.3 and 10.6 years stratospheric residence time, reached in the second year after the impact. Stratospheric residence time does not strongly influence minimum solar flux, but rather determines the time needed to regain the pre-impact value which is reached after 6, 10 and 20 years for the different residence times, respectively.

In addition to the sulfate aerosols' effect, we consider an enhanced CO_2 concentration due to the impact. For a sulfur mass of 100 Gt, about 1400 Gt of carbon dioxide are injected into the atmosphere [*Pierazzo et al.*, 1998], corresponding to an increase of the atmospheric CO_2 concentration by 180 ppm. Note that the amount of CO_2 released from the impact depends on the energy and angle of the impact, the fractions of carbonates in the impactor and the target as well as the recombination rate [*O'Keefe and Ahrens*, 1989; *Pierazzo et al.*, 1998]. Moreover, there could be additional CO_2 emissions from ocean outgassing and perturbations of the terrestrial biosphere, so we run additional simulation experiments adding a total of 360 ppm and 540 ppm of CO_2 as sensitivity experiments. Both sulfate aerosols and CO_2 produced during the impact event are assumed to be distributed globally and uniformly in our model simulations. A uniform aerosol distribution is a simplification, but may be a reasonable approximation given the magnitude and location of the Chicxulub impact. We assume that the shorter-term effects of dust are overshadowed by the aerosol effect. Furthermore, we neglect water vapour as the amount produced is uncertain and its tropospheric residence time is very short. Finally we do not consider the climatic consequences of ozone destruction after the impact [*Kring*, 2007] since they are probably of minor importance for the global climate. All impact experiments are performed for both end-Cretaceous climate states with 500 ppm and 1000 ppm of atmospheric CO_2 and are integrated for 100 years after the impact; the impact simulations for 2.1 years residence time are run for 1000 years.

3. Results

3.1. Global Cooling

The main result from our climate model simulations is a severe and persistent global cooling in the decades after the impact. Figure **??** (a) shows global annual mean surface air temperature during the 30 years following the impact for an atmospheric CO_2 concentration of 500 ppm before the impact, for the different aerosol residence times and for different CO_2 emission values from the impact. The temperature evolution for the different CO_2 emissions resulting from the impact is very similar; in the following, the discussion will focus on the simulation representing the intermediate emission value of 360 ppm.

For 2.1 years stratospheric residence time, which is the most conservative assumption for the simulations, global annual mean surface air temperature is reduced by 27°C when minimum temperature is reached in year 3 after the impact. This temperature difference is not sensitive to the CO_2 concentration before the impact: in the case of a pre-impact concentration of 1000 ppm, the temperature drops by an almost identical amount from +22°C to −5.0°C. Global annual mean surface air temperature remains below freezing for 3 years. For 4.3 years and 10.6 years stratospheric residence time, minimum global annual mean surface air temperature is even lower (cooling by 30°C and 34°C) and reached at later times (year 5 and 9 after the impact). In these simulations with longer residence times, global annual mean sub-freezing temperatures persist for 7 and 16 years, respectively. The drastic and prolonged cooling in particular in the 10.6-years residence time scenario raises the question, however, whether longer stratospheric residence times can really be reconciled with the palaeontological record, in particular with the observed fast recovery of productivity [*D'Hondt et al.*, 1998; *Alegret et al.*, 2012; *Sepúlveda et al.*, 2009]. In the following, we focus on the simulations with 2.1

years stratospheric residence time of the aerosols, representing the most conservative case.

The post-impact cooling observed in our simulations is accompanied by a marked expansion of snow and sea ice. Annual average surface albedo increases from 0.11 before the impact to 0.24 in the year with maximum ice cover in our standard simulation (500 ppm CO_2 preceding the impact, 2.1 years residence time, 360 ppm CO_2 from the impact). As an example for this expansion of snow and ice, Figure **??** (b) shows the time evolution of the global sea-ice fraction during the three decades after the impact. For our standard case of 2.1 years stratospheric aerosol residence time, the sea-ice fraction increases by a factor of six before declining towards its pre-impact value. Interestingly, the simulation with 10.6 years residence time exhibits a distinctly different behaviour. In this case, the sea-ice fraction strongly increases after the initial cooling period, indicating the beginning of a runaway caused by the positive ice-albedo feedback. This runaway is eventually slowed and reversed by the increasing solar radiation, however. For the other residence times, the reduction of solar radiation due to the impact is too short to initiate this process. This also means, however, that a perturbation with an even longer residence time might be sufficient to trigger a snowball runaway.

We note that the emission of CO_2 from the impact will lead to warming compared to the pre-impact state after the initial cooling period. Depending on the amount of CO_2 emitted from the impact, after 1000 years the climate is $1.0 - 2.6^\circ$C warmer than the pre-impact state for an initial CO_2 concentration of 500 ppm and $0.5 - 1.4^\circ$C warmer for 1000 ppm.

3.2. Regional Cooling

Regional temperature changes induced by the asteroid impact are even more severe than suggested by the global averages. Maps of surface air temperature of the pre-impact year and the year of minimum global annual mean temperature indicate pronounced regional cooling, in particular over continental areas and in polar regions (see, e.g., Fig. **??**, for 500 ppm of CO_2 preceding the impact, 2.1 years stratospheric residence time and 360 ppm of CO_2 from the impact). Global annual mean temperatures over land fall to -32°C in the coldest year (compared to $+15^\circ$C before the impact), with continental temperatures in the tropics reaching a mere -22°C (falling from $+27^\circ$C before the impact). In contrast, global mean sea-surface temperatures drop to $+5.9^\circ$C only from their pre-impact value of $+21^\circ$C. We note that our model shows an enhanced land-ocean warming ratio of ~ 2 in the tropics for idealised CO_2-increase scenarios [*Eby et al.*, 2013] as compared to a ratio of ~ 1.3 in other models [*Schmidt et al.*, 2014]. The cooling over land after the Chicxulub impact may therefore be overestimated in our model.

3.3. Deep-Ocean Temperature and Mixing

Because of the ocean's thermal inertia, surface temperature changes propagate only slowly into the deep ocean. It is therefore interesting to investigate longer-term temperature changes in the deep ocean. Figure **??** shows meridional profiles of ocean temperature changes for four timeslices up to 1000 years after the impact. In year 3 after the impact, the strong surface cooling results in very cold water masses in the upper $\sim$1000 m of the ocean at all latitudes, and down to the ocean floor at high latitudes. 100 years after the impact near-surface ocean layers show evidence of warming due to the CO_2 released after the impact, while the cold water masses have reached the abyss, with pronounced cooling in the deep ocean at high latitudes. The most striking feature at this point of time, however, is a bubble of cold water at depths of $\sim$500$-$2000 m which is particularly pronounced in the Northern tropics and subtropics. Regionally, this bubble is located in the Northern Atlantic (not shown). After 500 years, the situation is characterised by warmer waters in the upper half of the ocean and slightly cooler water persisting in the deep ocean. The cold bubble has weakened and is restricted to the Northern subtropics and to depths of $\sim$2000$-$3000 m. 1000 years after the impact, warming has reached the deep ocean, with only few localised regions of minor cooling persisting in the abyss of the Southern Ocean and in the Northern subtropics.

Finally we will explore how the cooling due to the Chicxulub impact affects ocean mixing and potentially the marine biosphere. Figure **??** shows the mixed-layer depth before the impact and in the coldest year after the event. In the late-Cretaceous climate preceding the impact, the mixed layer depth is comparable to a simulation of the present-day climate state. This changes dramatically after the impact. The sudden atmospheric cooling triggered by the impact leads to strongly enhanced ocean mixing and deep-water formation notably at mid latitudes. The collapsed ^{13}C gradient observed at the Cretaceous-Paleogene boundary could provide geologic evidence for this mixing [*Zachos et al.*, 1989], although a decrease in marine productivity might have contributed to the changes in ^{13}C as well. The vigorous ocean mixing after the impact will transport nutrients from the deep ocean towards the surface. We argue that the increase in available nutrients should result in a pronounced rise of ocean primary production following the initial decrease due to the darkness after the impact. Additional nutrients from impact ejecta [*Parkos et al.*, 2015] could further intensify ocean primary productivity. Depending on the availability of light and limiting nutrients like iron, this could result in regional plankton blooms, as proposed by geologic explorations [*Hollis et al.*, 1995]. The plankton blooms could also have created toxins with profound effects on marine near-surface ecosystems [*Wilde and Berry*, 1986; *Castle and Rodgers Jr.*, 2009]. This scenario would have to be further explored with a model for the marine biogeochemistry.

4. Discussion

In this Section, we briefly compare our results with earlier modeling work and proxy evidence. Comparable modeling studies considering the aerosols' effect and using coupled climate models do not exist. *Pope et al.* [1997] use a radiative-transfer model to roughly estimate the global cooling from sulfate aerosols, finding values similar to the ones reported here. With respect to proxy data, it is difficult to compare the cooling found in our simulations because a very high time resolution is necessary to record the fast climatic changes associated with the impact. Furthermore, the prominent proxy carriers for the surface ocean, calcareous microfossils, suffered from the extinction.

However, two recent studies [*Vellekoop et al.*, 2014; *Vellekoop et al.*, 2016] use TEX_{86} palaeo-thermometry of shallow marine sediments to estimate sea-surface temperature changes across the Cretaceous-Paleogene boundary. From the Brazos River section (Texas), *Vellekoop et al.* [2014] reconstruct pre-impact temperatures of 30–31°C in good agreement with the tropical Late-Cretaceous sea-surface temperature from well-preserved foraminifer shells [*Pearson et al.*, 2001]. For comparison, the pre-impact annual mean sea-surface temperature of 24°C in this region in our simulation is somewhat lower. At the boundary, *Vellekoop et al.* [2014] report a drop in sea-surface temperature in the Gulf of Mexico of up to 7°C lasting for months to decades, but not longer than 100 years. Averaged over the decade after the impact, the sea-surface temperature drops by 10°C, in good agreement with the proxy study, assuming that the resolution of their record is about a decade. *Vellekoop et al.* [2014] also report an increase in ocean temperatures by $1-2$°C after the impact cooling, in agreement with the warming seen in our simulations due to the additional CO_2 released from the impact. *Vellekoop et al.* [2016] use TEX_{86} data extracted from cores from the New Jersey palaeo-shelf to reconstruct temperatures of ∼26°C at the end of the Cretaceous as well as an abrupt ∼3°C cooling at the boundary to the Paleogene. As for the Texas record, our pre-impact temperature of ∼19°C is lower than the TEX_{86} estimate; however, our cooling of ∼9°C is more pronounced than the proxy signal at this location.

It should be kept in mind, however, that a detailed comparison of local proxy records is hampered by the comparatively coarse spatial resolution of our model as well as uncertainties concerning the temporal resolution [*Vellekoop et al.*, 2016] and calibration [*Ho and Laepple*, 2016] of TEX_{86} temperature estimates.

For some locations, proxies document local cooling persisting for longer timescales of millennia. *Galeotti et al.* [2004] analyse records of dinoflagellate cysts and benthic foraminifera across the Cretaceous-Paleogene boundary in the Tunisian shelf region and present evidence for millennial-scale cooling indicated by a brief expansion of boreal species into the western Tethys Ocean. Similarly, *Vellekoop et al.* [2015] report repeated cooling pulses in this region during the first thousands of years after the impact. *Galeotti et al.* [2004] use energy-balance estimates and one idealised simulation with a coupled atmosphere-ocean model under present-day boundary conditions to explore the ocean-response timescale to different levels of impact aerosol cooling and interpret the millennial-scale cooling as evidence for persisting cool water masses in the deep ocean. Cooling pulses on the Tunisian shelf could then be explained by local upwelling of cold water [*Vellekoop et al.*, 2015]. The bubble of cooler ocean water in the Northern Atlantic region found in our simulations supports this notion, although the cooler water masses do not persist for more than one millennium in our simulations, mostly due to the warming from the CO_2 released during the impact.

5. Conclusions

In summary, our climate-modelling study demonstrates severe cooling and vigorous ocean mixing in the wake of the Chicxulub impact. These results are in general agreement with proxy data, but a detailed comparison is hampered by the time resolution of empirical records, questions of temperature-proxy calibration and the low spatial resolution of our model. Although we cannot conclude from our model results that the impact was exclusively responsible for the mass extinction at the end of the Cretaceous, the dramatic reduction in temperature and the expected profound perturbation of the marine biosphere due to the change in ocean circulation in our simulations certainly suggest a key role of the impact in the extinction event. The Chicxulub impact and the Deccan Trap volcanism might also have acted in concert, of course, either by the impact triggering more intense eruptions as recently argued [*Renne et al.*, 2015] or by delivering the final blow to a biosphere already stressed by the effects of the eruptions [*White and Saunders*, 2005; *Arens and West*, 2008; *Renne et al.*, 2013]. Future modeling studies will have to explore the interaction between these two causes as well as the effects on Earth's marine and terrestrial biosphere in more detail.

Acknowledgments.
The authors would like to thank A. Brugger, M. Hofmann, W. Kießling, T. Laepple, W. Lucht, R. Luther, W. von Bloh as well as K. Wünnemann for discussions and J. Sewall for providing Cretaceous boundary conditions. The authors gratefully acknowledge the European Regional Development Fund (ERDF), the German Federal Ministry of Education and Research and the Land Brandenburg for supporting this project by providing resources on the high performance computer system at the Potsdam Institute for Climate Impact Research. The work was partly funded by the German Federal Ministry of Education and Research BMBF within the Collaborative Project "Bridging in Biodiversity Science – BIBS" (funding number 01LC1501A-H). The source code for the model used in this study, the data and input files necessary to reproduce the experiments, and model output data are available from the authors upon request (brugger@pik-potsdam.de, feulner@pik-potsdam.de). All data are archived at the Potsdam Institute for Climate Impact Research (PIK).

References

Alegret, L., E. Thomas, and K. C. Lohmann (2012), End-Cretaceous marine mass extinction not caused by productivity collapse, *Proc. Natl. Acad. Sci. USA*, *109*, 728–732, doi: 10.1073/pnas.1110601109.

Alvarez, L. W., W. Alvarez, F. Asaro, and H. V. Michel (1980), Extraterrestrial Cause for the Cretaceous-Tertiary Extinction, *Science*, *208*(4448), 1095–1108, doi: 10.1126/science.208.4448.1095.

Arens, N. C., and I. D. West (2008), Press-pulse: a general theory of mass extinction?, *Paleobiology*, *34*(4), 456–471, doi: http://dx.doi.org/10.1666/07034.1.

Bahcall, J. N., M. H. Pinsonneault, and S. Basu (2001), Solar models: Current epoch and time dependences, neutrinos, and helioseismological properties, *Astrophys. J.*, *555*(2), 990–1012, doi:10.1086/321493.

Bambach, R. K. (2006), Phanerozoic biodiversity mass extinctions, *Annu. Rev. Earth Planet. Sci.*, *34*, 127–155, doi: 10.1146/annurev.earth.33.092203.122654.

Castle, J. W., and J. H. Rodgers Jr. (2009), Hypothesis for the role of toxin-producing algae in Phanerozoic mass extinctions based on evidence from the geologic record and modern environments, *Environmental Geosciences*, *16*, 1–23, doi: 10.1306/eg.08110808003.

Covey, C., S. L. Thompson, P. R. Weissman, and M. C. MacCracken (1994), Global climatic effects of atmospheric dust from an asteroid or comet impact on Earth, *Global Planet. Change*, *9*(3-4), 263–273, doi:10.1016/0921-8181(94)90020-5.

D'Hondt, S., P. Donaghay, J. C. Zachos, D. Luttenberg, and M. Lindinger (1998), Organic Carbon Fluxes and Ecological Recovery from the Cretaceous-Tertiary Mass Extinction, *Science*, *282*, 276, doi:10.1126/science.282.5387.276.

Eby, M., A. J. Weaver, K. Alexander, K. Zickfeld, A. Abe-Ouchi, A. A. Cimatoribus, E. Crespin, S. S. Drijfhout, N. R. Edwards, A. V. Eliseev, G. Feulner, T. Fichefet, C. E. Forest, H. Goosse, P. B. Holden, F. Joos, M. Kawamiya, D. Kicklighter, H. Kienert, K. Matsumoto, I. I. Mokhov, E. Monier, S. M. Olsen, J. O. P. Pedersen, M. Perrette, G. Philippon-Berthier, A. Ridgwell, A. Schlosser, T. Schneider von Deimling, G. Shaffer, R. S. Smith, R. Spahni, A. P. Sokolov, M. Steinacher, K. Tachiiri, K. Tokos, M. Yoshimori, N. Zeng, and F. Zhao (2013), Historical and idealized climate model experiments: an intercomparison of Earth system models of intermediate complexity, *Clim. Past*, *9*, 1111–1140, doi: 10.5194/cp-9-1111-2013.

Feulner, G. (2009), Climate-modelling of mass-extinction events: a review, *Int. J. Astrobiol.*, *8*, 207–212, doi: doi:10.1017/S1473550409990061.

Feulner, G. (2011), Are the most recent estimates for Maunder Minimum solar irradiance in agreement with temperature reconstructions?, *Geophys. Res. Lett.*, *38*, L16706, doi: 10.1029/2011GL048529.

Fichefet, T., and M. A. M. Maqueda (1997), Sensitivity of a global sea ice model to the treatment of ice thermodynamics and dynamics, *J. Geophys. Res.*, *102*(C6), 12,609–12,646, doi:10.1029/97JC00480.

Galeotti, S., H. Brinkhuis, and M. Huber (2004), Records of post Cretaceous-Tertiary boundary millennial-scale cooling from the western Tethys: A smoking gun for the impact-winter hypothesis?, *Geology*, *32*, 529, doi:10.1130/G20439.1.

Gupta, S. C., T. J. Ahrens, and W. Yang (2001), Shock-induced vaporization of anhydrite and global cooling from the K/T impact, *Earth Planet. Sci. Lett.*, *188*, 399–412, doi: 10.1016/S0012-821X(01)00327-2.

Ho, S. L., and T. Laepple (2016), Flat meridional temperature gradient in the early eocene in the subsurface rather than surface ocean, *Nature Geoscience*, *9*(8), 606–610, doi: 10.1038/ngeo2763.

Hofmann, M., and M. A. Morales Maqueda (2006), Performance of a second-order moments advection scheme in an Ocean General Circulation Model, *J. Geophys. Res.*, *111*, C05006, doi: 10.1029/2005JC003279.

Hollis, C. J., K. A. Rodgers, and R. J. Parker (1995), Siliceous plankton bloom in the earliest Tertiary of Marlborough, New Zealand, *Geology*, *23*(9), 835–838, doi:10.1130/0091-7613(1995)023<0835:SPBITE>2.3.CO;2.

Holton, J. R., P. H. Haynes, M. E. McIntyre, A. R. Douglass, R. B. Rood, and L. Pfister (1995), Stratosphere-troposphere exchange, *Rev. Geophys.*, *33*, 403–439, doi: 10.1029/95RG02097.

Hong, S. K., and Y. I. Lee (2012), Evaluation of atmospheric carbon dioxide concentrations during the Cretaceous, *Earth Planet. Sci. Lett.*, *327*, 23–28, doi:10.1016/j.epsl.2012.01.014.

Kopp, G., and J. L. Lean (2011), A new, lower value of total solar irradiance: Evidence and climate significance, *Geophys. Res. Lett.*, *38*(1), L01706, doi:10.1029/2010GL045777.

Kring, D. A. (2007), The Chicxulub impact event and its environmental consequences at the Cretaceous-Tertiary boundary, *Palaeogeogr. Palaeoclimatol. Palaeoecol.*, *255*(1-2), 4–21, doi: doi:10.1016/j.palaeo.2007.02.037.

McCormick, M. P., L. W. Thomason, and C. R. Trepte (1995), Atmospheric effects of the Mt Pinatubo eruption, *Nature*, *373*, 399–404, doi:10.1038/373399a0.

Montoya, M., A. Griesel, A. Levermann, J. Mignot, M. Hofmann, A. Ganopolski, and S. Rahmstorf (2005), The earth system model of intermediate complexity CLIMBER-3. Part I: description and performance for present-day conditions, *Clim. Dyn.*, *25*(2-3), 237–263, doi:10.1007/s00382-005-0044-1.

Ohno, S., T. Kadono, K. Kurosawa, T. Hamura, T. Sakaiya, K. Shigemori, Y. Hironaka, T. Sano, T. Watari, K. Otani, T. Matsui, and S. Sugita (2014), Production of sulphate-rich vapour during the Chicxulub impact and implications for ocean acidification, *Nat. Geosci.*, *7*, 279–282, doi: 10.1038/ngeo2095.

O'Keefe, J. D., and T. J. Ahrens (1989), Impact production of CO2 by the Cretaceous/Tertiary extinction bolide and the resultant heating of the earth, *Nature*, *338*, 247–249, doi: 10.1038/338247a0.

Pacanowski, R. C., and S. M. Griffies (1999), The MOM-3 Manual, *Tech. Rep. 4*, GFDL Ocean Group, NOAA/Geophysical Fluid Dynamics Laboratory, Princeton, NJ.

Parkos, D., A. Alexeenko, M. Kulakhmetov, B. C. Johnson, and H. J. Melosh (2015), NO_x production and rainout from Chicxulub impact ejecta reentry, *J. Geophys. Res.*, *120*(12), 2152–2168, doi:10.1002/2015JE004857.

Pearson, P. N., P. W. Ditchfield, J. Singano, K. G. Harcourt-Brown, C. J. Nicholas, R. K. Olsson, N. J. Shackleton, and M. A. Hall (2001), Warm tropical sea surface temperatures in the Late Cretaceous and Eocene epochs, *Nature*, *413*(6855), 481–487, doi:10.1038/35097000.

Petoukhov, V., A. Ganopolski, V. Brovkin, M. Claussen, A. Eliseev, C. Kubatzki, and S. Rahmstorf (2000), CLIMBER-2: a climate system model of intermediate complexity. Part I: model description and performance for present climate, *Clim. Dyn.*, *16*(1), 1–17, doi:10.1007/PL00007919.

Pierazzo, E., D. A. Kring, and H. J. Melosh (1998), Hydrocode simulation of the Chicxulub impact event and the production of climatically active gases, *J. Geophys. Res.*, *103*(E12), 28,607–28,625, doi:10.1029/98JE02496.

Pierazzo, E., A. N. Hahmann, and C. Sloan (2003), Chicxulub and climate: radiative perturbations of impact-produced S-bearing gases, *Astrobiology*, *3*(1), 99–118, doi: 10.1089/153110703321632453.

Pope, K. O. (2002), Impact dust not the cause of the Cretaceous-Tertiary mass extinction, *Geology*, *30*(2), 99–102, doi:10.1130/0091-7613(2002)030<0099:IDNTCO>2.0.CO;2.

Pope, K. O., K. H. Baines, A. C. Ocampo, and B. A. Ivanov (1994), Impact winter and the Cretaceous/Tertiary extinctions: Results of a Chicxulub asteroid impact model, *Earth Planet. Sci. Lett.*, *128*(3-4), 719–725, doi:10.1016/0012-821X(94)90186-4.

Pope, K. O., K. H. Baines, A. C. Ocampo, and B. A. Ivanov (1997), Energy, volatile production, and climatic effects of the Chicxulub Cretaceous/Tertiary impact, *J. Geophys. Res.*, *102*(E9), 21,645–21,664, doi:10.1029/97JE01743.

Renne, P. R., A. L. Deino, F. J. Hilgen, K. F. Kuiper, D. F. Mark, W. S. Mitchell, L. E. Morgan, R. Mundil, and J. Smit (2013), Time Scales of Critical Events Around the Cretaceous-Paleogene Boundary, *Science*, *339*, 684–687, doi: 10.1126/science.1230492.

Renne, P. R., C. J. Sprain, M. A. Richards, S. Self, L. Vanderkluysen, and K. Pande (2015), State shift in Deccan volcanism at the Cretaceous-Paleogene boundary, possibly induced by impact, *Science*, *350*(6256), 76–78, doi:10.1126/science.aac7549.

Royer, D. L. (2006), CO_2-forced climate thresholds during the Phanerozoic, *Geochim. Cosmochim. Ac.*, *70*(23), 5665–5675, doi:10.1016/j.gca.2005.11.031.

Royer, D. L., M. Pagani, and D. J. Beerling (2012), Geobiological constraints on Earth system sensitivity to CO2 during the Cretaceous and Cenozoic, *Geobiology*, *10*(4), 298–310, doi: 10.1111/j.1472-4669.2012.00320.x.

Schmidt, G. A., J. D. Annan, P. J. Bartlein, B. I. Cook, E. Guilyardi, J. C. Hargreaves, S. P. Harrison, M. Kageyama, A. N. LeGrande, B. Konecky, S. Lovejoy, M. E. Mann, V. Masson-Delmotte, C. Risi, D. Thompson, A. Timmermann, L.-B. Tremblay, and P. Yiou (2014), Using palaeo-climate comparisons to constrain future projections in CMIP5, *Clim. Past*, *10*, 221–250, doi:10.5194/cp-10-221-2014.

Schoene, B., K. M. Samperton, M. P. Eddy, G. Keller, T. Adatte, S. A. Bowring, S. F. R. Khadri, and B. Gertsch (2015), U-Pb geochronology of the Deccan Traps and relation to the end-Cretaceous mass extinction, *Science*, *347*(6218), 182–184, doi: 10.1126/science.aaa0118.

Schulte, P., L. Alegret, I. Arenillas, J. A. Arz, P. J. Barton, P. R. Bown, T. J. Bralower, G. L. Christeson, P. Claeys, C. S. Cockell, G. S. Collins, A. Deutsch, T. J. Goldin, K. Goto, J. M. Grajales-Nishimura, R. A. F. Grieve, S. P. S. Gulick, K. R. Johnson, W. Kiessling, C. Koeberl, D. A. Kring, K. G. MacLeod, T. Matsui, J. Melosh, A. Montanari, J. V. Morgan, C. R. Neal, D. J. Nichols, R. D. Norris, E. Pierazzo, G. Ravizza, M. Rebolledo-Vieyra, W. U. Reimold, E. Robin, T. Salge, R. P. Speijer, A. R. Sweet, J. Urrutia-Fucugauchi, V. Vajda, M. T. Whalen, and P. S. Willumsen (2010), The Chicxulub Asteroid Impact and Mass Extinction at the Cretaceous-Paleogene Boundary, *Science*, *327*(5970), 1214–1218, doi: 10.1126/science.1177265.

Sepúlveda, J., J. E. Wendler, R. E. Summons, and K.-U. Hinrichs (2009), Rapid Resurgence of Marine Productivity After the Cretaceous-Paleogene Mass Extinction, *Science*, *326*(5949), 129–132, doi:10.1126/science.1176233.

Sewall, J. O., R. S. W. van de Wal, K. van der Zwan, C. van Oosterhout, H. A. Dijkstra, and C. R. Scotese (2007), Climate model boundary conditions for four Cretaceous time slices, *Clim. Past*, *3*(4), 647–657, doi:10.5194/cp-3-647-2007.

Vellekoop, J., A. Sluijs, J. Smit, S. Schouten, J. W. H. Weijers, J. S. Sinninghe Damst, and H. Brinkhuis (2014), Rapid short-term cooling following the Chicxulub impact at the CretaceousPaleogene boundary, *Proc. Natl. Acad. Sci. USA*, *111*(21), 7537–7541, doi:10.1073/pnas.1319253111.

Vellekoop, J., J. Smit, B. van de Schootbrugge, J. W. H. Weijers, S. Galeotti, J. S. Sinninghe Damsté, and H. Brinkhuis (2015), Palynological evidence for prolonged cooling along the Tunisian continental shelf following the K–Pg boundary impact, *Palaeogeogr. Palaeocl.*, *426*, 216–228, doi: 10.1016/j.palaeo.2015.03.021.

Vellekoop, J., S. Esmeray-Senlet, K. G. Miller, J. V. Browning, A. Sluijs, B. van de Schootbrugge, J. S. Sinninghe Damsté, and H. Brinkhuis (2016), Evidence for Cretaceous-Paleogene boundary bolide impact winter conditions from New Jersey, USA, *Geology*, *44*(8), 619–622, doi:10.1130/G37961.1.

White, R., and A. Saunders (2005), Volcanism, impact and mass extinctions: incredible or credible coincidences?, *Lithos*, *79*, 299–316, doi:doi:10.1016/j.lithos.2004.09.016.

Wilde, P., and W. B. N. Berry (1986), The role of oceanographic factors in the generation of global bio-events, *Lecture Notes in Earth Sciences*, *8*, 75–91, doi:10.1007/BFb0010185.

Zachos, J. C., M. A. Arthur, and W. E. Dean (1989), Geochemical evidence for suppression of pelagic marine productivity at the Cretaceous/Tertiary boundary, *Nature*, *337*(6202), 61–64, doi:10.1038/337061a0.

Corresponding authors: J. Brugger, G. Feulner, Potsdam Institute for Climate Impact Research, P.O. Box 60 12 03, D–14412 Potsdam, Germany (brugger@pik-potsdam.de, feulner@pik-potsdam.de)

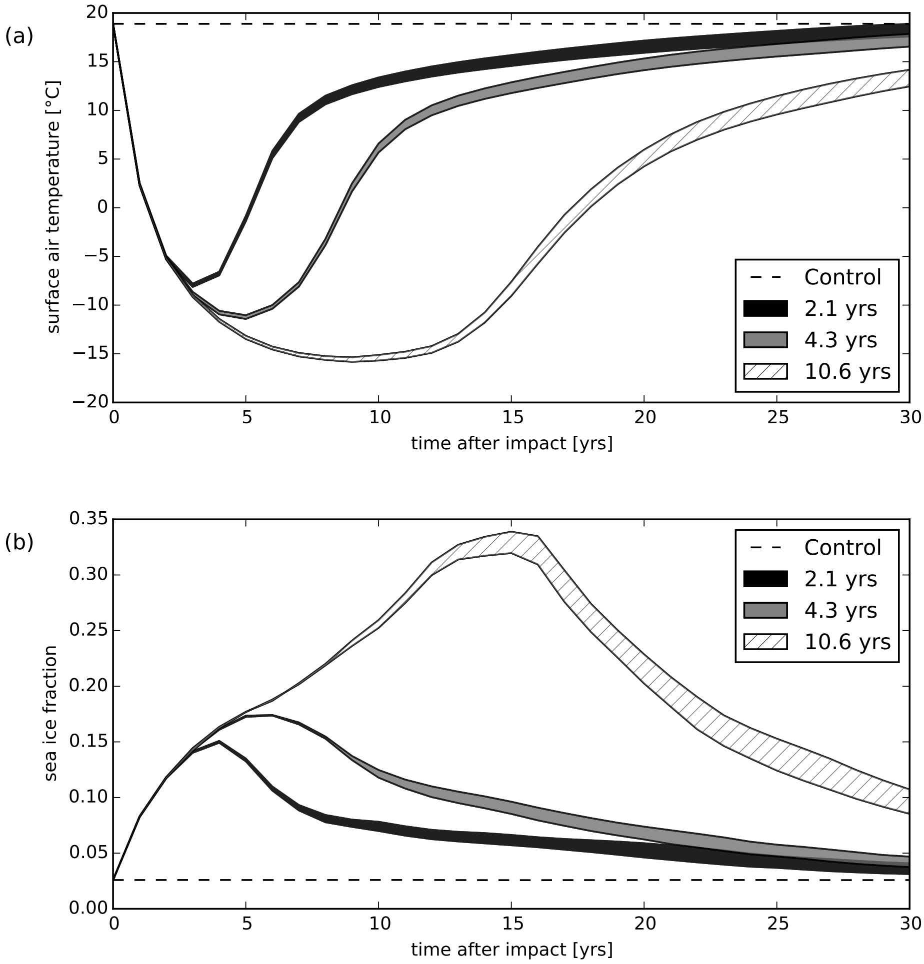

Figure 1. (a) Simulated global annual mean surface air temperature during the 30 years after the impact for the baseline state with 500 ppm of carbon dioxide and for the three different stratospheric aerosol residence times. For each residence time, the shaded region marks the uncertainty due to the carbon-dioxide released from the impact alone and from the impact and the biosphere, respectively, ranging from 180 ppm to 540 ppm. (b) Global sea-ice fraction during the 30 years after the impact for the baseline state with 500 ppm of carbon dioxide and for the three different stratospheric aerosol residence times in our simulations. As in Figure **??**, the shading marks the uncertainty due to the carbon-dioxide released in the wake of the impact.

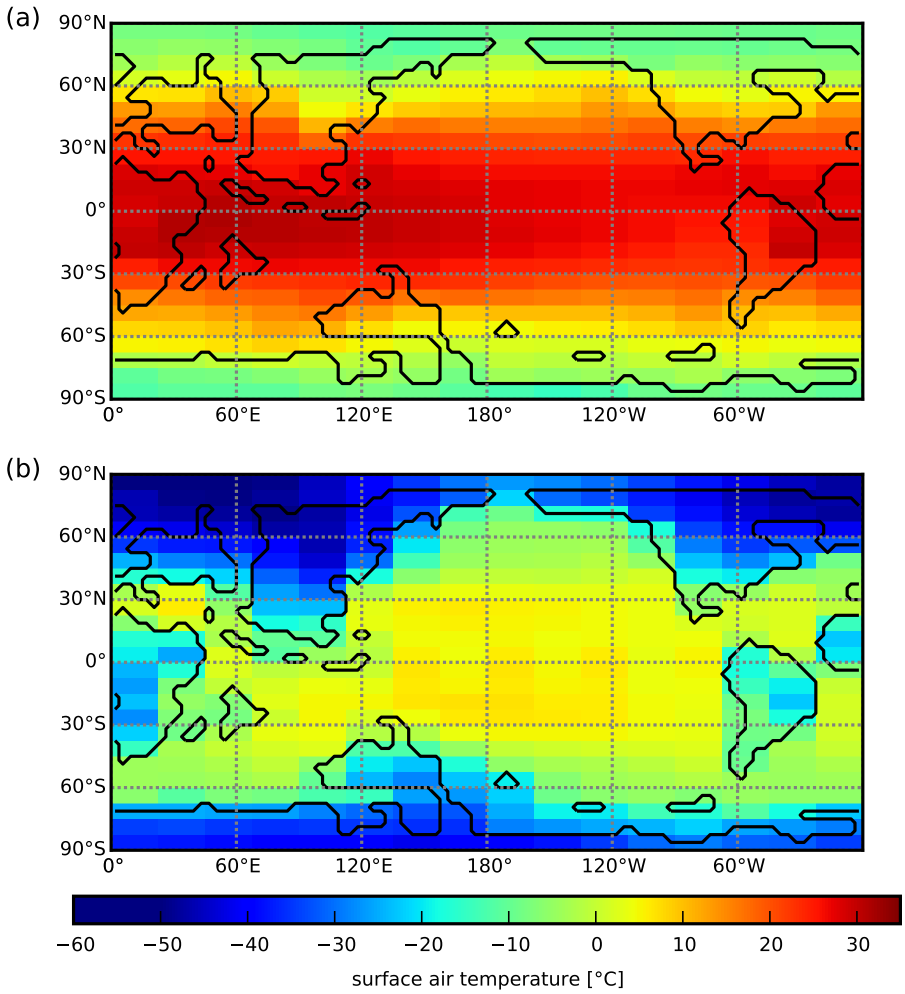

Figure 2. Map of annual simulated mean surface air temperature before the impact (a) and for the coldest year after the impact (b) for the baseline climate state with 500 ppm of carbon dioxide, a stratospheric residence time of 2.1 years and additional carbon-dioxide emissions of 360 ppm.

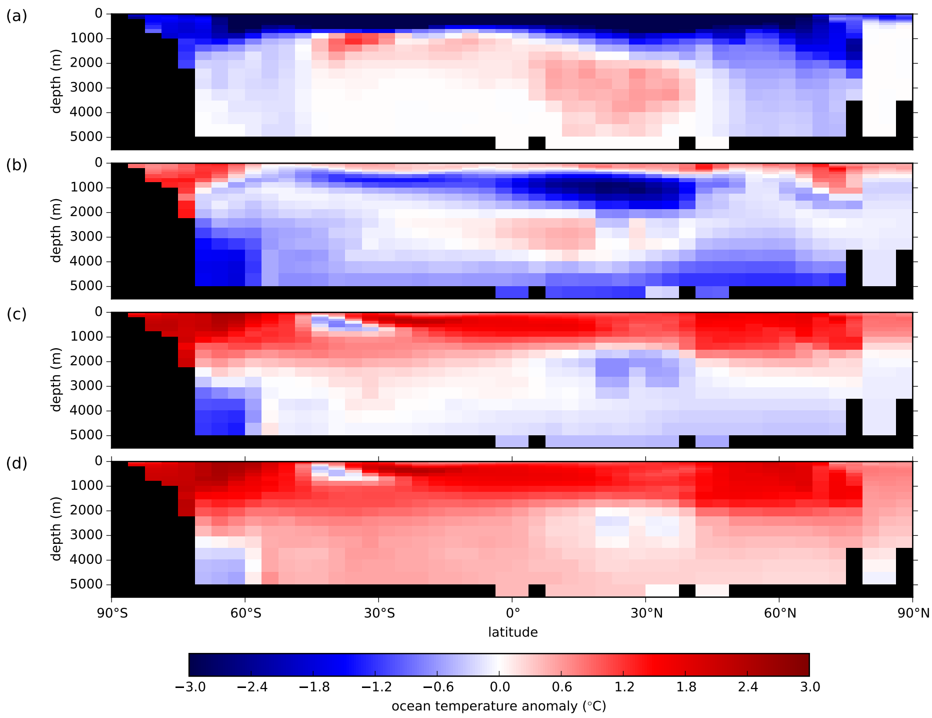

Figure 3. Meridional profiles of ocean temperature anomalies relative to the control run (a) 3 years, (b) 100 years, (c) 500 years, and (d) 1000 years after the impact. The range of the colour bar has been chosen to emphasise anomalies on longer time-scales; the near-surface cooling in panel (a) therefore exceeds this range.

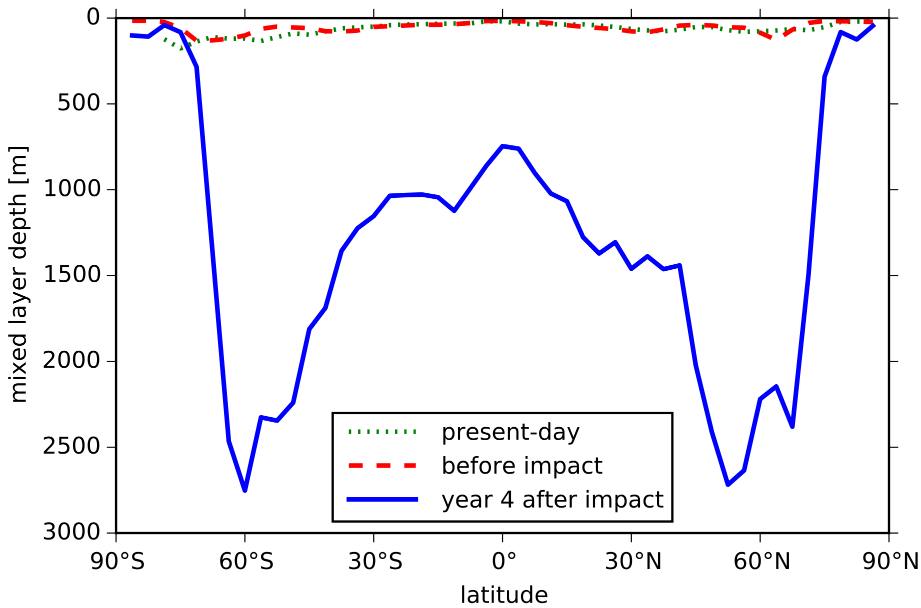

Figure 4. Ocean mixed layer depth before the impact and in the coldest year for the baseline simulation with 500 ppm of carbon dioxide, 2.1 years residence time and 360 ppm of carbon dioxide from the impact. The present-day mixed-layer depth from a simulation for the end of the 20th century [*Feulner*, 2011] is shown for comparison.

2.4. A pronounced spike in ocean productivity triggered by the Chicxulub impact

ADVANCING EARTH AND SPACE SCIENCE

Geophysical Research Letters

RESEARCH LETTER
10.1029/2020GL092260

A Pronounced Spike in Ocean Productivity Triggered by the Chicxulub Impact

Julia Brugger[1,2,3], Georg Feulner[1], Matthias Hofmann[1], and Stefan Petri[1]

[1]Earth System Analysis, Potsdam Institute for Climate Impact Research, Member of the Leibniz Association, Potsdam, Germany, [2]Institute of Physics and Astronomy, University of Potsdam, Potsdam-Golm, Germany, [3]Senckenberg Biodiversity and Climate Research Centre (SBiK-F), Frankfurt, Germany

Key Points:
- We investigate the effects of sulfate aerosols, carbon dioxide and dust produced by the Chicxulub impact on climate and the marine biosphere
- Nutrients from the deep ocean and the projectile induce a short increase in marine primary productivity after the impact-induced darkness
- Simulated post-impact warming and carbon isotope changes indicate substantial emissions of carbon from the terrestrial biosphere

Supporting Information:
Supporting Information may be found in the online version of this article.

Correspondence to:
J. Brugger and G. Feulner,
brugger@pik-potsdam.de;
feulner@pik-potsdam.de

Citation:
Brugger, J., Feulner, G., Hofmann, M., & Petri, S. (2021). A pronounced spike in ocean productivity triggered by the Chicxulub impact. *Geophysical Research Letters*, *48*, e2020GL092260. https://doi.org/10.1029/2020GL092260

Received 23 DEC 2020
Accepted 24 MAY 2021

Abstract There is increasing evidence linking the mass-extinction event at the Cretaceous-Paleogene boundary to an asteroid impact near Chicxulub, Mexico. Here we use model simulations to explore the combined effect of sulfate aerosols, carbon dioxide and dust from the impact on the oceans and the marine biosphere in the immediate aftermath of the impact. We find a strong temperature decrease, a brief algal bloom caused by nutrients from both the deep ocean and the projectile, and moderate surface ocean acidification. Comparing the modeled longer-term post-impact warming and changes in carbon isotopes with empirical evidence points to a substantial release of carbon from the terrestrial biosphere. Overall, our results shed light on the decades to centuries after the Chicxulub impact which are difficult to resolve with proxy data.

Plain Language Summary The sudden disappearance of the dinosaurs and many other species during the end-Cretaceous mass extinction 66 million years ago marks one of the most profound events in the history of life on Earth. The impact of a large asteroid near Chicxulub, Mexico, is increasingly recognized as the trigger of this extinction, causing global darkness and a pronounced cooling. However, the links between the impact and the changes in the biosphere are not fully understood. Here, we investigate how life in the ocean reacts to the perturbations in the decades and centuries after the impact. We find a short-lived algal bloom caused by the upwelling of nutrients from the deep ocean and nutrient input from the impactor.

1. Introduction

During its more than half a billion year long history, the evolution of animal and plant life on Earth was repeatedly disrupted by major mass-extinction events (Bambach, 2006). Among these biodiversity crises, the extinction at the Cretaceous-Paleogene (K-Pg) boundary (Renne et al., 2013) is unique: On the one hand, it is similar to many other mass-extinction events because of its association with continental flood basalt eruptions (Ernst & Youbi, 2017), in this case forming the Deccan Traps large igneous province in India (Schoene et al., 2019). On the other hand, it is the only extinction event which has been convincingly linked to an asteroid impact (Alvarez et al., 1980; Kring, 2007; Schulte et al., 2010), despite the fact that such large impacts with potentially global effects are statistically expected to occur once every 100–150 million years (Schmieder & Kring, 2020).

Initially put forward four decades ago (Alvarez et al., 1980), the hypothesis that the impact of a ~10 km asteroid was the main cause of the end-Cretaceous mass extinction event is now supported by multiple lines of evidence (Schulte et al., 2010). Particularly over the last few years, a number of studies on the events around the Cretaceous-Paleogene boundary have shed light on several important aspects. High-precision dating of zircons established the timing of the Deccan Trap eruptions (Schoene et al., 2019), indicating major pulses of volcanic activity ~50 kyr before and ~150 kyr after the impact, limiting their contribution to the extinction event which coincides with the impact. Data from the recent crater drilling project illuminate the immediate aftermath of the impact (Gulick et al., 2019) and, combined with improved geodynamic models, suggest a steeply inclined impact releasing significant amounts of carbon and sulfur from sedimentary rocks (Artemieva et al., 2017; Collins et al., 2020). Climate model simulations show that the formation of stratospheric sulfate aerosols leads to a colder and longer impact winter (Brugger et al., 2017) compared to the effects of impact dust alone. High-resolution proxy data confirm a pronounced short-term

Geophysical Research Letters 10.1029/2020GL092260

surface ocean cooling in the months to decades after the impact (Vellekoop et al., 2014, 2016), followed by longer-term warming (Vellekoop et al., 2014, 2018). Furthermore, proxy studies report rapid ocean acidification which likely started in the century after the impact and lasted for several thousand years (Henehan et al., 2019). The breakdown of the $\delta^{13}C$ gradient from the surface to the deep ocean (Henehan et al., 2019; Sepúlveda et al., 2019; Zachos et al., 1989) probably indicates severe changes in the ocean's biological pump, but the detailed processes are still poorly understood. In particular, the immediate consequences of the impact on marine productivity during the first years to centuries after the impact cannot be reconstructed by proxy data due to a lack in temporal resolution.

Model experiments simulating the effects of sulfate aerosols from the impact on the climate indicate severe cooling resulting in strong ocean convection (Brugger et al., 2017). The resulting upwelling of nutrients from the deep ocean could increase marine primary productivity following the period of post-impact darkness, but it is unclear whether productivity remains limited by other critical nutrients (in particular iron) and how the marine biosphere is affected by the combined changes in light, temperature, ocean circulation, and nutrient distribution. Here, we address this question by modeling immediate impact-induced changes in climate and nutrient supply and their repercussions for the marine biosphere.

2. Materials and Methods

2.1. Model

We use the Earth-system model of intermediate complexity CLIMBER-3α+C (Hofmann et al., 2019; Montoya et al., 2005). The ocean model is a modified version of MOM3 (Hofmann & Morales Maqueda, 2006; Pacanowski & Griffies, 1999), run at a horizontal resolution of 3.75° x 3.75° with 24 vertical levels of variable thickness. Additionally, CLIMBER-3α+C includes a sub-model (Hofmann et al., 2019) which is similar to HAMOCC3.1 (Six & Maier-Reimer, 1996) and accounts for the dynamics of marine biogeochemistry and the carbon cycle. The stable carbon isotope fractionation of phytoplankton is parameterized as a function depending on the concentration of aquatic carbon dioxide (Hofmann et al., 1999), while for the inorganic carbonate system and the air-sea gas exchange the approach by Maier-Reimer (Maier-Reimer, 1993) is used. The sea-ice model (Fichefet & Maqueda, 1997) is a dynamic/thermodynamic model in two dimensions with the same horizontal resolution as the ocean model. The statistical-dynamical atmosphere model (Petoukhov et al., 2000) has a coarse resolution of 22.5° in longitude and 7.5° in latitude; it contains a module to simulate terrestrial sources, atmospheric transport and deposition of dust (Bauer & Ganopolski, 2010; Hofmann et al., 2019). The model version used for this study includes an improved lapse rate parametrization and more realistic ice and snow albedo values (Feulner & Kienert, 2014).

2.2. Boundary Conditions and Pre-Impact Climate State

An equilibrium simulation of the end-Cretaceous climate is the basis of all impact simulations. This equilibrium state is modeled using a Maastrichtian (70 Ma) continental configuration and vegetation distribution (Sewall et al., 2007), a solar constant of 1354 W/m^2, based on the present-day solar constant of 1361 W/m^2 (Kopp & Lean, 2011) and a standard solar model (Bahcall et al., 2001), and idealized orbital parameters (circular orbit, obliquity 23.5°). Proxy data for the Late Cretaceous give a wide range of CO_2 concentrations ranging from 240 ppm (Foster et al., 2017; Nordt et al., 2003) to 1,500 ppm (Royer, 2006). For the time just before the impact, there is evidence that atmospheric CO_2 concentrations were below 800 ppm (Foster et al., 2017; Hong & Lee, 2012; Nordt et al., 2002, 2003; Royer et al., 2012). We have adjusted the carbonate chemistry in the ocean to yield atmospheric CO_2 levels close to 500 ppm, a medium value within the range of proxy estimates: Starting from close to pre-industrial conditions (≈280 ppm), we have modified the ocean's alkalinity until the model approaches equilibrium at a value of 502 ppm after 11,400 model years. The equilibrium pre-impact state has a total alkalinity of 2,348 μeq L^{-1} and global annual mean amounts of dissolved inorganic carbon (DIC) of 2,328 μmol L^{-1}, of inorganic phosphate of 2.28 μ mol L^{-1} and silicate of 81.4 μ mol L^{-1}. For comparison, the measured present-day values are 2,353 μeq L^{-1} for the total alkalinity, 2,241 μ mol L^{-1} for DIC (Key et al., 2004), 2.1 μ mol L^{-1} for phosphate and 88.2 μ mol L^{-1} for silicate (objectively analyzed climatologies, Garcia et al., 2018). In addition to this baseline simulation

Geophysical Research Letters 10.1029/2020GL092260

with ≈500 ppm of CO_2, we have performed an equilibrium simulation with ≈1,165 ppm for sensitivity tests (see supporting information).

The simulated global annual mean surface air temperature for the late-Cretaceous climate state with ≈500 ppm of atmospheric CO_2 is 19.0°C, about 4°C higher than the pre-industrial temperature. Further discussion of this pre-impact state including figures for the temperature distribution as well as a description of the sensitivity simulation with a higher atmospheric CO_2 concentration can be found in the supporting information. The modeled global mean marine net primary productivity (NPP) for the pre-impact climate state is 48 GtC/year. In a late-Holocene configuration of the model, the simulated global mean marine NPP is about 27 GtC/year, at the lower end of the range of CMIP5 values (Fu et al., 2016), but well within the broad interval (50 ± 28 Gt C/year) of observational estimates (Malone et al., 2017).

2.3. Modeling the Climatic Effects of the Impact

We explore the effects of sulfate aerosols, carbon dioxide (CO_2) and dust produced by the Chicxulub impact on the climate and the marine biosphere. To model the radiative effect of the sulfate aerosols we use a time series of visible transmission for 2.1 years stratospheric residence time and for a load of 100 Gt S with 80% of the sulfur ligated as SO_2 and 20% as SO_3 (Brugger et al., 2017; Pierazzo et al., 2003). Note that more recent investigations with geophysical impact models suggest higher sulfur masses based on new limits for the impact angle and the target composition (Artemieva et al., 2017). However, as the radiative effect does not increase for sulfur loads larger than 30 Gt (Pierazzo et al., 2003), we do not consider the radiative effect of larger sulfur masses. In our standard simulations it is assumed that sulfate aerosols are transferred directly to the ocean after leaving the stratosphere (Pierazzo et al., 2003), with 100% of the sulfur passed to the ocean. To derive a time sequence for the sulfur flux to the ocean we use data for the stratospheric sulfate aerosol concentration decreasing over 6 years (Pierazzo et al., 2003) to calculate the monthly flux to the ocean. We also test the influence of additional sulfur deposition to the ocean on shorter timescales of 10 days after the impact as it was suggested that sulfate aerosols are scavenged by larger and faster settling silicate particles (Ohno et al., 2014; Tyrrell et al., 2015).

Additionally, we consider the atmospheric and oceanic effects of an increased atmospheric CO_2 concentration due to the impact. For our standard impact simulation we use an additional carbon mass of 115 Gt. This represents the carbon release primarily from the vapourization of carbonate rocks (Artemieva et al., 2017). CO_2 is equally distributed over 10 days after the impact assuming instantaneous formation. As for the sulfate aerosols, a globally uniform distribution is used. We also test the sensitivity to C masses between 0 and 4,115 Gt (Artemieva et al., 2017; Pierazzo et al., 1998, 2003; Tyrrell et al., 2015), considering additional C from wildfires (additional 1,500 Gt) and decomposed soil organic carbon (additional 2,500 Gt assuming to be instantaneously released, Tyrrell et al., 2015). We use $\delta^{13}C$ values of −3‰ for the C from the carbonate rocks (Kettrup et al., 2000) and −27‰ for C from organic material, assuming a plant mixture of C_3 and C_3+CAM plants (Gilman & Edwards, 2020; Osborne & Sack, 2012).

As it was shown that the radiative effects of impact dust were dominated by the effects of sulfate aerosols (Pierazzo et al., 2003; Pope, 2002) and possibly soot (Bardeen et al., 2017), we only consider the effects of the impact dust from the projectile on the ocean, in particular from the important nutrients iron and phosphorus. We explicitly model the atmospheric transport and deposition of impact dust from the projectile to derive the dust distribution in the ocean. To estimate the amount of iron and phosphor distributed in the ocean, we assume that the impactor was a carbonaceous chondrite of type CV, CO or CR (Kyte, 1998). These chondrites have typical iron and phosphorus fractions of 22.5% and 0.104%, respectively (Braukmüller et al., 2018). The modeling of the dust distribution and transport as well as the increase of the bioavailability after the impact is described in detail in the supporting information. For sensitivity tests, we also run the standard impact simulation (115 Gt C and 100 Gt S) and an impact simulation with additional 1,500 Gt C for the pre-impact state with 1,165 ppm of CO_2.

Geophysical Research Letters 10.1029/2020GL092260

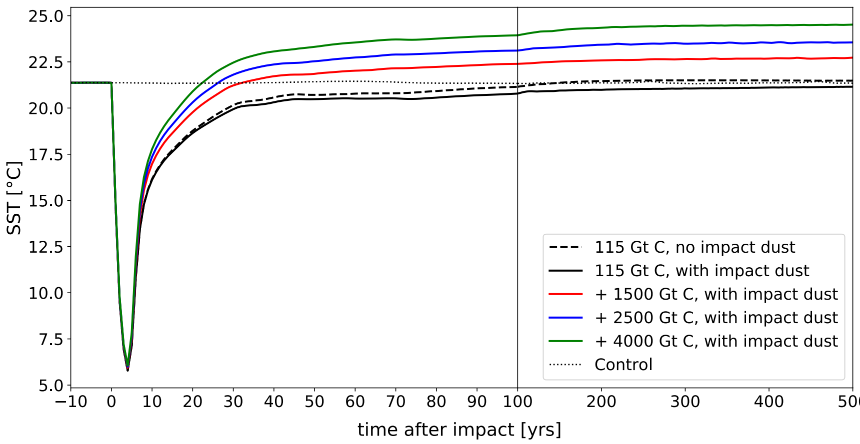

Figure 1. Sea surface temperature evolution for different amounts of carbon released due to the impact. Annual and global mean sea surface temperature before and after the impact for simulations with (solid lines) and without the effects of dust produced during the impact (dashed line) as well as for different amounts of organic carbon released from terrestrial reservoirs (colored lines).

3. Results

3.1. Temperature Changes in the Millennium After the Impact

The strong reduction in incoming solar radiation due to the stratospheric sulfate aerosols from the impact (Brugger et al., 2017; Pierazzo et al., 2003) has far-reaching implications for climate and life. This is most evident in the severe global cooling in the first decades after the impact. Global annual mean sea surface temperatures (SSTs) are reduced from 21.4°C by about ~15°C in the fourth year after the impact (Figure 1). Temperatures recover over the following centuries, approaching pre-impact values after 1,000 years. For a higher late-Cretaceous CO_2 concentration, the impact induces a cooling of very similar magnitude in the immediate aftermath of the impact. More detailed results and discussion for the impact simulations with higher CO_2 concentration can be found in the supporting information (Table S1, Figures S9–S11 and supporting information S5).

Tracing the decadal-scale cooling induced by the impact in geological records is challenging. However, high-resolution proxy data for the Brazos River region (Vellekoop et al., 2014) and for the New Jersey shelf region (Vellekoop et al., 2016) indicate cooling of 7°C (resolved on timescales of months to decades) and 3°C (resolved on timescales of decades to centuries), respectively, in good agreement with the cooling simulated in our model and averaged over appropriate timescales (see Table S1 in supporting information). Furthermore, the data for the Brazos region (Vellekoop et al., 2014, 2018) indicate a long-term increase of SST of 1−2°C in the early Paleogene starting in the centuries after the impact. In our simulations, the amplitude of SST changes at this location is very similar to the global value; therefore we can directly compare the global SST curves shown in Figure 1 with the proxy estimates. With carbon emissions from the impact only (and the response of the marine biosphere), our standard simulation shows no significant warming in the centuries after the impact. However, one would expect additional carbon emissions from the terrestrial biosphere (e.g., from dying vegetation, wildfires, or soil decomposition) which are not taken into account in this model experiment. Simulations with a series of larger carbon emissions (Figure 1) show that the best agreement with the Brazos River proxy data is achieved for additional 1,500 Gt C from terrestrial sources for the late-Cretaceous simulations with 500 ppm atmospheric CO_2 concentration. For a higher pre-impact CO_2 level, the long-term warming after the impact is smaller for the same amount of additional carbon (see Table S1, Figure S9 and supporting information S5), which is to be expected for a significantly higher baseline CO_2 concentration. Therefore, if the late-Cretaceous atmospheric CO_2 concentration was higher than 500 ppm, the proxy comparison for the pre-impact warming suggests the addition of even more carbon from terrestrial sources. A decrease of 1.2‰ in $\delta^{18}O$ of fine fraction carbonate for Caravaca, Spain, in the

Geophysical Research Letters 10.1029/2020GL092260

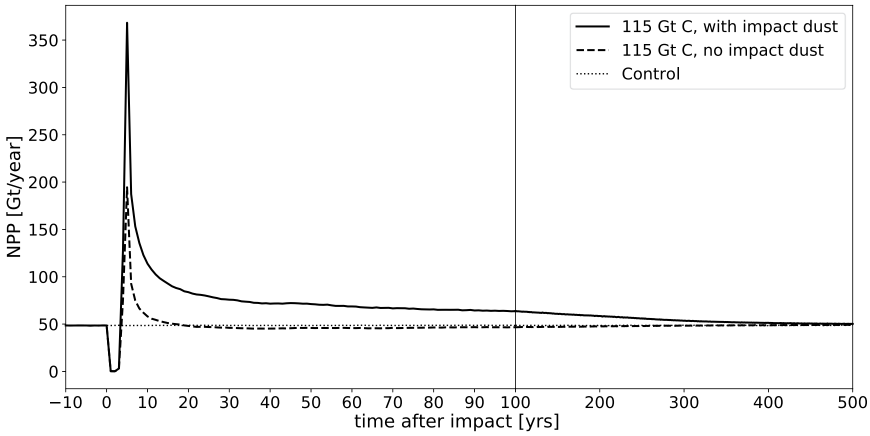

Figure 2. Effects of the impact on the marine biosphere. Annual and global mean ocean net primary productivity before and after the impact for simulations with (solid line) and without the effects of dust produced during the impact (dashed line).

centuries and first millennia after the impact (Kaiho et al., 1999) also supports a warming after the impact, but the suggested strong warming of ∼5°C (Kaiho et al., 1999) is highly uncertain due to diagenesis, the superposition of different vital effects (e.g., Ziveri et al., 2003) linked to the complex composition of fine fraction carbonate, and the fact that $\delta^{18}O$ of sea water is not constrained.

3.2. A Brief Peak of Net Primary Productivity After the Impact

The Chicxulub impact had profound short-term repercussions for the marine biosphere. In our simulations, the global annual mean NPP in the ocean drops to almost zero in the three years following the impact before briefly peaking at a maximum value about a factor of seven higher than the pre-impact NPP (Figure 2). Although the NPP peak lasts only for a few years, higher productivity persists for decades to centuries, returning to pre-impact levels only after ∼500 years.

The almost complete shutdown of marine NPP in the first years after the impact is caused by both the low light levels and the resulting temperature decrease. With the solar flux starting to recover already two years after the impact and reaching its pre-impact value after seven years (Brugger et al., 2017), global annual mean marine NPP exceeds pre-impact levels of 48 Gt/year in the fourth year after the impact and culminates in a sharp peak at a value of 368 Gt/year in year five. This increase in NPP is caused by two mechanisms: First, the severe surface cooling of the ocean following the impact induces strong ocean mixing and deep water formation, leading to a deep mixed layer, in particular in the mid-latitudes (see supporting information and Brugger et al. (2017) for figures and further discussion). This results in the transport of a large amount of nutrients from the deep ocean to the surface, thus increasing the productivity. Second, considerable amounts of iron and phosphorus are delivered to the ocean by the impact dust originating from the iron-rich projectile. These nutrients with increased bioavailability (see Section 2.3 and supporting information) are sufficient to sustain elevated levels of the NPP for several centuries. In contrast, the nutrients brought to the surface ocean by deep mixing are quickly consumed, as shown by a simulation without dust from the impact (see Figure 2).

The uptake of large amounts of carbon during the period of high ocean productivity results in lower atmospheric CO_2 concentrations and consequently decreases temperatures. Hence, earlier simulations without marine biogeochemistry show a very similar cooling, but a faster recovery where pre-impact temperatures are exceeded already after less than 100 years (Brugger et al., 2017).

Regionally, the increase in marine NPP starts in the tropics where light and ocean temperature exceed the critical thresholds necessary for photosynthesis earliest (Figure S1 in supporting information). As the cooling of the ocean's surface induces strong ocean mixing in particular in the mid-latitudes (Brugger

Geophysical Research Letters 10.1029/2020GL092260

et al., 2017) bringing large amounts of nutrients to the surface ocean, the high primary productivity quickly expands to these regions. The nutrients from the impact dust are quickly spread in the ocean and hence do not cause significant local effects, but amplify the regional NPP patterns also observed in the simulation without impact dust. NPP stays below its pre-impact value for more than 10 years after the impact only in the very high Northern latitudes as a result of the very low ocean temperatures in this region. Note that productivity in coastal regions could have been even higher due to nutrient input from the terrestrial biosphere (Vellekoop et al., 2018) not taken into account in our model.

Blooms of dinoflagellates and cyanobacteria associated with regional maxima in the NPP could result in the production of toxins with detrimental effects for marine near-surface ecosystems. This mechanism described here for the first time could thus play a role in the context of the immediate effects of the impact on the marine biosphere. We note that the increased marine productivity might be dampened by self-limiting feedbacks of the algal bloom (Jackson & Lochmann, 1992; Shigesada & Okubo, 1981) which are not represented in our model. Another aspect not considered here is the formation of cloud condensation nuclei as a consequence of algal blooms. Planktonic algae produce dimethylsulfide (DMS) which form sulfate aerosols in the atmosphere acting as cloud condensation nuclei. Higher densities of cloud condensation nuclei influence cloud albedo and lifetime, and could therefore prolong the cooling after the impact (Charlson et al., 1987; Feulner et al., 2015).

Although there are no empirical data on the productivity immediately after the impact, it has been suggested that marine primary productivity could have been strongly limited only during the short period with direct environmental consequences of the impact, potentially only for a decade (D'Hondt, 2005), consistent with our results. A combined interpretation of proxy data, the fossil record and model results indicates that marine primary productivity recovered to normal or regionally high values (Hollis et al., 1995, 2003; Lowery et al., 2020; Sepúlveda et al., 2009, 2019; Vellekoop et al., 2017, 2018) much earlier than the biological pump, but that the remineralization depth of organic matter was shallower, leading to a decrease in the export productivity ("Living Ocean" hypothesis, D'Hondt et al., 1998). Estimates for the recovery time for the marine primary productivity are constrained by the age models of the proxy studies and vary between a century (Sepúlveda et al., 2009), and tens of thousands of years (Henehan et al., 2019; Sepúlveda et al., 2019). Hence, our results suggest a convincing scenario for the immediate effect of the impact on primary productivity which cannot be resolved by proxy data and fits the observation of regionally heterogenous recovery of productivity (Sepúlveda et al., 2019). Nevertheless, there might have been some additional, prolonged effects limiting primary productivity in the centuries to millennia after the boundary, both as consequences of the impact as well as other changes across the boundary (Arthur et al., 1987), which are not represented in our model.

3.3. Carbon Isotopes Suggest Significant Release of Terrestrial Carbon

The strong perturbations at the K-Pg boundary induce severe changes in the marine carbon cycle leaving traces in the ocean's dissolved inorganic carbon δ^{13}C values. This signal depends both on the amount of carbon emitted due to the impact and on its isotopic signature; it is therefore important to assign appropriate δ^{13}C values to modeled carbon fluxes from different sources (see Section 2.3). We find an immediate reduction of δ^{13}C in the surface ocean (Figure 3 for the region around Shatsky Rise in the Northern Pacific). The decrease is caused by the enhanced ocean mixing transporting inorganic C with lower δ^{13}C from the deeper ocean to the surface, combined with the reduced primary productivity in the first years after the impact. These processes dominate the simulation with only 115 Gt C: after a short decrease δ^{13}C starts to rise during the productivity maximum before approaching a new equilibrium slightly above the pre-impact value. In contrast, δ^{13}C values in the simulations with carbon released from the terrestrial biosphere are determined by these additional amounts of isotopically light carbon, decreasing the ocean's δ^{13}C significantly. Surface δ^{13}C starts to increase and approaches a new equilibrium value when the added carbon is exported to the deeper ocean. Hence, the reduction of δ^{13}C in the deep ocean is smaller and delayed compared to the surface ocean, resulting in a reduced δ^{13}C gradient from the surface to the deep ocean.

The immediate effect of the Chicxulub impact on δ^{13}C in the first millennium after the event are resolved in detail in our simulations, but not covered by proxy data due to a lack of temporal resolution. However, if we interpret the earliest surface proxy data after the impact as a smeared signal for the time since the K-Pg

Geophysical Research Letters 10.1029/2020GL092260

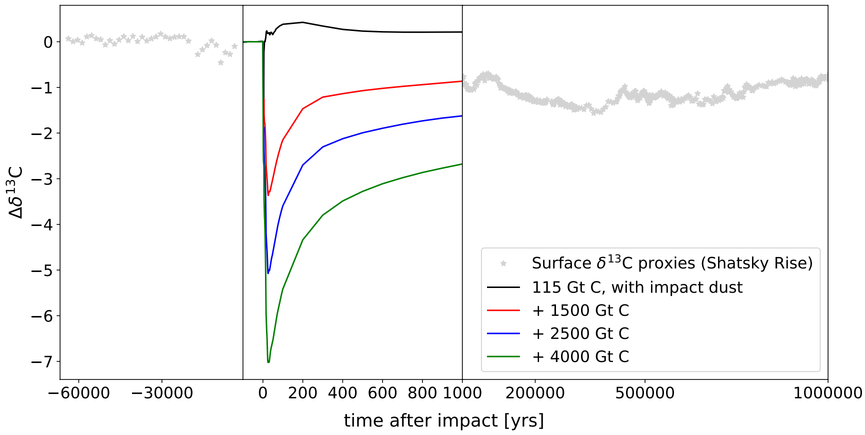

Figure 3. Changes of surface carbon isotope ratios of dissolved inorganic carbon at Shatsky Rise, Pacific. Colored lines show modeled changes in $\delta^{13}C$ for the 1,000 years after the impact relative to the 100-year pre-impact mean for simulations with different amounts of carbon. The model results are embedded in changes in surface $\delta^{13}C$ from proxy data from bulk carbonate (Table S11 in Hull et al., 2020), assuming an absolute age for the K-Pg boundary of 66.022 Ma (Table S3 in Hull et al., 2020) relative to the mean of the pre-impact proxy values.

boundary, again our simulation with an additional amount of 1,500 Gt C from the terrestrial biosphere shows the best agreement with the proxy data (see Figure 3), confirming the release of significant quantities of carbon from the terrestrial biosphere already suggested by the temperature evolution. This finding also holds for a significantly higher atmospheric CO_2 concentration before the impact (see Figure S10 in the supporting information). We note that a comparison of modeled $\delta^{13}C$ data for the deep ocean with benthic proxy data is challenging because of the higher variability and lower temporal resolution of the benthic $\delta^{13}C$ data for this period (Henehan et al., 2019; Hull et al., 2020).

3.4. Moderate Ocean Acidification Followed by a Fast Recovery

The paleontologic record of the end-Cretaceous shows a significantly higher extinction rate of marine calcifying organisms (Tyrrell et al., 2015). This could be a consequence of ocean acidification caused by the fast release of CO_2 and H_2SO_4 during the impact. However, the occurrence of an acidified ocean is still debated, as the observed extinction patterns differ strongly among different calcifying species, making it difficult to get a clear understanding of the extent of acidification and its effects on the biosphere (D'Hondt, 2005; Dishon et al., 2020; Kiessling & Baron-Szabo, 2004; Kiessling & Simpson, 2011; Tyrrell et al., 2015).

To explore the influence of impact-related carbon and sulfur emissions, we model their effects on the ocean's carbonate saturation state and pH. Consistent with our findings from the changes in temperature and $\delta^{13}C$, we assume an additional carbon amount of 1,500 Gt C; for sulfur, we use the most recent estimate of 325 Gt S (Artemieva et al., 2017). Model experiments with higher C and S masses are discussed in the SI (Section 3 and Figures S2, S4 and S5).

We find an immediate reduction of surface global mean pH, with a maximum surface pH decrease of 0.36 units four years after the impact (see Figure S2 in supporting information). The subsequent emerging peak in ocean productivity and the accompanying high carbon uptake leads to a short increase in pH before it decreases again. These fast changes immediately after the impact are followed by a transient recovery over the next 500 years, equilibrating at 0.23 pH units below the pre-impact value. Data from the Geulhemmerberg succession show a pH reduction of ~0.25 for the millennium following the impact, but possibly even for a shorter time scale of ~100 years (Henehan et al., 2019). This is in excellent agreement with our modeled pH reduction of 0.28 pH units in this region averaged over the century after the impact.

To assess the influence on calcifiers, Figure 4 shows the surface ocean aragonite saturation state Ω_a. The critical value for the saturation state Ω varies for different calcifying species (Ries et al., 2009) and depends

Geophysical Research Letters 10.1029/2020GL092260

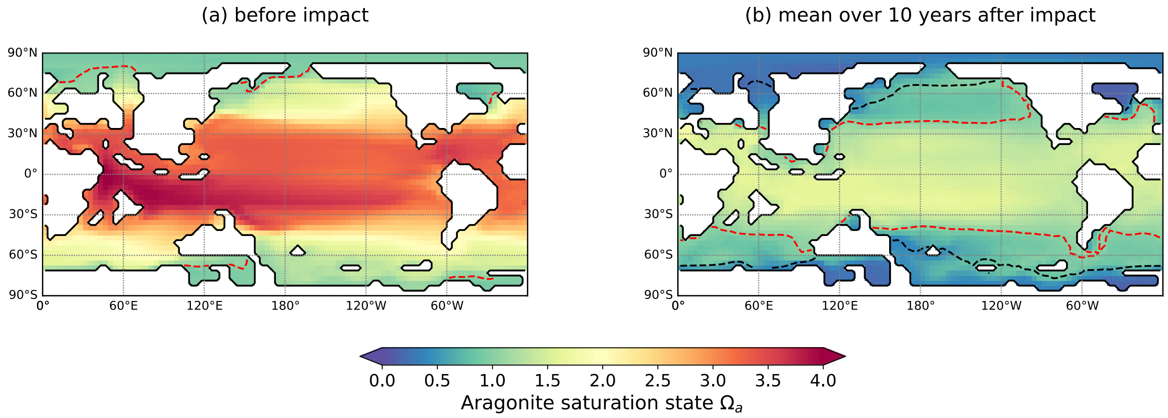

Figure 4. Effects of carbon and sulfur emissions from the impact on ocean acidification. Surface ocean aragonite saturation state before the impact (a) and for the average over the 10 years after the impact. The $\Omega_a = 1$ line is shown in red. The dashed black line in (b) shows $\Omega_a = 1$ for the 1,000 years after the impact.

on marine carbonate chemistry (Bach et al., 2015). Here we assume that calcifying organisms begin to dissolve for $\Omega < 1$. Globally, Ω_a is strongly reduced in the 10 years after the impact, and it falls below the critical value of 1 at latitudes higher than ~40°. Although Ω_a quickly starts to recover and the line defining $\Omega_a = 1$ retrenches to higher latitudes, Ω_a globally stays below the pre-impact values in the 1,000 years after the impact. The calcite saturation state Ω_c, which is generally higher than Ω_a due to the lower solubility of calcite in ocean water, shows similar patterns (see Figure S3 in supporting information). Ω_c falls below the critical value of 1 for latitudes greater than ~60° averaged for the 10 years after the impact before $\Omega_c = 1$ retrenches to higher latitudes.

In summary, we find rapid surface ocean acidification which, however, recovers quickly. The potential habitat for calcifiers after the impact is restricted to lower latitudes. For corals and rudists favoring warm waters, however, it is hard to distinguish whether the strong temperature decrease or the aragonitic undersaturation was more critical in limiting their habitat. As the surface ocean is undersaturated in calcite only at high latitudes, the global extinction of planktic foraminifera (D'Hondt, 2005) is difficult to explain primarily with ocean acidification. Our results thus indicate that surface ocean acidification after the Chicxulub impact caused regionally the extinction of some groups of calcifiers. However, the extinction of a large fraction of globally distributed calcifiers, as observed in the fossil record, cannot be caused by undersaturation alone, because it was not widespread enough.

4. Discussion

Our modeling results for the immediate consequences of the Chicxulub impact on the climate and the marine biosphere indicate rapid cooling, a sharp and short-lived increase of marine primary productivity following a brief productivity collapse, and moderate ocean acidification. The longer-term warming trend observed in proxy data and the comparison of surface $\delta^{13}C$ data with our model results suggest an additional carbon release of ~1,500 Gt from the terrestrial biosphere. If the carbon is the result of wildfires caused by the infrared radiation of the reentering ejecta (Robertson et al., 2013), the produced soot would have further reduced the incoming surface short wave radiation with significant effects on photosynthesis (Bardeen et al., 2017; Tabor et al., 2020). In addition, nutrients brought into the ocean by the wildfire ash could have intensified and prolonged the increase in marine primary productivity and the algal bloom (Abram et al., 2003). Proxy data indicate an additional nutrient flux resulting from land-derived material during the terrestrial mass extinction, leading in particular to increased productivity in the neritic zone during the centuries to millennia following the K-Pg boundary (Vellekoop et al., 2018). Future modeling studies will have to explore the full range of interactions between climate and the terrestrial and marine biosphere.

AGU ADVANCING EARTH AND SPACE SCIENCE
Geophysical Research Letters 10.1029/2020GL092260

Recent studies on the interaction of Deccan volcanism and the Chicxulub impact support the notion that the impact was the major driver of the end-Cretaceous mass extinction (Hull et al., 2020; Sprain et al., 2019). From these findings and our results we conclude that the combination of several abrupt and vigorous changes caused by the Chicxulub impact triggered the end-Cretaceous mass extinction. In addition, life-history traits (D'Hondt, 2005), geographic distribution (Dishon et al., 2020), the respective ecosystem (D'Hondt, 2005) and chance survival (D'Hondt, 2005) could have determined the selectivity during the extinction. The interaction of these ecological and evolutionary factors with the modeled direct consequences of the impact would have to be further investigated, for example with ecological niche models.

Data Availability Statement

All model input and output files as well as the preprocessing and postprocessing scripts used to generate model input and the figures in the study are available online (https://doi.org/10.5880/PIK.2020.008). The source code for the model used in this study is archived at the Potsdam Institute for Climate Impact Research and is made available upon request.

Acknowledgments
The authors would like to thank Eva Bauer who laid the foundation for the implementation of dust production and transport in our model, Rosie Sheward and David Evans for their help with the interpretation of proxy data, and Johan Vellekoop and one anonymous reviewer for very helpful comments. The authors gratefully acknowledge the European Regional Development Fund (ERDF), the German Federal Ministry of Education and Research and the Land Brandenburg for supporting this project by providing resources on the high performance computer system at the Potsdam Institute for Climate Impact Research. The work was partly funded by the German Federal Ministry of Education and Research BMBF within the Collaborative Project "Bridging in Biodiversity Science – BIBS" (funding number 01LC1501A-H) and the VeWA consortium (Past Warm Periods as Natural Analogues of our high-CO_2 Climate Future) by the LOEWE programme of the Hessen Ministry of Higher Education, Research and the Arts, Germany. J.B. acknowledges support by a PhD Completion Grant from the Potsdam Graduate School.

References

Abram, N. J., Gagan, M. K., McCulloch, M. T., Chappell, J., & Hantoro, W. S. (2003). Coral reef death during the 1997 Indian Ocean dipole linked to Indonesian wildfires. *Science*, *301*(5635), 952–955. https://doi.org/10.1126/science.1083841
Alvarez, L. W., Alvarez, W., Asaro, F., & Michel, H. V. (1980). Extraterrestrial cause for the cretaceous-tertiary extinction. *Science*, *208*(4448), 1095–1108. https://doi.org/10.1126/science.208.4448.1095
Artemieva, N., Morgan, J., & Party, E. S. (2017). Quantifying the release of climate-active gases by large meteorite impacts with a case study of Chicxulub. *Geophysical Research Letters*, *44*(20), 10180–10188. https://doi.org/10.1002/2017GL074879
Arthur, M., Zachos, J., & Jones, D. (1987). Primary productivity and the Cretaceous/Tertiary boundary event in the oceans. *Cretaceous Research*, *8*(1), 43–54. https://doi.org/10.1016/0195-6671(87)90011-5
Bach, L. T., Riebesell, U., Gutowska, M. A., Federwisch, L., & Schulz, K. G. (2015). A unifying concept of coccolithophore sensitivity to changing carbonate chemistry embedded in an ecological framework. *Progress in Oceanography*, *135*, 125–138. https://doi.org/10.1016/j.pocean.2015.04.012
Bahcall, J. N., Pinsonneault, M. H., & Basu, S. (2001). Solar models: Current epoch and time dependences, neutrinos, and helioseismological properties. *The Astrophysical Journal*, *555*(2), 990–1012. https://doi.org/10.1086/321493
Bambach, R. K. (2006). Phanerozoic biodiversity mass extinctions. *Annual Review of Earth and Planetary Sciences*, *34*, 127–155. https://doi.org/10.1146/annurev.earth.33.092203.122654
Bardeen, C. G., Garcia, R. R., Toon, O. B., & Conley, A. J. (2017). On transient climate change at the Cretaceous-Paleogene boundary due to atmospheric soot injections. *Proceedings of the National Academy of Sciences of the United States of America*, *114*, E7415–E7424. https://doi.org/10.1073/pnas.1708980114
Bauer, E., & Ganopolski, A. (2010). Aeolian dust modeling over the past four glacial cycles with CLIMBER-2. *Global and Planetary Change*, *74*, 49–60. https://doi.org/10.1016/j.gloplacha.2010.07.009
Braukmüller, N., Wombacher, F., Hezel, D. C., Escoube, R., & Münker, C. (2018). The chemical composition of carbonaceous chondrites: Implications for volatile element depletion, complementarity and alteration. *Geochimica et Cosmochimica Acta*, *239*, 17–48. https://doi.org/10.1016/j.gca.2018.07.023
Brugger, J., Feulner, G., Hofmann, M., & Petri, S. (2021). Model data for simulations of ocean biogeochemistry after the Chicxulub impact. *GFZ Data Services*, https://doi.org/10.5880/PIK.2020.008
Brugger, J., Feulner, G., & Petri, S. (2017). Baby, it's cold outside: Climate model simulations of the effects of the asteroid impact at the end of the Cretaceous. *Geophysical Research Letters*, *44*(1), 419–427. https://doi.org/10.1002/2016GL072241
Charlson, R. J., Warren, S. G., Lovelock, J. E., & Andreae, M. O. (1987). Oceanic phytoplankton, atmospheric sulphur, cloud albedo and climate. *Nature*, *326*, 655–661. https://doi.org/10.1038/326655a0
Collins, G. S., Patel, N., Davison, T. M., Rae, A. S. P., Morgan, J. V., Gulick, S. P. S., et al. (2020). A steeply-inclined trajectory for the Chicxulub impact. *Nature Communications*, *11*. https://doi.org/10.1038/s41467-020-15269-x
D'Hondt, S. (2005). Consequences of the Cretaceous/Paleogene mass extinction for marine ecosystems. *Annual Review of Ecology, Evolution and Systematics*, *36*, 295–317. https://doi.org/10.1146/annurev.ecolsys.35.021103.105715
D'Hondt, S., Donaghay, P., Zachos, J. C., Luttenberg, D., & Lindinger, M. (1998). Organic carbon fluxes and ecological recovery from the Cretaceous-Tertiary mass extinction. *Science*, *282*, 276–279. https://doi.org/10.1126/science.282.5387.276
Dishon, G., Grossowicz, M., Krom, M., Guy, G., Gruber, D. F., & Tchernov, D. (2020). Evolutionary traits that enable Scleractinian corals to survive mass extinction events. *Scientific Reports*, *10*(10), 3903. https://doi.org/10.1038/s41598-020-60605-2
Ernst, R. E., & Youbi, N. (2017). How large Igneous provinces affect global climate, sometimes cause mass extinctions, and represent natural markers in the geological record. *Palaeogeography, Palaeoclimatology, Palaeoecology*, *478*, 30–52. https://doi.org/10.1016/j.palaeo.2017.03.014
Feulner, G., Hallmann, C., & Kienert, H. (2015). Snowball cooling after algal rise. *Nature Geoscience*, *8*, 659–662. https://doi.org/10.1038/ngeo2523
Feulner, G., & Kienert, H. (2014). Climate simulations of Neoproterozoic snowball Earth events: Similar critical carbon dioxide levels for the Sturtian and Marinoan glaciations. *Earth and Planetary Science Letters*, *404*, 200–205. https://doi.org/10.1016/j.epsl.2014.08.001
Fichefet, T., & Maqueda, M. A. M. (1997). Sensitivity of a global sea ice model to the treatment of ice thermodynamics and dynamics. *Journal of Geophysical Research*, *102*(C6), 12609–12646. https://doi.org/10.1029/97JC00480
Foster, G. L., Royer, D. L., & Lunt, D. J. (2017). Future climate forcing potentially without precedent in the last 420 million years. *Nature Communications*, *8*, 14845. https://doi.org/10.1038/ncomms14845

Geophysical Research Letters 10.1029/2020GL092260

Fu, W., Randerson, J. T., & Moore, J. K. (2016). Climate change impact on net primary production (NPP) and export production (EP) regulated by increasing stratification and phytoplankton community structure in the CMIP5 models. *Biogeosciences*, *13*, 5151–5170. https://doi.org/10.5194/bg-13-5151-2016

Garcia, H. E., Weathers, K., Paver, C. R., Smolyar, I., Boyer, T. P., Locarnini, R. A., & Reagan, J. R. d. (2018). World ocean Atlas 2018, Volume 4: Dissolved inorganic nutrients (phosphate, nitrate and nitrate+nitrite, silicate). In Mishonov Technical, A. (Ed.), *NOAA Atlas NESDIS* (Vol. 84), NOAA.

Gilman, I. S., & Edwards, E. J. (2020). Crassulacean acid metabolism. *Current Biology*, *30*(2), R57–R62. https://doi.org/10.1016/j.cub.2019.11.073

Gulick, S. P. S., Bralower, T. J., Ormö, J., Hall, B., Grice, K., Schaefer, B., et al. (2019). The first day of the Cenozoic. *Proceedings of the National Academy of Sciences of the United States of America*, *116*(39), 19342–19351. https://doi.org/10.1073/pnas.1909479116

Henehan, M. J., Ridgwell, A., Thomas, E., Zhang, S., Alegret, L., Schmidt, D. N., et al. (2019). Rapid ocean acidification and protracted Earth system recovery followed the end-Cretaceous Chicxulub impact. *Proceedings of the National Academy of Sciences of the United States of America*, *116*(45), 22500–22504. https://doi.org/10.1073/pnas.1905989116

Hofmann, M., Broecker, W. S., & Lynch-Stieglitz, J. (1999). Influence of a [CO_2(aq)] dependent biological C-isotope fractionation on glacial 13C/12C ratios in the ocean. *Global Biogeochemical Cycles*, *13*, 873–883. https://doi.org/10.1029/1999GB900063

Hofmann, M., Mathesius, S., Kriegler, E., van Vuuren, D., & Schellnhuber, H. J. (2019). Strong time dependence of ocean acidification mitigation by atmospheric carbon dioxide removal. *Nature Communications*, *10*, 5592. https://doi.org/10.1038/s41467-019-13586-4

Hofmann, M., & Morales Maqueda, M. A. (2006). Performance of a second-order moments advection scheme in an Ocean General Circulation Model. *Journal of Geophysical Research*, *111*, C05006. https://doi.org/10.1029/2005JC003279

Hollis, C. J., Rodgers, K. A., & Parker, R. J. (1995). Siliceous plankton bloom in the earliest Tertiary of Marlborough, New Zealand. *Geology*, *23*(9), 835–838. https://doi.org/10.1130/0091-7613(1995)023<0835:SPBITE>2.3.CO;2

Hollis, C. J., Rodgers, K. A., Strong, C. P., Field, B. D., & Rogers, K. M. (2003). Paleoenvironmental changes across the Cretaceous/Tertiary boundary in the northern Clarence valley, southeastern Marlborough, New Zealand. *New Zealand Journal of Geology and Geophysics*, *46*(2), 209–234. https://doi.org/10.1080/00288306.2003.9515005

Hong, S. K., & Lee, Y. I. (2012). Evaluation of atmospheric carbon dioxide concentrations during the Cretaceous. *Earth and Planetary Science Letters*, *327*, 23–28. https://doi.org/10.1016/j.epsl.2012.01.014

Hull, P. M., Bornemann, A., Penman, D. E., Henehan, M. J., Norris, R. D., Wilson, P. A., et al. (2020). On impact and volcanism across the Cretaceous-Paleogene boundary. *Science*, *367*(6475), 266–272. https://doi.org/10.1126/science.aay5055

Jackson, G. A., & Lochmann, S. E. (1992). Effect of coagulation on nutrient and light limitation of an algal bloom. *Limnology & Oceanography*, *37*(1), 77–89. https://doi.org/10.4319/lo.1992.37.1.0077

Kaiho, K., Kajiwara, Y., Tazaki, K., Ueshima, M., Takeda, N., Kawahata, H., et al. (1999). Oceanic primary productivity and dissolved oxygen levels at the Cretaceous/Tertiary Boundary: Their decrease, subsequent warming, and recovery. *Paleoceanography*, *14*(4), 511–524. https://doi.org/10.1029/1999PA900022

Kettrup, B., Deutsch, A., Ostermann, M., & Agrinier, P. (2000). Chicxulub impactites: Geochemical clues to the precursor rocks. *Paleoceanography*, *35*, 1229–1238. https://doi.org/10.1111/j.1945-5100.2000.tb01511.x

Key, R. M., Kozyr, A., Sabine, C. L., Lee, K., Wanninkhof, R., Bullister, J. L., et al. (2004). A global ocean carbon climatology: Results from Global Data Analysis Project (GLODAP). *Global Biogeochemical Cycles*, *18*(4), GB4031. https://doi.org/10.1029/2004GB002247

Kiessling, W., & Baron-Szabo, R. (2004). Extinction and recovery patterns of scleractinian corals at the Cretaceous-Tertiary boundary. *Palaeogeography, Palaeoclimatology, Palaeoecology*, *214*(3), 195–223. https://doi.org/10.1016/j.palaeo.2004.05.025

Kiessling, W., & Simpson, C. (2011). On the potential for ocean acidification to be a general cause of ancient reef crises. *Global Change Biology*, *17*(1), 56–67. https://doi.org/10.1111/j.1365-2486.2010.02204.x

Kopp, G., & Lean, J. L. (2011). A new, lower value of total solar irradiance: Evidence and climate significance. *Geophysical Research Letters*, *38*(1), L01706. https://doi.org/10.1029/2010GL045777

Kring, D. A. (2007). The Chicxulub impact event and its environmental consequences at the Cretaceous-Tertiary boundary. *Palaeogeography, Palaeoclimatology, Palaeoecology*, *255*(1–2), 4–21. https://doi.org/10.1016/j.palaeo.2007.02.037

Kyte, F. T. (1998). A meteorite from the Cretaceous/Tertiary boundary. *Nature*, *396*, 237–239. https://doi.org/10.1038/24322

Lowery, C. M., Bown, P. R., Fraass, A. J., & Hull, P. M. (2020). Ecological response of plankton to environmental change: Thresholds for extinction. *Annual Review of Earth and Planetary Sciences*, *48*(1), 403–429. https://doi.org/10.1146/annurev-earth-081619-052818

Maier-Reimer, E. (1993). Geochemical cycles in an ocean general circulation model. Preindustrial tracer distributions. *Global Biogeochemical Cycles*, *7*, 645–677. https://doi.org/10.1029/93GB01355

Malone, T., Azzaro, M., Bode, A., Brown, E., Calumpong, H., Duce, R., & Wang, J. (2017). Primary production, cycling of nutrients, surface layer and plankton. In United Nations (Ed.), *The first global integrated marine Assessment, World ocean Assessment I* (pp. 119–148). Cambridge University Press. https://doi.org/10.1017/9781108186148

Montoya, M., Griesel, A., Levermann, A., Mignot, J., Hofmann, M., Ganopolski, A., & Rahmstorf, S. (2005). The Earth system model of intermediate complexity CLIMBER-3α. Part I: Description and performance for present-day conditions. *Climate Dynamics*, *25*(2–3), 237–263. https://doi.org/10.1007/s00382-005-0044-1

Nordt, L., Atchley, S., & Dworkin, S. (2002). Paleosol barometer indicates extreme fluctuations in atmospheric CO_2 across the Cretaceous-Tertiary boundary. *Geology*, *30*(8), 703–706. https://doi.org/10.1130/0091-7613(2002)030<0703:PBIEFI>2.0.CO;2

Nordt, L., Atchley, S., & Dworkin, S. (2003). Terrestrial evidence for two greenhouse events in the latest Cretaceous. *GSA Today*, *13*, 4–9. https://doi.org/10.1130/1052-5173(2003)013<4:teftge>2.0.co;2

Ohno, S., Kadono, T., Kurosawa, K., Hamura, T., Sakaiya, T., Shigemori, K., et al. (2014). Production of sulphate-rich vapor during the Chicxulub impact and implications for ocean acidification. *Nature Geoscience*, *7*, 279–282. https://doi.org/10.1038/ngeo2095

Osborne, C. P., & Sack, L. (2012). Evolution of C_4 plants: A new hypothesis for an interaction of CO_2 and water relations mediated by plant hydraulics. *Philosophical Transactions of the Royal Society B*, *367*(1588), 583–600. https://doi.org/10.1098/rstb.2011.0261

Pacanowski, R. C., & Griffies, S. M. (1999). *The MOM-3 manual* (Tech. Rep. No. 4). Princeton, NJ: GFDL Ocean Group, NOAA/Geophysical Fluid Dynamics Laboratory.

Petoukhov, V., Ganopolski, A., Brovkin, V., Claussen, M., Eliseev, A., Kubatzki, C., & Rahmstorf, S. (2000). CLIMBER-2: A climate system model of intermediate complexity. Part I: Model description and performance for present climate. *Climate Dynamics*, *16*(1), 1–17. https://doi.org/10.1007/PL00007919

Pierazzo, E., Hahmann, A. N., & Sloan, C. (2003). Chicxulub and climate: Radiative perturbations of impact-produced S-bearing gases. *Astrobiology*, *3*(1), 99–118. https://doi.org/10.1089/153110703321632453

Geophysical Research Letters 10.1029/2020GL092260

Pierazzo, E., Kring, D. A., & Melosh, H. J. (1998). Hydrocode simulation of the Chicxulub impact event and the production of climatically active gases. *Journal of Geophysical Research*, *103*(E12), 28607–28625. https://doi.org/10.1029/98JE02496

Pope, K. O. (2002). Impact dust not the cause of the Cretaceous-Tertiary mass extinction. *Geology*, *30*(2), 99–102. https://doi.org/10.1130/0091-7613(2002)030<0099:idntco>2.0.co;2

Renne, P. R., Deino, A. L., Hilgen, F. J., Kuiper, K. F., Mark, D. F., Mitchell, W. S., et al. (2013). Time Scales of critical events Around the Cretaceous-Paleogene boundary. *Science*, *339*, 684–687. https://doi.org/10.1126/science.1230492

Ries, J. B., Cohen, A. L., & McCorkle, D. C. (2009). Marine calcifiers exhibit mixed responses to CO_2-induced ocean acidification. *Geology*, *12*(12), 1131–1134. https://doi.org/10.1130/G30210A.1

Robertson, D. S., Lewis, W. M., Sheehan, P. M., & Toon, O. B. (2013). K-Pg extinction: Reevaluation of the heat-fire hypothesis. *Journal of Geophysical Research: Biogeosciences*, *118*(1), 329–336. https://doi.org/10.1002/jgrg.20018

Royer, D. L. (2006). CO_2-forced climate thresholds during the Phanerozoic. *Geochimica et Cosmochimica Acta*, *70*(23), 5665–5675. https://doi.org/10.1016/j.gca.2005.11.031

Royer, D. L., Pagani, M., & Beerling, D. J. (2012). Geobiological constraints on Earth system sensitivity to CO_2 during the Cretaceous and Cenozoic. *Geobiology*, *10*(4), 298–310. https://doi.org/10.1111/j.1472-4669.2012.00320.x

Schmieder, M., & Kring, D. A. (2020). Earth's impact events through geologic time: A list of recommended ages for terrestrial impact structures and deposits. *Astrobiology*, *20*(1), 91–141. https://doi.org/10.1089/ast.2019.2085

Schoene, B., Eddy, M. P., Samperton, K. M., Keller, C. B., Keller, G., Adatte, T., & Khadri, S. F. R. (2019). U-Pb constraints on pulsed eruption of the Deccan Traps across the end-Cretaceous mass extinction. *Science*, *363*(6429), 862–866. https://doi.org/10.1126/science.aau2422

Schulte, P., Alegret, L., Arenillas, I., Arz, J. A., Barton, P. J., Bown, P. R., et al. (2010). The Chicxulub asteroid impact and mass extinction at the Cretaceous-Paleogene boundary. *Science*, *327*(5970), 1214–1218. https://doi.org/10.1126/science.1177265

Sepúlveda, J., Alegret, L., Thomas, E., Haddad, E., Cao, C., & Summons, R. E. (2019). Stable isotope constraints on marine productivity across the Cretaceous-Paleogene mass extinction. *Paleoceanography and Paleoclimatology*, *34*(7), 1195–1217. https://doi.org/10.1029/2018PA003442

Sepúlveda, J., Wendler, J. E., Summons, R. E., & Hinrichs, K.-U. (2009). Rapid resurgence of marine productivity after the Cretaceous-Paleogene mass extinction. *Science*, *326*(5949), 129–132. https://doi.org/10.1126/science.1176233

Sewall, J. O., van de Wal, R. S. W., van der Zwan, K., van Oosterhout, C., Dijkstra, H. A., & Scotese, C. R. (2007). Climate model boundary conditions for four Cretaceous time slices. *Climate of the Past*, *3*(4), 647–657. https://doi.org/10.5194/cp-3-647-2007

Shigesada, N., & Okubo, A. (1981). Analysis of the self-shading effect on algal vertical distribution in natural waters. *Journal of Mathematical Biology*, *12*(3), 311–326. https://doi.org/10.1007/BF00276919

Six, K., & Maier-Reimer, E. (1996). Effects of plankton dynamics on seasonal carbon fluxes in an ocean general circulation model. *Global Biogeochemical Cycles*, *10*, 559–583. https://doi.org/10.1029/96GB02561

Sprain, C. J., Renne, P. R., Vanderkluysen, L., Pande, K., Self, S., & Mittal, T. (2019). The eruptive tempo of Deccan volcanism in relation to the Cretaceous-Paleogene boundary. *Science*, *363*(6429), 866–870. https://doi.org/10.1126/science.aav1446

Tabor, C. R., Bardeen, C. G., Otto-Bliesner, B. L., Garcia, R. R., & Toon, O. B. (2020). Causes and climatic consequences of the impact winter at the Cretaceous-Paleogene boundary. *Geophysical Research Letters*, *47*(3), e60121. https://doi.org/10.1029/2019GL085572

Tyrrell, T., Merico, A., & Mckay, D. I. A. (2015). Severity of ocean acidification following the end Cretaceous asteroid impact. *Proceedings of the National Academy of Sciences of the United States of America*, *112*(21), 6556–6561. https://doi.org/10.1073/pnas.1418604112

Vellekoop, J., Esmeray-Senlet, S., Miller, K. G., Browning, J. V., Sluijs, A., van de Schootbrugge, B., et al. (2016). Evidence for Cretaceous–Paleogene boundary bolide "impact winter" conditions from New Jersey, USA. *Geology*, *44*(8), 619–622. https://doi.org/10.1130/G37961.1

Vellekoop, J., Sluijs, A., Smit, J., Schouten, S., Weijers, J. W. H., Sinninghe Damsté, J. S., & Brinkhuis, H. (2014). Rapid short-term cooling following the Chicxulub impact at the Cretaceous–Paleogene boundary. *Proceedings of the National Academy of Sciences of the United States of America*, *111*(21), 7537–7541. https://doi.org/10.1073/pnas.1319253111

Vellekoop, J., Woelders, L., Açikalin, S., Smit, J., van de Schootbrugge, B., Yilmaz, I. O., et al. (2017). Ecological response to collapse of the biological pump following the mass extinction at the Cretaceous–Paleogene boundary. *Biogeosciences*, *14*(4), 885–900. https://doi.org/10.5194/bg-14-885-2017

Vellekoop, J., Woelders, L., van Helmond, N. A., Galeotti, S., Smit, J., Slomp, C. P., et al. (2018). Shelf hypoxia in response to global warming after the Cretaceous-Paleogene boundary impact. *Geology*, *46*(8), 683–686. https://doi.org/10.1130/G45000.1

Zachos, J. C., Arthur, M. A., & Dean, W. E. (1989). Geochemical evidence for suppression of pelagic marine productivity at the Cretaceous/Tertiary boundary. *Nature*, *337*(6202), 61–64. https://doi.org/10.1038/337061a0

Ziveri, P., Stoll, H., Probert, I., Klaas, C., Geisen, M., Ganssen, G., & Young, J. (2003). Stable isotope 'vital effects' in coccolith calcite. *Earth and Planetary Science Letters*, *210*(1), 137–149. https://doi.org/10.1016/S0012-821X(03)00101-8

3

Discussion and Conclusions

Exploring the causal links between past changes in climate and mass extinctions reveals key-concepts of how the Earth system responds to extreme perturbations. Not least this is relevant to better assess the far-reaching consequences of present and future climate and biodiversity change. As shown in this thesis, climate modeling is an excellent tool for this purpose. This chapter explores the answers given in the articles to the guiding questions formulated in Section 1.4 and discusses links between the articles. In addition, next steps for the investigation of the Devonian and Late Cretaceous mass extinctions are proposed. To conclude, the results are placed in a larger context and lessons are drawn for today's sixth extinction.

The systematic study of the sensitivity of the Devonian climate using CLIMBER-3α (Brugger *et al.*, 2019) shows a minor influence of continental configuration, vegetation cover, orbital configuration and insolation on climate. Changes in these parameters cannot explain the variations observed in the sea surface temperature reconstruction for the Devonian based on proxy data (Joachimski *et al.*, 2009). This contrasts with the results of two other modeling studies: First, Le Hir *et al.* (2011) find a temperature increase of $\approx 4\,°C$ due to decreased surface albedo during the spread of land plants in the Devonian which is large enough to counteract the temperature decrease associated with the accompanying increased silicate weathering. By contrast, the changes in biogeophysical parameters in our simulations lead to a temperature increase of only $0.1\,°C$ comparing the Early and the Late Devonian. We find that one reason for this difference is the lower albedo value for bare soil used in our simulations compared to Le Hir *et al.* (2011) which represents, however, better the early existence of microbial mats on rocks (Sanromá *et al.*, 2013). Second, the modeling results of De Vleeschouwer *et al.* (2014) show a significant influence of orbital parameters on climate in the Late Devonian which are supported by results from cyclostratigraphic analysis of the stratigraphic record of the Late Devonian (De Vleeschouwer *et al.*, 2017). Although our median orbit simulations show temperature patterns comparable with the ones presented in

De Vleeschouwer *et al.* (2014), we find only a small influence of obliquity and eccentricity on temperature. We attribute this discrepancy to differences in the representation of ocean dynamics and their interplay with sea-ice formation and dynamics in the two models. In summary, our study on the sensitivity of the Devonian climate to various parameters suggests that changes in the atmospheric CO_2 concentration, likely caused by the evolution of land plants, were the dominant driver of changes in climate during the Devonian. However, based on proxy evaluation substantiated with model results, the second study on the Devonian (Dahl *et al.*, submitted) shows evidence that atmospheric CO_2 concentrations were significantly lower than in earlier CO_2 reconstructions for the Early Devonian (e.g., Foster *et al.*, 2017, Royer, 2006) and stayed almost constant during the Devonian. We suggest that the appearance of early vascular plants induced a significant drop in atmospheric CO_2 due to increased weathering already from ≈ 440 Ma to ≈ 410 Ma. Conversely, plants with deeper root systems during the emergence of forests in the Devonian have weathered less as the deeper roots recycle nutrients more efficiently. In combination with our result in Brugger *et al.* (2019), which shows that the influence of biogeophysical plant parameters on temperature is small, this argues against the link between land plant evolution during the Devonian, temperature changes, and oceanic extinction events, as suggested in Algeo *et al.* (1995), Algeo & Scheckler (1998), Dahl & Arens (2020). In summary, our two studies on the Devonian do not support the two most thoroughly investigated hypotheses to date, which are that either land plant evolution (Algeo *et al.*, 1995, Algeo & Scheckler, 1998, Le Hir *et al.*, 2011) or a special combination of orbital parameters (De Vleeschouwer *et al.*, 2013, 2014, 2017) triggered the biodiversity changes during the Devonian.

Our two studies also show and discuss the difficulties and uncertainties that arise when studying the Devonian: Proxies used for previous Devonian CO_2 reconstructions have been inadequately calibrated and verified (Dahl *et al.*, submitted). Carbon isotope fractionation, which is used in Dahl *et al.* (submitted), has been shown to be a robust method to reconstruct atmospheric CO_2 concentrations for the deglaciation after the Last Glacial Maximum (Schubert & Jahren, 2015) and is therefore suggested to use for the reconstruction of deep-time CO_2 concentrations as well (Dahl *et al.*, submitted). Still, the inclusion of water use efficiency and the precise assignment of time to plant fossils is subject to uncertainty (see Supplementary Information to Dahl *et al.*, submitted). Temperature proxies also contain a variety of uncertainties: Reconstructing temperature from $\delta^{18}O$ is based on a calibration standard (Lécuyer *et al.*, 2003, Vennemann *et al.*, 2002) and an equation to convert $\delta^{18}O$ values to paleotemperature (Lécuyer *et al.*, 2013) which are not consistent among studies for the Devonian (Joachimski *et al.*, 2009, Henkes *et al.*, 2018, Brugger *et al.*, 2019). In addition, the very high Devonian temperatures reconstructed for the Devonian might indicate that the oxygen isotope composition of seawater differed from the composition of the present ocean (Jaffrés *et al.*, 2007, van Geldern *et al.*, 2006).

A further aspect to consider is that a large part of the $\delta^{18}O$ proxies used for comparison with our model data (Joachimski *et al.*, 2009) might not represent global values but rather local signals strongly influenced by narrow bays and passages in the early phase of the Paleotethys' formation. This would make it difficult to combine $\delta^{18}O$ values from different locations for different times in one record, as it was done in Brugger *et al.* (2019).

From the modeling perspective, the challenge lies in modeling the complex interactions of the terrestrial and marine carbon cycle for the Devonian which would be necessary to get a more complete picture of the role of land plant evolution on climate and biodiversity. Detailed knowledge about the weathering process, its feedback mechanism and its precise mathematical formulation is still debated (Caves *et al.*, 2016, Penman *et al.*, 2020, Ibarra *et al.*, 2019, D'Antonio *et al.*, 2019, Oeser & von Blanckenburg, 2020). Conceptual carbon cycle models provide great tools to test the influence of certain parameters on weathering and the carbon cycle in general, as is done in Dahl *et al.* (submitted) using the COPSE model (Carbon-Oxygen-Phosphorous-Sulfur-Evolution), a model of biogeochemical cycling over the Phanerozoic (Bergman *et al.*, 2004, Lenton *et al.*, 2018). Several other studies also investigated the Devonian carbon cycle with carbon cycle models of different complexity (e.g., Berner & Kothavala, 2001, Simon *et al.*, 2007). The long time scale of several thousand years on which weathering works hampers the direct implementation of weathering processes in more complex coupled climate models. Thus, a useful way forward would be to use the results of detailed studies with carbon cycle models of varying complexity of how land plants affect weathering as input into coupled climate models.

In contrast to the very broad investigation of the Devonian, the studies of the end-Cretaceous mass extinction (Brugger *et al.*, 2017, 2021) build on the much more detailed knowledge of this extinction (e.g. Alvarez *et al.*, 1980, Pope, 2002, Pierazzo *et al.*, 1998, Pierazzo *et al.*, 2003, Artemieva & Morgan, 2009, Artemieva *et al.*, 2017). This extinction enjoys great popularity due to its spectacular impact scenario and the extinction of the dinosaurs. The goal of our studies was to better understand the climatic effects of the Chicxulub impact on a timescale of years to thousand years post-impact, which are difficult to resolve with proxy data, in order to assess the role the impact played in the extinction.

A key result of our two climate modeling studies is that the strong dimming of solar irradiation induced by stratospheric sulfate aerosols formed during the Chicxulub impact has a variety of far-reaching consequences for both terrestrial and marine climate and life: In Brugger *et al.* (2017) we show a drastic global cooling as a result of the reduced solar irradiation. The sudden drop of sea surface temperatures causes vigorous deep water formation and ocean mixing. Hence, nutrients are transported from the deep ocean to the ocean surface and this nutrient transport results in a strong and short increase

of marine net primary productivity (NPP) after a period of zero NPP related to the darkness after the impact. The NPP increase enhances the ocean's carbon consumption, therefore prolongs the recovery of temperatures and decreases the warming effect of carbon originating from the impact (Brugger *et al.*, 2021). The described perturbations of the ocean are indirectly triggered by sulfate aerosols via the cooling of the surface ocean. In addition, the direct consequences of adding sulfur to the ocean is explored in Brugger *et al.* (2021). The results suggest that the extinction of a large fraction of marine calcifying organisms, as globally observed in the fossil record, can only be explained for the high latitudes by ocean acidification. Summarized, the formation of sulfate aerosols as a result of the Chicxulub impact causes drastic global cooling, influences ocean productivity, but is likely not responsible for pronounced ocean acidification.
Another important result of Brugger *et al.* (2021) is linked to the initial idea suggested by Alvarez *et al.* (1980) regarding the importance of the impact dust for the end-Cretaceous mass extinction: Based on several earlier studies (Pope *et al.*, 1997, Pope, 2002, Pierazzo *et al.*, 2003) we presumed that the atmospheric effect of impact dust is irrelevant for decreasing the incoming solar radiation compared to the effect of stratospheric sulfate aerosols. However, we showed that the impact dust is highly relevant for the marine biosphere: The high percentage of iron contained in the Chicxulub projectile enhances the NPP increase to almost seven times of pre-impact levels and significantly prolongs the recovery to 400 years. The algal bloom caused by the combination of ocean mixing and additional nutrient input from the impact dust likely led to toxic conditions in the surface ocean, with severe consequences for marine near-surface ecosystems.

The comparisons with proxy data confirm in both Brugger *et al.* (2017) and Brugger *et al.* (2021) the general trends in temperature and are helpful in determining the most realistic case of sensitivity experiment. However, a closer comparison is hampered by the lack of proxies representing the time in the immediate aftermath of the impact (i.e., less than 500 years after the impact) accurately and at sufficiently high resolution. Although new techniques revealing proxy information with higher temporal resolution have been developed (e.g., Vellekoop *et al.*, 2014, Vellekoop *et al.*, 2016), the room for improvement, and therefore the available information from proxy data, is inherently limited. Hence, only models can provide information about the immediate post-impact processes. A further obstacle in the model-proxy comparison is the coarse spatial resolution of our model which makes a comparison with localized proxies difficult.
A long discussed question in the investigation of the Chicxulub impact is whether the infrared radiation radiated by the reentering ejecta triggered global wildfires (e.g., Wolbach *et al.*, 1988, Toon *et al.*, 1997, Kring, 2007, Gulick *et al.*, 2019 and Section 1.2.5). In this case the additional amounts of terrestrial carbon identified in Brugger *et al.* (2021) to match model and proxy results could at least partly be the result of the fires. Bardeen *et al.* (2017) and Tabor *et al.* (2020) use a climate model including

atmospheric chemistry to explore the effect of a global soot injection as a consequence of the Chicxulub impact. They find a global surface cooling which is comparable to the cooling simulated in our model experiments, both considering the amount of temperature reduction as well as the effective timescale. However, the surface solar flux is reduced to less than 1% of the pre-impact level. Although this is stronger than the reduction caused by sulfate aerosols and lies below the limit for photosynthesis, we do not expect a striking difference in the response of the biosphere as the temperature reduction caused by sulfate aerosols is already a limiting factor for photosynthesis. Still, further insight could be obtained by simulations with an atmospheric chemistry model which combine the effect of sulfur, soot and dust and explore their interaction.

In Brugger *et al.* (2017) we investigated the climatic effects of the Chicxulub impact and derived first assumptions for the consequences for life. By adding a biogeochemical ocean model in Brugger *et al.* (2021) we were able to directly simulate the effects for the marine biosphere. Simulations using a terrestrial vegetation model would complete the picture. To do so present-day plant functional types in the standard vegetation models would need to be adjusted to the Cretaceous flora. The scarce knowledge of Cretaceous plants makes this a challenging task. A simplified method reducing the considered characteristics of the plant functional types to a basic level could be a possible approach. To better understand the dynamics of the mass extinction ecological niche modeling could give further information.

Recently, there has been considerable progress regarding the question of the contribution of impact versus volcanism to the mass extinction. Looking at the processes induced by the Chicxulub impact and simulated in our studies, we can state that the impact's consequences on a timescale of decades to millennia were likely sufficient to trigger a global extinction. A combination of proxy data and simulations with a simple model confirms this by showing evidence that only the impact, but not Deccan volcanism coincided with the mass extinction (Hull *et al.*, 2020). Hence, although Deccan volcanism seems to have led to additional perturbations which destabilized the Earth system before and after the impact (Schoene *et al.*, 2019, Sprain *et al.*, 2019), we conclude that the impact played the triggering role in the end-Cretaceous mass extinction.

Although comparison is difficult, we can derive some insights from studying past mass extinctions for the sixth mass extinction we face today. Already, on average, approximately 25% of species are currently threatened with extinction in assessed animal and plant groups (Díaz *et al.*, 2019a,b). Although we observe severe climate change already today, the present biodiversity loss is not yet the result of human-induced climate change, but mostly caused by overexploitation and land use change (Maxwell *et al.*, 2016, Leclère *et al.*, 2020). The contribution of climate change to the mass extinction is expected to increase significantly in the future (Urban, 2015). Human intervention in nature, composed of overexploitation, land-use change, pollution and climate change (Maxwell *et al.*, 2016) which are all taking place on very short timescales, is not comparable to any perturbation the Earth system has experienced so far (Williams *et al.*, 2015). Hence, comparison with past mass extinctions is only possible to a certain degree.

A comparable aspect of the end-Cretaceous mass extinction and the sixth extinction is the timescale on which the perturbations occur: although the speed of the current perturbation is not comparable to the extremely short timescales of perturbation immediately after the Chicxulub impact (Rae *et al.*, 2021), both perturbations were much faster than the intrinsic changes to which the different components of the Earth system can adapt.

Furthermore, in both the Devonian and the end-Cretaceous mass extinctions, the combined effect of multiple stressors likely contributed to weakening of the system. The combination of changes in land plant cover and orbital parameters would be an example for the Devonian extinctions. For the end-Cretaceous mass extinction the joint effect of the Deccan Traps eruptions and the Chicxulub impact was already discussed earlier. Also today we see multiple, but human-induced, stressors for the Earth system. A better understanding of the interaction of mutiple stressors and how life responds is of great importance (for example Gunderson *et al.* (2016) for the marine realm).

On a much more general level one can deduce from the four studies forming this thesis how sensitive the Earth system is to changes in the carbon cycle: The studies on the Devonian show that atmospheric CO_2 concentrations critically determine the climate state and are coupled to changes in the biosphere (Brugger *et al.*, 2019, Dahl *et al.*, submitted). In addition, our studies on the end-Cretaeous mass extinction show that the climate system recovers slowly from strong perturbations of the carbon cycle: the increase of atmospheric CO_2, but also the carbon cycle changes in the ocean induced by the increased productivity as well as the carbon added to the ocean, are effective on centennial to millennial timescales. Together, this indicates that carbon cycle perturbations play a critical role in mass extinctions, as also hypothesized by Rothman (2017): He suggests that mass extinctions take place if a marine carbon cycle perturbation either exceeds a critical rate (on long timescales) or a critical size (on short timescales). Based on past mass extinctions he calculates a critical carbon mass for the sixth mass extinction and finds that this will be surpassed in 2100 for all scenarios but the scenario RCP 2.6. Exploring future atmospheric CO_2 concentrations Tierney *et al.* (2020) find that atmospheric CO_2 concentrations will only recover on geological time scales for a RCP 4.5 and RCP 8.5 scenario. Thus, for humans and other life the current and future human-induced changes in the Earth system “will appear to be a permanent state shift” (Tierney *et al.*, 2020). In summary, the above comparisons show the far-reaching consequences of our decisions about future emissions, but also the responsibility of today’s societies for future generations.

The studies collected in this thesis contribute to a deeper understanding of past mass extinction events as examples of extreme perturbations of the Earth system. First and foremost, the results presented in this thesis expand the ideas and the knowledge about the two extinction events studied. In addition, however, the results also give an indication of the effect of human-induced climate change on the biosphere.

4

Appendix

Supplementary Information: On the Sensitivity of the Devonian Climate to Continental Configuration, Vegetation Cover, Orbital Configuration, CO_2 Concentration, and Insolation

Supplementary Information: Low atmospheric CO_2 levels before the emergence of forested ecosystems

Supplementary Information: A pronounced spike in ocean productivity triggered by the Chicxulub impact

Supporting Information for “On the sensitivity of the Devonian climate to continental configuration, vegetation cover, orbital configuration, CO_2 concentration and insolation”

Julia Brugger[1,2,3], Matthias Hofmann[1], Stefan Petri[1], and Georg Feulner[1]

[1]Potsdam-Institut für Klimafolgenforschung (PIK), Mitglied der Leibniz-Gemeinschaft, Postfach 60 12 03, 14412 Potsdam, Germany

[2]Universität Potsdam, Institut für Physik und Astronomie, Karl-Liebknecht-Straße 24/25, 14476 Potsdam, Germany

[3]Berlin-Brandenburgisches Institut für Biodiversitätsforschung, Altensteinstraße 34, 14195 Berlin, Germany

Contents of this file

1. Figures S1 to S7

Introduction

In the Supporting Information to our article, we present additional figures, in particular showing surface-air temperature difference maps illustrating the sensitivity to changes in continental configurations (Figure S1), in the value of the solar constant (Figure S3),

---

Corresponding author: Julia Brugger and Georg Feulner, brugger@pik-potsdam.de and feulner@pik-potsdam.de

in atmospheric carbon-dioxide levels (Figure S4) and to the choice of bare-land albedo (Figure S6). In addition, we have added figures for the ocean surface temperatures and velocities for different continental configurations (Figure S2), for the difference of cloud cover for different vegetation cover (Figure S5) and for evaporation–precipitation patterns (Figure S7).

References

De Vleeschouwer, D., Crucifix, M., Bounceur, N., & Claeys, P. (2014). The impact of astronomical forcing on the Late Devonian greenhouse climate. *Global Planet Change*, *120*, 65-80. doi: 10.1016/j.gloplacha.2014.06.002

Le Hir, G., Donnadieu, Y., Goddéris, Y., Meyer-Berthaud, B., Ramstein, G., & Blakey, R. C. (2011). The climate change caused by the land-plant invasion in the Devonian. *Earth Planet Sc Lett*, *310*, 203-212. doi: 10.1016/j.epsl.2011.08.042

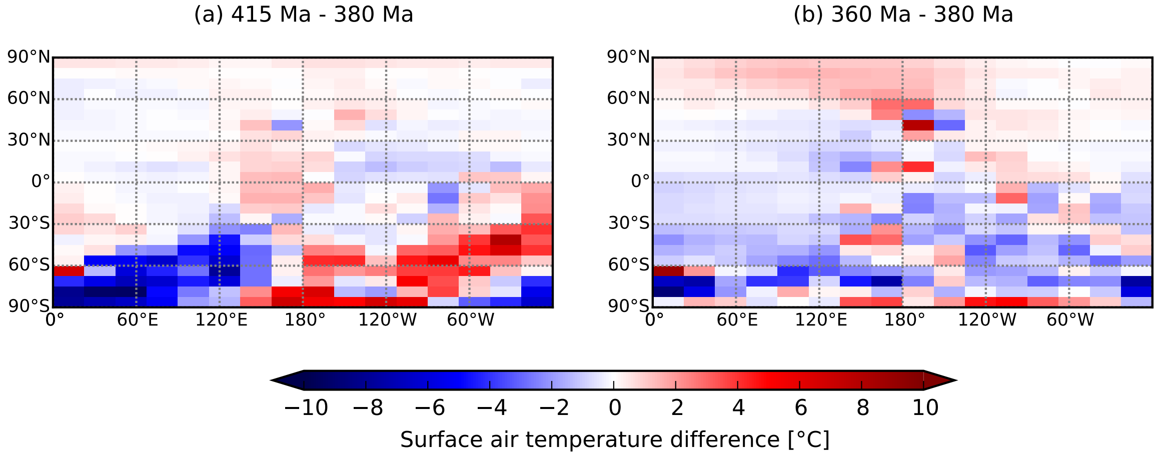

Figure S1. Surface air temperature differences between different Devonian continental configurations, showing the difference between (a) 415 Ma and 380 Ma and (b) 360 Ma and 380 Ma. As the differences between continental configurations are most pronounced at high southern latitudes, surface air temperature differences are largely concentrated in this region and determined by the different distribution of land and ocean areas. For all simulations the atmospheric CO_2 concentration is 1500 ppm, the solar constant is 1319 W/m^2, orbital configuration is a median orbit (obliquity $\varepsilon = 23.5°$, eccentricity $e = 0$) and land cover is set to bare land.

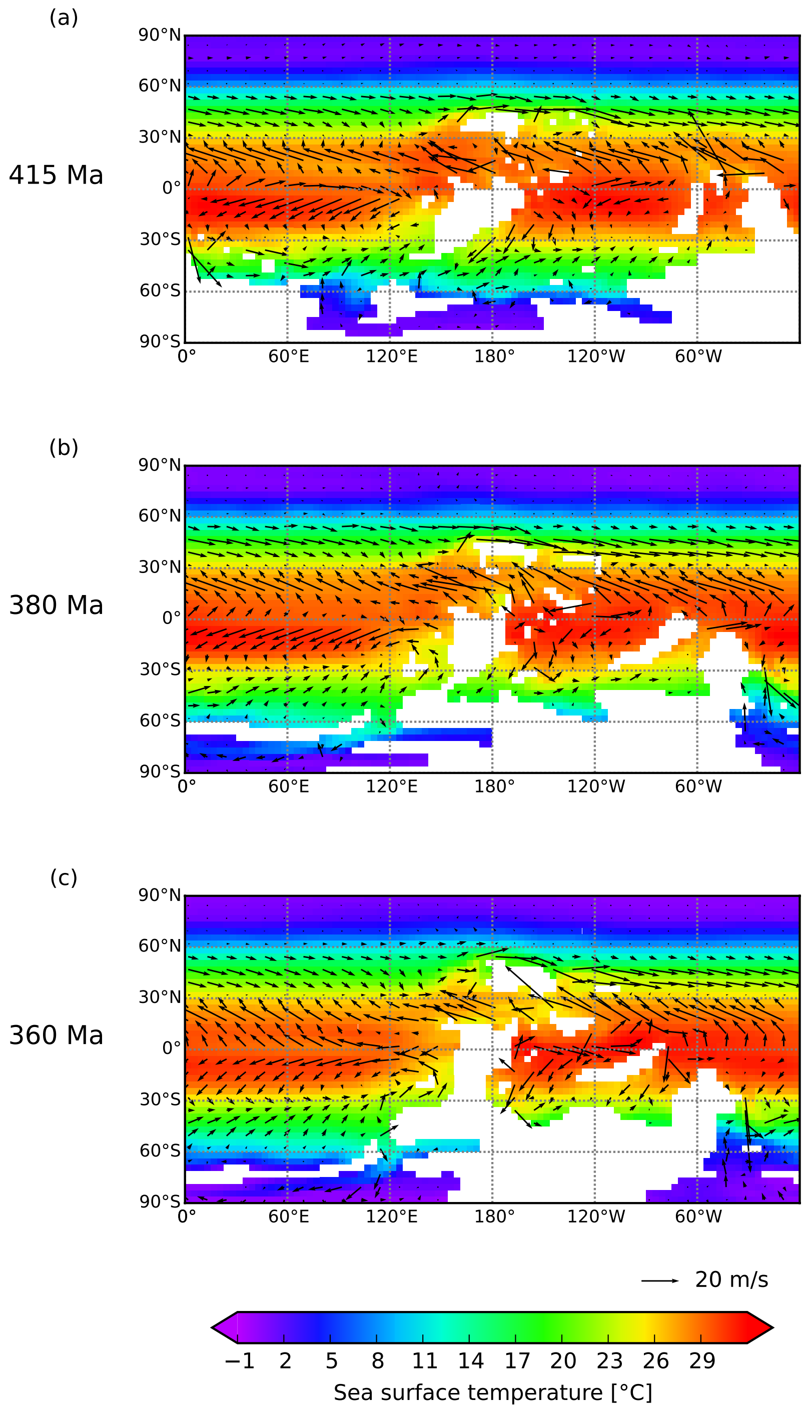

Figure S2. Sea surface temperature and ocean surface velocities for the three Devonian continental configurations. Ocean surface velocities are determined by the continental configuration and influence sea surface temperature distributions. For all simulations the atmospheric CO_2 concentration is 1500 ppm, the solar constant is 1319 W/m^2, orbital configuration is a median orbit and land cover is set to bare land.

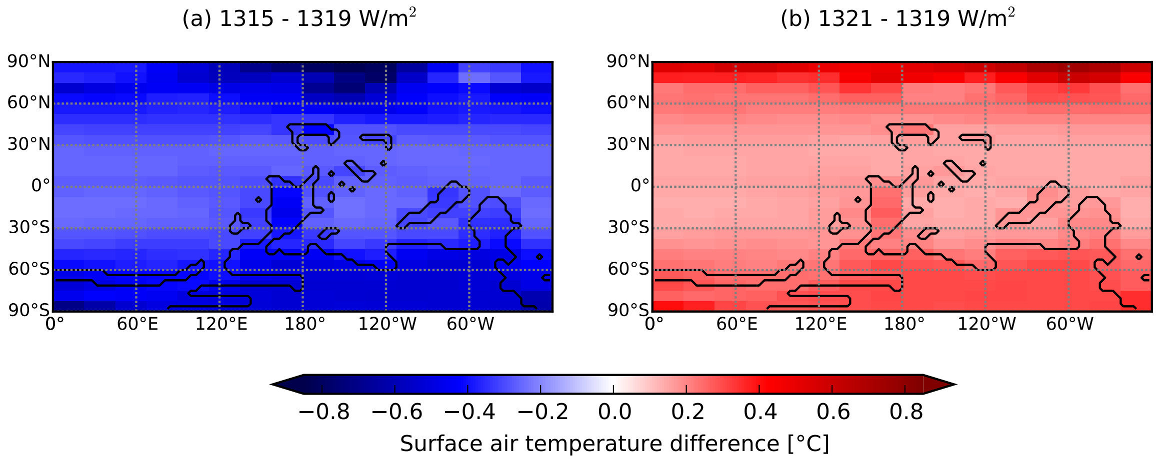

Figure S3. Surface air temperature differences for different values of the solar constant, showing the difference between (a) 1315 and 1319 W/m^2 and (b) 1321 and 1319 W/m^2. The effect of an increasing solar constant is largest at high northern latitudes which is linked to differences in sea ice. For all simulations the continental configuration for 380 Ma is chosen, atmospheric CO_2 concentration is 1500 ppm, orbital configuration is a median orbit and land cover is set to bare land.

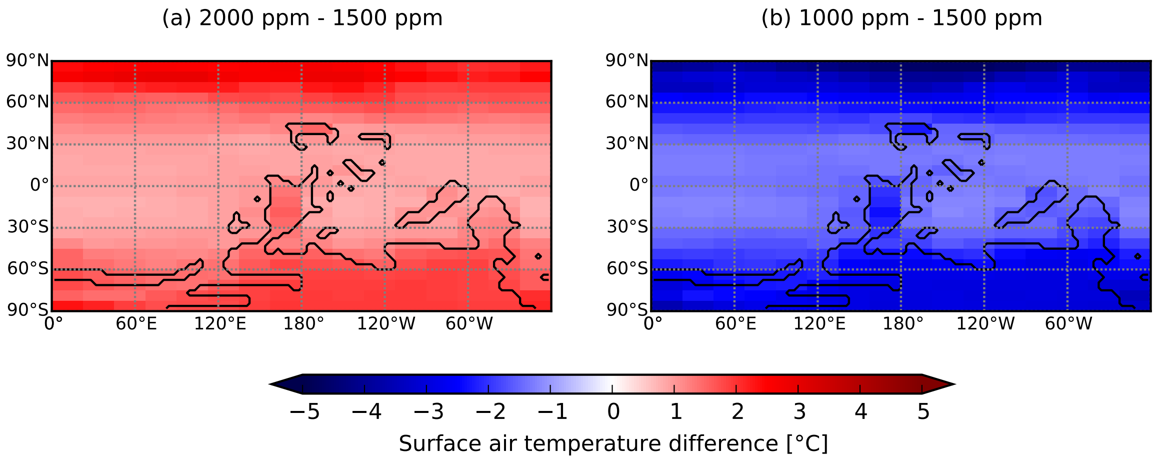

Figure S4. Surface air temperature differences for different CO_2 concentrations, showing the difference between (a) 2000 and 1500 ppm and (b) 1000 and 1500 ppm. The warming effect of a higher CO_2 concentration is largest at high latitudes, in particular in the Northern hemisphere. For all simulations the continental configuration for 380 Ma is chosen, the solar constant is 1319 W/m^2, orbital configuration is a median orbit and land cover is set to bare land.

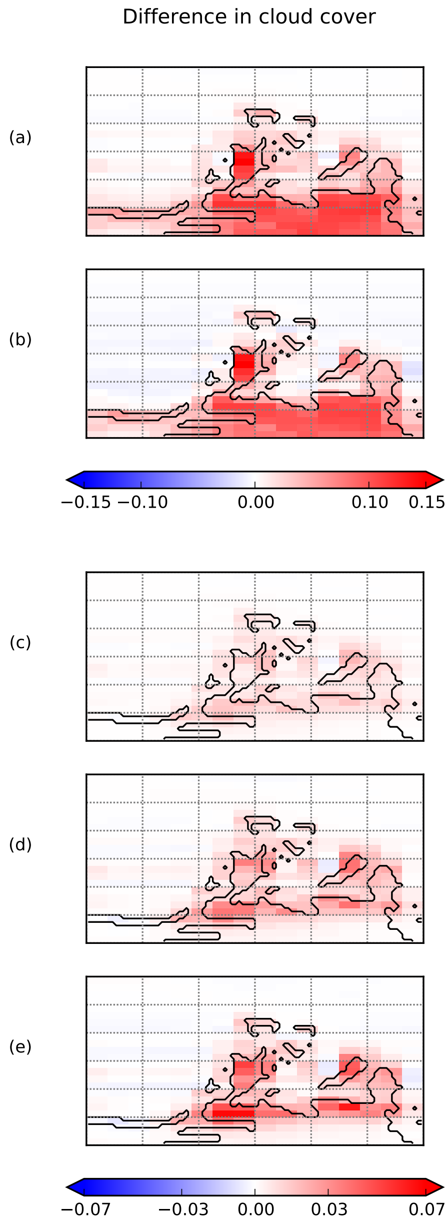

Figure S5. Differences in fraction of total cloud cover for different vegetation cover, showing the difference between (a) shrub cover and bare land, (b) tree cover and bare land, (c) Early Devonian vegetation cover and bare land, (d) Middle Devonian vegetation cover and bare land, and (e) Late Devonian vegetation cover and bare land. Increased vegetation leads to increased total cloud cover and is mostly confined over continents. The patterns are similar to the evaporation difference patterns in Fig. 4. For all simulations the continental configuration for 380 Ma is chosen, the solar constant is 1319 W/m^2, atmospheric CO_2 concentration is 1500 ppm and orbital configuration is a median orbit.

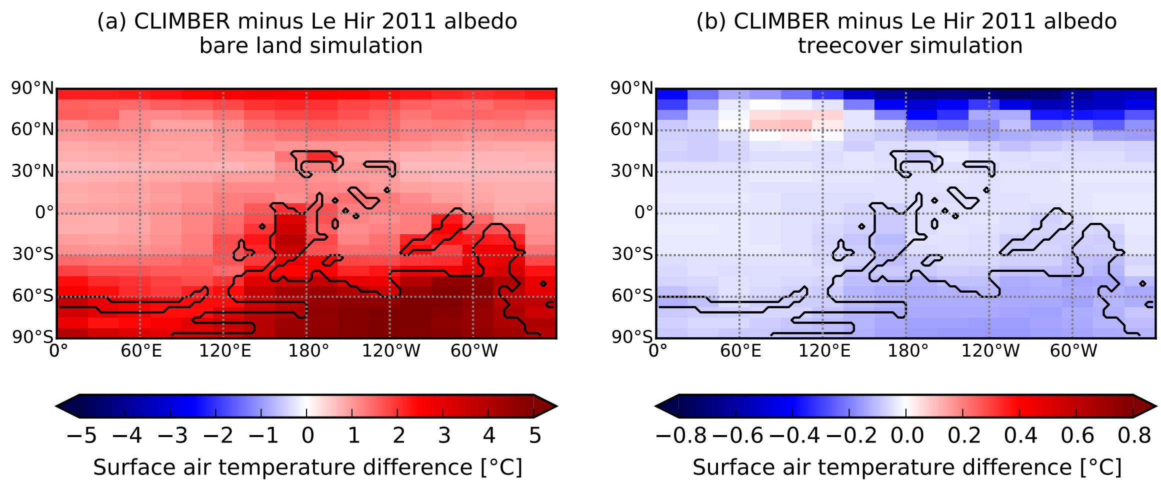

Figure S6. Surface air temperature differences for different albedo values. (a) Difference between a simulation without vegetation cover using the CLIMBER bare land albedo minus a simulation with the higher bare land albedo of Le Hir et al. (2011). The higher albedo of the Le Hir et al. (2011) simulations translates into a significant surface air temperature decrease, largely located over the continents. In panel (b) the surface air temperature difference between simulations with land covered by trees using the CLIMBER tree albedo minus one with the tree albedo of Le Hir et al. (2011) is shown. As the tree albedo differs only marginally, the temperature differences are small. The colder temperatures of the CLIMBER simulations come along with a slightly smaller sea-ice fraction in the high northern latitudes which is accompanied by a stronger temperature difference in this region. For all simulations the continental configuration for 380 Ma is chosen, atmospheric CO_2 concentration is set to 1500 ppm, the solar constant is 1319 W/m^2 and orbital configuration is a median orbit.

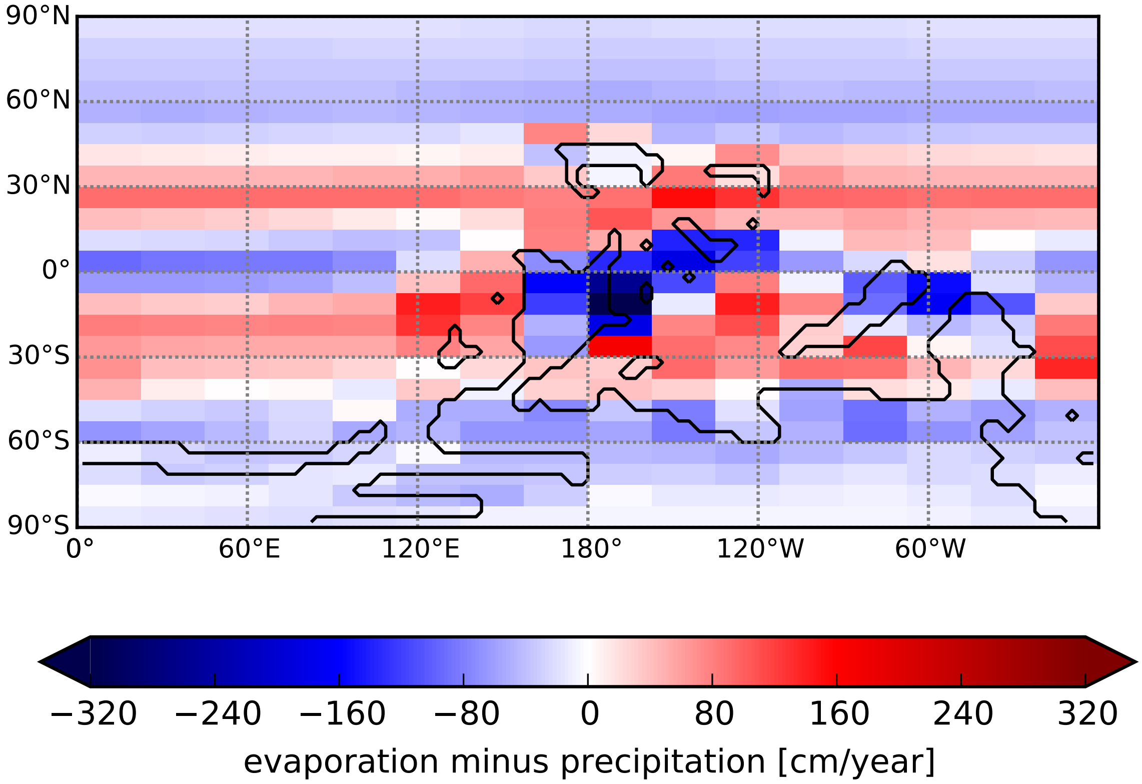

Figure S7. Evaporation minus precipitation for a simulation with the continental configuration for 380 Ma, an atmospheric CO_2 concentration of 1500 ppm, a solar constant of 1319 W/m^2, a median orbit for the orbital configuration and bare land. The patterns of the difference compare well with the model results and the lithic indicators of paleoclimate shown in De Vleeschouwer et al. (2014), Fig. 15. The smaller amplitude found in our simulation can mostly be attributed to the coarser spatial resolution of our model.

Supplementary Materials to

Low atmospheric CO_2 levels before the emergence of forested ecosystems

Dahl TW[1], Harding MAR[1], Brugger J[2,3,4], Feulner G[2], Norrman K[5], and Junium CK[6]

[1]GLOBE institute, University of Copenhagen, Øster Voldgade 5-7, DK-1350 Copenhagen K, Denmark

[2]Earth System Analysis, Potsdam Institute for Climate Impact Research, Member of the Leibniz Association, Potsdam, Germany

[3]Senckenberg Biodiversity and Climate Research Centre (SBiK-F), Frankfurt am Main, Germany

[4]Institute for Physics and Astronomy, University of Potsdam, Potsdam, Germany

[5]Center for Integrative Petroleum Research, King Fahd University of Petroleum and Minerals, Saudi Arabia

[6]Department of Earth and Environmental Sciences, Syracuse University, Syracuse New York, 13244, USA

Section S1. Geological setting and samples

S.1.1 Fossil locality and age

Macrofossils of the early land flora from the Yea district in central Victoria, Australia, occur both in Late Silurian sediments (Gorstian Ludlow; 427.4-425.6 Ma) and sediments of Early Devonian age (Early Pragian-Early Emsian; 410.8–407.6 Ma)[1,2,3]. Due to structural folding and scarcity of diagnostic age markers in the area, it has proven challenging to assign an age to fossils from localities where only one of the plant assemblages have been found. Nevertheless, we find that the *Baragwanathia* samples studied here comes from the younger assemblage.

Plant macrofossils from the fossil collection of Museums Victoria were investigated for the carbon isotope analyses of early terrestrial plants. The specimens were collected by Isabel Cookson at Mt Pleasant from a cutting in "the old road" 1.25 mi south of Alexandra towards Thornton (for maps, see Earp 2019). At this locality, she described several plant macrofossils including *Baragwanathia longifolia* (in #15154, #15173, #15174, #15183), *Hedeia corymbose (cf Yarravia)*, and *Zosterophyllum australianum*[4].The samples contain numerous small plant fragments in which many fossils preserve thick brown to black mineralization containing organic tissue well suited for organic characterization and carbon isotope analysis (described in more detail in S1.3).

In 1935, Isabel Cookson acknowledged that the age of the plant assemblage at Mt Pleasant was an unresolved stratigraphic problem. Since then, graptolite biostratigraphy has settled that the fossil assemblage from Mt Pleasant are Early Devonian in age and roughly coeval with the younger plant assemblages observed near Yea (~30 km to the west) and Matlock (~75 km to the southeast).

The wider Alexandra area is a broad northwest-southeast striking synclinorium with a large number of impersistent folds 10s to 100s meters apart and generally only traceable for kilometers. Closer to the sample location, the structure is that of an anticlinorium passing through the town of Alexandra. The Mt Pleasant Road cutting sits on the uniformly dipping western limb of the anticlinorium[3]. Figure S1 shows the stratigraphy across the anticlinorial folding where Mt Pleasant road cuts through thin bedded siltstone. Cookson described the plant remains from fine-grained sandstone beds, which have been identified at the P4 interval (Figure S1). At this level, the early land plant *Hedeia corymbose* is found together with early Devonian index fossils (*Uncinatograptus sp.* cf. *U. thomasi* and *Nowakia sp.* ex gr. *N. acuaria*). This confines the age of the Mt Pleasant land plant fossils to the Pragian or earliest Emsian, and we can assign an age of the studied samples of ~409.1 ±1.5 Ma according to GTS2020.

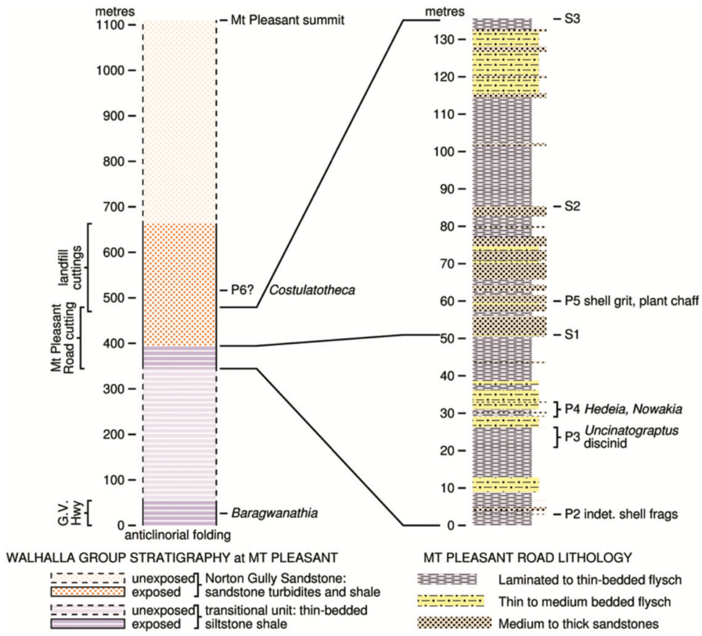

Figure S1. Stratigraphy and lithology of Mt Pleasant according to Earp 2019[3].

The exceptional preservation of the plant macrofossils has been interpreted as flysch deposition in a very-low-energy depositional environment with occasional bursts of high-energy turbidites carrying allochthonous fossils from shallower waters[3].At Mt Pleasant, the plant fragments are smaller than for example the Late Silurian plant assemblage from Limestone Rd near Yea. The taphonomy is consistent with abrupt transport from the place where the plants grew to the site where they were buried. Thus, we rule out a marine origin of the macroplant community, as considered for a related plant species, *Baragwanathia brevifolia*, in the Barrandian area, Czech Republic[5].

S1.2 Sample characterization

The plant fossils are preserved as incrustations in fine-grained sandstone, also recognized as thin to medium bedded flysch[3,4]. The plant itself is now covered in a brown mineral matrix with some organic matter preserved (see below, S1.3). The preservation of the brown material distinguishes the Mt Pleasant fossils from other fossils that we inspected from the Limestone Rd and Frenchman Spur localities that were impression fossils[4].Twenty-five fragments with terrestrial plant remains in four rock specimens were analyzed 41 times. All fossils of taxonomic value, including type- and holotypes, were avoided (Figure S2–S5).

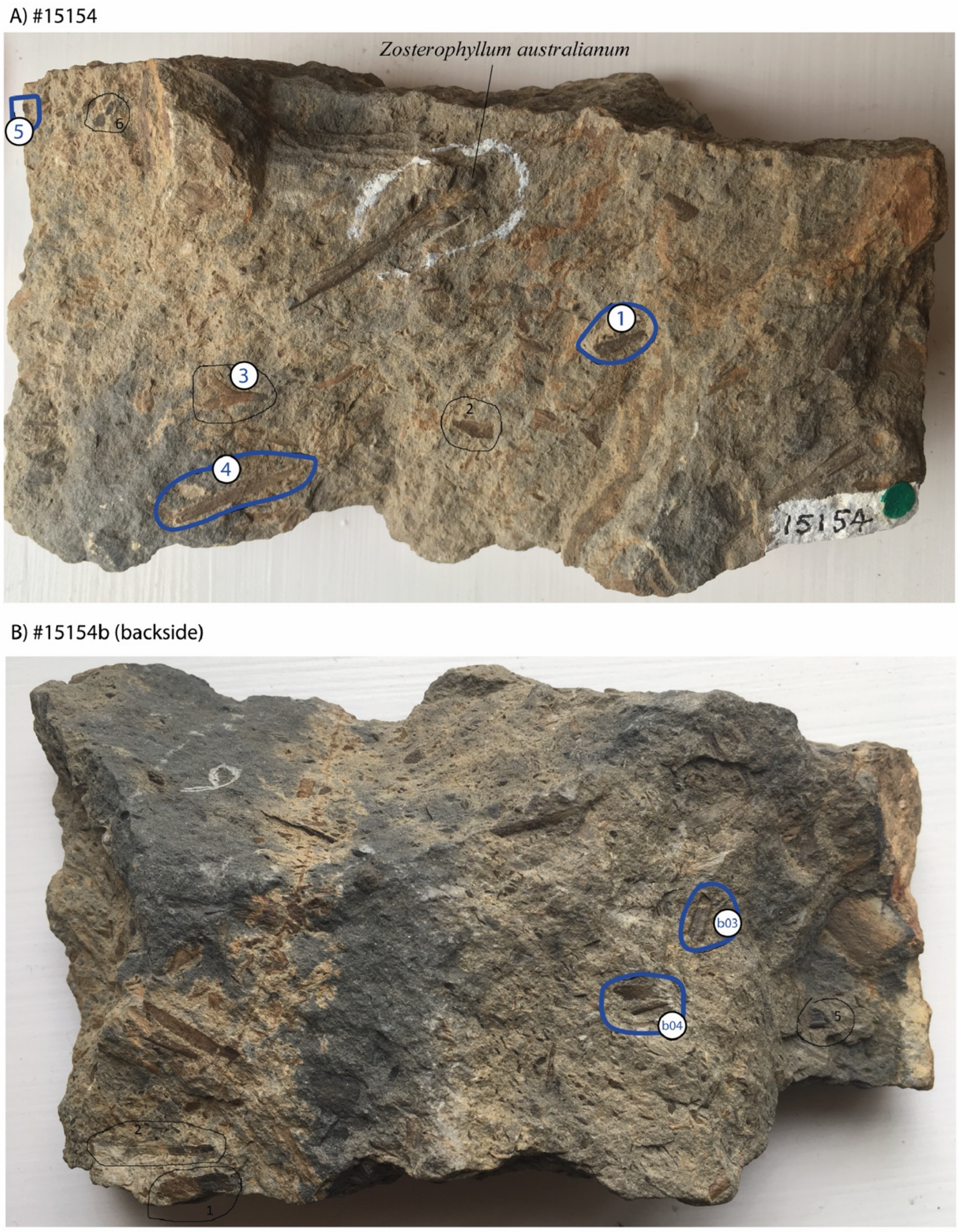

Figure S2. Sample #15154 and names of fragments studied.

A) #15173

Figure S3. Sample #15173 and names of fragments studied.

A) #15183

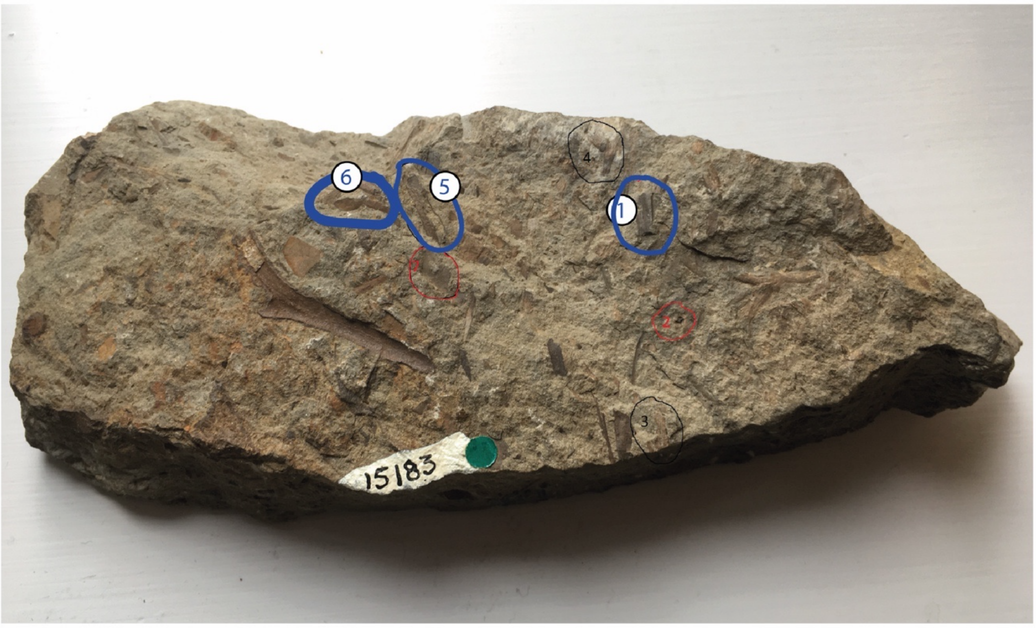

B) #15183b (backside)

Figure S4. Sample #15183 and names of fragments studied.

S1.3 Characterization of the fossilized plant tissue

S1.3.1 Carbon compounds

Time-of-Flight Secondary Ion Mass Spectrometry (TOF-SIMS) was used to produce semi-quantitative maps of elemental composition in one representative fossil fragment from sample #15153.

Figure S5 summarizes the main results, where calcium (Ca) intensity follows aluminum (Al), whereas carbon-nitrogen (CN^-) follows that of phosphorous (PO_3^-). These data provide clear evidence that carbon is present in the brown mineral matrix, and that C is mainly hosted in an organic phase dispersed over the surface of the fossil, and not in inorganic form; i.e. carbonates.

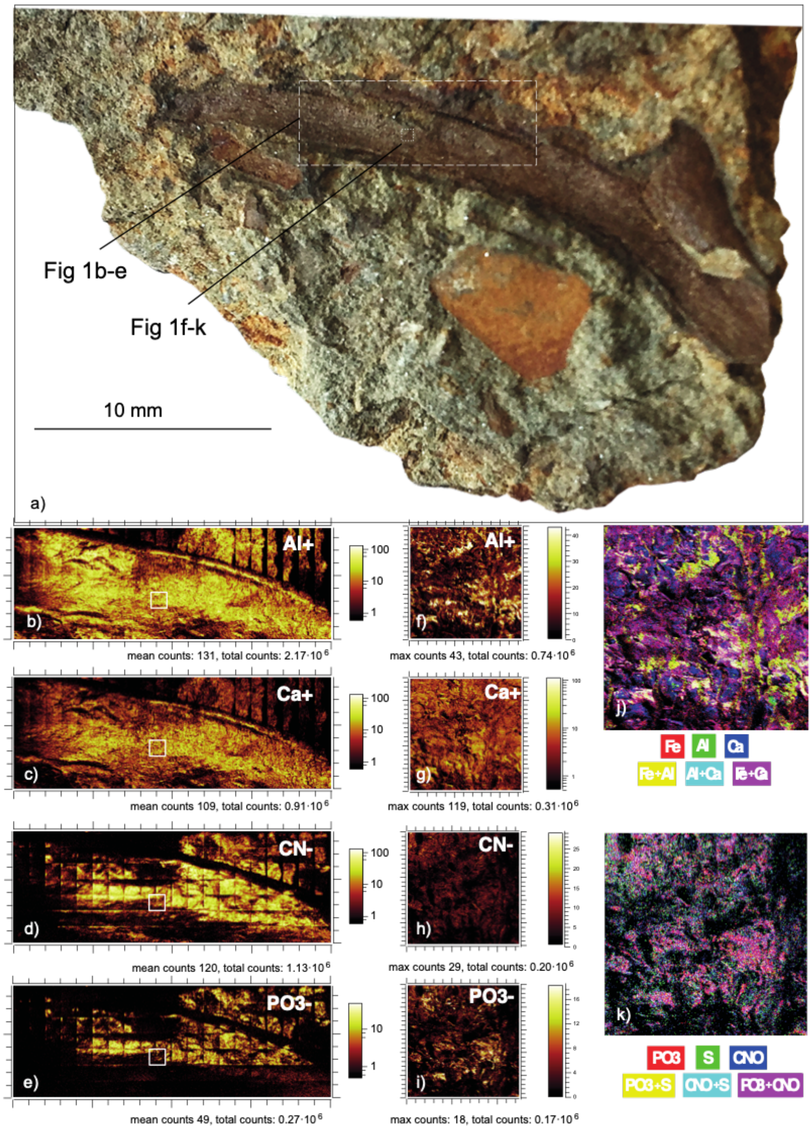

Figure S5. TOF-SIMS characterization of #15184. a) Optical image. Zooms b-e) and f-k) are 10 and 0.5 mm wide, respectively.

S1.3.2 Carbon isotopes

The carbon isotope composition was measured in 25 fragments of fossilized organic plant tissue (Table S1). Repeated analyses were made on 14 of these fragments and two fragments were analyzed three times. The $\delta^{13}C_{plant}$ data from fossils fits with a normal distribution (Darling-Anderson criteria) with an average value of 26.7±1.2‰ (1SD, n =24). The variance is larger than analytical uncertainty of the analysis estimated from the reproducibility of standard reference materials (<0.3‰). The isotope variability is real in the sense that variation between distinct plant fragment is also greater than variance during repeated analyses of the same fragments (except in #15183_01). Thus, we interpret the isotope variation as representative of carbon isotope fractionation in the Baragwanathia flora.

Table S1. Carbon isotope data from the Yea fossil flora. Sample #15154 contain Zosterophyl, and #15173 contain fossils described as Baragwanathia longifolia. The taxonomy of the studied plant fragments.

NMV #	Material analyzed	$\delta^{13}C$ (V-PDB)
#15154	Branched stems	
Fragment 01		-24.4‰
Fragment 02		-27.6‰
Fragment 03		-27.4‰, -27.2‰
Fragment 04		-25.6‰
Fragment 05		-27.9‰, -26.0‰
Fragment 06		-26.7‰, -25.1‰
Fragment b03		-25.2‰, -25.6‰
Fragment b04		-29.8‰
Fragment b05		-25.1‰
#**15173**	Branched stems	
Fragment 02		-28.3‰, -28.2‰
Fragment 04		-28.5‰
#**15174**	Branched stems	
Fragment 01		-26.6‰, -26.8‰
Fragment b02		-27.7‰
Fragment b03		-25.6‰, -24.6‰
Fragment b04		-26.3‰
#15183	Branched stems	

Fragment 01		-24.5‰, -27.9‰, -27.6‰
Fragment 04		-27.6‰
Fragment 05		-28.2‰, -28.2‰
Fragment 06		-27.1‰, -27.4‰
Fragment 08		-26.6‰, -27.3‰
Fragment b01		-26.6‰
Fragment b03		-27.0‰
Fragment b04		-26.2‰, -26.6‰, -25.7‰
Fragment b05		-25.2‰, -25.5‰
#15184	Branched stems	
Fragment 02		-26.4‰, -26.3‰
All analyses, mean ± SD (n)		-26.68 ± 1.24‰ (n = 41)
All fragments, mean ± SD (n)		-26.75 ± 1.24‰ (n = 25)
Mean fragments ± SE		**-26.75 ± 0.25‰**
Reference materials		
ANU Sucrose		-10.5±0.3 (n= 3, 1SD)
Peach leaves		-26.0±0.1 (n= 10, 1SD)
USGS 61 (certified -35.05‰)*		-35.10 ± 0.56 (n= 4, 1SD)
USGS 62 (certified -14.79‰)*		-14.81 ± 0.35 (n= 4, 1SD)

**run at 30–90 nanomoles of C.*

Section S2. Carbon isotope fractionation in terrestrial plants versus ambient CO_2 level

S2.1 The CO_2 paleo barometer

Plants fractionate carbon isotopes during CO_2 uptake mainly due to carboxylation by the Rubisco enzyme and secondly as a result of diffusion into the cell. The net isotope fractionation (Δ_{leaf}) between plant tissue (δ_p) and ambient air (δ_a) is given as $\Delta = (\delta_a - \delta_p)/(1 + \delta_p)$[6]. For the geological past, atmospheric δ_a might be estimated from the marine $\delta^{13}C$ record, see section 2.2.

In living C3 plants, Δ_{leaf} reflects the balance between photosynthesis and stomatal conductance, and varies with climate and plant characteristics[7,8]. Δ_{leaf} is a continuous function of the partial pressure of CO_2 in the ambient environment[6].The following relationship applies across a wide range of C3 plants:

$$\Delta^{13}C = A \cdot B\ (pCO_2 + C) / [A + B \cdot (pCO_2 + C)] \qquad \text{eq. S1}$$

Where A = 28.26, B = 0.22, C = 23.9.

Schubert et al. 2012[6] calibrated this proxy against the paleo-CO_2 record obtained from gas inclusions in ice cores record across the latest deglaciation, where Δ_{leaf} increased globally by 2.1‰ and atmospheric CO_2 levels increased from 200 to 280 ppm. This model is similar to calibrations obtained from culture experiments at controlled CO_2 levels (Fig. 1).

Equation 1 predicts that a 5.7‰ decline in $\Delta^{13}C$ from 27.4‰ to 21.7‰ should be observed if atmospheric CO_2 declined from 4000 ppm to 400 ppm. The magnitude of fractionation declines dramatically at lower CO_2 levels.

A compilation of $\Delta^{13}C_{leaf}$ data from Devonian C3 plants was presented by Wan et al. (2019)[11]. These data are shown along with the new data from the *Baragwanathia* flora in Figure S6.

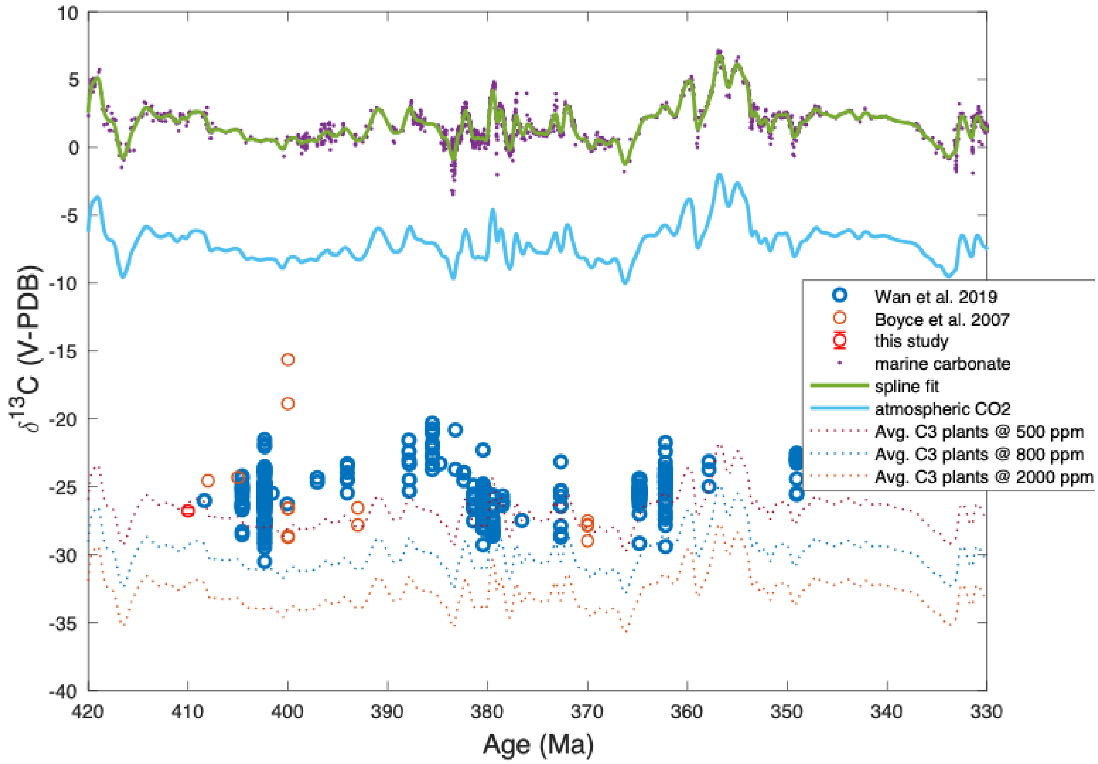

Figure S6. The carbon isotope composition of seawater (green) and air (blue) is determined from the marine carbonate record assuming air-seawater offset of 6.9¸‰ (Figure S9). Error envelopes represent the uncertainty. The record of terrestrial C3 plants constrain CO2-dependndent carbon isotope fractionation. The dotted curves show the expected composition of C3 plants at atmospheric pCO_2 levels of 500, 800 and 2000 ppmv.

Atmospheric pCO_2 obtained by inverting the $\Delta^{13}C$ record using all C3 plants (eq. S1) is shown in Figure S7 along with three other calibrations based on controlled culture experiments with modern lycophytes (*Selaginella*) or other related sporophytes (calibrations shown in Figure 1).

The studied plant fragments of the Yea flora yield a $\Delta_{leaf} = 20.4\pm1.1‰$ (2 SE) corresponding to an atmospheric pCO_2 of 500^{+130}_{-29} ppm (2 SE) where the error represent uncertainty associated with the various physiological responses in closest living representative species. The analytical error associated with isotope data propagates to the pCO_2 estimate with a smaller error, e.g. 450^{+50}_{-41} ppm (2SE) for lycophyte *S. kraussiana*. The field-based calibration from Pleistocene-Holocene C3 plants in eq. S1, we obtain an even lower atmospheric pCO_2 level of 309^{+76}_{-56} ppm.

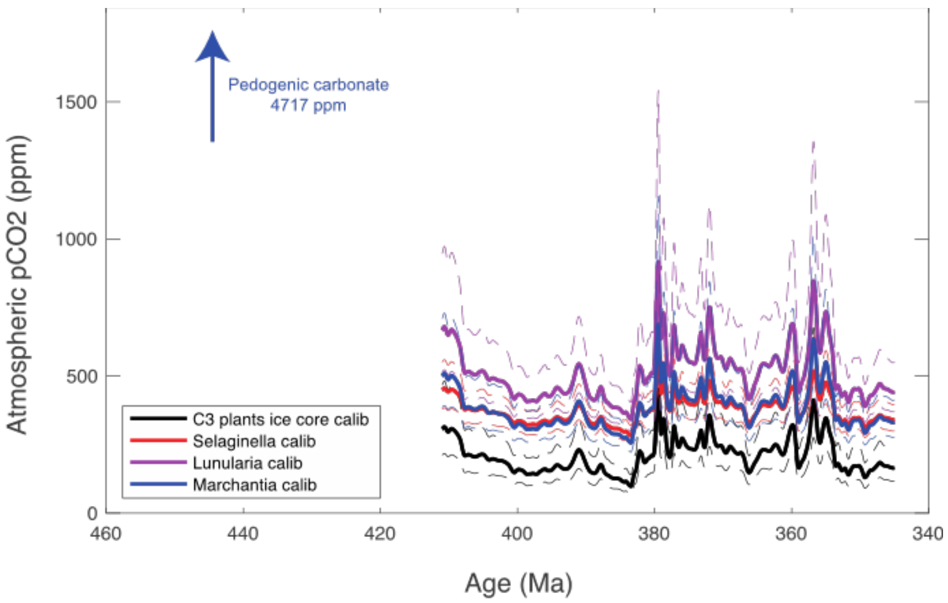

Figure S7. Atmospheric CO_2 constraints calculated from the $\Delta^{13}C_{leaf}$ spline fit data. using various calibration curves from C3 plants during the Pleistocene-Holocene[6], controlled experiments with modern lycophyte (Selaginella kraussiana), thalloid liverworts (Marchantia polymorpha, Lunularia cruciate) and monilophytes (Equisetum telmateia)[12].

S2.1.1 The effect of water utilization efficiency

In addition, spatial Δ_{leaf} variability in land plants also arises from variability in water availability[10]. This is because Δ_{leaf} is strictly a function of the CO_2 concentration in the substomatal cavities (c_i), and c_i depends on the flux of CO_2 into the leaf and CO_2 removal from the leaf by assimilative C fixation. The CO_2 flux into the cell is not only a function of ambient CO_2 levels, but also depends on stomatal conductance into the leaf. At lower water availability, plants down-regulate their stomatal conductance (i.e. enhance their Water Utilization Efficiency, WUE), so that Δ_{leaf} generally decrease. Hence, at constant atmospheric pCO_2, Δ_{leaf} is a time-integrated measure of WUE, although leaf temperature and mesophyll conductance are confounding factors. The relative effect of these factors is clear from a comparison of fractionations (Δ_{leaf}) observed in modern C3 plants as a function of mean annual precipitation rate (Fig. S6). Here, fractionations can be muted by ~4‰ in drier areas, but are relatively constant at >1000 mm/yr.

Potentially, spatial records of fossilized plant material can be used to constrain water utilization efficiency (WUE) and proximity to aquifers the early flora, as has been suggested for Mid-Late Devonian land plants[11]. Our new data from the *Baragwanathia* flora comes from humid, tropical settings with mean annual precipitation in excess of 1500 mm/yr according to our paleoclimate models (Section S4). Therefore, a high water use efficiency for the *Baragwanathia* flora (that are physiologically similar to modern lycophytes) can be ruled out as explanation for muted fractionations observed in the Early Devonian plant fragments.

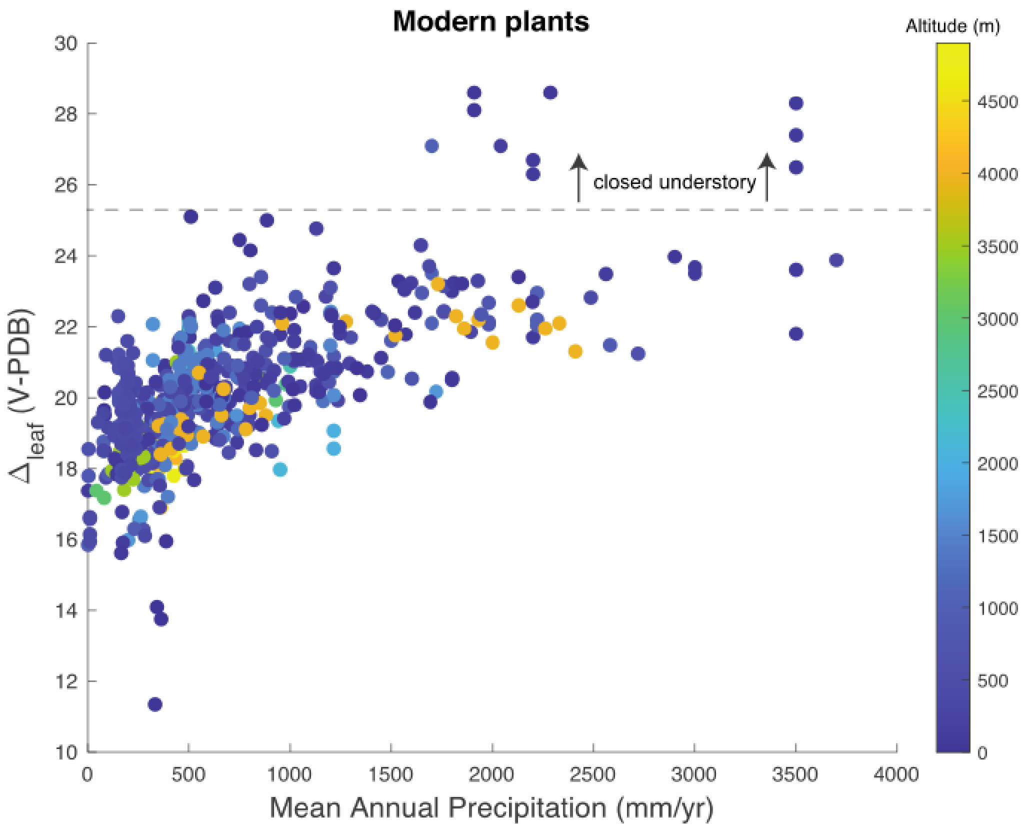

Figure S8. Carbon isotope fractionation, $\Delta_{leaf} = \delta^{13}C_{air} - \delta^{13}C_{leaf}$, in modern C3 plants versus mean annual precipitation, calculated using atmospheric $\delta^{13}C_{air}$ = -6.9‰ and $\delta^{13}C_{plant}$ data from Kohn et al., (2010)[13]; Diefendorf et al., (2010)[8]. Modern C3 plants in closed understory settings induce larger fractionations, but this effect is negligible for the low vegetation of the Early Devonian.

S2.2 Carbon isotope composition of early Devonian atmosphere

The carbon isotope composition of the atmosphere, $\delta^{13}C_{air}$, is in equilibrium with the oceanic pool of dissolved inorganic carbon pool that, in turn, is to first order determining the isotope composition of marine carbonates, $\delta^{13}C_{CARB}$.

Diagenetic alteration can induce large overprints on $\delta^{13}C_{CARB}$ records, especially if altered by meteroric fluids. Therefore, it is important to compare data from several localities (Table S2). A temperature-dependent isotope fractionation occurs between aqueous CO_2 and marine carbonate precipitates. Table S2 summarizes how this offset varies according to our paleoclimate model (Fig. S9).

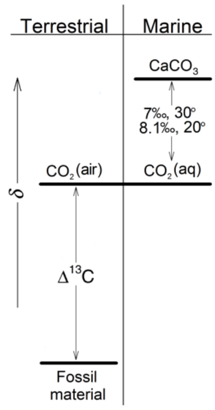

Figure S9. Carbon isotope fractionation between carbon in (fossil) terrestrial plants, CO_2 in air and marine carbonates (after Hayes et al., 2003[14]).

Table S2. Carbon isotope composition of Early Devonian (L. Pragian, ~410 Ma) atmosphere derived from marine carbonates and the temperature-dependent carbon isotope difference between dissolved inorganic carbon (DIC) in seawater and atmospheric CO_2.

	Locality	Age (Ma)	$\delta^{13}C_{CARB}$ † [‰]	$T_{avg.surf}$ ¥ (°C)	$\Delta^{13}C_{DIC-CO2(air)}$ ƒ [‰]	$\delta^{13}C_{air}$ Ω [‰]	Refs
CE	Central Europe	Pragian	2.0±1.0	22.6±5.0	9.04±0.57	-5.8±1.2	A
NE	Nevada. USA	L. Pragian	1.0±1.0	21.8±5.0	9.13±0.57	-6.9±1.2	B
SI	Nizhnig Sergi and Tabulska. Siberia	Pragian	1.0±1.0	22.6±5.0	9.04±0.57	-6.8±1.2	C
OK	Haragan Bois d'Arc limestone. Oklahoma	Lochkovian	1.0±0.7	21.7±5.0	9.14±0.57	-6.1±0.9	D
	Average		**1.5±0.5**			**-6.4±0.5**	

† The range of carbon isotope values in marine limestones from the given time interval and location. ¥ Surface temperature estimates obtained from the Paleoclimate model with 500 ppm CO_2 (Fig. S4) adopting a conservative uncertainty of ±5°C. ʃ Equilibrium fractionation between dissolved inorganic carbon (DIC) and atmospheric CO_2 at the given range of temperatures according to Hayes 2005. Ω Estimated carbon isotope composition of atmospheric CO_2 using equation 10 in Hayes et al., (2003)[14] assuming a constant isotopic offset between the studied limestone formations and open-ocean seawater of 1.2‰. The uncertainty estimate is propagated from the estimated temperature range and uncertainty in $\delta^{13}C_{CARB}$. A – Buggisch & Joachimski (2006)[15]. B – Saltzman 2002[16]. C – Veizer et al., (1999)[17]. D – Gao et al.,(1993) (reporting an independent temperature estimate of T = 25±7°C from the Haragan Bois d'Arc limestone).

Section S3. Other atmospheric CO_2 proxies

S.3.1 Stomatal proxies for paleoatmospheric CO_2

The density of stomata in land plants has been used to infer atmospheric CO_2 pressure in the Early Devonian[3]. A low stomatal density (SD = 4.5±3.9), and a low ratio of stomata to epidermis cells (stomatal index, SI) in two extinct plants has been used to suggest high atmospheric CO_2 in the Early Devonian[18].The data comes from the zosterophyll *Sawdonia ornata* and the non-vascular polysporangiophyte *Aglaophyton major* with no living descendants. Both plants were assumed to occupy poorly drained habitats in which the plants with minimal number of stomatal cells would have a selective advantage by preventing water loss[3]. To interpret ambient CO_2 levels from stomatal indices, the fossils data was compared to extant plants thought to represent their nearest living representative[18]. Here, we estimate and propagate the uncertainty of this measure by offering stomatal densities for three modern lycophytes that are physiologically similar to *Baragwanathia* species.

The stomatal density in Early Devonian *Baragwanathia* fossil plants from Canada and Australia are distinctly higher (SD = 28–110 mm^{-2}) than the extinct fossils used for previous paleo-CO_2 constraints, also supporting a lower atmospheric CO_2 levels than previously thought. We compared values from all Early Devonian plant fossils and modern lycophytes grown in culture and in the field and propagated the errors in the calculation of paleo-atmospheric CO_2 levels (Table S2)[4]

Table S3. Stomatal data from Early Devonian plants and extant lycophytes.

Species	Age [Ma]	Locality	Stomatal density [mm^{-2}]	Predicted Atm. pCO_2 (PAL)	Ref.
		Fossil lycophytes			
Aglaophyton major	Pragian-Emsian 410-393 Ma	Rhynie Chert, Aberdeenshire, Scotland	4.5±3.9	1.1–193	[3]
Sawdonia ornata	Pragian-Emsian 410-393 Ma	Gaspé, Canada and Whitney, England	4.3±1.9	3.9–48	[3]
Baragwanathia longifolia	Pragian-Emsian 410-393 Ma	Victoria, Australia	109.5[a]	0.08–1.1	[4]
Baragwanathia abitibiensis	Mid-Upp. Emsian ~400-393 Ma	Sextant Fm, N. Ontario, Canada	28	0.33–4.1	[4]

Extant lycophytes grown at ~400 ppm CO_2					
Huperzia phlegmaria	0	Botanical Garden, Copenhagen, Denmark (MAP ~1500 mm/yr, RH = ~80%)	116	1[c]	This study
Huperzia squarrosa	0		9.3	1	This study
Lycopodium annotinum	0	Næstved, Copenhagen (MAP = 640±80 mm/yr, RH = 70-95%)	29.4[b]	1	This study

PAL – Present-day Atmospheric Level (400 ppm). MAP–Mean Annual Precipitation RH– Relative Humidity. [a)]Pore surface area ~232 μm^2, [b)]440 μm^2.

We note that the ability for land plants to adapt stomatal density also depends on the size of the plant cells and stomata[19]. The ratio of stomata and epidermis cells (stomatal index) and volume density (mm^{-3}) has not be determined in *Baragwanathia*, but the surface area of each stomata pore in the fossil plant is found to be smaller (~only half) of that in living lycophytes. Therefore, the predicted atmospheric CO_2 level in Table S2 might be underestimated and we adopt a factor of ~2 uncertainty based on stomata size.

For comparison to modern analogue species, we compared the stomatal density of three species of lycophytes, *Huperzia squarrosa*, *Lycopodium annotinum* and *Huperzia phlegmaria*, grown under present-day atmospheric pCO_2 (410 ppm). Table S3 shows the stomatal densities range from 9.3, 29.4, and 115 mm^{-2}, indistinguishable from that observed in the oldest lycophytes *Baragwanathia longifolia* and *Baragwanathia abitiensis* (110 and 28 mm^{-1}, respectively), Therefore, stomatal data is consistent with low atmospheric pCO_2 in the early Devonian similar to today.

Taking both calibration error and uncertainty interspecies variability into accounts, we find that the paleo-CO_2 constraints from stomatal density in *Baragwanathia* ranges from 32 to 3120 ppm. This result is fully consistent with low and far more precise atmospheric CO_2 levels obtained from carbon isotopes in fossil land plants.

S.3.2 Pedogenic goethite proxy for paleoatmospheric CO_2

Ambient CO_2 concentrations influence the fraction, X, of CO_2 that can be substituted into goethite minerals during precipitation in soils; i.e. $X = FeCO_3OH / (FeOOH + FeCO_3OH)$. This phenomenon has been used to derive high atmospheric CO_2 concentrations from pedogenic goethite in the Late Ordovician Potters Mill paleosol in New York, USA. Previous analyses reported a concentration of 4800 ppm and a recent uncertainty estimate yielded ±1900 ppm (1SD). This important constraint on Earth's climate before vascular ecosystems depends on several assumptions and we show the error propagation of this calculation here.

The derivation of Late Ordovician atmospheric pCO_2 from pedogenic goethite relies on six major assumptions:

1. The $\delta^{13}C$ of Late Ordovician atmosphere CO_2 is assumed to have been -6.5±1.0‰[5].

2. Goethite precipitation incorporate CO_2 with an equilibrium isotopic fractionation that induce a constant 5.0‰ offset (no uncertainty) between the CO_2 in the mineral and ambient air.

3. There is a positive trend of $\delta^{13}C$ vs. 1/X in pedogenic goethite from a paleosol profile at Potters Mill, which is assumed to represent a mixing line with atmospheric CO_2 and soil-respired CO_2 as the two end-member C sources, according to the following equation:

   $$\delta^{13}C = (\delta^{13}C_A - \delta^{13}C_O) \cdot X_A \cdot [1/X] + \delta^{13}C_O. \qquad \text{eq. S1}$$

   Data from the Potters Mill paleosol yields a slope and intercept ($\delta^{13}C = A \cdot /1/X) + B$) with the following uncertainties (2SE): $A = (\delta^{13}C_A - \delta^{13}C_O) \cdot X_A = 0.01594 \pm 0.00136$ and $B = \delta^{13}C_O = -20.39 \pm 0.35$

4. Pedogenic goethites incorporate CO_2 in response to ambient CO_2 levels, according to the following equation:

   $$\log(X) = \log pCO_2 + \Delta S^0/(2.303 \cdot R) - \Delta H^0/(2.303 \cdot R) \qquad \text{eq. S2}$$

   where R is the universal gas constant and $\Delta S^0/(2.303 \cdot R) = 6.04$ (Yapp & Poths 1992).

5. The pedogenic goethite from Potters Mill are assumed to follow equation S2 for phosphatized goethite, $\Delta H^0 = 30$ kJ (and not for unphosphatized goethite, where $\Delta H^0 = 8$–16 kJ)[6]. The calculation is highly sensitive to this assumption (see Fig. S7).

6. Soil pH is assumed not to alter equation 2, even though it affects the proportion of CO_2 among dissolved inorganic carbon phases.

With these assumptions, the Potters Mills paleosol leads to an atmospheric pCO_2 constraint for the Late Ordovician of 4717^{+2066}_{-1270} ppm (3447–6784 ppm, 2SD), excluding deviations from assumptions listed above. The derivation is illustrated in Fig. S1.

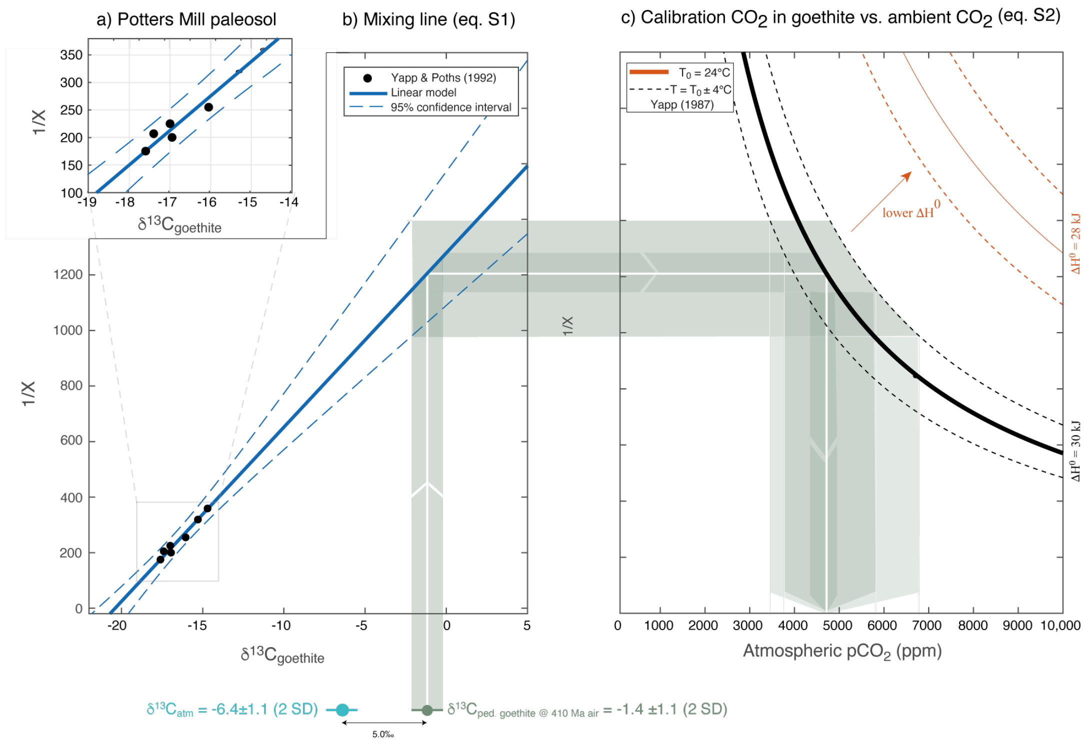

Figure S10. A) Carbon isotope data (d13C) and mole fraction of CO_2 in goethite ($X = n(Fe(CO_3)OH)/[n(FeOOH)+ n(Fe(CO_3)OH])$ is inversely correlated in the Late Ordovician Potters mill paleosol. B) A linear fit is interpreted as a mixing line (eq. S1) that describes the isotopic consequences as a function of the relative proportion of CO_2 derived from soil respiration and from the atmosphere. Assuming the isotope composition of the Late Ordovician atmosphere, it is possible to derive the CO2 mole fraction (X) that goethite would adopt if only exposed to atmospheric CO_2 (in the absence of soil respired CO_2). C) A thermodynamic relation exists between the molar content of CO_2 substituted into goethite and ambient CO_2 levels (eq. S2). This function is sensitive to whether goethite is phosphatized.

S.3.3 Paleosol carbonate proxy for paleoatmospheric CO_2

A soil-based CO_2 paleobarometer was introduced by Cerling (1991)[21] and has subsequently been applied to paleosols of the past 400 Ma. Conceptually, the proxy is based on isotopic analyses of calcite that precipitates in soils while the soil is in direct communication with the atmosphere. The atmospheric CO_2 level is obtained by assuming that pedogenic calcite contains CO_2 derived from a binary mixing soil-respired CO_2 and atmospheric CO_2. The inferred atmospheric pCO_2 depends critically on how much CO_2 is contributed via soil respiration (Sz) and the isotope composition of soil-respired CO_2. The value for Sz is kept fixed and typical values ranges from 440 to 50,000 ppm. Traditionally, Sz has been estimated by characterizing the soil type of the paleosol, but this is not possible for early Devonian paleosols. In addition, we note that there are large spatial $\delta^{13}C$ variability (~8‰) in soils from the same region (e.g., Caves et al. 2016[22]). Figure S11 shows a reasonable error estimate for the Devonian pCO_2 associated with uncertainty of Sz only.

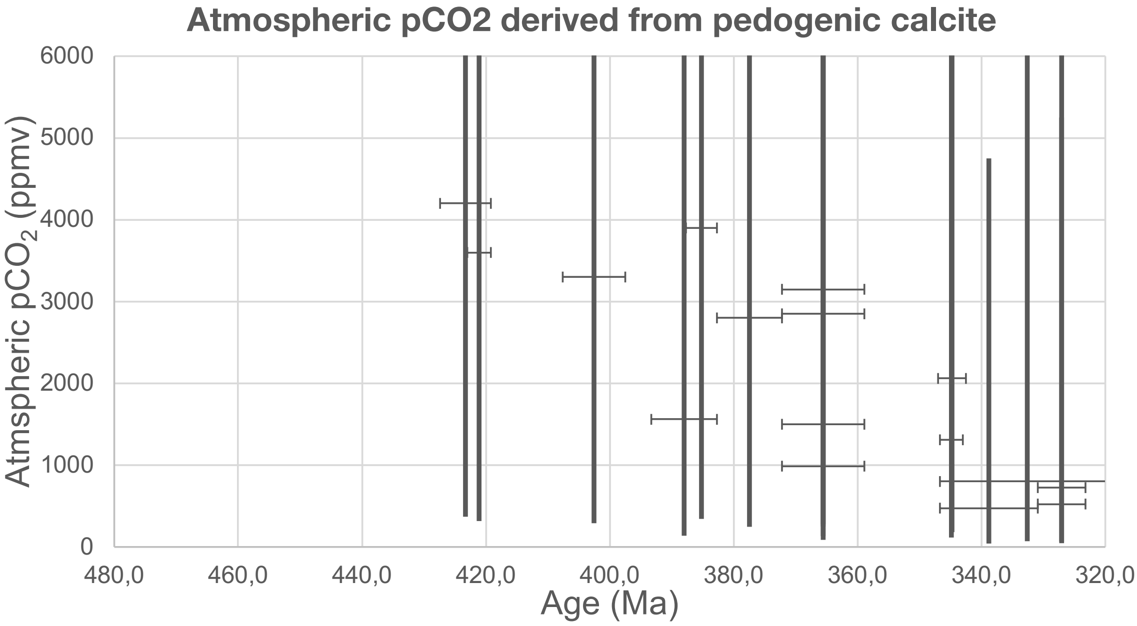

Figure S11. *The carbon isotope composition of pedogenic calcite in paleosols constrain atmospheric pCO2. Error bars represent the plausible range of CO2 contributed from soil respiration, where Sz = 440-50,000 ppm with mid-point set to Sz = 2000 as in Foster et al. (2017)*[1].

Section S4. Early Devonian Climate model.

S4.1 Early Devonian climate state

We simulated the Early Devonian climate using CLIMBER-3α (see Methods) to assess the climatic conditions at various CO_2 levels, and specifically the annual mean precipitation that influence the carbon isotope fractionation in land plants (Fig S6).

Three scenarios were explored where atmospheric CO_2 levels were fixed at 2000 ppm, 800 ppm and 500 ppm. In all scenarios, surface temperatures above 25°C occur in the tropics throughout the year and temperatures below freezing point occur in polar regions during winter. The global mean temperature declines from 22.1°C, 17.9°C to 15.0°C. Accordingly, the sea-ice fraction increases in the polar regions, respectively.

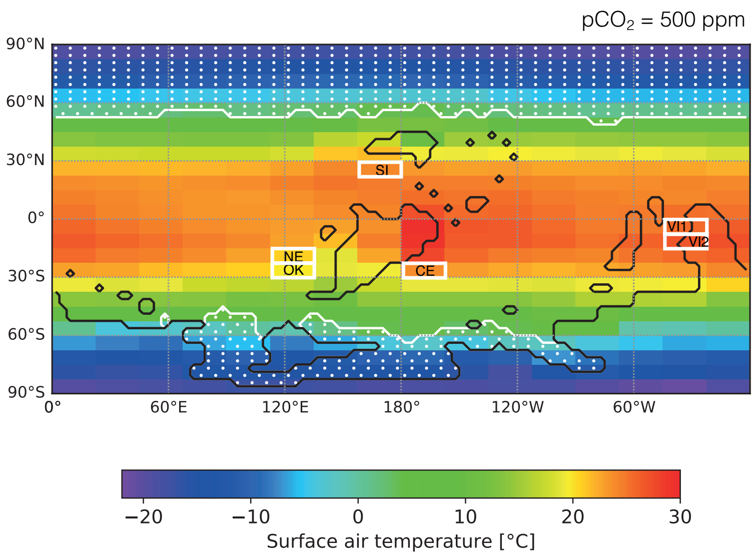

Figure S11. Annual mean surface-air temperature for the early Devonian (400 Ma) at atmospheric pCO2 of 500 ppmv. Sample localities are marked with two options for the Yea flora (VI1, VI2) and marine limestone deposits used to constrain atmospheric d13C include CE – Central Europe, NE – Nevada, SI – Siberia, OK – Oklahoma (See Table S1).

Figure S12 shows that at 500 ppm, sea ice accumulates in the Antarctic ocean around Gondwana during Southern winters, whereas temperatures up to ~20°C occur in the continental interior during warmer summers (high obliquity and high eccentricity). The model considers snow cover on the continent, but does not explicitly model ice sheet growth. Figure S13 shows average duration of snow cover over the course of 1000 years in different solar insolation states. The permanence of polar ice sheets is not determined further here.

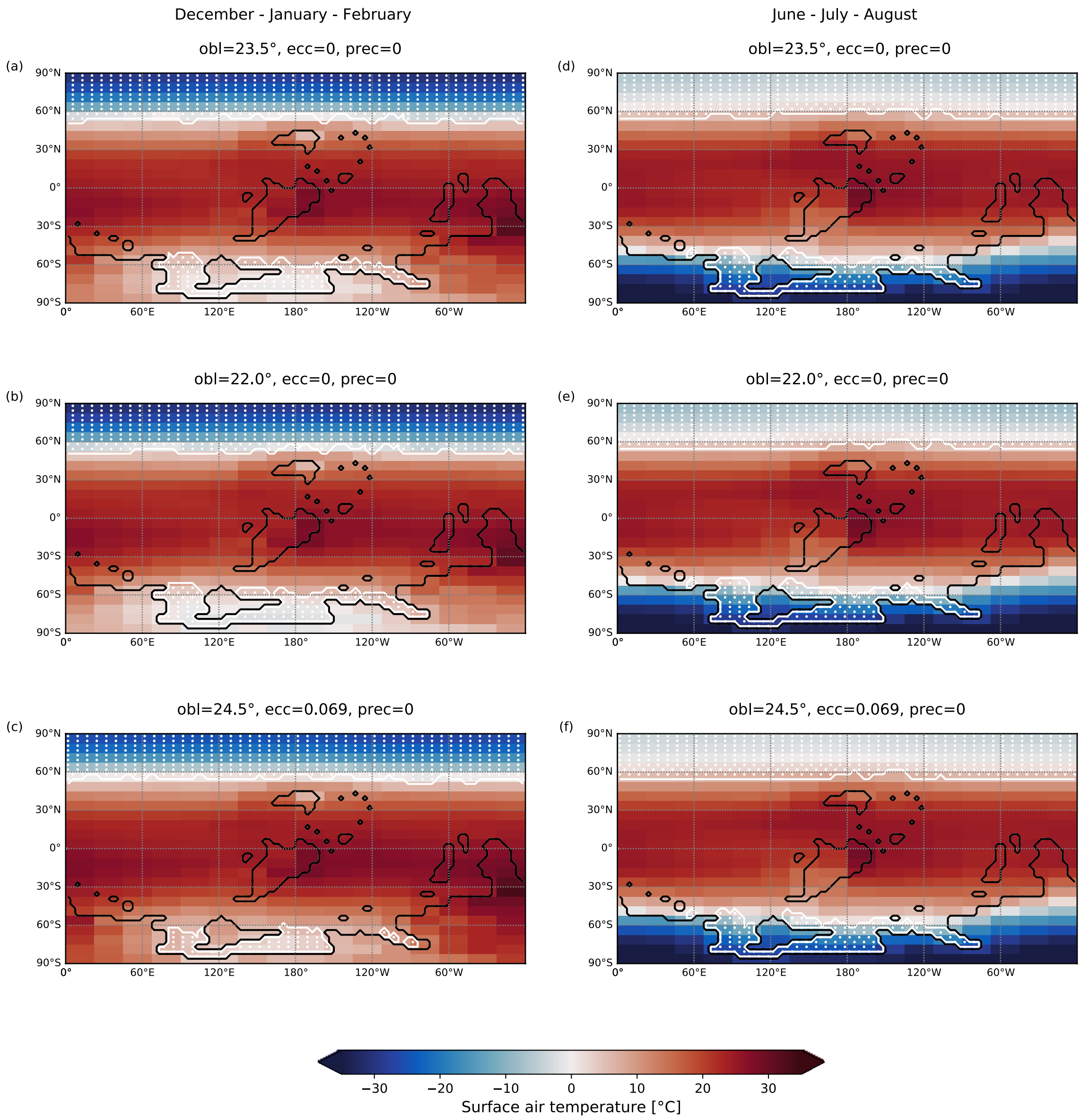

Figure S12. Devonian Paleoclimate at 500 ppm for Southern summer (left) and Southern winter (right) across three distinct orbital configurations with obliquity 22–24.5°, eccentricity = 0–0.069, and precession 0.

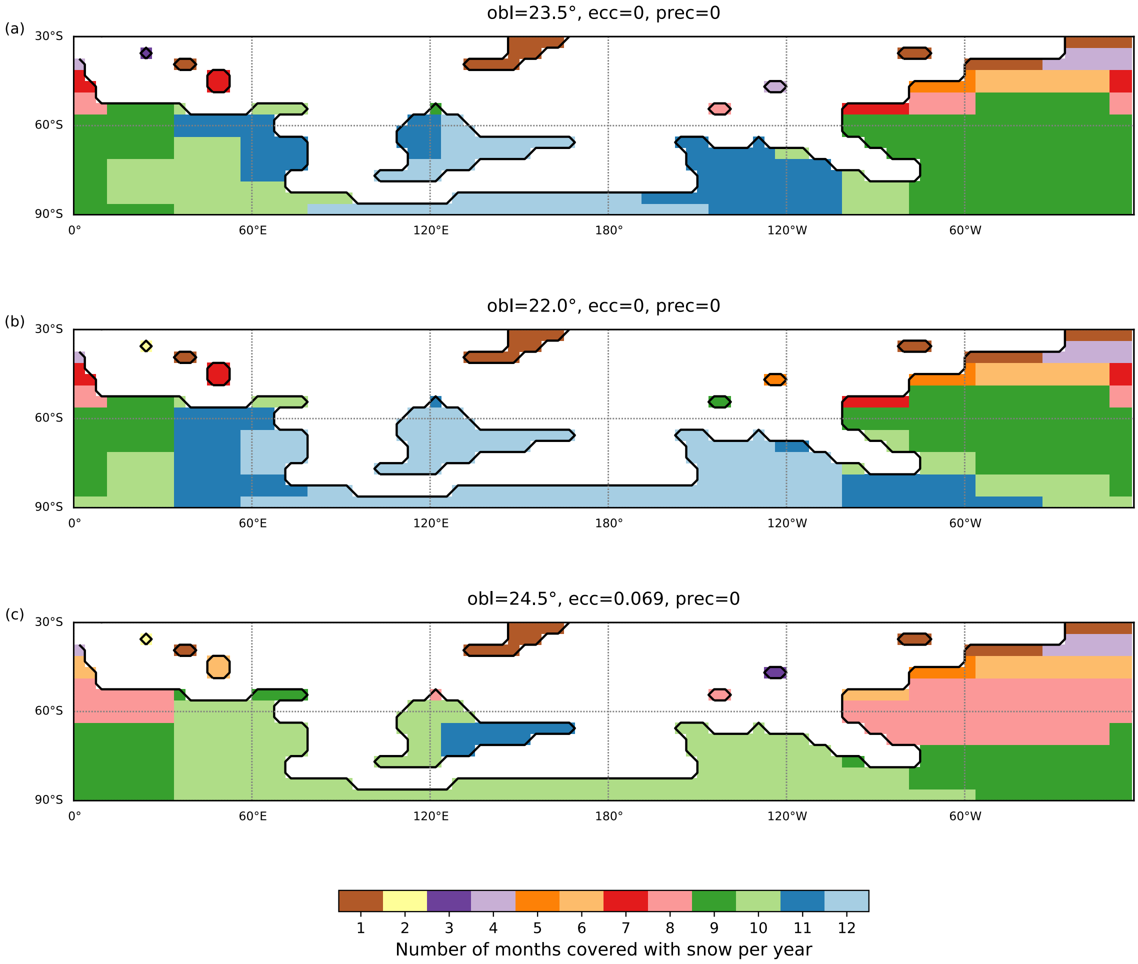

Figure S13. Duration of snow cover in Early Devonian Climate simulations with 500 ppm CO_2. The snow cover represents the average over 1000 years at the same three solar insolation configurations as in Fig S12. The south pole is not permanently snow covered in the obliquity = 24.5° case.

S4.2 Mean annual precipitation at the Yea flora

The paleoclimate model simulations provide mean annual precipitation (MAP) for the Yea fossil site in Victoria, Australia (Table S4). For all realistic atmospheric pCO_2 levels 500-2000 ppm, the flora would have grown in humid tropical settings with 2-3-fold higher MAP than in modern C3 plants that upregulate WUE with concomitant smaller C isotope fractionation. Therefore, the fossil land plants from the *Baragwanathia* flora should reliably record atmospheric CO_2 according to eq. S1.

Table S4. Mean annual surface-air temperature over land (T_{land}) and mean annual precipitation (MAP) at the Yea fossil site in Victoria, Australia, according to the paleoclimatic model (CLIMBER-3α*).* Land temperatures are averages for the land area in each model grid cell, the average of V11 and V12 is calculated by taking the land fraction of the two grid cells into account.

Insolation state	Location	0–7.5°S (OF = 0.42)[¥]		7.5-15°S (OF = 0.67)	
Obliquity (ε), eccentricity (e), precession (ϖ)	**pCO_2 [ppm]**	**T_{land} [¥] (°C)**	**MAP[¥] (mm/yr)**	**T_{land} [¥] (°C)**	**MAP[¥] (mm/yr)**
ε = 23.5°, e = 0, ϖ = 0	500	26.5	1770	25.0	2148
ε = 22.0°, e = 0, ϖ = 0	500	26.6	1815	25.0	2208
ε = 24.5°, e = 0.069, ϖ = 0	500	26.8	1770	25.4	2148
ε = 23.5°, e = 0, ϖ = 0	800	28.7	2218	27.3	2591
ε = 23.5°, e = 0, ϖ = 0	2000	32.1	3184	30.9	3585

OF – Ocean fraction in grid cells (VI1 and VI2) where the fossil site is located (Fig S9).

Section S5. Revised COPSE model for the Mid-Paleozoic

To evaluate conditions that might have facilitated low atmospheric CO_2 in the Devonian, we used the Carbon-Oxygen-Phosphorous-Sulfur Evolution (COPSE) Earth system model framework with adjusted forcing parameters on weathering to fit simultaneously fit observational constraints on atmospheric pCO_2 and pO_2 (Figure S10). We adapted two distinct versions of the model (COPSE2016 and COPSE reloaded), which has different parameterizations of climate sensitivity, ocean anoxia and more[23,24]. Figures S10 and S11 shows the original and revised models that fit the new observational constraints.

The effects of early plant enhancement of silicate (and carbonate) weathering is assumed to scale with mudrock proportion in continental deposits[25], because mineral surface area and plant-assisted suspension of finer grains exposed to weathering fluids (baffling) would likely increase the rates of rock dissolution. Second, the evolution of land plants (“E”) ramps up in the Silurian suggesting plant-assisted weathering became widespread earlier than previously assumed. Recent models introduced selective P weathering (F) to increase oceanic P input during the establishment of non-vascular flora. For simplicity, we omitted this forcing as it is neither required nor necessary. The C/P ratio of terrestrial organic deposits is kept constant until massive coal deposition in the Pennsylvanian (~320 Ma). These changes are sufficient to cause a 10-fold decline in atmospheric CO_2 and a 2-fold increase in atmospheric pO_2, but we also had to adjust the degassing rate of the Early Devonian in order to fit the new observational constraint from the *Baragwanathia* floras.

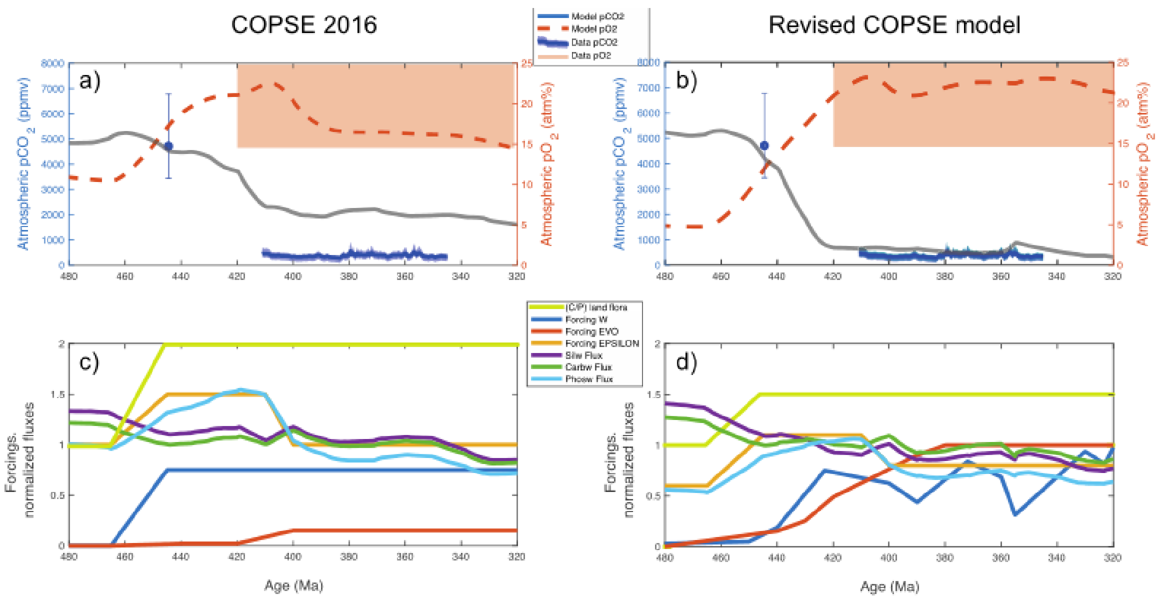

Figure S13. COPSE model simulations for the evolution of the global biogeochemicall cycles are shown, where a) shows the atmospheric pO2 and pCO2 trajectories for the original parameter settings and c) forcings used in the COPSE 2016 model[23]. The revised model is shown in panels b and d. The observational constraints on pO2 and pCO2 from the charcoal record and plant fossil isotopes are shown in a and b.

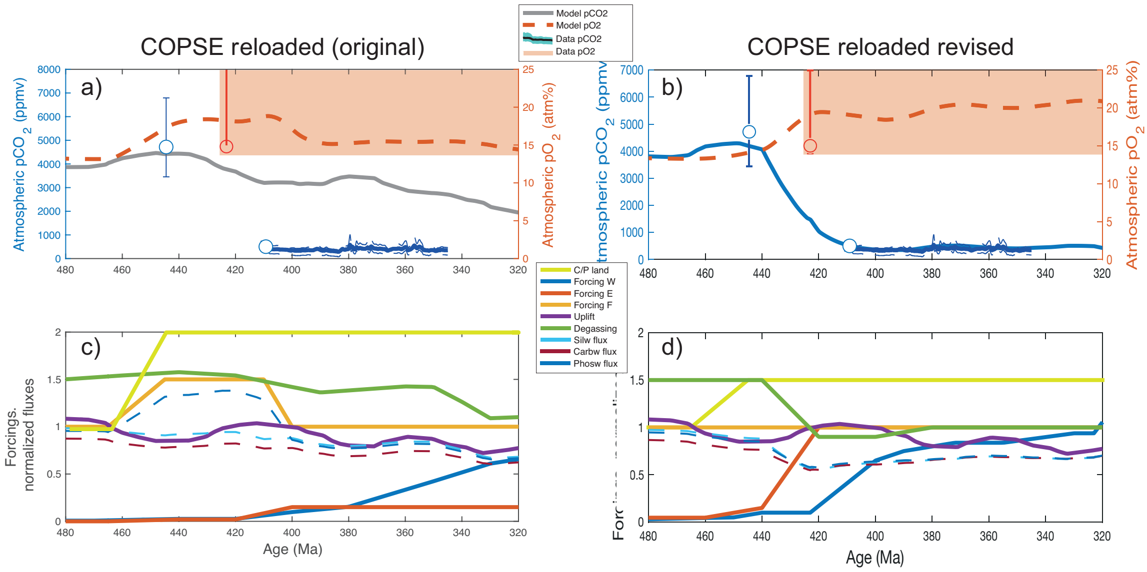

Figure S14. Simulations of the global biogeochemical cycles using COPSE reloaded framework[24]. a) Original model and b,d) revised model with distinct forcings on weathering efficiency (W), land plant evolution (E), selective P weathering (F) and volcanic degassing. The observational constraints on atmospheric pO_2 and pCO_2 from the charcoal record and plant fossil isotopes are shown in a and b. For simplicity, the models shown here ignores the activation energy of silicate weathering is 50 kJ/mol corresponding to a granitic composition ($k_T = 0.0724$) and no temporal variations in lithology.

References

1. Garratt, M.J. New evidence for a Silurian (Ludlow) age for the earliest Baragwanathia flora. *Alcheringa*, **2:3**, 217-224 (1978).
2. Rickards, R.B. The age of the earliest club mosses: the Silurian *Baragwanathia* flora in Victoria, Australia. *Geol. Mag*. **137**, 207–209 (2000).
3. Earp, C. *Costulatotheca schleigeri* (Hyolitha: Orthothecida) from the Walhalla Group (Early Devonian) at Mount Pleasant, central Victoria, Australia. *Alcheringa Australas. J. Palaeontol.* **43**, 220–227 (2019).
4. Cookson, I. IV—On plant-remains from the Silurian of Victoria, Australia, that extend and connect floras hitherto described. *Philos. Trans. R. Soc. Lond. B. Biol. Sci.* **225**, 127–148 (1935).
5. Kraft, P., Kvaček, Z. Where the lycophytes come from? – a piece of the story from the Silurian of peri-Gondwana. *Gondwana Res*. **45**, 180–190 (2017).
6. Schubert, B. A., Jahren, A. H. The effect of atmospheric CO2 concentration on carbon isotope fractionation in C3 land plants. *Geochim. Cosmochim. Acta* **96**, 29 – 43 (2012).
7. Farquhar, G., O'Leary, M. & Berry, J. On the Relationship Between Carbon Isotope Discrimination and the Intercellular Carbon Dioxide Concentration in Leaves. *Funct. Plant Biol.* **9**, 121 (1982).
8. Diefendorf, A. F., Mueller, K. E., Wing, S. L., Koch, P. L. & Freeman, K. H. Global patterns in leaf 13C discrimination and implications for studies of past and future climate. *Proc. Natl. Acad. Sci.* **107**, 5738–5743 (2010).
9. Schubert, B. A. & Jahren, A. H. Global increase in plant carbon isotope fractionation following the Last Glacial Maximum caused by increase in atmospheric pCO_2. *Geology* **43**, 435–438 (2015).
10. Farquhar, G.D., Ehleringer, J. R. and Hubick, K. T. Carbon Isotope Discrimination and Photosynthesis, *Annu. Rev. Plant. Physiol. Plant. Mol. Biol.* **40**, 503-537 (1989).
11. Wan, Z., Algeo, T.J., Gensel, P.G., Scheckler, S.E., Stein, W.E., Cressler, W.L., Berry, C.M., Xu, H., Rowe, H.D., Sauer, P.E. Environmental influences on the stable carbon isotopic composition of Devonian and Early Carboniferous land plants. *Palaeogeogr. Palaeoclimatol. Palaeoecol*. **531** (2019).
12. Porter, A. S., Yiotis, C. Montanez, I. P. & McElwain, J. C. Evolutionary differences in $\Delta^{13}C$ detected between spore and seed bearing plants following exposure to a range of atmospheric

O_2:CO_2 ratios; implications for paleoatmosphere reconstructions. *Geochim. Cosmochim. Acta* **213**, 517-533 (2017).

13. Kohn, M. J. Carbon isotope compositions of terrestrial C3 plants as indicators of (paleo)ecology and (paleo)climate. *Proc. Natl. Acad. Sci.* **107**, 19691–19695 (2010).
14. Hayes, J. M., Strauss, H. & Kaufman, A. J. The abundance of ^{13}C in marine organic matter and isotopic fractionation in the global biogeochemical cycle of carbon during the past 800 Ma. *Chem. Geol.* **161**, 103-125, (1999).
15. Buggisch, W. & Joachimski, M.M. Carbon isotope stratigraphy of the Devonian of Central and Southern Europe. *Palaeogeogr. Palaeoclimatol. Palaeoecol*. **240**, 68-88 (2006).
16. Saltzman, M. R. Carbon isotope ($\delta^{13}C$) stratigraphy across the Silurian-Devonian transition in North America: evidence for a perturbation of the global carbon cycle. *Palaeogeogr. Palaeoclimatol. Palaeoecol.* **187**, 83-100 (2002)
17. Veizer, J., Ala, D. Azmy, K., Bruckschen, P., Buhl, D. Bruhn, F., Carden, G. A. F., Diener, A., Ebneth, S., Godderis, Y., Jasper, T., Korte, C., Pawellek, F., Podlaha, O. G., Strauss, H. $^{87}Sr/^{86}Sr$, $\delta^{13}C$ and $\delta^{18}O$ evolution of Phanerozoic seawater. *Chem. Geol.* **161**, 59-88 (1999).
18. McElwain, J. & Chaloner, W. Stomatal Density and Index of Fossil Plants Track Atmospheric Carbon Dioxide in the Palaeozoic. *Ann. Bot.* **76**, 389–395 (1995).
19. Royer, D. L. Stomatal density and stomatal index as indicators of paleoatmospheric CO_2 concentration. *Rev. Palaeobot. Palyno*. **114**, 1-28 (2001).
20. Yapp, C. J. & Poths, H. Ancient atmospheric CO_2 pressures inferred from natural goethites. *Nature* **355**, 342–344 (1992).
21. Cerling, T. E., Carbon dioxide in the atmosphere: Evidence from Cenozoic and Mesozoic paleosols, *Am. J. Sci.* **291**, 377– 400 (1991).
22. Caves, J. K., Jost, A. B., Lau, K. V. & Maher, K. Cenozoic carbon cycle imbalances and a variable weathering feedback. *Earth Planet. Sci. Lett.* **450**, 152–163 (2016).
23. Lenton, T. M. *et al.* Earliest land plants created modern levels of atmospheric oxygen. *Proc Natl Acad Sci U A* **113**, 9704–9 (2016).
24. Lenton, T. M., Daines, S. J. & Mills, B. J. W. COPSE reloaded: An improved model of biogeochemical cycling over Phanerozoic time. *Earth-Sci. Rev.* **178**, 1–28 (2018).
25. McMahon, W. J. & Davies, N. S. Evolution of alluvial mudrock forced by early land plants. *Science* **359**, 1022–1024 (2018).

Supporting Information for "A pronounced spike in ocean productivity triggered by the Chicxulub impact"

Julia Brugger[1,2,3], Georg Feulner[1], Matthias Hofmann[1], Stefan Petri[1]

[1]Earth System Analysis, Potsdam Institute for Climate Impact Research, Member of the Leibniz Association, D-14473 Potsdam, Germany

[2]Institute of Physics and Astronomy, University of Potsdam, D-14476 Potsdam-Golm, Germany

[3]Senckenberg Biodiversity and Climate Research Centre (SBiK-F), D-60325 Frankfurt am Main, Germany

Contents of this file

1. Text S1 to S5
2. Figures S1 to S11
3. Table S1

Corresponding author: J. Brugger, G. Feulner Earth System Analysis, Potsdam Institute for Climate Impact Research, D-14473 Potsdam, Germany. (brugger@pik-potsdam.de; feulner @pik-potsdan.de)

Introduction

In this Supplementary Material to our article, we describe the modeled late-Cretaceous climate state more in depth (Text S1, Figure S1, Figure S2). We also give more detailed information about modeling the dust distribution and the bioavailablity of nutrients (Text S2). In addition, we show maps of the changes in mixed-layer depth and the overturning streamfunction (Figure S8) and describe the observed changes in Text S3. Furthermore, we discuss the effect of high C and S masses for ocean acidification (Text S4, Figure S4 and Figure S7). We also describe the influence of higher CO_2 concentrations in the pre-impact state on the effects of the impact (Text S5, Figures S9, S10, S11.). We provide additional information on the temperature decrease after the impact for different timescales at different locations for a late-Cretaceous CO_2 concentration of 500 ppm and 1165 ppm which are useful for the comparison with proxy data (Table S1). In addition, we show maps for the change in NPP after the impact for the standard run with 115 Gt C and 100 Gt S (Figure S3). We also present additional figures for the discussion of ocean acidification in our article for the simulation with additional 1500 Gt C and 325 Gt S (Figure S4 and Figure S5 for the calcite saturation state).

Text S1. Additional information on the modeled late-Cretaceous climate state

For an atmospheric CO_2 concentration of ≈500 ppm and late-Cretaceous boundary conditions, as described in the boundary conditions section of the main article, the global annual mean surface air temperature is 19.0°C. Figure S1 shows the zonal surface air temperature distribution and a map for surface air temperature. The equator-to-pole gradient of 38°C is larger than suggested by proxy data (Upchurch et al., 2015), but the modeled temperature distribution is in good agreement with a comparable simulation in Niezgodzki, Knorr, Lohmann, Tyszka, and Markwick (2017). We also explored a simulation with the same boundary conditions, but a higher late-Cretaceous atmospheric CO_2 concentration which approached equilibrium at a level of ≈1165 ppm. Here, the global annual mean surface air temperature is 22.2°C and the zonal surface air temperature distribution and a map for surface air temperature are shown in Figure S2. The equator-to-pole gradient is 34°C and thus smaller than for the 500 ppm run, but still large compared to proxy data. Hence, as many other climate models (Huber & Caballero, 2011; Upchurch et al., 2015; Niezgodzki et al., 2017; Kump & Pollard, 2008) our model simulates lower polar temperatures for climate states with high CO_2 concentrations compared to temperatures reconstructed from proxy data. The causes are still under exploration, both on the modeling (Niezgodzki et al., 2017; Zhu et al., 2019) and the proxy (Davies et al., 2009, 2019; Evans et al., 2018) side. However, we argue that the effect of the strong cooling after the impact both on the ocean circulation as well as on the marine biosphere does not change significantly for warmer polar temperatures as the magnitude of cooling is so large. Hence, for investigating the effects of a perturbation like the Chicxulub impact, uncertainties in the modeled temperature gradient of the initial climate state should not influence the consequences of the impact significantly.

Text S2. Additional information on model input

Text S2.1. Dust distribution

Using data from geophysical impact modeling for a wet target, a projectile radius of 7.2 km, an impact angle of 45°, a projectile velocity of $18\,\mathrm{km\,h^{-1}}$ and a projectile density of $2500\,\mathrm{kg\,m^{-3}}$ (Artemieva & Morgan, 2009), we calculate a dust mass of $m_{\mathrm{dust}} = 2900\,\mathrm{Gt}$ originating from the projectile and distributed outside the crater. We started with an initial distribution after the impact of 43% m_{dust} (Artemieva & Morgan, 2009) in a radius of 3000 km around the crater, scaled with r^{-3}. The rest of the projectile dust mass is distributed equally around the globe over 10 days.

Text 2.2. Bioavailability of iron and phosphorus from the projectile dust

Only a small fraction of the iron and phosphorus in the ocean is bioavailable. For an unperturbed ocean, we assume a bioavailability of 0.2% for iron and 2% for phosphorus. As the bioavailability of iron and phosphorus in the ocean is suggested to be enhanced when sulfate aerosols are present (Hand et al., 2004; Myriokefalitakis et al., 2016), we increase the bioavailability by a factor of 10 for the area outside the 3000 km radius. Closer to the impact site, the fraction of large ejected fragments is higher, leading to a lower bioavailability than for fine dust. Therefore, we use the equilibrium bioavailability close to the impact site and increase it reaching the 10-fold bioavailability at a radius of 3000 km by taking into account the fractions of globally distributed dust and of additional dust in the 3000 km radius for each cell.

Text S3. Changes in the mixed-layer depth and global overturning streamfunction

Figure S8 shows maps of the mixed-layer depth for the pre-impact state and different times after the impact for the standard simulation (115 Gt C and 100 Gt S) in the first column. We observe a deepening of the mixed layer which is strongest in the mid-latitudes. As this deepening is caused by the strong cooling of surface waters which then sink to the deeper ocean, the change in mixed-layer depth is largest for the coldest year after the impact. The sinking of the cold water masses induces a strong global overturning, as shown in the second column. Mixed-layer depth and global overturning circulation recover on the same time scale as sea surface temperature, i.e., after 100 years they approach a state similar to the one before the impact.

Text S4. Effect of high C and S addition on ocean acidification

To assess the influence of higher C and S masses on ocean acidification, as discussed in earlier studies (Tyrrell et al., 2015; Ohno et al., 2014), we here present the change in pH for simulations with different C and S masses and show maps of the aragonite and calcite surface saturation state after the impact for the respective simulations. In addition to our standard procedure of adding S over a period of 6 years to the ocean (Pierazzo et al., 2003) (labeled *S slow* in the figures), we test the influence of adding the large amount of 1920 Gt S (Tyrrell et al., 2015) during a short time of 10 days (labeled *S fast* in the figures), as this was suggested as a realistic scenario (Ohno et al., 2014) with strong influence on ocean acidification (Tyrrell et al., 2015).

We find a strong influence of the fast addition of the large S amount on the immediate pH reduction (dashed lines in Figure S4). The effect on the recovery and the new equilibrium value is weaker. In contrast, the strong increase of the additional C amount shows a strong effect on the recovery and the new equilibrium value. Comparing maps for the $CaCO_3$ surface saturation state, we find that the effect of the fast addition of 1920 Gt S shifts the $\Omega = 1$ line to significantly lower latitudes for the mean of the first 10 years after the impact. To sustain a strong undersaturation for a longer period of 1000 years, the combination of high C and S amounts is necessary, as shown in Figure S7 (c) and (d). Hence, our results confirm that the amounts of C and S needed to cause a $CaCO_3$ undersaturation sufficient to trigger the end-Cretaceous extinction of calcifiers is in disagreement with recent estimates of C and S production during the impact (Artemieva & Morgan, 2009; Tyrrell et al., 2015).

Text S5. Impact simulations based on higher atmospheric CO_2 pre-impact simulation

To address the uncertainty in reconstructions of late-Cretaceous CO_2 concentrations, we here discuss the results of impact simulations based on a pre-impact CO_2 level of 1165 ppm. The pre-impact surface air temperature is 22.2 °C and the pre-impact sea-surface temperature is 23.7 °C. For the standard impact run (115 Gt C and 100 Gt S) and the impact run with additional 1500 Gt C, the dimming effect of the sulfate aerosols induces a temperature decrease comparable with the temperature decrease for the pre-impact simulation with 500 ppm (see Table S1 and Figure S9). However, the longer-term warming effect of the additional CO_2 is smaller, as to be expected for a higher baseline atmospheric CO_2 concentration. Comparing simulations for the 500 and the 1165 ppm late-Cretacous climate states, Figure S10 shows that the changes in $\delta^{13}C$ are very similar. The ocean's pH value is smaller for the high pre-impact CO_2 concentration, but the reduction in pH caused by the impact as well as the recovery is comparable with the effect of the impact on the 500 ppm late-Cretaceous simulation (Figure S11).

References

Artemieva, N., & Morgan, J. (2009). Modeling the formation of the K-Pg boundary layer. *Icarus*, *201*(2), 768 - 780. doi: 10.1016/j.icarus.2009.01.021

Davies, A., Hunter, S. J., Gréselle, B., Haywood, A. M., & Robson, C. (2019). Evidence for seasonality in early Eocene high latitude sea-surface temperatures. *Earth Planet. Sc. Lett.*, *519*, 274-283. doi: 10.1016/j.epsl.2019.05.025

Davies, A., Kemp, A. E. S., & Pike, J. (2009). Late Cretaceous seasonal ocean variability from the Arctic. *Nature*, *460*, 254-258. doi: 10.1038/nature08141

Evans, D., Sagoo, N., Renema, W., Cotton, L. J., Müller, W., Todd, J. A., ... Affek, H. P. (2018). Eocene greenhouse climate revealed by coupled clumped isotope-Mg/Ca thermometry. *Proc. Natl. Acad. Sci. USA*, *115*(6), 1174–1179. doi: 10.1073/pnas.1714744115

Hand, J., Mahowald, N., Chen, Y., Siefert, R., Luo, C., Subramaniam, A., & Fung, I. (2004). Estimates of atmospheric-processed soluble iron from observations and a global mineral aerosol model: Biogeochemical implications. *J. Geophys. Res.*, *109*. doi: 10.1029/2004JD004574

Huber, M., & Caballero, R. (2011). The early Eocene equable climate problem revisited. *Clim. Past*, *7*(2), 603–633. doi: 10.5194/cp-7-603-2011

Hull, P. M., Bornemann, A., Penman, D. E., Henehan, M. J., Norris, R. D., Wilson, P. A., . . . Zachos, J. C. (2020). On impact and volcanism across the Cretaceous-Paleogene boundary. *Science*, *367*(6475), 266–272. doi: 10.1126/science.aay5055

Kump, L. R., & Pollard, D. (2008). Amplification of Cretaceous Warmth by Biological Cloud Feedbacks. *Science*, *320*(5873), 195–195. doi: 10.1126/science.1153883

Myriokefalitakis, S., Nenes, A., Baker, A. R., Mihalopoulos, N., & Kanakidou, M. (2016). Bioavailable atmospheric phosphorous supply to the global ocean: a 3-D global modeling study. *Biogeosciences*, *13*(24), 6519–6543. doi: 10.5194/bg-13-6519-2016

Niezgodzki, I., Knorr, G., Lohmann, G., Tyszka, J., & Markwick, P. J. (2017). Late Cretaceous climate simulations with different CO_2 levels and subarctic gateway configurations: A model-data comparison. *Paleoceanography*, *32*(9), 980-998. doi: 10.1002/2016PA003055

Ohno, S., Kadono, T., Kurosawa, K., Hamura, T., Sakaiya, T., Shigemori, K., . . . Sugita, S. (2014). Production of sulphate-rich vapour during the Chicxulub impact and implications for ocean acidification. *Nat. Geosci.*, *7*, 279-282. doi: 10.1038/ngeo2095

Pierazzo, E., Hahmann, A. N., & Sloan, C. (2003). Chicxulub and climate: radiative perturbations of impact-produced S-bearing gases. *Astrobiology*, *3*(1), 99–118. doi: 10.1089/153110703321632453

Tyrrell, T., Merico, A., & Mckay, D. I. A. (2015). Severity of ocean acidification following the end Cretaceous asteroid impact. *Proc. Natl. Acad. Sci. USA*, *112*(21), 6556– 6561.

doi: 10.1073/pnas.1418604112

Upchurch, J., G. R., Kiehl, J., Shields, C., Scherer, J., & Scotese, C. (2015, 08). Latitudinal temperature gradients and high-latitude temperatures during the latest Cretaceous: Congruence of geologic data and climate models. *Geology*, *43*(8), 683-686. doi: 10.1130/G36802.1

Zhu, J., Poulsen, C. J., & Tierney, J. E. (2019). Simulation of Eocene extreme warmth and high climate sensitivity through cloud feedbacks. *Sci. Adv.*, *5*(9). doi: 10.1126/sciadv.aax1874

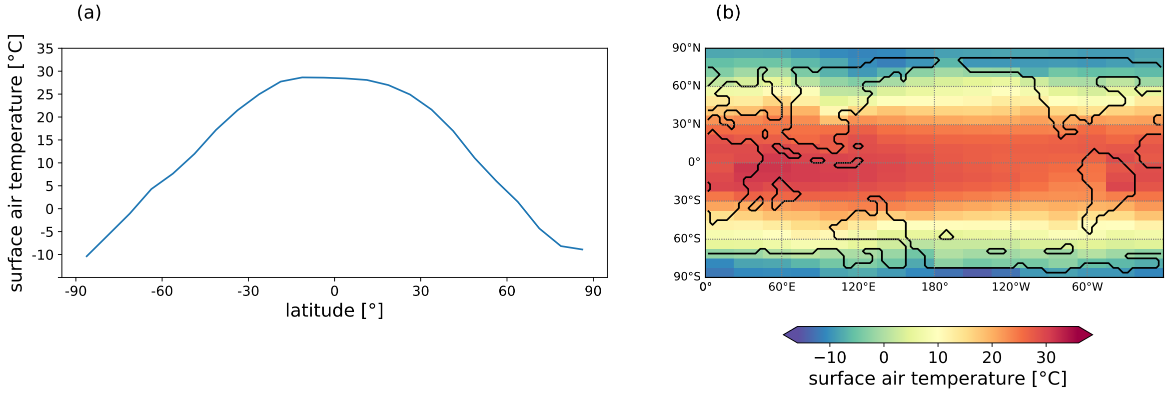

Figure S1. Surface air temperature for the late-Cretaceous climate state, 500 ppm atmospheric CO_2 concentration. (a) Annual and zonal means of surface air temperatures. (b) Map of annual mean surface air temperatures.

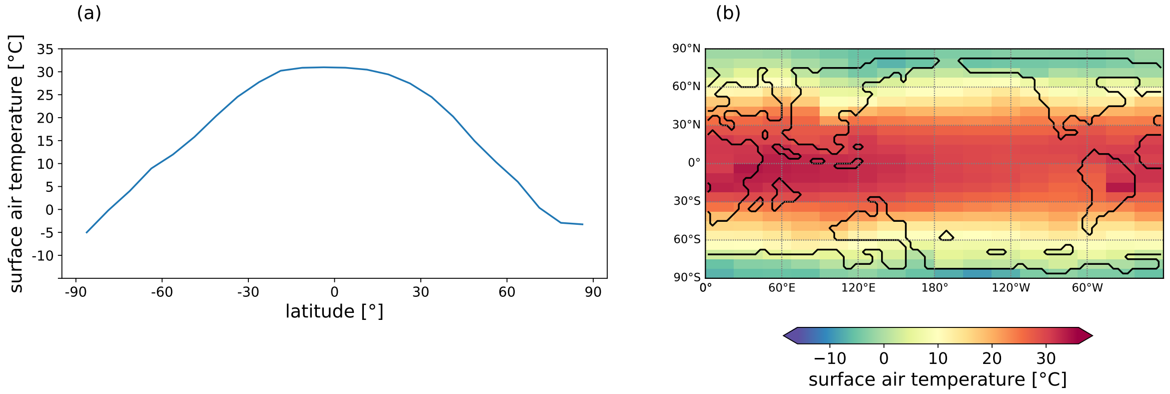

Figure S2. Surface air temperature for the late-Cretaceous climate state, 1165 ppm atmospheric CO_2 concentration. (a) Annual and zonal means of surface air temperatures. (b) Map of annual mean surface air temperatures.

Δ SST	**year 4**	**10-yrs mean**	**100-yrs mean**	**500-yrs mean**	**1000-yrs mean**
global	−15.6	−9.9	−2.1	−0.7	−0.4
global, 1165 ppm	−15.5	−9.6	−1.8	−0.3	−0.1
Brazos	−14.7	−9.8	−1.7	−0.5	−0.3
New Jersey	−11.3	−8.9	−2.2	−0.8	−0.5
+1500 Gt C	−15.4	−9.4	−0.8	+0.9	+1.1
+1500 Gt C, 1165 ppm	−15.4	−9.3	−1.1	+0.5	+0.8

Table S1. Sea surface temperature change for different time intervals and locations after the impact. Sea surface temperature changes for different times after the impact relative to mean of 100 years before the impact for the global mean, in the region around Brazos and in the region around New Jersey based on the standard impact run (115 Gt C, 100 Gt S) for a late-Cretaceous atmospheric CO_2 concentration of 500 ppm. In addition, the difference for the global mean of a run with additional 1500 Gt C from terrestrial sources is given. Global changes in SST are also shown for the high CO_2 pre-impact run (1165 ppm atmospheric CO_2 concentration). Note that the control simulation for the high CO_2 concentration shows a small drift which we take into account in the calculation of the temperature differences here ($\approx$+0.1°C per millennium).

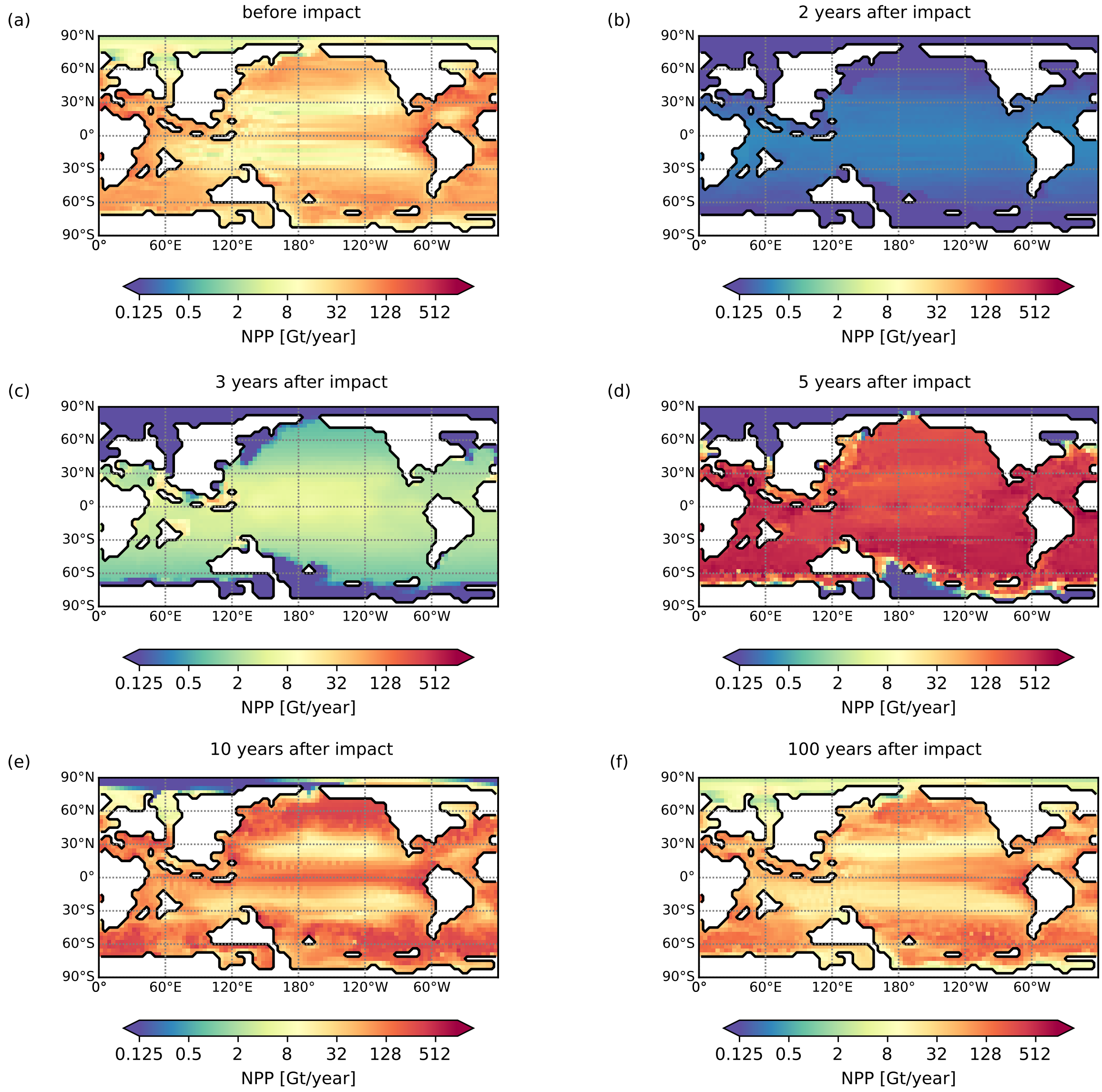

Figure S3. Maps of ocean primary productivity before and after the impact. Annual net primary productivity (NPP) before the impact (a, 100-year mean) and for 2 (b), 3 (c), 5 (d), 10 (e) and 100 (f) years after the impact for the standard run (115 Gt C and 100 Gt S). The maximum global mean NPP is reached in year 5 after the impact.

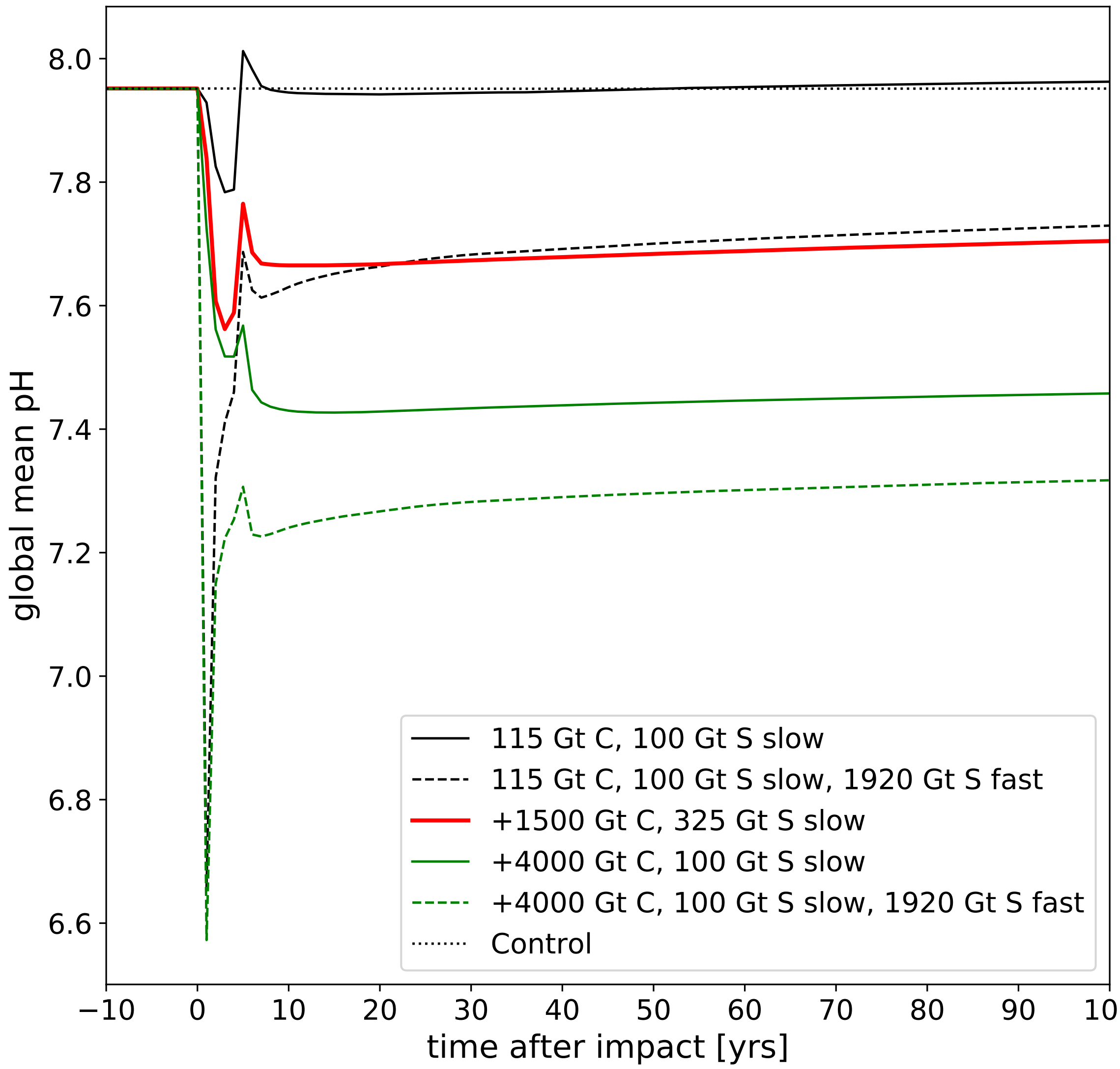

Figure S4. Change of global annual mean ocean pH after the impact for different amounts of carbon and sulfur. Global annual mean pH before and after the impact for 115 Gt C and 100 Gt S (black line) added during the impact; 115 Gt C, 100 Gt S and additional 1920 Gt S added in the first 10 days after the impact (black dashed line); additional 1500 Gt C and 325 Gt S (red line); additional 4000 Gt C and 100 Gt S (green line); additional 4000 Gt C, 100 Gt S and additional 1920 Gt S added in the first 10 days after the impact (green dashed line).

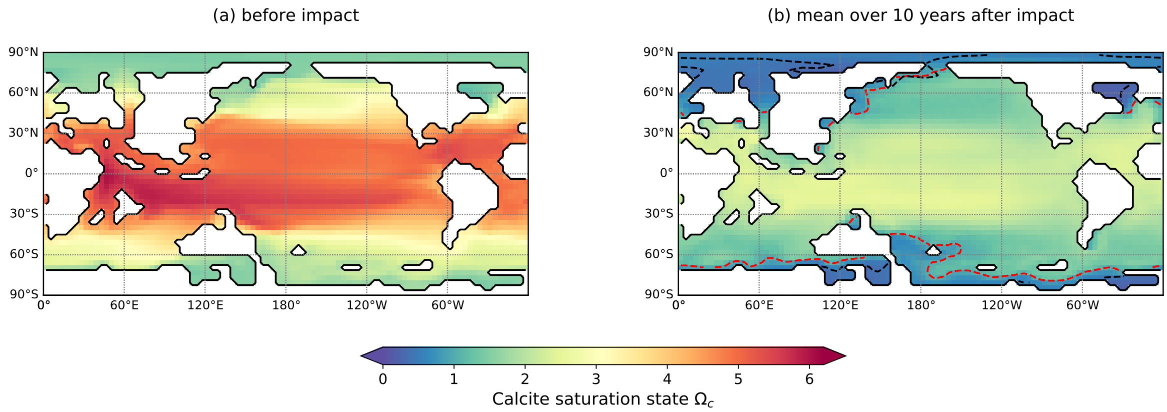

Figure S5. Effects of carbon and sulfur emissions from the impact on ocean acidification. Surface ocean calcite saturation state before the impact (a) and for the average over the 10 years after the impact for 1615 Gt C and 325 Gt S. The $\Omega_c = 1$ line is shown in red. The dashed black line in (b) shows $\Omega_a = 1$ for the 1000 years after the impact.

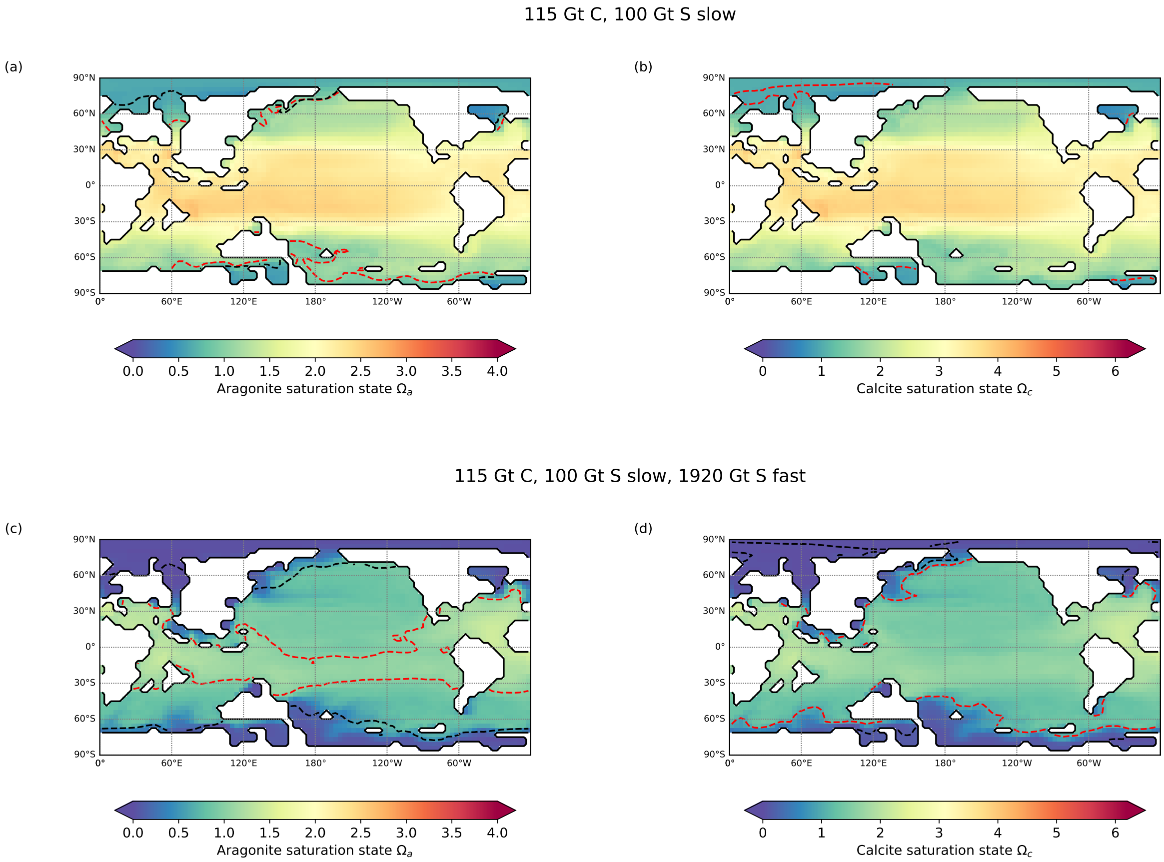

Figure S6. Surface ocean aragonite and calcite saturation state after the impact for 115 Gt C and different amounts of sulfur. Shown is the mean over the first 10 years after the impact and the contour lines for $\Omega = 1$ for the 10-year mean after the impact and 1000 years after the impact for the standard run with 115 Gt C and 100 Gt S (a and b) and the standard run with additional 1920 Gt S added in 10 days (c and d).

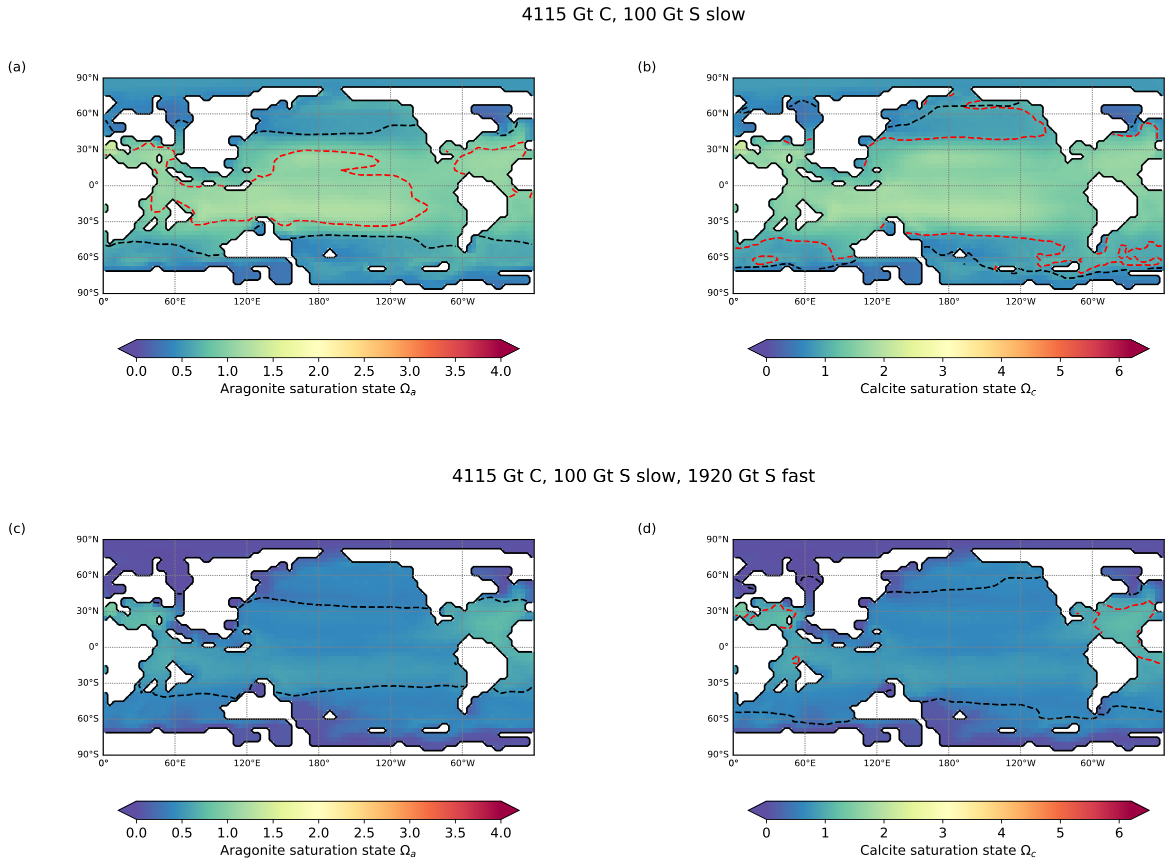

Figure S7. Surface ocean aragonite and calcite saturation state after the impact for 4115 Gt C and different amounts of sulfur. Shown is the mean over the first 10 years after the impact and the contour lines for $\Omega = 1$ for the 10-year mean after the impact and 1000 years after the impact for a run with 4115 Gt C, 100 Gt S (a and b) and additional 1920 Gt sulfur added in 10 days (c and d).

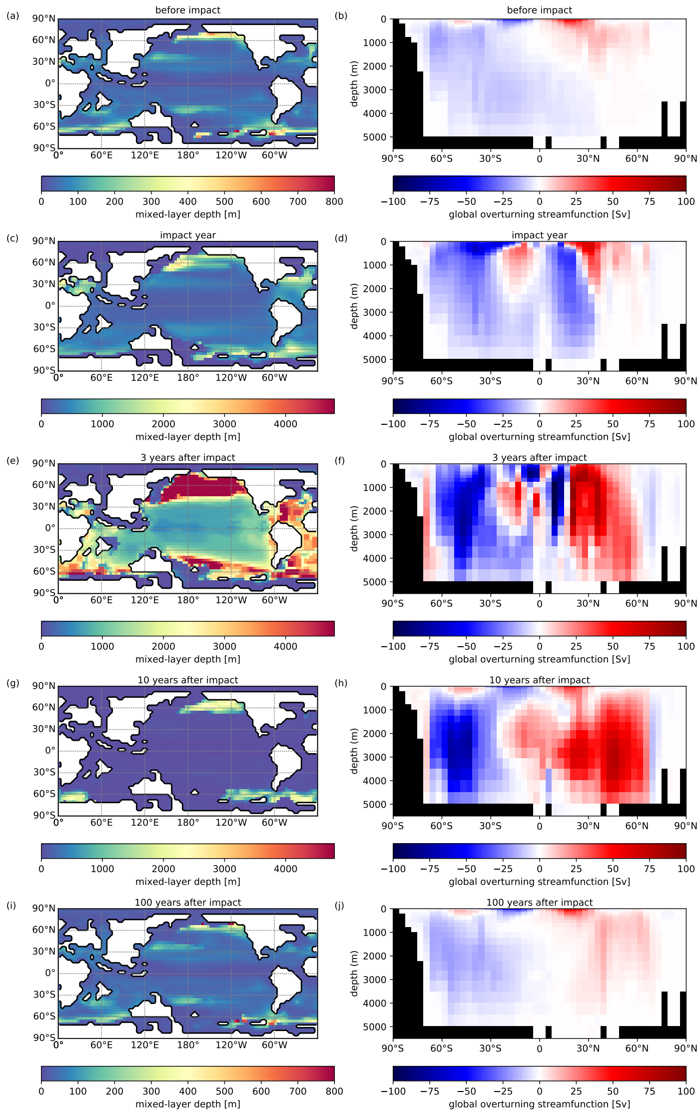

Figure S8. Changes in ocean circulation after the impact. Shown is the mixed-layer depth (first column) and the global overturning circulation (second column) for the pre-impact state (a, b), impact year (c, d), 3 years after the impact (e, f), 10 years after the impact (g, h) and 100 years after the impact (i, j). Note the different color scales for the pre-impact state and 100 years after the impact for the mixed-layer depth.

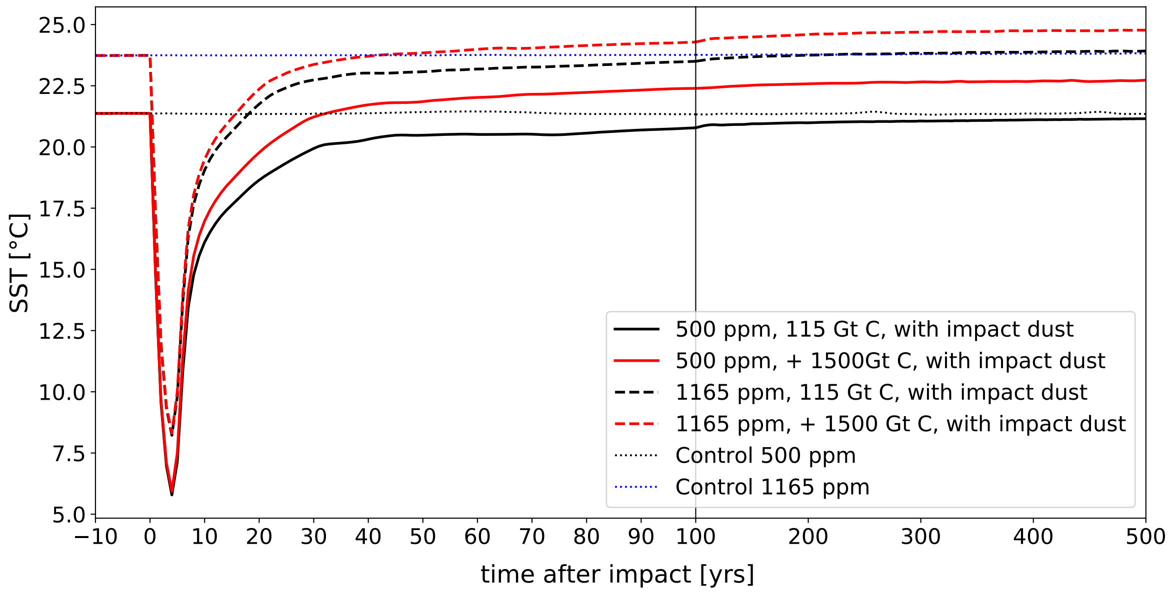

Figure S9. Sea surface temperature evolution for 500 ppm and 1165 ppm late-Cretaceous CO_2 concentration. Annual and global mean sea surface temperature before and after the impact for simulations with 115 Gt C and 100 Gt S (black) and additional 1500 Gt C and 100 Gt S added during the impact (red) for the 500 ppm and 1165 ppm (dashed) late-Cretaceous CO_2 concentration.

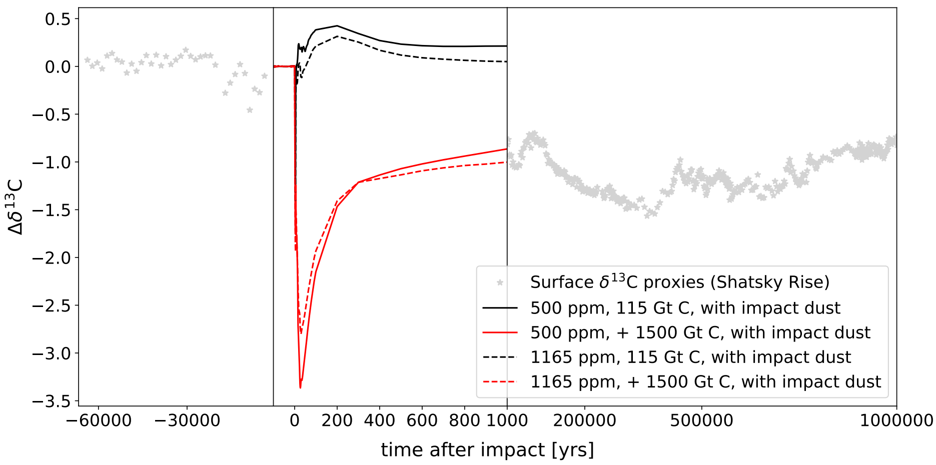

Figure S10. Changes of surface carbon isotope ratios of dissolved inorganic carbon at Shatsky Rise, Pacific, 500 ppm and 1165 ppm late-Cretaceous atmospheric CO_2 concentration. Coloured lines show modeled changes in $\delta^{13}C$ for the 1000 years after the impact relative to the 100-year pre-impact mean for simulations with different amounts of carbon. Dashed lines show modeled changes in $\delta^{13}C$ based on a 1165 ppm late-Cretaceous atmospheric CO_2 concentration for 115 and additional 1500 Gt C. The model results are embedded in changes in surface $\delta^{13}C$ from proxy data from bulk carbonate (Table S11 in Hull et al., 2020), assuming an absolute age for the K-Pg boundary of 66.022 Ma (Table S3 in Hull et al., 2020) relative to the mean of the pre-impact proxy values.

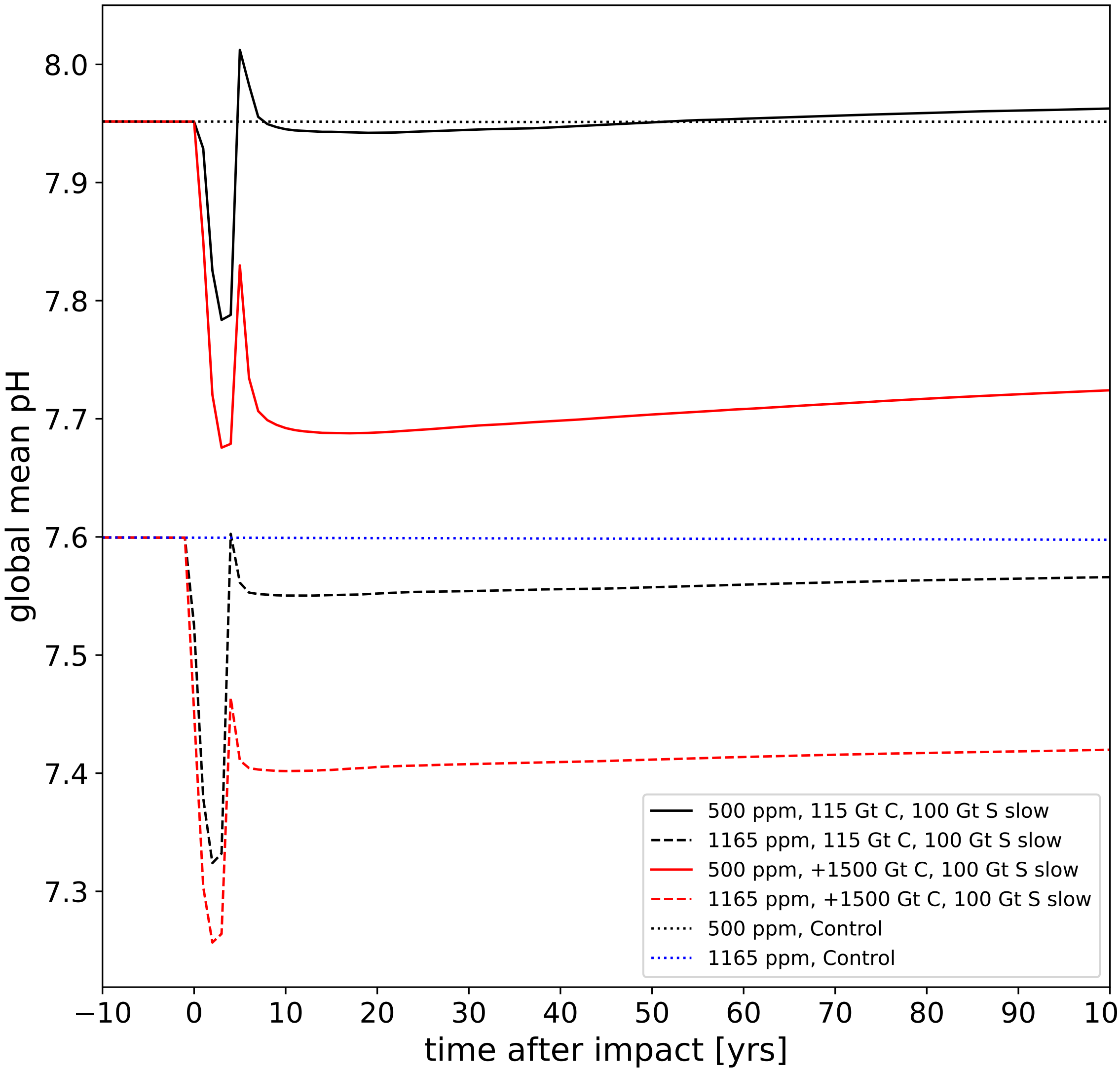

Figure S11. Change of global annual mean ocean pH after the impact for 500 ppm and 1165 ppm late-Cretaceous CO_2 concentration Global annual mean pH before and after the impact for 115 Gt C and 100 Gt S (black) and additional 1500 Gt C and 100 Gt S added during the impact (red) for the 500 ppm and 1165 ppm (dashed) late-Cretaceous CO_2 concentration. The control simulations for both late-Cretaceous simulations are shown as dotted lines.

Danksagung

Auf dem langen Weg dieser Arbeit haben mich viele Menschen auf unterschiedliche Art und Weise unterstützt und damit dazu beigetragen, dass ich an ihr in der Intensität und Dauer arbeiten konnte, wie ich es mir gewünscht habe.

Ich danke

ganz besonders ***Georg Feulner*** für deine intensive Betreuung; die vielen wissenschaftlichen Gespräche und Diskussionen, die mich so geprägt haben; das gemeinsame Gehen von manchmal ganz schön steinigen Wegen.

Stefan Rahmstorf für die vertrauensvolle Unterstützung meiner Arbeit.

Sonja Keel für deine Unterstützung als Mentorin, insbesondere am Anfang dieser Arbeit.

Stefan Petri für die vielfältigste Unterstützung, die man sich vorstellen kann. Insbesondere für die geduldige und humorvolle gemeinsame Lösung von CLIMBER Problemen.

Matthias Hofmann für die Ausdauer bei der Arbeit am Ozeanmodell und die vielen Einblicke in das Modell.

meinen vielen Kolleginnen und Kollegen am PIK für den guten wissenschaftlichen Austausch, aber auch für die vielen bereichernden und erfüllenden Begegnungen und Gespräche außerhalb der Wissenschaft. Insbesondere danke ich Klaus, Levke, Moritz, Jan, Willem, Vivien, Mona, Kristine und Fabian.

Gitta und Christine für eure gute Organisation im Hintergrund.

Thomas Nocke für die Flexibilität während meiner Arbeit im recam Projekt.

der Potsdam Graduate School für die Unterstützung mit einem Abschlussstipendium.

meiner neuen Arbeitsgruppe in Frankfurt, und insbesondere Thomas Hickler, für die Unterstützung bei den letzten Schritte dieser Arbeit.

Willem, Niels, Henning, Felix und Anna für eure hilfreichen Anmerkungen und guten Diskussionen im Schreibprozess dieser Arbeit.

meinen lieben Freundinnen und Freunden in Potsdam, dass ihr mein Leben außerhalb des PIKs immer so bunt und erfüllt gemacht habt.

Werner und Andreas für die tägliche Unterstützung dabei, Wissenschaft und Laufen vereinbaren zu können.

meinen Eltern Astrid und Martin sowie meiner Schwester Anna für eure bedingungslose Unterstützung und das Vertrauen in mich.

Felix für deine Unterstützung, deine Geduld, fürs Dasein.

Bibliography

Algeo, T. J., & Scheckler, S. E. 1998. Terrestrial-marine teleconnections in the Devonian: links between the evolution of land plants, weathering processes, and marine anoxic events. *Trans. R. Soc. Lond., B, Biol. Sci.*, **353**, 113–130.

Algeo, T. J., Berner, R. A., Maynard, J. B., & Scheckler, S. E. 1995. Late Devonian Oceanic Anoxic Events and Biotic Crises: "Rooted" in the Evolution of Vascular Land Plants? *GSA Today*, **5**(3), 45, 64–66.

Alley, R. B., Marotzke, J., Nordhaus, W., Overbeck, J., Peteet, D., Pielke, R., Pierhumbert, R., Rhines, P., Stocker, T., Talley, L., Wallace, J. M., Isern, A., Dandelski, J., Elfring, C., Gopnik, M., Kelly, M., Bachim, J., & Carlisle, A. 2002. *Abrupt Climate Change: Inevitable Surprises.* Washington, DC: National Research Council, The National Academies Press.

Alroy, J. 2008. Dynamics of origination and extinction in the marine fossil record. *Proc. Natl. Acad. Sci. USA*, **105**, 11536–11542.

Alroy, J., Aberhan, M., Bottjer, D. J., Foote, M., Fürsich, F. T., Harries, P. J., Hendy, A. J. W., Holland, S. M., Ivany, L. C., Kiessling, W., Kosnik, M. A., Marshall, C. R., McGowan, A. J., Miller, A. I., Olszewski, T. D., Patzkowsky, M. E., Peters, S. E., Villier, L., Wagner, P. J., Bonuso, N., Borkow, P. S., Brenneis, B., Clapham, M. E., Fall, L. M., Ferguson, C. A., Hanson, V. L., Krug, A. Z., Layou, K. M., Leckey, E. H., Nürnberg, S., Powers, C. M., Sessa, J. A., Simpson, C., Tomašových, A., & Visaggi, C. C. 2008. Phanerozoic Trends in the Global Diversity of Marine Invertebrates. *Science*, **321**(5885), 97–100.

Alvarez, L. W., Alvarez, W., Asaro, F., & Michel, H. V. 1980. Extraterrestrial Cause for the Cretaceous-Tertiary Extinction. *Science*, **208**(4448), 1095–1108.

Artemieva, N., & Morgan, J. 2009. Modeling the formation of the K-Pg boundary layer. *Icarus*, **201**(2), 768 – 780.

Artemieva, Natalia, Morgan, Joanna, & Party, Expedition 364 Science. 2017. Quantifying the Release of Climate-Active Gases by Large Meteorite Impacts With a Case Study of Chicxulub. *Geophys. Res. Lett.*, **44**(20), 10,180–10,188.

Bailer-Jones, C.A.L. 2009. The evidence for and against astronomical impacts on climate change and mass extinctions: a review. *Int. J. Astrobiol.*, **8**(3), 213–219.

Bambach, R., Knoll, Andrew, & Wang, Steve. 2004. Origination, extinction, and mass depletions of marine diversity. *Paleobiology*, **30**(12), 522.

Bambach, R. K. 2006. Phanerozoic Biodiversity Mass Extinctions. *Annu. Rev. Earth Planet. Sci.*, **34**(1), 127–155.

Bambach, R. K., Knoll, Andrew H., & Sepkoski, J. John. 2002. Anatomical and ecological constraints on Phanerozoic animal diversity in the marine realm. *Proc. Natl. Acad. Sci. USA*, **99**(10), 6854–6859.

Bardeen, C. G., Garcia, R. R., Toon, O. B., & Conley, A. J. 2017. On transient climate change at the Cretaceous-Paleogene boundary due to atmospheric soot injections. *Proc. Natl. Acad. Sci. USA*.

Barnosky, A., Matzke, N., Tomiya, S., Wogan, G., Swartz, B., Quental, T., Marshall, C., McGuire, J., Lindsey, E., Maguire, K. C., Mersey, B., & Ferrer, E. 2011. Has the Earth's Sixth Mass Extinction Already Arrived? *Nature*, **471**(03), 51–7.

Beljaars, A., Balsamo, G., Bechtold, P., Bozzo, A., Forbes, R., Hogan, R. J., Köhler, M., Morcrette, J., Tompkins, A. M., Viterbo, P., & Wedi, N. 2018. The Numerics of Physical Parametrization in the ECMWF Model. *Front. Earth Sci.*, **6**, 137.

Benton, M. J. 1995. Diversification and extinction in the history of life. *Science*, **268**(5207), 52–58.

Bergman, N.M, Lenton, T.M., & Watson, A. 2004. COPSE: A new model of biogeochemical cycling over Phanerozoic time. *Am. J. Sci.*, **304**(05), 397–437.

Berner, R. A., & Kothavala, Z. 2001. Geocarb III: A Revised Model of Atmospheric CO2 over Phanerozoic Time. *Am. J. Sci.*, **301**(2), 182–204.

Bond, David P.G., & Wignall, Paul B. 2014. Large igneous provinces and mass extinctions: An update. *Pages 29–55 of:* Keller, G., & Kerr, A. C. (eds), *Volcanism, Impacts, and Mass Extinctions: Causes and Effects*. Geol Soc. Am. Spec. Paper 505.

Boyce, C. K., & Lee, J.-E. 2017. Plant Evolution and Climate Over Geological Timescales. *Annu. Rev. Earth Planet. Sci.*, **45**, 61–87.

Brugger, J., Feulner, G., & Petri, S. 2017. Baby, it's cold outside: Climate model simulations of the effects of the asteroid impact at the end of the Cretaceous. *Geophys. Res. Lett.*, **44**(1), 419–427.

Brugger, J., Hofmann, M., Petri, S., & Feulner, G. 2019. On the Sensitivity of the Devonian Climate to Continental Configuration, Vegetation Cover, Orbital Configuration, CO_2 Concentration, and Insolation. *Paleoceanography and Paleoclimatology*, **34**(8), 1375–1398.

Brugger, J., Feulner, G., Hoffmann, M., & Petri, S. 2021, in press. A pronounced spike in ocean productivity triggered by the Chicxulub impact. *Geophys. Res. Lett.*, **48**, e2020GL092260.

Brune, S., Williams, S.E., & Müller, R.D. 2017. Potential links between continental rifting, CO_2 degassing and climate change through time. *Nature Geos.*, **10**, 941–946.

Burgess, S.D., Muirhead, J.D., & Bowring, S.A. 2017. Initial pulse of Siberian Traps sills as the trigger of the end-Permian mass extinction. *Nat. Commun.*, **8**, 164.

Butterfield, N. J. 2003. Exceptional fossil preservation and the Cambrian explosion. *Integr. Comp. Biol.*, **43**(1), 166–177.

Cascales-Miñana, B., & Cleal, C. J. 2014. The plant fossil record reflects just two great extinction events. *Terra Nova*, **26**(3), 195–200.

Caves, J. K., Jost, A. B., Lau, K. V., & Maher, K. 2016. Cenozoic carbon cycle imbalances and a variable weathering feedback. *Earth Planet. Sci. Lett.*, **450**, 152–163.

Chamberlin, T. 1909. Diastrophism as the ultimate basis of correlation. *The Journ. of Geol.*, **17**, 685–693.

Chapman, C., & Morrison, D. 1994. Impacts on the Earth by asteroids and comets: assessing the hazard. *Nature*, **367**, 33 – 40.

Ciais, P., Sabine, C., Bala, G., Bopp, L., Brovkin, V., Canadell, J., Chhabra, A., DeFries, R., Galloway, J., Heimann, M., Jones, C., Le Quéré, C., Myneni, R.B., Piao, S., & Thornton, P. 2013. Carbon and Other Biogeochemical Cycles. *In:* Stocker, T.F., Qin, D., Plattner, G.-K., Tignor, M., Allen, S.K., Boschung, J., Nauels, A., Xia, Y., Bex, V., &

Midgley, P. M. (eds), *Climate Change 2013: The Physical Science Basis. Contribution of Working Group I to the Fifth Assessment Report of the Intergovernmental Panel on Climate Change.* Cambridge University Press, Cambridge, United Kingdom and New York, NY, USA.

Clack, Jennifer A. 2007. Devonian climate change, breathing, and the origin of the tetrapod stem group. *Integrative and Comparative Biology*, **47**(4), 510–523.

Claussen, M., Mysak, L. A., Weaver, A., Crucifix, M., Fichefet, T., Loutre, M., Weber, S.L., Alcamo, J., Alexeev, V., Berger, A., Calov, R., Ganopolski, A., Goosse, H., Lohmann, G., Lunkeit, F., Mokhov, I., Petoukhov, V., Stone, P., & Wang, Z. 2002. Earth system models of intermediate complexity: Closing the gap in the spectrum of climate system models. *Clim. Dyn.*, **18**(03), 579–586.

Copper, Paul, & Scotese, Christopher. 2003. Megareefs in Middle Devonian supergreenhouse climates. *in Chan, M.A., and Archer, A.W., eds., Extreme depositional environments: Mega end members in geologic time: Boulder, Colorado, Geol S Am S*, **370**, 209–230.

Covey, C., Thompson, S. L., Weissman, P. R., & MacCracken, M. C. 1994. Global climatic effects of atmospheric dust from an asteroid or comet impact on Earth. *Glob. Planet. Change*, **9**(3), 263 – 273.

Crowley, T., & North, G. 1988. Abrupt Climate Change and Extinction Events in Earth History. *Science*, **240**(06), 996–1002.

Cuvier, G. 1825. *Discours sur les révolutions de la surface du globe.* Paris: G. Dufour.

Cuvier, G., & Jameson, R. 1818. *Essay on the Theory of the Earth.* New York: Kirk & Mercein.

Dahl, T. W., & Arens, S. K. M. 2020. The impacts of land plant evolution on Earth's climate and oxygenation state – An interdisciplinary review. *Chem. Geol.*, **547**, 119665.

Dahl, T. W., Hammarlund, E. U., Anbar, A. D., Bond, D. P. G., Gill, B. C., Gordon, G. W., Knoll, A. H., Nielsen, A. T., Schovsbo, N. H., & Canfield, D. E. 2010. Devonian rise in atmospheric oxygen correlated to the radiations of terrestrial plants and large predatory fish. *Proc. Natl. Acad. Sci. USA*, **107**(42), 17911–17915.

Dahl, T. W., Harding, M. A. R., Brugger, J., Feulner, G., Norrman, K., & Junium, C. submitted. Low atmospheric CO_2 levels before the emergence of forested ecosystems. *Nat. Commun.*

Danabasoglu, G., Lamarque, J.-F., Bacmeister, J., Bailey, D. A., DuVivier, A. K., Edwards, J., Emmons, L. K., Fasullo, J., Garcia, R., Gettelman, A., Hannay, C., Holland, M. M., Large, W. G., Lauritzen, P. H., Lawrence, D. M., Lenaerts, J. T. M., Lindsay, K., Lipscomb, W. H., Mills, M. J., Neale, R., Oleson, K. W., Otto-Bliesner, B., Phillips, A. S., Sacks, W., Tilmes, S., van Kampenhout, L., Vertenstein, M., Bertini, A., Dennis, J., Deser, C., Fischer, C., Fox-Kemper, B., Kay, J. E., Kinnison, D., Kushner, P. J., Larson, V. E., Long, M. C., Mickelson, S., Moore, J. K., Nienhouse, E., Polvani, L., Rasch, P. J., & Strand, W. G. 2020. The Community Earth System Model Version 2 (CESM2). *J. Adv. Model. Earth Syst.*, **12**(2), e2019MS001916.

Darwin, C. 1859. *On the origin of species by means of natural selection.* London: John Murray.

De Vleeschouwer, D., Rakocinski, M., Racki, G., Bond, D., Sobień, K., Bounceur, N., Crucifix, M., & Claeys, P. 2013. The astronomical rhythm of Late-Devonian climate change (Kowala section, Holy Cross Mountains, Poland). *Earth Planet Sc Lett*, 25–37.

De Vleeschouwer, D., Crucifix, M., Bounceur, N., & Claeys, P. 2014. The impact of astronomical forcing on the Late Devonian greenhouse climate. *Glob. Planet. Change*, **120**, 65–80.

De Vleeschouwer, D., Da Silva, A., Sinnesael, M., Chen, D., Day, J. E., Whalen, M. T., Guo, Z., & Claeys, P. 2017. Timing and pacing of the Late Devonian mass extinction event regulated by eccentricity and obliquity. *Nat. Commun.*, **8:2268**.

D'Hondt, S. 2005. Consequences of the Cretaceous/Paleogene Mass Extinction for Marine Ecosystems. *Annu. Rev. Ecol. Evol. Sys.*, **36**(11), 295–317.

Díaz, S., Settele, J., Brondízio, E. S., Ngo, H. T., Agard, J., Arneth, A., Balvanera, P., Brauman, K. A., Butchart, S. H. M., Chan, K. M. A., Garibaldi, L. A., Ichii, K., Liu, J., Subramanian, S. M., Midgley, G. F., Miloslavich, P., Molnár, Z., Obura, D., Pfaff, A., Polasky, S., Purvis, A., Razzaque, J., Reyers, B., Chowdhury, R. R., Shin, Y.-J., Visseren-Hamakers, I., Willis, K. J., & Zayas, C. N. 2019a. Pervasive human-driven decline of life on Earth points to the need for transformative change. *Science*, **366**(6471).

Díaz, S., Settele, J., Brondízio, E., Guùze, M., Agard, J., Arneth, A. Balvanera, P., Brauman, K., Butchart, S., Chan, K., Garibaldi, L., Ichii, K., Liu, J., Subramanian, S. M., Midgley, G., Miloslavich, P., Molnár, Z., Obura, D., Pfaff, A., Polasky, S., Purvis, A., Razzaque, J., Reyers, B., Chowdhury, R. R., Shin, Y.-J., Visseren-Hamakers, I., Willis, K., , & Zayas, C. 2019b. *Summary for policymakers of the global assessment report on biodiversity and ecosystem services of the Intergovernmental Science-Policy Platform on Biodiversity and Ecosystem Services.* Tech. rept. IPBES Secretariat, Bonn, Germany.

Donges, Jonathan F, Winkelmann, Ricarda, Lucht, Wolfgang, Cornell, Sarah E, Dyke, James G, Rockström, Johan, Heitzig, Jobst, & Schellnhuber, Hans Joachim. 2017. Closing the loop: Reconnecting human dynamics to Earth System science. *The Anthropocene Review*, **4**(2), 151–157.

Dunne, J. P., Horowitz, L. W., Adcroft, A. J., Ginoux, P., Held, I. M., John, J. G., Krasting, J. P., Malyshev, S., Naik, V., Paulot, F., Shevliakova, E., Stock, C. A., Zadeh, N., Balaji, V., Blanton, C., Dunne, K. A., Dupuis, C., Durachta, J., Dussin, R., Gauthier, P. P. G., Griffies, S. M., Guo, H., Hallberg, R. W., Harrison, M., He, J., Hurlin, W., McHugh, C., Menzel, R., Milly, P. C. D., Nikonov, S., Paynter, D. J., Ploshay, J., Radhakrishnan, A., Rand, K., Reichl, B. G., Robinson, T., Schwarzkopf, D. M., Sentman, L. T., Underwood, S., Vahlenkamp, H., Winton, M., Wittenberg, A. T., Wyman, B., Zeng, Y., & Zhao, M. 2020. The GFDL Earth System Model Version 4.1 (GFDL-ESM 4.1): Overall Coupled Model Description and Simulation Characteristics. *J. Adv. Model. Earth Syst.*, **12**(11), e2019MS002015.

D'Antonio, M. P., Ibarra, D. E., & Boyce, K. 2019. Land plant evolution decreased, rather than increased, weathering rates. *Geology*, **48**(1), 29–33.

Ebersole, J., Ikejiri, T., Blewitt, H., & Ebersole, S. 2013. An Overview of Late Cretaceous Vertebrates from Alabama. *Bull. Alab. Mus. Nat. Hist.*, **31**(05).

Eide, E. A. 2005. ANALYTICAL METHODS | Geochronological Techniques. *Pages 77–91 of:* Selley, R. C., Cocks, L. R. M., & Plimer, I. R. (eds), *Encyclopedia of Geology.* Oxford: Elsevier.

Ellis, J., & Schramm, D. N. 1995. Could a nearby supernova explosion have caused a mass extinction? *Proc. Natl. Acad. Sci. USA*, **92**(1), 235–238.

Ernst, Richard E., & Youbi, Nasrrddine. 2017. How Large Igneous Provinces affect global climate, sometimes cause mass extinctions, and represent natural markers in the geological record. *Palaeogeogr. Palaeoclimatol. Palaeoecol.*, **478**, 30 – 52.

Erwin, D. 2008. Extinctions as the Loss of Evolutionary History. *In:* Avise, J., Hubbel, S., & Ayala, F. (eds), *In the Light of Evolution, Volume II: Biodiversity and Extinction*. The National Academies Press.

Eyring, V., Bony, S., Meehl, G. A., Senior, C. A., Stevens, B., Stouffer, R. J., & Taylor, K. E. 2016. Overview of the Coupled Model Intercomparison Project Phase 6 (CMIP6) experimental design and organization. *Geosci. Model Dev.*, **9**(5), 1937–1958.

Fan, J., Shen, S., Erwin, D. H., Sadler, P. M., MacLeod, N., Cheng, Q., Hou, X., Yang, J., Wang, X., Wang, Y., Zhang, H., Chen, X., Li, G., Zhang, Y., Shi, Y., Yuan, D., Chen, Q., Zhang, L., Li, C., & Zhao, Y. 2020. A high-resolution summary of Cambrian to Early Triassic marine invertebrate biodiversity. *Science*, **367**(6475), 272–277.

Fastovsky, D. E., & Sheehan, P. 2005. The Extinction of the Dinosaurs in North America. *Gsa Today*, **15**(03).

Feulner, G. 2009. Climate modelling of mass-extinction events: a review. *Int. J. Astrobiol.*, **8**(3), 207–212.

Feulner, G. 2017. Formation of most of our coal brought Earth close to global glaciation. *Proc. Natl. Acad. Sci. USA*, **114**, 11333–11337.

Feulner, G., & Kienert, H. 2014. Climate simulations of Neoproterozoic snowball Earth events: Similar critical carbon dioxide levels for the Sturtian and Marinoan glaciations. *Earth Planet. Sci. Lett.*, **404**, 200 – 205.

Fichefet, T., & Morales Maqueda, M. A. 1997. Sensitivity of a global sea ice model to the treatment of ice thermodynamics and dynamics. *J. Geophys. Res.*, **102**(C6), 12609–12646.

Fields, B. D., Melott, A. L., Ellis, J., Ertel, A. F., Fry, B. J., Lieberman, B. S., Liu, Z., Miller, J. A., & Thomas, B. C. 2020. Supernova triggers for end-Devonian extinctions. *Proc. Natl. Acad. Sci. USA*, **117**(35), 21008–21010.

Finnegan, S., Heim, N. A., Peters, S. E., & Fischer, W. W. 2012. Climate change and the selective signature of the Late Ordovician mass extinction. *Proc. Natl. Acad. Sci. USA*, **109**(18), 6829–6834.

Fischer, A. G., & Arthur, M. A. 1977. Secular Variations In The Pelagic Realm. *In: Deep-Water Carbonate Environments*. SEPM (Soc. Sediment. Geol.).

Foote, M. 1994. Temporal variation in extinction risk and temporal scaling of extinction metrics. *Paleobiology*, **20**(4), 424–444.

Foster, G., Royer, D., & Lunt, D. 2017. Future climate forcing potentially without precedent in the last 420 million years. *Nat. Commun.*, **8**, 14845.

Friedrich, O., Norris, R., & Erbacher, J. 2012. Evolution of middle to Late Cretaceous oceans - A 55 m.y. record of Earth's temperature and carbon cycle. *Geology*, **40**(02), 107–110.

Gao, T., Yin, X., Shih, C., Rasnitsyn, A. R., Xu, X., Chen, S., Wang, C., & Ren, D. 2019. New insects feeding on dinosaur feathers in mid-Cretaceous amber. *Nat. Commun.*, **10**, 5424.

Ginot, S., & Goudemand, N. 2020. Global climate changes account for the main trends of conodont diversity but not for their final demise. *Glob. and Planet. Change*, **195**, 103325.

Grieve, R. 1998. Extraterrestrial impacts on Earth: The evidence and the consequences. *Geol. Soc. Spec. Publ.*, **140**(01), 105–131.

Gulick, S. P. S., Bralower, T. J., Ormö, J., Hall, B., Grice, K., Schaefer, B., Lyons, S., Freeman, K. H., Morgan, J. V., Artemieva, N., Kaskes, P., de Graaff, S. J., Whalen, M. T., Collins, G. S., Tikoo, S. M., Verhagen, C., Christeson, G. L., Claeys, P., Coolen, M. J. L., Goderis, S., Goto, K., Grieve, R. A. F., McCall, N., Osinski, G. R., Rae, A. S. P., Riller, U., Smit, J., Vajda, V., Wittmann, A., & the Expedition 364 Scientists. 2019. The first day of the Cenozoic. *Proc. Natl. Acad. Sci. USA*, **116**(39), 19342–19351.

Gunderson, A. R., Armstrong, E. J., & Stillman, J. H. 2016. Multiple Stressors in a Changing World: The Need for an Improved Perspective on Physiological Responses to the Dynamic Marine Environment. *Ann. Rev. Mar. Sci.*, **8**(1), 357–378.

Hallam, A., & Wignall, P.B. 1997. *Mass Extinctions and their Aftermath.* 1 edn. Oxford, UK: Oxford Univeristy Press.

Hay, W. W. 1996. Tectonics and climate. *Geol. Rundschu.*, **85**, 409–437.

Henkes, G. A., Passey, B. H., Grossman, E. L., Shenton, B. J., Yancey, T. E., & Pérez-Huerta, A. 2018. Temperature evolution and the oxygen isotope composition of Phanerozoic oceans from carbonate clumped isotope thermometry. *Earth Planet. Sci. Lett.*, **490**, 40 – 50.

Herrmann, A. D., Patzkowsky, M. E., & Pollard, D. 2003. Obliquity forcing with 8–12 times preindustrial levels of atmospheric pCO2 during the Late Ordovician glaciation. *Geology*, **31**(6), 485–488.

Hess, Dieter. 2005. *Systematische Botanik : 4 Tabellen.* Stuttgart: Ulmer.

Hildebrand, A., Penfield, G., Kring, D., Pilkington, M., Camargo, Z., & Jacobsen, S. 1991. Chicxulub Crater: A possible Cretaceous/Tertiary boundary impact crater on the Yucatan Peninsula, Mexico. *Geology*, **19**(09), 867–871.

Hofmann, M., & Morales Maqueda, M. A. 2006. Performance of a second-order moments advection scheme in an Ocean General Circulation Model. *J. Geophys. Res. Oceans*, **111**(C5).

Hofmann, M., Mathesius, S., Kriegler, E., van Vuuren, D.P., & Schellnhuber, H. J. 2019. Strong time dependence of ocean acidification mitigation by atmospheric carbon dioxide removal. *Nature Commun.*, **10**, 5592.

Huber, B., MacLeod, K., Watkins, D., & Coffin, M. 2018. The rise and fall of the Cretaceous Hot Greenhouse climate. *Glob. Planet. Change*, **167**(08).

Hull, P. 2015. Life in the Aftermath of Mass Extinctions. *Curr. Biol.*, **25**(19), R941 – R952.

Hull, P. M., & Darroch, S. A. F. 2013. Mass Extinctions and the Structure and Function of Ecosystems. *Paleont. Soc. Papers*, **19**, 115–156.

Hull, P. M., Bornemann, A., Penman, D. E., Henehan, M. J., Norris, R. D., Wilson, P. A., Blum, P., Alegret, L., Batenburg, S. J., Bown, P. R., Bralower, T. J., Cournede, C., Deutsch, A., Donner, B., Friedrich, O., Jehle, S., Kim, H., Kroon, D., Lippert, P. C., Loroch, D., Moebius, I., Moriya, K., Peppe, D. J., Ravizza, G. E., Röhl, U., Schueth, J. D., Sepúlveda, J., Sexton, P. F., Sibert, E. C., Śliwińska, K. K., Summons, R. E., Thomas, E., Westerhold, T., Whiteside, J. H., Yamaguchi, T., & Zachos, J. C. 2020. On impact and volcanism across the Cretaceous-Paleogene boundary. *Science*, **367**(6475), 266–272.

Ibarra, D. E., Caves Rugenstein, J. K., Bachan, A., Baresch, A., Lau, K. V., Thomas, D. L., Lee, J., Boyce, C. K., & Chamberlain, C. P. 2019. Modeling the consequences of land plant evolution on silicate weathering. *Am. J. Sci.*, **319**(1), 1–43.

Irmis, R. B., & Whiteside, J. H. 2012. Delayed recovery of non-marine tetrapods after the end-Permian mass extinction tracks global carbon cycle. *Proc. R. Soc. Lond. B. Biol. Sci.*, **279**(1732), 1310–1318.

Jaffrés, J. B. D., Shields, G. A., & Wallmann, K. 2007. The oxygen isotope evolution of seawater: A critical review of a long-standing controversy and an improved geological water cycle model for the past 3.4 billion years. *Earth Sci. Rev.*, **83**(1), 83–122.

Joachimski, Michael, Breisig, S, Buggisch, Werner, Talent, John, Mawson, Ruth, Gereke, M, Morrow, J.R., Day, Jed, & Weddige, K. 2009. Devonian climate and reef evolution: Insights from oxygen isotopes in apatite. *Earth. Planet. Sc. Lett*, **284**, 599–609.

Jurikova, H., Gutjahr, M., Wallmann, K., Flögel, S., Liebetrau, V., Posenato, R., Angiolini, L., Garbelli, C., Brand, U., Wiedenbeck, M., & Eisenhauer, A. 2020. Permian–Triassic mass extinction pulses driven by major marine carbon cycle perturbations. *Nat. Geosci.*, **13**(11).

Keller, G. 1988. Biotic turnover in benthic foraminifera across the cretaceous/tertiary boundary at El Kef, Tunisia. *Palaeogeogr., Palaeoclim., Palaeoecol.*, **66**(3), 153 – 171.

Keller, G. 1994. K-T Boundary Issues. *Science*, **264**(5159), 641–641.

Keller, G. 2003. Biotic effects of impacts and volcanism. *Earth Planet. Sci. Lett.*, **215**(1), 249 – 264.

Keller, G., Adatte, T., Berner, Z., Harting, M., Baum, G., Prauss, M., Tantawy, A., & Stueben, D. 2007. Chicxulub impact predates K–T boundary: New evidence from Brazos, Texas. *Earth Planet. Sci. Lett.*, **255**(3), 339 – 356.

Keller, G., Mateo, P., Monkenbusch, J., Thibault, N., Punekar, J., Spangenberg, J. E., Abramovich, S., Ashckenazi-Polivoda, S., Schoene, B., Eddy, M. P., Samperton, K. M., Khadri, S. F. R., & Adatte, T. 2020. Mercury linked to Deccan Traps volcanism, climate change and the end-Cretaceous mass extinction. *Glob. Planet. Change*, **194 (2020) 103312**, 1–17.

Kirchner, J. W., & Weil, A. 2000. Correlations in fossil extinction and origination rates through geological time. *Proc. R. Soc. Lond. B. Biol. Sci.*, **267**(1450), 1301–1309.

Knoop, V., & Müller, K. 2009. *Gene und Stammbäume: Ein Handbuch zur molekularen Phylogenetik*. 2 edn. Spektrum Akademischer Verlag.

Kring, D. A. 2007. The Chicxulub impact event and its environmental consequences at the Cretaceous–Tertiary boundary. *Palaeogeogr., Palaeoclimatol., Palaeoecol.*, **255**(1), 4 – 21.

Labandeira, Conrad C. 2005. The Fossil Record of Insect Extinction: New Approaches and Future Directions. *Am Entomol.*, **51**(1), 14–29.

Landwehrs, J. P., Feulner, G., Hofmann, M., & Petri, S. 2020. Climatic fluctuations modeled for carbon and sulfur emissions from end-Triassic volcanism. *Earth Planet. Sci. Lett.*, **537**, 116174.

LARSON, R. L. 1991. Latest pulse of Earth: Evidence for a mid-Cretaceous superplume. *Geology*, **19**(6), 547–550.

LE HIR, GUILLAUME, DONNADIEU, YANNICK, GODDÉRIS, YVES, MEYER-BERTHAUD, BRIGITTE, RAMSTEIN, GILLES, & BLAKEY, RONALD C. 2011. The climate change caused by the land-plant invasion in the Devonian. *Earth Planet. Sci. Lett.*, **310**, 203–212.

LECLÈRE, D., BARRETT, M., BUTCHART, S., CHAUDHARY, A., DE PALMA, A., DECLERCK, F., DI MARCO, M., DOELMAN, J., DÜRAUER, M., FREEMAN, R., HASEGAWA, T., HELLWEG, S., HILBERS, J., HILL, S., HUMPEN"ODER, F., JENNINGS, N., KRISZTIN, T., & YOUNG, L. 2020. Bending the curve of terrestrial biodiversity needs an integrated strategy. *Nature*, **585**(09), 1–6.

LÉCUYER, C., PICARD, S., GARCIA, J., SHEPPARD, S. M. F., GRANDJEAN, P., & DROMART, G. 2003. Thermal evolution of Tethyan surface waters during the Middle-Late Jurassic: Evidence from δ^{18}O values of marine fish teeth. *Paleoceanography*, **18**(3).

LÉCUYER, C., AMIOT, R., TOUZEAU, A., & TROTTER, J. 2013. Calibration of the phosphate δ^{18}O thermometer with carbonate–water oxygen isotope fractionation equations. *Chem. Geol.*, **347**, 217–226.

LENTON, T., & WATSON, A. 2011. *Revolutions that made the Earth*. 1 edn. Oxford, UK: Oxford Univeristy Press.

LENTON, T., CROUCH, M., JOHNSON, M., PIRES, N, & DOLAM, L. 2012. First plants cooled the Ordovician. *Nat. Geosci.*, **5**, 86–89.

LENTON, T. M., HELD, H., KRIEGLER, E., HALL, J. W., LUCHT, W., RAHMSTORF, S., & SCHELLNHUBER, H. J. 2008. Tipping elements in the Earth's climate system. *Proc. Natl. Acad. Sci. USA*, **105**(6), 1786–1793.

LENTON, T. M., DAINES, S. J., & MILLS, B. J. W. 2018. COPSE reloaded: An improved model of biogeochemical cycling over Phanerozoic time. *Earth Sci. Rev.*, **178**, 1–28.

LINDSTRÖM, S., VAN DE SCHOOTBRUGGE, B., HANSEN, K. H., PEDERSEN, G. K., ALSEN, P., THIBAULT, N., DYBKJAER, K., BJERRUM, C. J., & NIELSEN, L. H. 2017. A new correlation of Triassic–Jurassic boundary successions in NW Europe, Nevada and Peru, and the Central Atlantic Magmatic Province: A time-line for the end-Triassic mass extinction. *Palaeogeogr. Palaeoclimatol. Palaeoecol.*, **478**, 80 – 102.

LUCAS, S. G., & TANNER, L. H. 2015. End-Triassic nonmarine biotic events. *J. Palaeogeogr.*, **4**(4), 331 – 348.

Lucas, S.G., & Tanner, L.H. 2018. The Missing Mass Extinction at the Triassic-Jurassic Boundary. *Pages 721–785 of:* Tanner, L. (ed), *The Late Triassic World. Topics in Geobiology*, vol. 46. Springer, Cham.

Maxwell, Sean, Fuller, Richard, Brooks, Thomas, & Watson, James. 2016. Biodiversity: The ravages of guns, nets and bulldozers. *Nature*, **536**(08), 143–145.

McFarlane, N. 2011. Parameterizations: representing key processes in climate models without resolving them. *WIREs Clim. Change*, **2**(4), 482–497.

McGhee, G. R., Gilmore, J. S., Orth, C. J., & Olsen, E. 1984. No geochemical evidence for an asteroidal impact at late Devonian mass extinction horizon. *Nature*, **308**(5960), 629–631.

McGuffie, K., & Henderson-Sellers, A. 2014. *The Climate Modelling Primer*. 4 edn. West Sussex, UK: Wiley Blackwell.

McLean, D. M. 1985. Deccan traps mantle degassing in the terminal Cretaceous marine extinctions. *Cretaceous Research*, **6**(3), 235 – 259.

Melott, A.L., Lieberman, B.S., Laird, C.M., Martin, L.D., Medvedev, M.V., Thomas, B.C., Cannizzo, J.K., Gehrels, N., & Jackman, C.H. 2004. Did a gamma-ray burst initiate the late Ordovician mass extinction? *Int. J. Astrobiol.*, **3**(1), 55–61.

Milankovitch, M. 1941. *Kanon der Erdbestrahlung und seine Anwendung auf das Eiszeitenproblem*. Königlich Serbische Akademie, Belgrad.

Montoya, M., Griesel, A., Levermann, A., Mignot, J., Hofmann, M., Ganopolski, A., & Rahmstorf, S. 2005. The earth system model of intermediate complexity CLIMBER-3α. Part I: description and performance for present-day conditions. *Clim. Dyn.*, **25**(2-3), 237–263.

Neukum, G., Ivanov, B., & Hartmann, W. 2001. Cratering Records in the Inner Solar System in Relation to the Lunar Reference System. *Space Sci. Rev.*, **96**.

Newell, N. D. 1967. Revolutions in the History of Life. *In:* Albritton, C. Jr. (ed), *Uniformity and Simplicity: A Symposium on the Principle of the Uniformity of Nature*. Geological Society of America.

Nowak, H., Schneebeli-Hermann, E., & Kustatscher, E. 2019. No mass extinction for land plants at the Permian–Triassic transition. *Nat. Commun.*, **10**(384).

O'Brien, C. L., Robinson, S. A., Pancost, R. D., Sinninghe DamstDamsté, J. S., Schouten, S., Lunt, D. J., Alsenz, H., Bornemann, A., Bottini, C., Brassell, S. C., Farnsworth, A., Forster, A., Huber, B. T., Inglis, G. N., Jenkyns, H. C., Linnert, C., Littler, K., Markwick, P., McAnena, A., Mutterlose, J., Naafs, B. D. A., Püttmann, W., Sluijs, A., N. A. G. M. van Helmond, N. A. G. M., Vellekoop, J., Wagner, T., & Wrobel, N. E. 2017. Cretaceous sea-surface temperature evolution: Constraints from TEX_{86} and planktonic foraminiferal oxygen isotopes. *Earth-Science Reviews*, **172**, 224 – 247.

Oeser, R. A., & von Blanckenburg, F. 2020. Do degree and rate of silicate weathering depend on plant productivity? *Biogeosciences*, **17**(19), 4883–4917.

O'Leary, M. A., Bloch, J. I., Flynn, J. J., Gaudin, T. J., Giallombardo, A., Giannini, N. P., Goldberg, S. L., Kraatz, B. P., Luo, Z., Meng, J., Ni, X., Novacek, M. J., Perini, F. A., Randall, Z. S., Rougier, G. W., Sargis, E. J., Silcox, M. T., Simmons, N. B., Spaulding, M., Velazco, P. M., Weksler, M., Wible, J. R., & Cirranello, A. L. 2013. The Placental Mammal Ancestor and the Post–K-Pg Radiation of Placentals. *Science*, **339**(6120), 662–667.

Pacanowski, R. C., & Griffies, S. M. 1999. *The MOM-3 Manual.* Tech. rept. 4. GFDL Ocean Group, NOAA/Geophysical Fluid Dynamics Laboratory, Princeton, NJ.

Payne, J. L., Lehrmann, D. J., Wei, J., Orchard, M. J., Schrag, D. P., & Knoll, A. H. 2004. Large Perturbations of the Carbon Cycle During Recovery from the End-Permian Extinction. *Science*, **305**(5683), 506–509.

Penman, D. E., Caves Rugenstein, J. K., Ibarra, D. E., & Winnick, M. J. 2020. Silicate weathering as a feedback and forcing in Earth's climate and carbon cycle. *Earth Sci. Rev.*, **209**, 103298.

Petoukhov, V., Ganopolski, A., Brovkin, V., Claussen, M., Eliseev, A., Kubatzki, C., & Rahmstorf, S. 2000. CLIMBER-2: a climate system model of intermediate complexity. Part I: model description and performance for present climate. *Clim. Dyn.*, **16**(1), 1–17.

Pierazzo, E., Kring, D. A., & Melosh, H. J. 1998. Hydrocode simulation of the Chicxulub impact event and the production of climatically active gases. *J. Geophys. Res.*, **103**(E12), 28607–28625.

Pierazzo, E., Hahmann, A. N., & Sloan, C. 2003. Chicxulub and climate: radiative perturbations of impact-produced S-bearing gases. *Astrobiology*, **3**(1), 99–118.

Pope, K. O. 2002. Impact dust not the cause of the Cretaceous-Tertiary mass extinction. *Geology*, **30**(2), 99–102.

Pope, K. O., Baines, K. H., Ocampo, A. C., & Ivanov, B. A. 1997. Energy, volatile production, and climatic effects of the Chicxulub Cretaceous/Tertiary impact. *J. Geophys. Res. Planets*, **102**(E9), 21645–21664.

Porada, P., Lenton, T., Pohl, A., Weber, B., Mander, L., Donnadieu, Y., Beer, C., Pöschl, U., & Kleidon, A. 2016. High potential for weathering and climate effects of non-vascular vegetation in the Late Ordovician. *Nat. Commun.*, **7**(07), 12113.

Rae, J. W. B., Zhang, Y. G., Liu, X., Foster, G. L., Stoll, H. M., & Whiteford, R. D. M. 2021. Atmospheric CO_2 over the Past 66 Million Years from Marine Archives. *Annu. Rev. of Earth Planet. Sci.*, **49**(1), 599–631.

Raup, D. M. 1994. The role of extinction in evolution. *Proc. Natl. Acad. Sci. USA*, **91**(15), 6758–6763.

Raup, D. M., & Sepkoski, J. J. 1982. Mass Extinctions in the Marine Fossil Record. *Science*, **215**(4539), 1501–1503.

Raup, D. M., & Sepkoski, J. J. 1984. Periodicity of extinctions in the geologic past. *Proc. Natl. Acad. Sci. USA*, **81**(3), 801–805.

Raup, D. M., & Sepkoski, J. J. 1986. Periodic extinction of families and genera. *Science*, **231**(4740), 833–836.

Reid, G., Isaksen, I., Holzer, T., & Crutzen, P. J. 1976. Influence of ancient solar-proton events on the evolution of life. *Nature*, **259**, 177–179.

Renne, P. R., Deino, A. L., Hilgen, F. J., Kuiper, K. F., Mark, D. F., Mitchell, W. S., Morgan, L. E., Mundil, R., & Smit, J. 2013. Time Scales of Critical Events Around the Cretaceous-Paleogene Boundary. *Science*, **339**(Feb.), 684–687.

Rigo, M., Onoue, T., Tanner, L. H., Lucas, S. G., Godfrey, L., Katz, M. E., Zaffani, M., Grice, K., Cesar, J., Yamashita, D., Maron, M., Tackett, L. S., Campbell, H., Tateo, F., Concheri, G., Agnini, C., Chiari, M., & Bertinelli, A. 2020. The Late Triassic Extinction at the Norian/Rhaetian boundary: Biotic evidence and geochemical signature. *Earth Sci. Rev.*, **204**, 103180.

Robertson, D. S., Lewis, W. M., Sheehan, P. M., & Toon, O. B. 2013. K-Pg extinction: Reevaluation of the heat-fire hypothesis. *J. Geophys. Res. Biogeosci.*, **118**(1), 329–336.

Rohde, R., & Muller, R. 2005. Cycles in fossil diversity. *Nature*, **434**(04), 208–10.

ROTHMAN, D. H. 2017. Thresholds of catastrophe in the Earth system. *Sci. Adv.*, **3**(9).

ROYER, D. L. 2006. CO_2-forced climate thresholds during the Phanerozoic. *Geochim. Cosmochim. Ac.*, **70**(23), 5665–5675.

RUDDIMAN, W. F. 2013. *Earth's climate - Past and Future*. 4 edn. New York: W. H. Freeman and Company.

SAHNEY, S., & BENTON, M. J. 2008. Recovery from the most profound mass extinction of all time. *Proc. R. Soc. Lond. B. Biol. Sci.*, **275**(1636), 759–765.

SANROMÁ, E., PALLÉ, E., & GARCÍA MUNÕZ, A. 2013. On the Effects of the Evolution of Microbial Mats and Land Plants on the Earth as a Planet. Photometric and Spectroscopic Light Curves of Paleo-Earths. *Astrophys. J.*, **766**, 133.

SCHELLNHUBER, H. 1999. 'Earth system' analysis and the second Copernican revolution. *Nature*, **402**, C19–C23.

SCHMIDT, A., SKEFFINGTON, R., THORDARSON, T., SELF, S. PIERS, FORSTER, M., RAP, A., RIDGWELL, A., FOWLER, D., WILSON, M., MANN, G. W., WIGNALL, P. W., & CARSLAW, K. S. 2016. Selective environmental stress from sulphur emitted by continental flood basalt eruptions. *Nature Geosci.*, **9**, 77–82.

SCHMIEDER, M., & KRING, D. A. 2020. Earth's Impact Events Through Geologic Time: A List of Recommended Ages for Terrestrial Impact Structures and Deposits. *Astrobiology*, **20**(1), 91–141.

SCHOENE, B., SAMPERTON, K. M., EDDY, M. P., KELLER, G., ADATTE, T., BOWRING, S. A., KHADRI, S. F. R., & GERTSCH, B. 2015. U-Pb geochronology of the Deccan Traps and relation to the end-Cretaceous mass extinction. *Science*, **347**(6218), 182–184.

SCHOENE, B., EDDY, M. P., SAMPERTON, K. M., KELLER, C. B., KELLER, G., ADATTE, T., & KHADRI, S. F. R. 2019. U-Pb constraints on pulsed eruption of the Deccan Traps across the end-Cretaceous mass extinction. *Science*, **363**(6429), 862–866.

SCHUBERT, B. A., & JAHREN, A. H. 2015. Global increase in plant carbon isotope fractionation following the Last Glacial Maximum caused by increase in atmospheric pCO2. *Geology*, 435–438.

SCHULTE, P., ALEGRET, L., ARENILLAS, I., ARZ, J. A., BARTON, P. J., BOWN, P. R., BRALOWER, T. J., CHRISTESON, G. L., CLAEYS, P., COCKELL, C. S., COLLINS, G. S., DEUTSCH, A., GOLDIN, T. J., GOTO, K., GRAJALES-NISHIMURA, J. M., GRIEVE, R. A. F., GULICK, S. P. S., JOHNSON, K. R., KIESSLING, W., Koeberl, C., Kring, . A., MacLeod, K. G., Matsui, T., Melosh, J., Montanari, A., Morgan, J. V., Neal, C. R., Nichols, D. J., Norris, R. D., Pierazzo, E., Ravizza, G., Rebolledo-Vieyra, M., Reimold, W. U., Robin, E., Salge, T., Speijer, R. P., Sweet, A. R., Urrutia-Fucugauchi, J., Vajda, V., Whalen, M. T., & Willumsen, P. S. 2010. The Chicxulub Asteroid Impact and Mass Extinction at the Cretaceous-Paleogene Boundary. *Science*, **327**(5970), 1214–1218.

Self, S., Schmidt, A., & Mather, T.A. 2014. Emplacement characteristics, time scales, and volcanic gas release rates of continental flood basalt eruptions on Earth. *Pages 310 – 337 of: Volcanism, Impacts, and Mass Extinctions: Causes and Effects*. Geol Soc. Am. Spec. Paper 505.

Sepkoski, J. J. 1986. Phanerozoic Overview of Mass Extinction. *Pages 277–295 of:* Raup, D. M., & Jablonski, D. (eds), *Patterns and Processes in the History of Life*. Berlin, Heidelberg: Springer Berlin Heidelberg.

Sepkoski, J. J. 1989. Periodicity in extinction and the problem of catastrophism in the history of life. *J. Geol. Soc. (London, U. K.)*, **146**(1), 7–19.

Sepkoski, J. J. 2002. A compendium of fossil marine animal genera. *Bull. Am. Paleontol.*, **363**, 1–560.

Sepkoski, J. J., & Raup, D. M. 1986. Was there 26-Myr periodicity of extinctions? *Nature*, **321**, 533.

Servais, T., & Harper, David A.T. 2018. The Great Ordovician Biodiversification Event (GOBE): definition, concept and duration. *Lethaia*, **51**(2), 151–164.

Sewall, J. O., van de Wal, R. S. W., van der Zwan, K., van Oosterhout, C., Dijkstra, H. A., & Scotese, C. R. 2007. Climate model boundary conditions for four Cretaceous time slices. *Clim. Past*, **3**(4), 647–657.

Simon, L., Goddéris, Y., Buggisch, W., Strauss, H., & Joachimski, M. M. 2007. Modeling the carbon and sulfur isotope compositions of marine sediments: Climate evolution during the Devonian. *Chem. Geol.*, **246**(1), 19–38.

Six, K.D., & Maier-Reimer, E. 1996. Effects of plankton dynamics on seasonal carbon fluxes in an ocean general circulation model. *Global Biogeochem. Cy.*, **10**, 559–583.

Smit, J., & Brinkhuis, H. 1996. The Geulhemmerberg Cretaceous/Tertiary boundary section (Maastrichtian type area, SE Netherlands); summary of results and a scenario of events. *Geologie en Mijnbouw*, **75**(01), 283–293.

Sonnenfeld, P. 1978. Effects of a variable sun at the beginning of the Cenozoic era. *Clim. Change*, **1**, 355–382.

Sprain, C. J., Renne, P. R., Vanderkluysen, L., Pande, K., Self, S., & Mittal, T. 2019. The eruptive tempo of Deccan volcanism in relation to the Cretaceous-Paleogene boundary. *Science*, **363**(6429), 866–870.

Steffen, W., Rockström, J., Richardson, K., Lenton, T. M., Folke, C., Liverman, D., Summerhayes, C. P., Barnosky, A. D., Cornell, S. E., Crucifix, M., Donges, J. F., Fetzer, I., Lade, S. J., Scheffer, M., Winkelmann, R., & Schellnhuber, H. J. 2018. Trajectories of the Earth System in the Anthropocene. *Proc. Natl. Acad. Sci. USA*, **115**(33), 8252–8259.

Stocker, T. 2018. *Introduction to Climate Modeling*. Bern: Physikalisches Institut Universität Bern.

Tabor, C. R., Bardeen, C. G., Otto-Bliesner, B. L., Garcia, R. R., & Toon, O. B. 2020. Causes and Climatic Consequences of the Impact Winter at the Cretaceous-Paleogene Boundary. *Geophys. Res. Lett.*, **47**(3).

Tanner, L. H., Lucas, S. G., & Chapman, M. G. 2004. Assessing the record and causes of Late Triassic extinctions. *Earth Sci. Rev.*, **65**(1), 103 – 139.

Tierney, J. E., Poulsen, C. J., Montañez, I. P., Bhattacharya, T., Feng, R., Ford, H. L., Hönisch, B., Inglis, G. N., Petersen, S. V., Sagoo, N., Tabor, C. R., Thirumalai, K., Zhu, J., Burls, N. J., Foster, G. L., Goddéris, Y., Huber, B. T., Ivany, L. C., Kirtland Turner, S., Lunt, D. J., McElwain, J. C., Mills, B. J. W., Otto-Bliesner, B. L., Ridgwell, A., & Zhang, Y. G. 2020. Past climates inform our future. *Science*, **370**(6517).

Toon, O. B., Zahnle, K., Morrison, D., Turco, R. P., & Covey, C. 1997. Environmental perturbations caused by the impacts of asteroids and comets. *Rev. Geophys.*, **35**(1), 41–78.

Twitchett, R. J. 2006. The palaeoclimatology, palaeoecology and palaeoenvironmental analysis of mass extinction events. *Palaeogeography, Palaeoclimatology, Palaeoecology*, **232**(2), 190 – 213.

Tyrrell, T., Merico, A., & Armstrong Mckay, D. I. 2015. Severity of ocean acidification following the end Cretaceous asteroid impact. *Proc. Natl. Acad. Sci. USA*, **112**(21), 6556– 6561.

Urban, M. C. 2015. Accelerating extinction risk from climate change. *Science*, **348**(6234), 571–573.

Urrutia-Fucugauchi, J., Marin, L., & Trejo-Garcia, A. 1996. UNAM Scientific Drilling Program of Chicxulub Impact Structure-Evidence for a 300 kilometer crater diameter. *Geophys. Res. Lett.*, **23**(13), 1565–1568.

Urrutia-Fucugauchi, J., Morgan, J., Stöffler, D., & Claeys, P. 2004. The Chicxulub Scientific Drilling Project (CSDP). *Meteorit. & Planet. Sci.*, **39**(6), 787–790.

Vajda, V., & Bercovici, A. 2014. The global vegetation pattern across the Cretaceous–Paleogene mass extinction interval: A template for other extinction events. *Glob. Planet. Change*, **122**, 29 – 49.

van Geldern, R., Joachimski, M.M., Day, J., Jansen, U., Alvarez, F., Yolkin, E.A., & Ma, X.-P. 2006. Carbon, oxygen and strontium isotope records of Devonian brachiopod shell calcite. *Palaeogeogr. Palaeocl.*, **240**(1), 47–67.

Vellekoop, J., Sluijs, A., Smit, J., Schouten, S., Weijers, J. W. H., Sinninghe Damsté, J. S., & Brinkhuis, H. 2014. Rapid short-term cooling following the Chicxulub impact at the Cretaceous–Paleogene boundary. *Proc. Natl. Acad. Sci. USA*, **111**(21), 7537–7541.

Vellekoop, J., Esmeray-Senlet, S., Miller, K. G., Browning, J. V., Sluijs, A., van de Schootbrugge, B., Sinninghe Damsté, J. S., & Brinkhuis, H. 2016. Evidence for Cretaceous–Paleogene boundary bolide "impact winter" conditions from New Jersey, USA. *Geology*, **44**(8), 619–622.

Vennemann, T., Fricke, H., Blake, R., O'Neil, J., & Colman, A. 2002. Oxygen isotope analysis of phosphates: A comparison of techniques for analysis of Ag_3PO_4. *Chem. Geol.*, **185**, 321–336.

Wade, D. C., Abraham, N. L., Farnsworth, A., Valdes, P. J., Bragg, F., & Archibald, A. T. 2019. Simulating the climate response to atmospheric oxygen variability in the Phanerozoic: a focus on the Holocene, Cretaceous and Permian. *Clim. Past*, **15**(4), 1463–1483.

Weart, S. 2013. Rise of interdisciplinary research on climate. *Proc. Natl. Acad. Sci. USA*, **110**(Supplement 1), 3657–3664.

Westerhold, T., Marwan, N., Drury, A. J., Liebrand, D., Agnini, C., Anagnostou, E., Barnet, J. S. K., Bohaty, S. M., De Vleeschouwer, D., Florindo, F., Frederichs, T., Hodell, D. A., Holbourn, A. E., Kroon, D., Lauretano, V., Littler, K., Lourens, L. J., Lyle, M., Pälike, H., Röhl, U., Tian, J., Wilkens, R. H., Wilson, P. A., & Zachos, J. C. 2020. An astronomically dated record of Earth's climate and its predictability over the last 66 million years. *Science*, **369**(6509), 1383–1387.

Williams, M., Zalasiewicz, J., Haff, P., Schwägerl, C., Barnosky, A. D., & Ellis, E. C. 2015. The Anthropocene biosphere. *The Anthropocene Review*, **2**(3), 196–219.

Wilson, G., Ekdale, E., Hoganson, J., Calede, J. J., & Vander Linden, A. 2016. A large carnivorous mammal from the Late Cretaceous and the North American origin of marsupials. *Nat. Commun.*, **7**, 13734.

Wolbach, W., Gilmour, I., Anders, E., Orth, C. J., & Brooks, R. R. 1988. Global fire at the Cretaceous– Tertiary boundary. *Nature*, **334**, 665–669.

Wünnemann, K., & Weiss, R. 2015. The meteorite impact-induced tsunami hazard. *Philos. T. R. Soc. A*, **373**(2053), 20140381.

Zeebe, Richard E. 2012. History of Seawater Carbonate Chemistry, Atmospheric CO2, and Ocean Acidification. *Annu. Rev. Earth Planet. Sci.*, **40**(1), 141–165.

Zhang, F., Dahl, T. W., Lenton, T. M., Luo, G., Shen, S., Algeo, T. J., Planavsky, N., Liu, J., Cui, Y., Qie, W., Romaniello, S. J., & Anbar, A. D. 2020. Extensive marine anoxia associated with the Late Devonian Hangenberg Crisis. *Earth Planet. Sci. Lett.*, **533**, 115976.

Erklärung

Diese Arbeit ist bisher an keiner anderen Hochschule eingereicht worden. Sie wurde selbständig und ausschließlich mit den angegebenen Mitteln angefertigt.

Potsdam, den 12. Januar 2022

Julia Brugger